An Experimental and Computational Investigation of the Inelastic Behaviour of Trabecular Bone

Nicola Kelly B.E. (2008)

A thesis submitted to the National University of Ireland as fulfilment of the requirements for the Degree of Doctor of Philosophy

September 2012

Department of Mechanical and Biomedical Engineering
College of Engineering and Informatics
National University of Ireland, Galway

Supervisor of Research: Dr. Patrick McGarry

Abstract

Achieving sufficient initial implant stability is of paramount importance for orthopaedic device longevity. In order to improve the design of orthopaedic devices it is essential to gain a better understanding of the mechanical behaviour of the peri-prosthetic bone, both during and following implantation. The overall aim of this thesis is to provide a better understanding of the post yield behaviour of trabecular bone using experimental and computational analyses, and to investigate the importance of multiaxial trabecular bone plasticity in the implantation and failure of orthopaedic devices.

An initial investigation of full and surface cementation techniques of the tibial component in total knee arthroplasty reveals a multiaxial stress state in the peri-prosthetic trabecular bone. High von Mises stress and pressure stress computed in the trabecular bone motivates the investigation of the multiaxial post yield behaviour of trabecular bone. Samples of natural and synthetic trabecular bone are tested under confined compression loading conditions. The ability of the Drucker-Prager, Mohr-Coulomb and crushable foam plasticity formulations to predict the experimental behaviour is investigated. In the case of the crushable foam plasticity formulation, increased pressure stress during confined compression results in material yielding followed by a stress plateau, as observed experimentally. In contrast the Drucker-Prager and Mohr-Coulomb plasticity formulations fail to capture the experimental results, as increased pressure stress inhibits material yielding. The role of the trabecular bone microarchitecture in the apparent level multiaxial yielding of trabecular bone is then considered using micro-computed tomography based finite element models.

Following this, two macroscale orthopaedic device applications that involve multiaxial trabecular bone plasticity are considered: the subsidence of a vertebral interbody fusion device; and the press-fit stem implantation of a tibial component. Continuum based pressure dependent crushable foam plasticity formulations accurately predict the subsidence forces and plastic zone size, observed during device subsidence. It is also demonstrated that the crushable foam plasticity formulation provides accurate predictions of implantation forces for tibial component implantation. Additionally, the importance of friction at the implant-bone interface is highlighted.

The work presented in this thesis provides insight into the multiaxial post yield behaviour of trabecular bone. The implementation of continuum based crushable foam plasticity formulations for the simulation of the inelastic behaviour of trabecular bone may aid in the future analysis, design and development of orthopaedic devices.

Publications

Journal Articles

The following publications have arisen from the work presented in this thesis.

1. Cawley DT, Kelly N, Simpkin A, Shannon FJ, McGarry JP (2012) Full and surface tibial cementation in total knee arthroplasty: A biomechanical investigation of stress distribution and remodeling in the tibia. Clin Biomech. 27 (4):390-397.

2. Kelly N, McGarry JP (2012) Experimental and numerical characterisation of the elasto-plastic properties of bovine trabecular bone and a trabecular bone analogue. J Mech Behav Biomed Mater. 9:184-197.

3. Kelly N, Harrison NM, McDonnell PF, McGarry JP (2012) An experimental and computational investigation of the post-yield behaviour of trabecular bone during vertebral device subsidence. Biomech Model Mechanobiol. *In Press*.

4. Cawley DT, Kelly N, McGarry JP, Shannon FJ (2013). Cementing techniques for the tibial component in primary total knee replacement. Bone Joint J. *In Press*.

5. Kelly N, Cawley DT, Shannon FJ, McGarry JP. An investigation of the inelastic behaviour of trabecular bone during the press-fit implantation of a tibial component in total knee arthroplasty. *Under Review.*

Conference Presentations

Peer Reviewed International Conferences:

1. Podium Presentation at the 8th European Solid Mechanics Conference, Graz, Austria. July 2012.

2. Podium and poster presentation at the 19th Annual Symposium on Computational Methods in Orthopaedic Biomechanics, Long Beach, CA, USA. January 2011.

3. Poster presentation at the Annual Meeting of the Orthopaedic Research Society, CA, USA. January 2011.

4. Podium presentation at the European Society of Biomechanics, Edinburgh, Scotland. July 2010.

5. Poster presentation at the ASME Summer Bioengineering Conference, Lake Tahoe, CA, USA. June 2009.

Peer Reviewed National Conferences:

1. Podium presentation at Bioengineering in Ireland, University of Limerick and NUIG. January 2009, 2011.

2. Podium and poster presentation at the Sir Bernard Crossland Symposium, Queens University Belfast April 2009 and University College Dublin April 2010.

Acknowledgements

Firstly, I would like to express my thanks to my supervisor, Dr. Patrick McGarry, for his invaluable knowledge, guidance and support throughout my studies. You have taught me so much.

I would like to thank Derek Cawley and Fintan Shannon for their assistance and guidance in the clinical aspects of this research. I would also like to thank Pat Kelly and Kumar Saidha from the Mechanical and Biomedical Engineering Laboratory NUIG for their technical assistance. Thanks also to Noel Harrison and Pat McDonnell for providing vertebral specimens, μCT scans and for their technical input. Thanks to Paul O'Doherty from Ortho Recon for the donation of TKA components and the loan of operative equipment.

I acknowledge the College of Engineering and Informatics, NUIG for providing me with a postgraduate scholarship that funded this research and also the SFI/HEA Irish Centre for High-End Computing (ICHEC) for the provision of computational facilities and support.

A huge thanks to my fellow postgraduate students; Anna, Cat, Cathal, Claire, Conleth, Dave, Eamonn, Enda, Emer, Eimear, Evelyn, the Fionas, Lizanne, Mary, Meadhbh, Noel, Paul, Reyhanneh, Ríona, Stefaan, Ted, Tom, Weaf and Will.

Mammy and Daddy, thank you so much for your love, support and for everything you have done to get me this far. A special thanks to my sisters Karen and Lisa and also to my friends.

Eddie, your patience is unending! Thank you for everything.

Table of Contents

Chapter 1

Introduction

1.1 Thesis Motivation and Rationale

Achieving sufficient initial implant stability is of paramount importance for orthopaedic device longevity. Cementless fixation of orthopaedic devices has become increasingly popular. Cementless arthroplasty stems achieve primary fixation through mechanical press-fit insertion into the trabecular bone. In order to prevent failure of cementless stemmed devices it is essential to gain a better understanding of the mechanical behaviour of the peri-prosthetic bone, both during and following implantation. To date, the effect of the surgical implantation process and the fixation technique of press-fit stems on the stress state in the surrounding peri-prosthetic trabecular bone is not well characterised. Trabecular bone is naturally confined *in vivo* by a stiff cortical bone shell and undergoes multiaxial loading during normal physiological conditions in addition to during the surgical implantation of a device. The insertion of an orthopaedic device alters the stress state in the surrounding trabecular bone. In order to develop improved design of orthopaedic devices that prevent failure due to aseptic loosening (Figure 1-1(a)) and resist subsidence into the peri-prosthetic bone (Figure 1-1(b)), the multiaxial inelastic behaviour of trabecular bone must be completely understood.

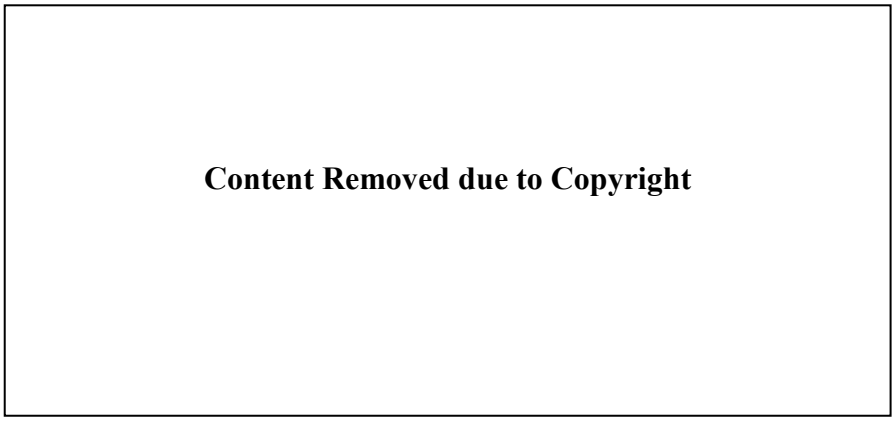

Figure 1-1 Failure of orthopaedic devices evident on x-ray images.
(a) Loosening of a tibial component in total knee arthroplasty (Wheeless 2012).
(b) Subsidence of a vertebral interbody fusion device (BJB 2012).

The overall aim of this thesis is:

To provide a better understanding of the post yield behaviour of trabecular bone using experimental and computational analyses. Furthermore, the importance of multiaxial trabecular bone plasticity in the implantation and failure of orthopaedic devices is investigated.

The flowchart in Figure 1-2 outlines the motivation and key findings of the four main studies, presented in Chapters 4, 5, 6 and 7.

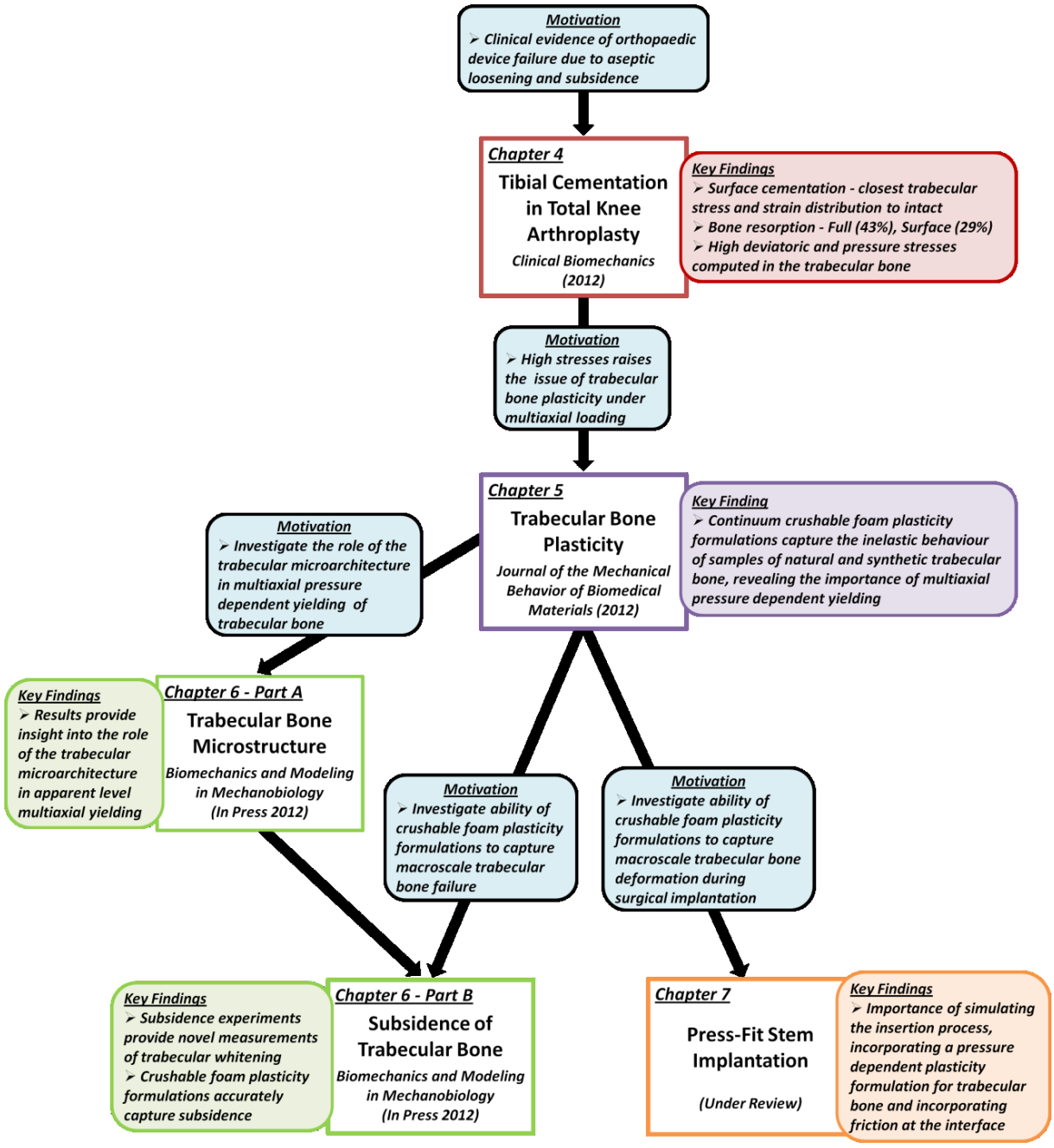

Figure 1-2 Flowchart of thesis motivation and key findings.

Chapter 4 – Tibial Component Cementation in Total Knee Arthroplasty (TKA)

In order to gain a better understanding of the effect of cemented and cementless stem fixation techniques of arthroplasty devices on the surrounding stress state in the peri-prosthetic trabecular bone an initial investigation is performed. This chapter is a joint experimental and computational investigation of full cementation (cemented stem) and surface cementation (cementless stem) fixation techniques of the tibial component in primary total knee arthroplasty. In addition to investigating cortical bone strains, a computational investigation of the alteration of stress and strain in the trabecular bone is performed. A key finding of this chapter is that for the surface cementation technique a more favourable stress state is computed in the proximal tibial trabecular bone which leads to less bone resorption predicted directly under the baseplate. As a result, more negative bone remodelling around the stem for full cementation may increase the rate of aseptic loosening . An important finding that also emerges from this chapter is the high deviatoric and pressure stresses computed in the proximal tibial peri-prosthetic trabecular bone for both cementation techniques. This important observation raises the issue of trabecular bone plasticity under multiaxial loading and provides motivation for an extensive experimental-computational investigation, as presented in Chapter 5.

Chapter 5 - Trabecular Bone Plasticity

Following the observation of a high multiaxial stress state in the confined trabecular bone in the proximal tibia in Chapter 4, further investigation of the mechanical behaviour of trabecular bone under multiaxial loading conditions is performed in Chapter 5. The chapter focuses in particular on the multiaxial pressure dependent post yield behaviour of trabecular bone due to a deficiency of knowledge in this area in the literature. In addition to mechanically testing tibial trabecular bone samples, samples of polyurethane foam are also investigated as this foam is a commonly employed analogue material for trabecular bone in the biomechanical testing of devices. A computational investigation of the post yield behaviour of both materials is performed, implementing the continuum based Drucker-Prager, Mohr-Coulomb and crushable foam constitutive plasticity formulations for both materials. In this chapter it is uncovered that the crushable foam plasticity formulations accurately

predict the multiaxial pressure dependent plasticity of the natural and synthetic trabecular bone. These findings provide motivation to, firstly, investigate the role of the trabecular bone microarchitecture in the multiaxial pressure dependent yielding of trabecular bone and, secondly, to investigate the ability of the crushable foam plasticity formulations to capture the macroscale subsidence of an orthopaedic device into an ovine vertebra.

Chapter 6 Part A - Trabecular Bone Microstructure

The investigations of Chapter 6 are subdivided into two distinct parts. In Part A, micro-computed tomography (μCT) based finite element models that explicitly represent the trabecular bone microarchitecture are loaded under uniaxial, confined and pure hydrostatic compression. The role of stress localisations at a trabeculae (microscale) level in the apparent level pressure dependent yield behaviour is investigated. Although commonly employed to investigate the mechanical behaviour of representative samples of trabecular bone, microstructural based models are very computationally demanding and hence are generally impractical to implement for macroscale applications which involve large trabecular volumes, large deformation, complex contact and inelastic material behaviour. The μCT simulations provide further validation of the use of a crushable foam plasticity formulation as a continuum representation of trabecular bone. In Part B of Chapter 6 the pressure dependent crushable foam plasticity formulations are used to simulate macroscale multiaxial inelastic deformation of trabecular bone during vertebral subsidence.

Chapter 6 Part B - Subsidence of Trabecular Bone

During the macroscale subsidence of a vertebral interbody fusion device, multiaxial large inelastic deformation of trabecular bone occurs. In this case, the trabecular bone is also naturally confined by the surrounding cortical bone, providing a multiaxial stress state. Therefore, this provides an ideal macroscale application to investigate the ability of continuum based crushable foam plasticity formulations to replicate the inelastic behaviour of natural trabecular bone. Continuum based von Mises, Hill and Drucker-Prager plasticity formulation are also considered. In order to quantify the trabecular bone deformation that occurs during the subsidence of a

device, experimental subsidence testing of a vertebral interbody fusion device into ovine vertebrae is also performed which provides a novel measurement of trabecular bone whitening. Whitening has been shown to be evidence of localised plastic deformation, crushing and microdamage of trabeculae (Jungmann et al. 2011; Thurner et al. 2007; Thurner et al. 2006). The ability of the crushable foam plasticity formulations to accurately predict both the experimentally measured subsidence forces and whitening zones is investigated.

Chapter 7 - Press-Fit Stem Implantation

To complete this body of work, a macroscale press-fit stem application is returned to in the final study. From the results of Chapter 4, it is postulated that, in addition to the fixation technique, the inelastic deformation of the peri-prosthetic trabecular bone during press-fit stem implantation may also influence the stress state. These observations, in addition to the multiaxial pressure dependent post yield behaviour observed for trabecular bone in Chapter 5, lead to the investigation of trabecular bone plasticity during macroscale surgical implantation. In this chapter, the multiaxial pressure dependent plastic deformation of the peri-prosthetic bone during the implantation process of the press-fit tibial component stem into synthetic tibiae is investigated. The role of friction at the bone-implant interface during implantation is also considered. To our knowledge, the multiaxial pressure dependent plasticity of trabecular bone has not previously been investigated during the insertion process of a press-fit arthroplasty stem. This final study uncovers the importance of: simulating the press-fit insertion process of orthopaedic devices; implementing friction at the bone-implant interface; and implementing a pressure dependent crushable foam plasticity formulation for the trabecular bone during implantation simulation.

1.2 Objectives

Having stated the main aim of the thesis above, the specific objectives of each study in the thesis are outlined in the following.

The objectives of the study in Chapter 4 are:

- To experimentally and computationally investigate the differences in peri-prosthetic stress state of a total knee arthroplasty tibial component for two fixation techniques, namely full cementation (cemented stem) and surface cementation (cementless stem).

The objectives of the study in Chapter 5 are:

- To experimentally investigate the multiaxial inelastic pressure dependent yield behaviour of samples of natural and synthetic trabecular bone.
- To investigate the ability of various pressure dependent plasticity formulations to replicate the multiaxial inelastic behaviour of both materials.

The objectives of the study in Chapter 6 are:

- To investigate the role of the trabecular microarchitecture in the multiaxial yield behaviour of trabecular bone using μCT based computational models.
- To investigate the ability of continuum based crushable foam plasticity formulations to capture the macroscale multiaxial inelastic deformation of trabecular bone during the subsidence of a vertebral fusion device.

The objectives of the study in Chapter 7 are:

- To investigate the multiaxial inelastic deformation of trabecular bone during the implantation of a press-fit tibial component stem in total knee arthroplasty.

1.3 Overview of Thesis

The following gives an outline of each chapter in the thesis.

In Chapter 2, a background to bone mechanics, total knee arthroplasty biomechanics and vertebral biomechanics is provided. A particular focus is on the mechanical properties and biomechanical loading of trabecular bone. Two orthopaedic devices, total knee arthroplasty and vertebral interbody fusion devices are described. It is worth noting that each of the subsequent technical studies (Chapters 4 to 7) also includes a focused discussion of the key literature directly relevant to each study, while Chapter 2 provides a more general background on bone mechanics and relevant orthopaedic devices.

In Chapter 3, the finite element theory and the constitutive plasticity formulations implemented in the computational work are outlined.

In Chapter 4, the full cementation and surface cementation techniques of the tibial component in total knee arthroplasty are investigated through experimental measurement of cortical bone strain in synthetic tibiae. A computational study is also performed to investigate the altered stress/strain distributions in the cortical and trabecular bone following both cementation techniques. Trabecular bone remodelling predictions are also provided for both cementation techniques. This chapter is published in the journal Clinical Biomechanics (Cawley et al. 2012). Derek Cawley and Nicola Kelly are officially listed as joint first authors on this publication.

In Chapter 5, representative samples of natural and synthetic trabecular bone are tested under uniaxial and confined compression loading conditions, representative of typical multiaxial physiological loading conditions of trabecular bone. The ability of the continuum based pressure dependent Drucker-Prager, Mohr-Coulomb and crushable foam constitutive plasticity formulations to replicate the experimental results is investigated. This chapter is published in the Journal of the Mechanical Behavior of Biomedical Materials (Kelly and McGarry 2012).

Chapter 6 is subdivided into two distinct parts. In Part A, the role of the trabecular bone microstructure in the apparent level multiaxial yield behaviour of trabecular bone is investigated using μCT based models of the trabecular microarchitecture. In Part B, the macroscale subsidence of a vertebral interbody fusion device into ovine vertebral trabecular bone is performed due to the large inelastic trabecular bone deformation that occurs during device subsidence. Experimental subsidence experiments are also performed in order to quantify whitening of the surrounding trabecular bone that occurs during subsidence. An investigation of the ability of numerous plasticity formulations to replicate the experimental results is undertaken. This chapter is published in the journal Biomechanics and Modeling in Mechanobiology (Kelly et al. 2012).

In Chapter 7, the implantation process of a press-fit stem of a total knee arthroplasty tibial component and the subsequent inelastic deformation of the peri-prosthetic trabecular bone is investigated. The von Mises and crushable foam plasticity formulations are implemented for the trabecular bone. The effect of friction at the implant-bone interface is also considered. This chapter has been submitted for journal publication and is currently under review.

Chapter 8 summarises the key findings of the thesis and outlines the significance of these findings for the analysis, design and development of orthopaedic devices. Some indications for possible future experimental and computational work are also provided.

References

BJB (2012) Subsidence of intervetebral fusion cages. University of Wisconsin-Madison. http://www.bjb.engr.wisc.edu/Research/Completed%20Projects/Subsidence/subsidence.html. Accessed 15/09/12 2012

Cawley, D. T., Kelly, N., Simpkin, A., Shannon, F. J., McGarry, J. P. (2012) Full and surface tibial cementation in total knee arthroplasty: A biomechanical investigation of stress distribution and remodeling in the tibia. Clin Biomech 27 (4):390-397.

Jungmann, R., Szabo, M. E., Schitter, G., Yue-Sing Tang, R., Vashishth, D., Hansma, P. K., Thurner, P. J. (2011) Local strain and damage mapping in single trabeculae during three-point bending tests. J Mech Behav Biomed Mater 4 (4):523-534.

Kelly, N., Harrison, N., McDonnell, P., McGarry, J. P. (2012) An experimental and computational investigation of the post-yield behaviour of trabecular bone during vertebral device subsidence. Biomech Model Mechanobiol:1-19.

Kelly, N., McGarry, J. P. (2012) Experimental and numerical characterisation of the elasto-plastic properties of bovine trabecular bone and a trabecular bone analogue. J Mech Behav Biomed Mater 9:184-197.

Thurner, P. J., Erickson, B., Jungmann, R., Schriock, Z., Weaver, J. C., Fantner, G. E., Schitter, G., Morse, D. E., Hansma, P. K. (2007) High-speed photography of compressed human trabecular bone correlates whitening to microscopic damage. Eng Fract Mech 74 (12):1928-1941.

Thurner, P. J., Erickson, B., Schriock, Z., Langan, J., Scott, J., Zhao, M., Weaver, J. C., Fantner, G. E., Turner, P., Kindt, J. H. (2006) High-speed photography of the development of microdamage in trabecular bone during compression. J Mater Res 21 (5):1093-1100.

Wheeless, C. R. (2012) Work up of the painful total knee arthroplasty. Wheeless' Textbook of Orthopaedics.
http://www.wheelessonline.com/ortho/work_up_of_the_painful_total_knee_arthroplasty. Accessed 15/09/12 2012

Chapter 2

Background

This chapter provides a background to bone mechanics, total knee arthroplasty biomechanics and vertebral biomechanics. A particular focus is on the mechanical properties and biomechanical loading of trabecular bone. Two orthopaedic devices that are in direct contact with trabecular bone, total knee arthroplasty and vertebral interbody fusion devices are described. It is worth noting that this chapter provides a more general background to the topics relevant to this body of work. Each of the subsequent technical studies (Chapters 4 to 7) also includes a focused discussion of the key literature directly relevant to each study.

2.1 Background to Bone Mechanics

The hierarchical structural organisation of bones such as the tibia, femur and vertebrae is complex, including levels at the macroscale, microscale, nanoscale and subnanoscale (Figure 2-1) (Rho et al. 1998). At the macroscale level (~1-5 mm) there are two types of bone, cortical (compact) and trabecular (cancellous) bone (Figure 2-2). As shown in Figure 2-2, an outer cortical shell surrounds irregular trabecular bone that is characterised by a less dense porous three dimensional interconnected network of rods and plates (~100-300 μm thick) interspersed with marrow (Fratzl and Weinkamer 2007; Martin et al. 1998). The density of cortical bone and individual trabeculae are approximately 1.8-2 g/cm^3 and 1.82 g/cm^3, respectively (Gibson and Ashby 1999). Although they have almost the same composition, trabecular and cortical bone differ in terms of their porosity which are approximately 75-95% and 5-10%, respectively (Fratzl and Weinkamer 2007; Martin et al. 1998). The mechanical properties of bone vary at differing structural levels and are influenced by many factors including the porosity and hierarchal structure.

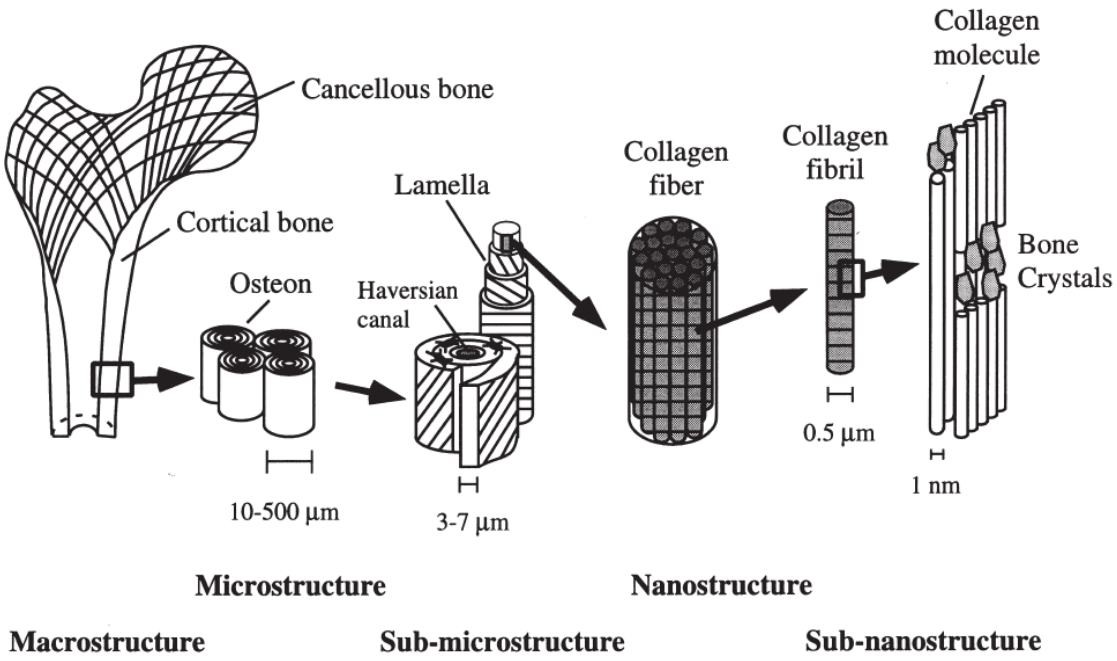

Figure 2-1 The hierarchical structure of bone as categorized by Rho et al. (1998): (a) cortical and trabecular bone; (b) osteons with Haversian systems; (c) lamellae; (d) collagen fiber assemblies of collagen fibrils; and (e) bone mineral crystals, collagen molecules and non-collagenous proteins.

2.1.1 Trabecular Bone

Trabecular bone is also known as cancellous or spongy bone and exists at the end of long bones such as the tibia and within the vertebral body (Figure 2-2). It is a complex, heterogeneous and anisotropic porous cellular solid. This natural composite material has an open porosity which contains bone marrow and is classified as an open cellular material. At a microscopic level, rods and plates represent the basic cellular structure of trabecular bone. Two anatomical sites that contain large amounts of trabecular bone, the proximal tibia and the lumbar vertebra, are considered in the present work.

Figure 2-2 The structure of a long bone.

2.1.1.1 Mechanical Properties of Trabecular Bone

The mechanical properties of trabecular bone are affected by several factors including anatomical location (Morgan et al. 2003; Morgan and Keaveny 2001), load, microarchitecture, bone mineral density (BMD) (Kopperdahl and Keaveny 1998; Morgan et al. 2003), sex, age (McCalden and McGeough 1997) and bone health (Li and Aspden 1997). The mechanical properties of representative samples of proximal tibial and vertebral trabecular bone tested under uniaxial compression are shown in Table 2-1. The measured Young's modulus and strength of samples of trabecular bone can vary by more than an order of magnitude (Table 2-1). Goldstein et al. (1983) reported a wide variation in Young's modulus within a single anatomic site, ranging from 4.2 to 430 MPa, for proximal tibial trabecular bone of five cadavers. Between anatomic site, the trabecular bone yield stress can vary by a factor of eight whereas yield strain can vary by approximately 20% (Morgan and Keaveny 2001). Trabecular bone yields at approximately 1% strain (Table 2-1) after which it can undergo large deformations of over 50% strain while maintaining its load bearing capacity. Trabecular bone displays strength asymmetry, displaying a higher yield stress in compression than in tension (Table 2-2). The Poisson's ratio of trabecular bone has been reported as ranging from 0.03 to 0.63 (Klever et al. 1985; Ulrich et al. 1999).

The mechanical properties of trabecular bone also depend on its porosity and the architectural arrangement of the trabeculae. The relative apparent density (or volume fraction) of trabecular bone can be calculated as the ratio of the density of bone to the density of a single trabecula (Gibson and Ashby 1999). The microarchitecture and density play a fundamental role in determining mechanical properties of trabecular bone and contribute to its anisotropy. The Young's modulus of trabecular bone is proportional to the square of the relative density (Gibson 2005). At low densities the trabecular structure consists of open cell rods and at higher densities the cells become more plate like and can fuse to a nearly closed cell structure (Gibson 2005; Gibson and Ashby 1999). The density of trabecular bone varies with anatomical site, with Morgan et al. (2003) measuring an apparent density of 0.09-0.75 g/cm^3 for human specimens from four different anatomical locations. Trabecular bone from the vertebra, which has a low density, is considered to have a thinner more rod-like trabeculae structure, whereas, trabecular bone from the proximal femur is denser and is considered to have a thicker more plate-like structure (Figure 2-3) (Hildebrand et al. 1999). Tibial specimens have a higher Young's modulus than vertebral specimens for a given density (Morgan et al. 2003).

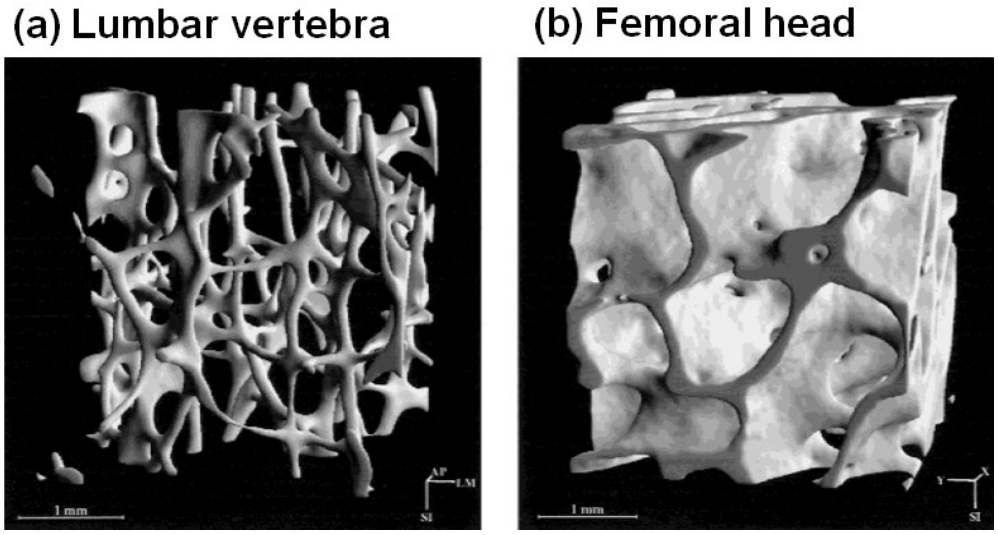

Figure 2-3 The microarchitecture of trabecular bone. (a) Low density rod-like trabeculae from the lumbar vertebra and (b) High density plate-like trabeculae from the proximal femur (Hildebrand et al. 1999).

Table 2-1 Mechanical properties of representative samples of trabecular bone tested in uniaxial compression from the literature. Values are presented as mean±standard deviation.

Anatomic Site	Specimen Origin	Apparent Density (g/cm^3)	Young's Modulus (MPa)	Yield Stress (MPa)	Yield Strain (%)	Author
Proximal tibia	Human	0.23±0.06	1091±634	5.83±3.42	0.73±0.06	(Morgan and Keaveny 2001)
Proximal tibia	Human		485±333			(Røhl et al. 1991)
Proximal tibia	Human		409±53			(Linde and Hvid 1989)
Proximal tibia	Bovine		2380±777	21.3±8.05	1.09±0.12	(Keaveny et al. 1994)
Proximal tibia	Bovine	0.55±0.11	2990±882, 1940±818			(Keaveny et al. 1997)
Proximal tibia	Human		31±18 to 336±86			(Goldstein et al. 1983)
Vertebra T10-L5	Human	0.18±0.05	344±148	2.02±0.92	0.77±0.06	(Morgan and Keaveny 2001)
Vertebra - lumbar	Human	0.14±0.06	165±110, 121±97			(Keaveny et al. 1997)
Vertebra	Human		67±45			(Mosekilde and Danielsen 1987)
Vertebra T10-L4	Human	0.17±0.04	291±113	1.92±0.84	0.84±0.06	(Kopperdahl and Keaveny 1998)
Vertebra L5	Ovine		1650±200			(Harrison et al. 2008)

Table 2-2 Yield strength asymmetry of trabecular bone tested in uniaxial compression and uniaxial tension from the literature. Values are presented as mean±standard deviation.

Anatomic Site	Specimen Origin	Compressive Yield Stress (MPa)	Tensile Yield Stress (MPa)	Author
Proximal tibia	Bovine	21.3±8.05	15.6±4.19	(Keaveny et al. 1994)
Vertebra T10-L4	Human	1.92±0.84	1.75±0.65	(Kopperdahl and Keaveny 1998)
Vertebra T10-L5	Human	2.02±0.92	1.72±0.64	(Morgan and Keaveny 2001)
Proximal tibia	Human	5.83±3.42	4.50±3.14	(Morgan and Keaveny 2001)

Bone is metabolically active and it is generally accepted that bone continuously responds and adapts in response to mechanical stress, through a process called bone remodelling (Wolff 1892). Therefore the continuous process of growth, resorption (bone loss) and formation (bone reconstruction) of bone are all relative to its mechanical environment and may occur due to mechanical stress, genetic factors, hormone response, environmental factors and cellular activity. However, the exact mechanism of bone remodelling is not fully understood. This functional adaptation of bone involves the process of bone removal by osteoclasts and bone formation by osteoblasts. Bone resorption due to a reduction in stress results in a decreased BMD as there is no remodelling stimulus to maintain the bone mass. The processes of resorption and formation need to be balanced to maintain sufficient bone mass. The trabecular orientation depends on the loading direction and the trabecular density depends on the magnitude of the loads (Carter et al. 1996; Huiskes et al. 1987; Huiskes et al. 1992).

Ageing and bone disease affect the mechanical properties of trabecular bone. The compressive strength of trabecular bone decreases with age, reducing approximately 10% every 10 years (McCalden and McGeough 1997). With ageing there is a disruption in the balance between the resorption and formation of bone resulting in increased resorption and decreased formation. Metabolic bone diseases, such as osteoporosis, also result in a reduction in bone mass and a deterioration of the trabecular microarchitecture which leads to an increase in fracture risk. In patients with osteoporosis a lower modulus (247 MPa), yield strength (2.5 MPa) and apparent density (0.28 g/cm^3) has been measured under uniaxial compression testing in proximal femoral specimens than in normal patients (310 MPa, 3.3 MPa and 0.47 g/cm^3, respectively) (Li and Aspden 1997). The implantation of a prosthetic device requires strong bone stock for optimal fixation; however, bone strength at the implantation site is often compromised due to osteoarthritis, osteoporosis, degenerative joint disease or disuse due to pain. Bone fracture can occur at high strain rates due to impact or may be caused by repetition (fatigue), prolonged (creep) or exceeding a stress or damage threshold level. Bone structure may also be compromised due to factors such as ageing, disease, diet, lack of exercise and surgery (Gupta and Zioupos 2008; Rho et al. 1998).

2.1.1.2 Biomechanics and Loading of Trabecular Bone

Knowledge of the complex *in vivo* loading conditions and mechanical behaviour of trabecular bone is particularly important in order to design successful orthopaedic devices to treat various bone pathologies. Trabecular bone is naturally confined by the surrounding stiff cortical shell and physiological loading results in a multiaxial stress state. During normal physiological loading conditions trabecular bone is typically loaded in the elastic regime. However during bone fracture, press-fit device implantation or the subsidence of an orthopaedic device, trabecular bone undergoes complex multiaxial inelastic deformation. Therefore, it is essential to understand the uniaxial and multiaxial loading conditions of trabecular bone.

Experimental Testing of Trabecular Bone

Experimental Uniaxial Compression Loading

In vitro mechanical compression testing is often performed on representative samples of trabecular bone (~5-15 mm). At this scale trabecular bone behaves as a continuum (Harrigan et al. 1988). Mechanical uniaxial compression tests are one of the most common tests performed on trabecular bone (Table 2-1) due to the ease of performing them and due to the fact that trabecular bone is often subjected to compressive loading. In addition to cadaveric specimens, trabecular bone from other species particularly ovine and bovine, have been widely used to characterise mechanical properties of trabecular bone (Table 2-1). Compression test specimens often vary in terms of the cross sectional area (cubic or cylindrical) and dimensions. Trabecular bone specimens used in such mechanical testing are prone to end-artifacts at the specimen periphery causing initial non-linear behaviour due to ease of crushing of the end trabeculae. Damage can occur at the specimen ends during compression testing due to disruption of the trabecular network (Linde et al. 1992; Odgaard and Linde 1991). Friction artifacts may lead to an over estimation of the modulus (Linde et al. 1992; Odgaard and Linde 1991). The size, aspect ratio, hydration and preconditioning of samples can also affect the measured mechanical properties (Keaveny et al. 1993; Keaveny et al. 1994a). Mechanical testing of trabecular bone is usually performed on hydrated specimens. To reduce end-artifacts, end supports such as the platens technique (specimen placed between parallel

loading platens) and the endcap technique (sample embedded in endcaps) have been employed. Due to such a varying test methodology, interpretation and application of results from representative samples of trabecular bone should be done with care.

For the mechanical testing in the present work, nominal stress, $\boldsymbol{\sigma}$, and nominal strain, $\boldsymbol{\varepsilon}$, are calculated from the load-displacement curves as

$$\boldsymbol{\sigma} = \frac{\mathrm{F}}{\mathrm{A}_0} \qquad \text{and} \qquad \boldsymbol{\varepsilon} = \frac{l - l_0}{l}$$

where F is the applied load, A_0 is the original undeformed cross-sectional area of the specimen and l_0 is the original length of the specimen. The Young's modulus, E, is calculated as the slope of the nominal stress-strain curve in the elastic regime. The yield stress, σ_y, is defined using the 0.2% strain offset method, whereby a straight line with a slope equal to the E with a 0.2% strain offset from the origin intersects the stress-strain curve. Figure 2-4 shows a typical stress-strain curve of a cubic sample of trabecular bone under uniaxial compression. The present work considers quasi-static loading of trabecular bone, where the strain rate is slow and rate effects are not considered. Additionally, all testing is performed on hydrated specimens at room temperature and hence the influence of temperature is not considered.

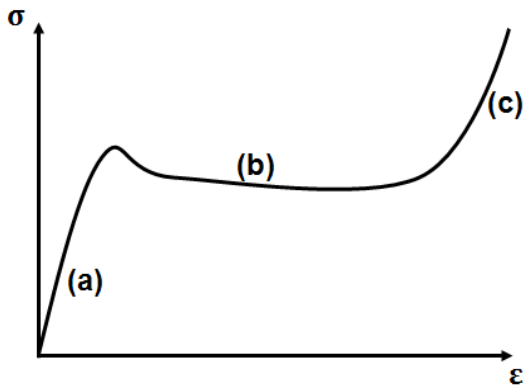

Figure 2-4 Schematic of a typical stress-strain curve of a cellular material such as trabecular bone showing the three distinct regions: (a) linear elastic; (b) stress plateau; and (c) densification.

The compressive stress-strain curve of a cellular material, such as foam or trabecular bone, is typically characterised by three distinct regions: (a) linear elastic; (b) stress plateau; and (c) densification (Figure 2-4). The initial linear elastic region occurs due to elastic bending of the cell walls, which is followed by material yield causing collapse of the cell walls (trabeculae) under constant load. This is followed by an

inelastic region where a near constant horizontal stress plateau occurs due to progressive cell wall damage, breakage and buckling under increased loading. Densification occurs when the cell walls contact and consolidate (whereby the density reaches that of the parent material) and the stress rapidly increases with increased strain (Gibson 2005; Gibson and Ashby 1999; Goldstein 1987; Neilsen et al. 1995; Szivek et al. 1993). The inelastic behaviour of cellular materials such as trabecular bone are strongly affected by hydrostatic pressure, display different strengths in tension and compression and are often anisotropic (Abrate 2008). Under compressive loading, trabecular bone displays a stiffness loss and develops permanent strain when it is loaded beyond its elastic limit, unloaded and then reloaded (Keaveny et al. 1999a). This indicates that trabecular bone displays evidence of both damage and plasticity. A reduction in modulus of up to 60% caused by damage within trabeculae was noted in specimen loaded beyond their yield point (Wachtel and Keaveny 1997).

Experimental Multiaxial Compression Loading

Although uniaxial compression tests are the most commonly performed mechanical compression test on trabecular bone, confined compression (Charlebois et al. 2010b; Linde and Hvid 1989) and multiaxial (Fenech and Keaveny 1999; Keaveny et al. 1999b; Rincon-Kohli and Zysset 2009) testing has also been performed. Linde and Hvid (1989) performed confined compression on human proximal tibial trabecular bone within the elastic regime, to a maximum strain of 0.8%. Linde and Hvid (1989) also performed compression testing of *in situ* trabecular specimens where the surrounding trabecular bone remained intact during loading. Confined compression testing of trabecular specimens from the human vertebra, radius, femoral head and calcanei was performed to large inelastic strains (~70%) by Charlebois et al. (2010b). Fenech and Keaveny (1999) performed axial-shear testing of bovine trabecular bone trabecular specimens, testing specimens in combined compression-torsion and combined tension-torsion. Keaveny et al. (1999b) tested bovine proximal tibial specimens to failure under triaxial compression with axial stress to radial pressure ratios of ~5 and ~8.3. Using cadaveric specimens from the femur, tibia, radius and vertebra, Rincon-Kohli and Zysset (2009) performed triaxial compression with axial stress to radial pressure ratios of ~9.5, ~4.6 and ~2.6.

Computational Models of Trabecular Bone

Experimental validation of a constitutive formulation for trabecular bone under physiologically relevant loading configurations is difficult and to date a complete multiaxial failure criterion that can accurately predict the complex multiaxial post yield behaviour of trabecular bone does not exist. Computational models have been used to assess the mechanical behaviour of trabecular bone, mainly under uniaxial compression loading. In addition to linear elastic material models, various non-linear constitutive formulations have been proposed in an attempt to replicate the experimentally observed inelastic behaviour of trabecular bone. Continuum based and microstructural based finite element models have been investigated for trabecular bone and both have associated advantages and disadvantages. High resolution microstructural models that are usually based on micro-computed tomography (μCT) scans have the advantage of incorporating the microstructural features of the trabecular bone, thus providing an accurate representation of the trabecular microarchitecture. However, such microstructural based models are computationally expensive and, hence, are usually limited in terms of contact conditions, material behaviour and deformation. Due to their computational efficiency, continuum based models are more practical for use in macroscale whole bone-implant models that involve large deformation, inelastic material behaviour and complex contact conditions.

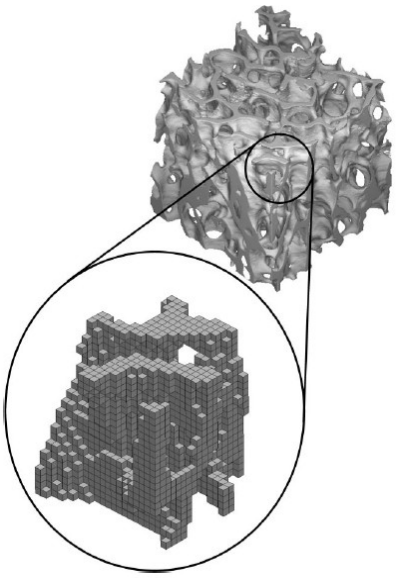

Figure 2-5 A microstructural based finite element model of a 5 mm cube of trabecular bone at 20 μm resolution. Inset: A section of the high-resolution finite element model showing the hexahedral geometry (Niebur et al. 2000).

Computational Uniaxial Compression Loading

Microstructural based high resolution finite element models of representative samples of trabecular bone have been investigated primarily using voxel based hexahedral geometry under uniaxial compression loading with linear elastic material models (Boyd et al. 2002; Harrison et al. 2008; Müller and Rüegsegger 1995; Nagaraja et al. 2005; Van Rietbergen et al. 1995).

Non-linear constitutive formulations have also been implemented for microstructural based finite element models to investigate the post yield behaviour of trabecular bone. Based on the post yield macroscopic testing of cortical bone specimens by Reilly and Burstein (1975) which show tension-compression strength asymmetry, Niebur et al. (2000) implemented a asymmetric bi-linear yield criterion for trabecular bone (Figure 2-6). The non-linear constitutive model of Niebur et al. (2000) reduces the post yield modulus of the trabecular material to 5% (of the elastic modulus) when critical principal strain is computed at a material point. This principal strain based criterion has also been implemented in various other studies for trabecular bone (Bayraktar et al. 2004; Bayraktar and Keaveny 2004; Harrison et al. 2012; MacNeil and Boyd 2008; Niebur et al. 2002; Verhulp et al. 2008). Guillén et al. (2011) implemented a multi-linear constitutive model, similar to the bi-linear principal strain based criterion of Niebur et al. (2000) which assumed perfect plastic material behaviour after an ultimate strain in compression and tension of 3% was exceeded.

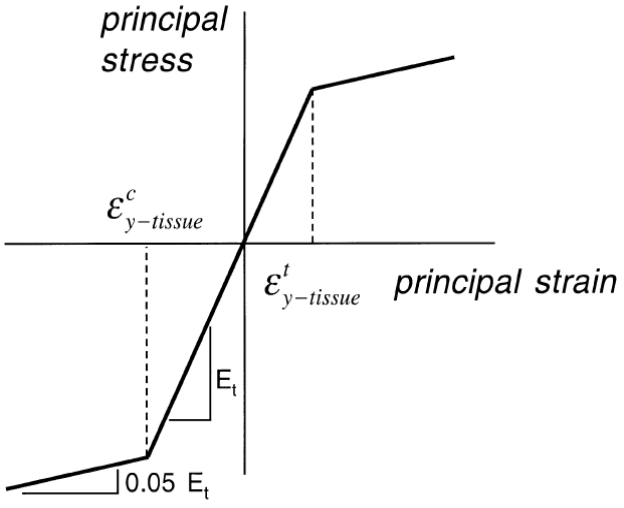

Figure 2-6 Schematic of the bi-linear principal strain based criterion (Niebur et al. 2000).

Also based on the testing of cortical bone specimens, Verhulp et al. (2008) implemented a principal strain based criterion that used a negative post yield modulus to incorporate post yield softening, and an elastic-perfectly plastic von Mises plasticity formulation for microstructural based models of trabecular bone loaded in uniaxial compression. A recent study by Harrison et al. (2012), modelling vertebral trabecular bone specimens under uniaxial compression incorporated material damage using the principal strain based criterion and fracture through element removal and cohesive forces in the trabecular microarchitecture.

Fabric based models which represent the trabecular bone morphology, have also been proposed to investigate the inelastic behaviour of trabecular bone where fabric tensors and volume fraction describe the heterogeneity and anisotropy of the bone, respectively (Charlebois et al. 2010a; Charlebois et al. 2010b; Chevalier et al. 2008; Rincon-Kohli and Zysset 2009; Zysset and Rincon-Kohli 2006; Zysset and Curnier 1996).

Computational Multiaxial Compression Loading

Using microstructural based finite element models with linear elastic material models, Van Rietbergen et al. (1995) and Boyd et al. (2002) performed apparent level confined compression loading up to a maximum of 1% strain. As the simulations of Van Rietbergen et al. (1995) and Boyd et al. (2002) are limited to the elastic regime they provide no insight into the multiaxial yield behaviour of trabecular bone. Using the principal strain based criterion, Niebur et al. (2002) simulated apparent level biaxial strain compression of microstructural based models of trabecular bone. In the on-axis and transverse directions apparent level compression was applied in a 1:1 ratio with no displacement in the other two directions, producing biaxial strain and triaxial stress (Niebur et al. 2002). Niebur et al. (2002) proposed a multiple-surface yield criterion with two intersecting yield ellipses for the on-axis and transverse yield points. Bayraktar et al. (2004) also used the principal strain based criterion at a trabecular level to simulate trabecular bone under normal-shear strain loading and proposed a modified super-ellipsoid yield criterion for trabecular bone in three dimensional principal strain space. Based on the modified super-ellipsoid yield criterion proposed by Bayraktar et al. (2004), Gupta et

al. (2007) considered a plasticity-like formulation with isotropic/kinematic hardening in strain space for trabecular bone.

Fenech and Keaveny (1999) investigated the ability of the von Mises plasticity formulation, the principal strain based criterion, the Tsai-Wu plasticity formulation and a cellular solid criterion to predict axial-shear failure experimental data. The cellular solid criterion, which was developed by Fenech and Keaveny (1999) for the axial-shear loading conditions, provided the best match to the experimental data. The Tsai-Wu plasticity formulation only reasonably predicted the combined axial-shear strength of the trabecular specimens (Fenech and Keaveny 1999). The original Tsai-Wu plasticity formulation (Tsai and Wu 1971) was also modified as a function of apparent density and applied to triaxial compression testing of bovine tibial trabecular bone by Keaveny et al. (1999b), but was shown to poorly predict the experimental data.

The confined (Charlebois et al. 2010b) and multiaxial (Rincon-Kohli and Zysset 2009) inelastic behaviour of trabecular bone have been investigated using fabric based models. Fabric and volume fraction reasonably predict the confined compression testing results of Charlebois et al. (2010b). Rincon-Kohli and Zysset (2009) used a fabric based conewise generalised Hill criterion to analyse the yield and strength data from triaxial compression testing.

In order to predict bone fracture, various plasticity formulations have been applied to continuum based finite element models of whole bones (cortical and trabecular bone) including the von Mises (Derikx et al. 2011; Keyak 2001; Keyak and Rossi 2000) and Drucker-Prager (Bessho et al. 2007; Derikx et al. 2011) plasticity formulations. The Drucker-Prager plasticity formulation provided superior predictions of the experimental failure of human cadaveric femoral bone, when compared to a von Mises plasticity formulation (Derikx et al. 2011). Bessho et al. (2007) tested cadaveric femurs to failure and implemented a principal strain based criterion for a whole bone femur model which is pressure dependent through the use of the Drucker-Prager equivalent stress.

2.1.2 Cortical Bone

Cortical or compact bone forms the outer structural shell of long bones such as the tibia and femur as well as the vertebral body. The mechanical behaviour of cortical bone is very different to that of trabecular bone. Cortical bone is anisotropic in terms of its elastic and strength properties and has a higher modulus in the longitudinal than transverse directions (Table 2-3). Cortical bone is much stiffer in comparison to trabecular bone (Table 2-3), hence physiological loading generally results in small deformations. Therefore, linear elasticity is often used to describe its mechanical behaviour.

Table 2-3 The Young's modulus of longitudinal cortical bone under compression (Wang et al. 2010).

Anatomic Site	Species	Young's Modulus	Author
Tibia	Human	25.9-35.3 GPa	(Burstein et al. 1976)
Tibia	Bovine	7.1 GPa	(Simkin and Robin 1973)
Femur	Human	15.2-18.1 GPa	(Burstein et al. 1976; McElhaney 1966)
Femur	Bovine	22.6 GPa	(Reilly and Burstein 1975)
Femur/tibia/humerus	Human	14.2 GPa	(Dempster and Liddicoat 1952)
Femur	Bovine	18.6 GPa	(McElhaney 1966)

2.1.3 Synthetic Bone

Synthetic bone substitutes, including commercially available sawbones, have been widely used as an experimental tool for the testing of device design (Agneskirchner et al. 2006; Bert and McShane 1998; Completo et al. 2007a; Completo et al. 2007b; Feerick et al. 2012; Luring et al. 2006; Vanlommel et al. 2011). Synthetic bones are advantageous as a substitute for cadaveric specimens for the testing of orthopaedics devices due to their availability, ease of handling, ease of preparation and lower inter-specimen variability (Cristofolini and Viceconti 2000; Cristofolini et al. 1996; Heiner and Brown 2001). Experimental testing of the mechanical and structural properties of synthetic sawbones has shown that they are comparable to natural bone (Chong et al. 2007; Cristofolini and Viceconti 2000; Currey 1984; Heiner 2008). The synthetic 4th generation composite sawbone tibiae (#3402, Pacific Research Labs, Inc. Vashon, WA) are geometrically similar to an adult male. A closed cell polyurethane foam core represents the trabecular bone which is surrounded by a cortex composed of a glass fiber reinforced epoxy resin (Figure 2-7).

Figure 2-7 The fourth generation composite sawbone tibia used in the present work with a 10 pcf (ρ = 0.16 g/cm^3) cellular rigid polyurethane foam core.

Two types of closed cell polyurethane foam are available, cellular rigid and solid rigid. A range of rigid closed cell polyurethane foams (grades 5-50, ρ = 0.08-0.8 g/cm^3) have been identified in ASTM F1839-08 (ASTM 2008). The synthetic fourth generation sawbone tibiae used in the present work in Chapters 4 and 7, are custom made with a cellular rigid 10 pcf (ρ = 0.16 g/cm^3) polyurethane foam core by the manufacturer, and have a Young's modulus (Table 2-4) within the range measured for human proximal tibial trabecular bone (4.2-430 MPa) (Goldstein et al. 1983). Table 2-4 provides details of the synthetic cortical and trabecular bone used in the present work (Chapters 4, 5 and 7).

Table 2-4 Details of the synthetic cortical (short fiber reinforced epoxy resin) and trabecular bone (polyurethane foam) materials tested in the present work.

Material	Type and Grade	Density (ρ)	Compressive Young's Modulus (E)	Compressive Strength (σ_y)
Epoxy Resin	Synthetic cortical bone	1.64 g/cm^3	16,700 MPa	157 MPa
Polyurethane foam	Cellular rigid - 10 pcf	0.16 g/cm^3	23 MPa	2.3 MPa
Polyurethane foam	Cellular rigid - 20 pcf	0.32 g/cm^3	137 MPa	5.4 MPa
Polyurethane foam	Solid rigid - 50 pcf	0.80 g/cm^3	1148 MPa	48 MPa

2.2 Total Knee Arthroplasty Biomechanics

2.2.1 The Knee Joint

The knee, the largest and most complex joint in the body, is a synovial hinge joint connecting the bones of the tibia, femur, fibula and patella (Figure 2-8). The bones of the knee along with the leg muscles, cartilage, meniscus, tendons and ligaments stabilise the knee and allow for motion. The femoral condyles are located at the distal surface of the femur and articulate with the proximal surface of the tibia, the tibial plateau, forming the tibio-femoral joint which flexes and extends the knee. The medial and lateral menisci lie between the joint and function to compensate for the incongruence of the articulating bones. The tibial plateau serves as the weight bearing portion of the knee and the outer portion of each tibial plateau contacts the medial and lateral menisci and the central portions articulate with the femoral condyles.

Figure 2-8 Anatomy of the knee.

The knee is mechanically a very complex joint. Identifying knee joint biomechanics is essential to device design and the prevention of knee disorders. Tibio-femoral motion is constrained by bone geometry, menisci and muscular attachments via tendons and ligaments. Knee flexion (0º-135º) occurs due to a combination of sliding and rolling between the femoral condyles and the tibial plateau. The adult human gait, the erect bipedal gait, involves a series of coordinated movements. One gait cycle is defined as the period from heel contact of one foot, to the next heel contact of the same foot, with duration of about one second. The gait cycle contains the swing and stance phase. As shown in (Figure 2-9), during the stance phase of walking there are three loading peaks: on heel strike; just after heel strike; and before

toe off (Andriacchi and Hurwitz 1997; Heinlein et al. 2009; Ramsey and Wretenberg 1999). Compressive loading of the knee joint is asymmetric. This asymmetry in load distribution on the tibial plateau is an important factor when considering compressive load distribution in the knee and is well documented in the literature (Bert and McShane 1998; Morrison 1970; Peters et al. 2003; Schipplein and Andriacchi 1991). Completo et al. (2007a; 2007b, 2008; 2009) loaded intact and implanted synthetic tibiae at a ratio of 60:40 (1060N:870N) to the medial and lateral plateau.

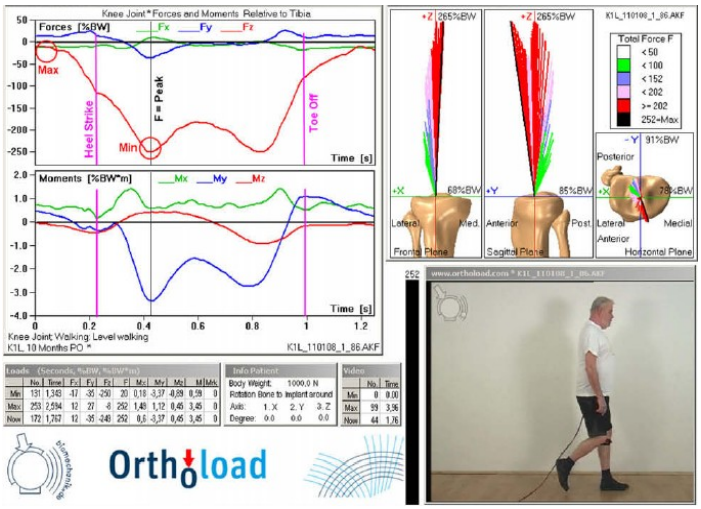

Figure 2-9 Typical pattern of knee joint forces and moments relative to the tibia experienced during level walking (Heinlein et al. 2009).

The most common causes of loss of knee function and pain are from degenerative knee joint diseases such as osteoarthritis, rheumatoid arthritis and post-traumatic arthritis. Osteoarthritis causes the menisci and the articular cartilage on the surfaces of the tibia and femur to soften and wear away, leaving the bone exposed. Bone on bone contact during articulation causes pain and stiffness. Rheumatoid arthritis results in thickening and chronic inflammation of the synovial membrane which can damage the cartilage. Other problems such as bone fracture or severe knee menisci and ligament tears may damage the articular cartilage over time. In response to pain, it is common to avoid the movement that causes pain and off-load or refrain from using the leg which leads to joint stiffness, decreased range of motion and decreased BMD. To date, no treatment exists that stops or reverses the progression of arthritis.

2.2.2 Total Knee Arthroplasty

Total knee arthroplasty (TKA) is an established and successful surgical procedure for treating end-stage degenerative knee joint disease caused by a variety of factors including trauma, disease and joint surface damage. TKA endeavours to restore the mechanical and functional aspects of the knee and allow the patient to return to normal daily activities. TKA typically involves removing the bony surfaces of the distal femur and proximal tibia as well as the joint space soft tissues and replacing them with a prosthetic device. In 2005, it was reported that approximately 440,000 are TKAs performed worldwide yearly (Zihlmann et al. 2005). Indications for primary TKA are broadening, with TKAs being performed on younger, heavier and more physically demanding patients. Due to an increased life expectancy and adiposity the number of TKA procedures is expected to increase yearly, with Kurtz et al. (2007) projecting that primary TKA demand will increase by 673% to 3.48 million procedures. The number of patients requiring revision TKA is also significant, with the demand for revision expected to double by 2015 and increase by 601% between 2005 and 2030 (Kurtz et al. 2007). In an international survey of 18 countries, Kurtz et al. (2011) reported that the average rate of primary and revision (combined) TKA was 175 procedures per 100,000 population.

Figure 2-10 The Genesis II Total Knee System (www.smithandnephew.com).

2.2.2.1 Implant Design and Materials

At present, a huge variety of TKA designs are available with a variety of different design aspects including fixed bearing, mobile bearing and rotating hinge designs. Current designs allow for the preservation of the posterior cruciate or for the resection or preservation of both cruciate ligaments. Modern designs take into consideration the complex biomechanics of the knee joint, asymmetrical loading, biocompatibility and complex motion. Current TKA designs are anatomically shaped and generally comprise of: a stemmed metal tibial component; a metal distal femoral component; a polymer liner; and a patellar component (Figure 2-10) (Öchsner and Ahmed 2010). Contemporary, tibial components contain a central stem that extends inferiorly from a flat tibial tray, which necessitates drilling of the proximal tibial metaphysis (Figure 2-10 and Figure 2-11). This modification has largely replaced previous models which anchored the implant with screws or short pegs. Modern central stems may contain a winged, cruciform, I-beam or side fins which are collectively called a keel. It has been shown that a central stem or keel enhances rotational stability and avoids anterior rocking force (Albrektsson et al. 1990). Walker et al. (1990) showed that the stem and fin design increases lift-off resistance in eccentric loading. The bearing surface, or liner, is commonly made of ultra high molecular weight polyethylene (UHMWPE) and sits between the tibial and femoral components via a locking mechanism on the tibial tray. The femoral component rotates freely on the liner and allows flexion, extension and slight rotation of the knee joint. Contemporary femoral components have the capability to externally rotate which optimizes rotational alignment.

The prosthesis used in the present work is the posterior cruciate ligament retaining Genesis II Total Knee System (Smith & Nephew, Memphis, TN, USA) as shown in Figure 2-10 and Figure 2-11. The 3° posterior sloped left size 8 tibial baseplate is a non-porous titanium alloy with an underlying press-fit stem and keel (Figure 2-11). The proximal 30 mm of the tibial stem is press-fit into the tibial metaphysis and the distal portion of the stem (30-50 mm) has a reduced diameter. A 9 mm UHMWPE liner is fit to the tibial baseplate via a locking mechanism. The load is distributed through left size 6 femoral component that rotates on the polyethylene liner.

Figure 2-11 The tibial component of the Genesis II TKS (www.smithandnephew.com). The tibial component is composed of a tibial tray (or baseplate) with an inferior central stem and side fins. The term keel refers to the stem and fins collectively.

2.2.2.2 Implant Fixation Techniques

Fixation of the tibial component in primary TKA may be achieved with bone cement (cemented) or without (cementless) bone cement. Fixation of orthopaedic device stems with polymethylmethacrylate (PMMA) bone cement has been used for over 40 years. PMMA bone cement usually comes in a two parts, a liquid and a paste, and is mixed in the theatre either by hand, by machine or in a vacuum. Pressurisation of the cement onto the bone allows for increased cement penetration into the porous trabecular bone. Tapered stem designs also increase pressurisation. Bone cement relies on mechanical interlock with the bone to achieve fixation (Öchsner and Ahmed 2010).

To achieve initial fixation, cementless tibial component stems are generally press-fit into the tibial metaphysis. For secondary fixation cementless stems contain a roughened or porous surface topography to encourage bone in-growth at the implant-bone interface (Öchsner and Ahmed 2010). Cementless implant fixation is a relatively new concept and has not shown superiority to cemented implants thus far (Gandhi et al. 2009; Rand et al. 2003). Ten year survivorship of 92% for cemented fixation and 61% for cementless fixation has been reported (Rand et al. 2003), however, a long term comparison of cemented and cementless fixation in TKA is not possible.

Cementation techniques in TKA vary greatly despite such a relatively common orthopaedic procedure. The two most common cementation techniques used for the tibial component are full (complete) cementation and surface (horizontal, partial or hybrid) cementation. Full cementation (FC) of the tibial component involves cement application across the proximal tibial cut surface as well as to the stem and keel of the implant, as illustrated in Figure 2-12(a). Surface cementation (SC) of the tibial component entails the application of cement solely across the proximal tibial cut surface, avoiding cementation of the stem and keel (cementless stem) (Figure 2-12(b)). SC tibial component stems are generally press-fit into the trabecular bone to achieve adequate fixation. For cemented primary TKA surgery, the optimal tibial component cementation technique (FC or SC) remains controversial.

Figure 2-12 Cementation fixation techniques of the tibial component (a) full cementation and (b) surface cementation (reproduced from www.smithandnephew.com).

2.2.2.3 Total Knee Arthroplasty Problems and Failure Modes

Millions of primary TKA procedures are performed annually and despite good clinical results with over 90% implant survival (Hofmann et al. 2006; Kolisek et al. 2009; Schai et al. 1998), the small percentage of reported failures represents a significant number of patients. In addition to being very frustrating to the patient, TKA failure is a considerable cost to healthcare systems worldwide. Some common TKA failure modes include loosening, migration, polyethylene wear, misalignment and infection (Austin et al. 2004; Sharkey et al. 2002). Revision TKA surgery, the standard treatment for a failed primary TKA, is more complicated and has less favourable outcomes than the primary surgery. Revision TKA frequently results in loss of bone stock during primary implant removal and repeat surgery. Revision

surgery is technically difficult and to compensate for the loss in bone mass, augments such as long stems, wedges and bone grafts are often required to adequately secure a revision implant. The focus of revision TKA is quite different to primary TKA and hence is outside the scope of the present work. However, facilitating any potential revision procedure warrants consideration during primary TKA.

Bone Quality and Stress Shielding

Bone quality is a major factor in implant stability and many patients presenting for TKA may have significant bone loss and/or decreased bone density. Bone loss leads to a weaker bone construct and may occur as a result of disease, bone defects and disuse bone resorption (weight avoidance). Furthermore bone loss post-TKA may occur due to implant design, fixation technique, malalignment, loosening or stress shielding. Stress shielding may occur post-implantation whereby the stresses in the bone remodel due to the altered mechanical loading. This adaptation of bone may progress for a number of years and may be a contributory factor to TKA component failure. A decrease in BMD adjacent to the implant post-TKA has been reported (Hernandez-Vaquero et al. 2008; Lonner et al. 2001; Munro et al. 2010; Regnér et al. 1999). In a clinical study measuring BMD seven years post-TKA using dual energy x-ray absorptiometry (DEXA) scanning, Lonner et al. (2001) compared a 4 cm stemmed FC component to the unoperated contralateral knee. Lonner et al. (2001) found significant proximal bone loss for FC with no significant differences in bone loss evident in the diaphysis, however, SC was not considered. Investigating BMD in SC versus the unoperated contralateral knee, proximal trabecular bone loss of up to 12.6% was measured at two years post-TKA for a cruciform and stemmed tibial component (Munro et al. 2010). Regnér et al. (1999) noted differences in BMD under the tibial plateau for cementless devices with different stem coatings. In an cadaveric study, Seki et al. (1997) measured proximal tibial cortical strains and in comparison to primary SC, primary FC reduced the mean principal strains of all gauges (solely measured at 1 mm from the cut surface) by 30-50%. The study of Seki et al. (1997) demonstrated that FC results in significant strain relief in the proximal tibial cortex; however trabecular strains were not investigated.

Bone remodelling has also been characterized mathematically. Simulation of bone remodelling can be used to investigate potential sites of bone resorption and formation. The following is a widely implemented strain adaptive bone remodelling algorithm (Huiskes et al. 1987; Huiskes et al. 1992; Ong et al. 2009; Weinans et al. 1993) whereby the apparent density is used characterise the bone morphology and strain energy density (SED) is the stimulus. Relative changes in SED are computed from a reference intact case, S_{ref}, and a post-implanted case, S_{post}. An increase in SED of ≥75% at any point in the bone results in positive remodelling i.e. bone formation, whereas, a decrease in SED of ≤75% results in negative remodelling i.e. bone resorption. The mechanical stimulus, s, is related to the resultant bone remodelling through the equations

$$(1-s)S_{ref} <= S_{post} <= (1+s)S_{ref}$$

where $s = 0.75$, S_{ref} is the SED for the intact bone and S_{post} is the SED for the bone post-implantation. A lazy zone, where no remodelling occurs, is the region between $(1-s)S_{ref}$ and $(1+s)S_{ref}$. The rate of change of density, ρ, is linearly related to the SED stimulus and the Young's modulus, E, is related to the remodelled bone density using the relationship

$$E = c\rho^3$$

where

$$c = 3790\ \mathrm{MPa}/(\mathrm{g/cm^3})^3$$

Mechanical Stability and Aseptic Loosening

The lack of post-operative implant stability is recognised as an important determinant in the aseptic loosening failure process of knee implants. Relative motion between the implant and bone may eventually lead to pain, stiffness, instability, rotation, subsidence and loss of function which may result in prosthesis loosening and subsequent failure of the component. Aseptic loosening, loosening of a prosthetic component without infection, is one of the most common causes of TKA revision surgery, accounting for 16.1-41.5% of revision procedures (AOA 2011; Bozic et al. 2010; CJRR 2008-2009; Sharkey et al. 2002). Loosening may be identified on an x-ray showing radiolucent lines at the bone-implant interface.

Mechanical stability of the tibial component is crucial to the long term outcome of TKA and is reliant on many factors that warrant consideration when cementing including: bone quality and porosity; bone preparation; cementation method; cement quantity and mantle thickness; cement penetration; viscosity; pressure; timing; temperature; and humidity. Such factors are largely due to the clinician's preference and are of major importance to surgical outcome. For cementless stems, mechanical stability is achieved through press-fitting into the trabecular bone and therefore should consider factors such as the bone quality and porosity in addition to the amount of interference. Further research into the consequences of such factors for cementless and cemented fixation would aid in future arthroplasty device design and development, ultimately increasing TKA survival rates. The following sections discuss the relevant literature regarding initial stability of the tibial component, with particular focus on FC (cemented stem) and SC (cementless stem) fixation techniques.

Cemented Fixation

To optimise long term tibial component stability in TKA, initial prosthetic fixation is of paramount importance. The fixation method has a significant influence on stability, particularly in poor quality bone. There is an ongoing debate in the orthopaedic community about which cementation technique for the tibial component is superior, SC or FC, with conflicting results from several studies (Bert and McShane 1998; Luring et al. 2006; Peters et al. 2003; Saari et al. 2008; Seki et al. 1997; Skwara et al. 2009). It is claimed that FC provides greater stability, better fixation and helps prevent aseptic loosening (Bert and McShane 1998; Luring et al. 2006). However, the metaphyseal cement at the stem in FC will complicate future revisions as it frequently results in loss of trabecular and cortical bone during removal of the primary implant (Bert and McShane 1998). Advocates of the SC technique claim it can achieve adequate fixation providing initial stability, maintain metaphyseal bone density thus leaving the bone less vulnerable to stress shielding (Hofmann et al. 2006; Seki et al. 1997; Skwara et al. 2009). An overview of studies in the literature that have investigated the FC and SC cementation techniques is provided in Table 2-5.

Clinical reviews have investigated SC and/or FC of the tibial component in primary TKA (Hofmann et al. 2006; Kolisek et al. 2009; Schai et al. 1998; Sharkey et al. 2002) with conflicting results, highlighting the need for a thorough biomechanical investigation of the optimal cementation technique. In a review of 212 revision TKAs, Sharkey et al. (2002) reported aseptic loosening of the tibial component as the second highest reason for revision (24.1%). Of these aseptically loose implants 21% were uncemented and 10.5% were SC, with the conclusion that SC should be abandoned (Sharkey et al. 2002). Interestingly, malalignment was deemed likely to account for nearly half of the aseptically loose cases (Sharkey et al. 2002). Schai et al. (1998) described a survival rate of 90% at 10 years from a series of 235 patients of which 226 were cemented (144 FC, 82 SC). 100% survivorship at 10 years was found for SC, with only one knee requiring tibial component revision and although only SC was considered, the SC technique was advocated as it conserves bone and limits bone loss upon revision (Kolisek et al. 2009). At midterm follow-up of 128 SC knees, Hofmann et al. (2006) reported excellent durable results with a survivorship of 98% at an average of 95 months with no tibial component revisions.

Table 2-5 Overview of studies that investigated the differences in the FC and SC cementation techniques of the tibial component.

Author	Cement Technique	Implant	Cement penetration/ mantle	Study Type	Investigated	Model	Results
(Skwara et al. 2009)	FC (*n* = 10) SC (*n* = 10)	Genesis II TKS, Smith & Nephew, Schenefeld, Germany	Not described	1000 and 10000 cycles 2000 N (3xBW), RSA	Micromotion, RSA	*In vitro* cadaver	No significant differences in initial stability. Failure (migration >2 mm) in 6 FC, 2 SC
(Peters et al. 2003)	FC (*n* = 12) SC (*n* = 12)	Maxim Complete Knee System, Biomet, Warsaw, IN, cruciate and I-beam stems	Average depth of cement mantle penetration 3.6-4.9 mm	6000 cycles to 1500N	Micromotion	*In vitro* cadaver	No difference between stem design or cementation method
(Bert and McShane 1998)	FC (*n* = 3) SC (*n* = 2)	Advantim C.F., Wright Medical Technology, TN	Refer to Table 2-6.	100 cycles 2446N (2xBW) PM biased	Micromotion	*In vitro* synthetic bone	Greater lift-off for SC with 1 mm cement mantle. No difference for 3 mm mantle
(Luring et al. 2006)	FC (*n* = 5) SC (*n* = 5)	PFC Sigma, DePuy, Warswa, IN	3 mm mantle under tray, FC stem mantle not described	Cyclic load to 2500 N (3xBW), 4 biased loadings: A; M; L; P	Micromotion	*In vitro* synthetic sawbone	Significantly increased mean max lift-off in SC. Proposed FC

(Seki et al. 1997)	FC, SC	metal backed tibial component modified for modular stem insertion	Not described	Micromotion - Cyclic load: 2250 N (60:40 M:L); 1500 N (M, L) Strain - Static load 2250 N	Micromotion Microstrain - cortical bone strains 1mm under tray	*In vitro* cadaver (*n*=8)	Primary FC reduced the mean principal strains of all gauges by 30-50% compared to SC
(Saari et al. 2008)	FC (*n* = 15) SC (*n* = 15)	PROFIX TKS, Smith & Nephew, Memphis, TN	Not described	RSA - Clinical and radiographic study at 2 years	Migration	*In vivo* human	No statistical difference at 2 years post-TKA
(Schai et al. 1998)	FC (*n* = 144) SC (*n* = 82)	PFC, Johnson & Johnson Inc. cruciate press-fit stem	Not described	Clinical and radiographic review	Survivorship at 10 years	*In vivo* human	Survival rate of 90% at 10 years

Abbreviations in Table: A = anterior; M = medial; L = lateral; P = posterior; PM = postero-medial.

Table 2-6 Full and surface cementation techniques used in the study of Bert and McShane (1998).

Cementation Technique	Cut surface	Stem
SC	1 mm cement mantle	Press-fit (no cement)
FC	1 mm cement mantle	1 mm cement mantle
FC	1 mm cement mantle	Press-fit with bone-cement interdigitation
SC	3 mm cement mantle	Press-fit (no cement)
FC	3 mm cement mantle	1 mm cement mantle

Micromotion, motion between the implant and surrounding bone that is not detectible with radiographs, has been shown to play a role in aseptic loosening. Micromotion studies investigating cementation technique have been performed using roentgen stereophotogrammetric (or radiostereometric) analysis (RSA) in both *in vivo* clinical (Saari et al. 2008) and *in vitro* studies via cyclic loading (Efe et al. 2011; Skwara et al. 2009). In a clinical RSA study, Saari et al. (2008) found no statistical differences in migration between FC and SC tibial components two years post-TKA with no revisions. Most of the previous biomechanical studies investigating tibial cementation in primary TKA have focused on cyclic loading to detect micromotion between the baseplate and cut surface with conflicting results on the optimum cementing technique (Table 2-5) (Bert and McShane 1998; Efe et al. 2011; Luring et al. 2006; Peters et al. 2003; Seki et al. 1997; Skwara et al. 2009).

Luring et al. (2006) measured a significantly increased mean maximum lift-off in the SC after a load of 2500 N (3xBW) in contrast to the FC, and proposed FC with deep cement penetration over SC to reduce micromotion and early loosening. In contrast the cadaveric study by Peters et al. (2003), comparing initial fixation and cement penetration depth in FC and SC tibial components with cruciate and I-beam stems, found no difference in micromotion between stem design or cementation method after 6000 cycles. The study indicated that SC component stability may be related to cement penetration depth (Peters et al. 2003). Although Skwara et al. (2009) found no significant differences between the initial stability of the FC and SC tibial

components after 1000 and 10000 cycles using RSA, tibial component migration showed a greater mean maximum total point motion, maximum lift-off and maximum subsidence for FC than SC. Failure, defined as migration greater than 2 mm, was found in six FC in comparison to two SC components which may lead to stress shielding and early component loosening (Skwara et al. 2009). Investigating micromotion in FC and SC using five different cementation configurations (Table 2-6), Bert and McShane (1998) demonstrated excellent stability (no difference in lift-off) with both techniques with a 3 mm surface mantle, although the study stated that a 3 mm mantle may be impractical. However, greater lift-off was observed for SC with a 1 mm cement mantle (Bert and McShane 1998). Using RSA, Efe et al. (2011) noted a significant difference in failure (migration >2 mm) in cementless tibial fixation (8/10 cases) in comparison to SC (2/10 cases) after 10,000 cycles. In addition to cortical strain measurements, Seki et al. (1997) investigated stem stability through micromotion during cyclic loading and detected no significant differences in micromotion between FC and SC.

The results of previous studies have not provided conclusive evidence on the optimum tibial cementation technique. Further investigation of the effects of cementing technique on the mechanisms of tibial component failure in TKA is warranted. Optimising cementation technique remains a priority in the endeavour to improve survivorship of TKA and secondarily, to facilitate ease of revision surgery.

Cement Application and Penetration

As aforementioned, in addition to the cementation technique, many other factors affect the outcome of cemented tibial components. Given the quality and porosity of trabecular bone, cement can permeate to varying degrees beyond the surface creating an interdigitated cement-bone interface. Cement penetration has been highlighted as playing a key role in implant stability between the full and surface cementation techniques (Bert and McShane 1998; Hofmann et al. 2006; Peters et al. 2003). Various authors have described methods for enhancing cement penetration including pulsatile lavage (Efe et al. 2011; Hofmann et al. 2006; Seki et al. 1997; Skwara et al. 2009), bone preparation (Hofmann et al. 2006), digital cement impaction, vacuuming mixing (Efe et al. 2011; Luring et al. 2006), cement gun (Efe et al. 2011; Skwara et

al. 2009; Vanlommel et al. 2011), cement application in its low viscous state (Hofmann et al. 2006; Vanlommel et al. 2011), peripheral lip on the tibial tray under surface (Hofmann et al. 2006) and impacting (hammering) the implant (Vanlommel et al. 2011). A cement penetration depth of 2.69 mm was noted in a follow-up study that showed a survivorship of 98% for an average of 95 months of SC knees (Hofmann et al. 2006). Kolisek et al. (2009) found excellent results at ten years for SC with a minimum of a 2 mm cement mantle. In an open pore synthetic model, representing osteoporotic trabecular bone, Vanlommel et al. (2011) concluded that optimal penetration of 3-5 mm was achieved for spatula or finger-packing of cement, with insufficient penetration on isolated cement application onto the tibial tray and excessive penetration when using the cement gun. For FC and SC, Peters et al. (2003) found no difference in the average cement mantle penetration depth (3.6-4.9 mm), however a correlation between micromotion and cement penetration depth in SC was noted.

2.3 Spinal Biomechanics

2.3.1 The Vertebral Column

The human spine, or vertebral column, is a complex mechanism composed of vertebrae separated by intervertebral discs. The vertebral column is divided into five regions which are, in cephalic to the caudal direction (head to toe): the cervical (7 vertebrae); thoracic (12); lumbar (5); sacrum (5); and coccyx (Figure 2-13(a)). The lumbar region, which is considered in the present work, contains five motion segments ranging from the L1-L2 to the L5-S1. A single functional spinal unit, also known as a spinal motion segment, consists of two vertebrae separated by an intervertebral disc (Figure 2-13(b)). Movement between adjacent vertebrae is slight; however the additive effect is considerable. The human vertebral column has numerous functions including; spinal cord protection, shock absorption, support, and allowing posture and movement. The specific curvature of the human spine maintains stability while allowing increased flexibility. The muscles, tendons and ligaments of the vertebral column are not of major concern in relation to this work, which deals primarily with the vertebral body.

Figure 2-13 (a) Regions and curvature of the spinal column (b) functional spinal unit (Vertical Health 2010).

The disc shaped vertebral body consists of trabecular bone surrounded by a hard outer shell of cortical bone (Figure 2-13(b)). The vertebral body, the primary weight bearing area of the vertebra, functions to withstand the large compressive loads experienced by the spinal column during physiological loading. Successive vertebrae are connected by the intervertebral discs, the facet joints and a range of ligaments. The bony vertebral endplates, the superior and inferior surfaces of the vertebral body, are composed of cortical bone. The vertebral endplate has a non-uniform strength and density and the central region is thinner and weaker than the periphery (Grant et al. 2001; Oxland et al. 2003). The vertebral endplates are covered in a thin plate of hyaline cartilage called the cartilage endplates. The cartilage endplates separate the intervertebral disc from the vertebral bodies and are sometimes referred to as part of the disc and others as part of the vertebrae, and typically have a thickness of ~1 mm in the lumbar region.

The spine permits physiological movement in the three anatomical planes of motion including flexion extension, lateral bending and pure/axial compression. The discs and facet joints maintain flexibility and motion and are responsible for carrying the compressive loading of the spine. The mechanical behaviour of the spine is dependent on the spine morphology and thus changing the spines morphology will inevitably change its mechanical behaviour.

Pain complaint is one of the main causes of medical visits (Raofi and Schappert 2006), with back pain being the most common musculoskeletal pain complaint. A survey in the USA reported that 26% of adults reported back pain in the previous three months (Deyo et al. 2006). The current solutions for lower back pain range from conservative care such as bed rest to surgical intervention. Low back pain is often associated with degenerative lumbar disc disease; however the aetiology of disc degeneration is unknown. Factors such as natural wear and tear, trauma, heavy lifting, infection, environment and genetics contribute to disc degeneration. Surgical intervention for disc degeneration and other disc associated problems include discectomy, total disc replacement, spinal fusion and spinal stabilization. Each treatment attempt to alleviate pain but do not restore the biomechanics of the spine to a normal physiological state.

2.3.2 Spinal Fusion

Spinal fusion, also known as spondylodesis, involves removing the complete intervertebral disc and joining two or more adjacent vertebrae. From 1990 to 2001 a 220% increase in lumbar spinal fusion surgery was reported in the USA, with over 122,000 lumbar fusion surgeries performed in 2001 for degenerative conditions (Deyo et al. 2005). An interbody fusion device, which is placed between adjacent vertebrae, endeavours to replace a damaged or diseased intervertebral disc and relies on the vertebral bodies for load transmission and mechanical support. Bone grafts may be contained in the device cage to promote fusion of adjacent vertebrae. Different types of interbody fusion exist and are named after the anatomical approach: anterior lumbar interbody fusion (ALIF); posterior lumbar interbody fusion (PLIF); transforaminal lumbar interbody fusion (TLIF); direct lateral interbody fusion (DLIF); and axial lumbar interbody fusion (AxiaLIF). Different interbody device designs require different bony endplate preparation techniques including: intact; partial removal; and complete removal. Clinically, full or partial endplate removal may be performed intentionally or unintentionally. Removal of the endplate exposes a host bed of bleeding trabecular bone, therefore allowing the exposure of potentially osteogenic cells allowing fusion of the bone graft material. Although advantageous from a biological point of view for graft incorporation and bone fusion, the mechanical effects of endplate removal on device subsidence may be substantial.

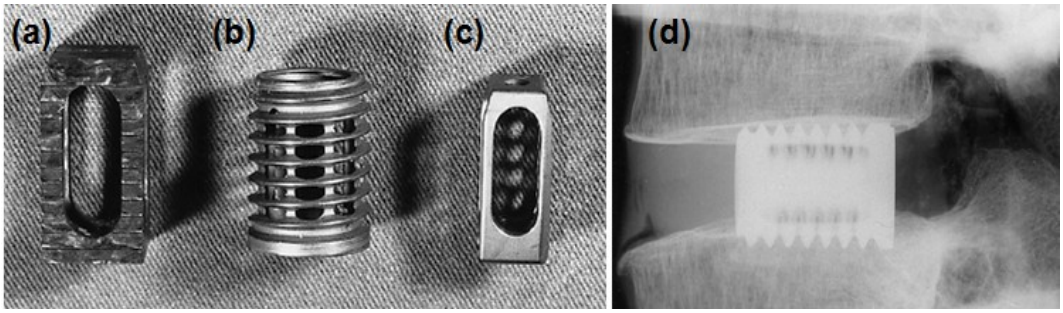

Figure 2-14 Examples of interbody fusion devices (a) Brantigan Cage, Brantigan, Acromed, Cleveland, Ohio (b) Ray Cage, Ray TFC, Surgical Dynamics, Concord, California (c) Stratec Cage, Stratec Medical, Oberdorf, Switzerland (d) Radiograph of a specimen inserted with a Rage Cage which requires slight bony endplate preparation during the surgical technique (Jost et al. 1998).

Although some device settling may be required to achieve fixation, excessive device subsidence into trabecular bone may ultimately lead to device failure. Device subsidence has been defined as either the migration of a device into the adjacent vertebral body or as a decrease in the disc space height of 2 mm (Beutler and Peppelman 2003; Chen et al. 2005; Choi and Sung 2006), 3 mm (Gercek et al. 2003) or 10% (height reduction) (Vaidya et al. 2007). A wide range of clinical interbody device subsidence rates have been reported, ranging from 3 to 76.7% (Beutler and Peppelman 2003; Chen et al. 2005; Choi and Sung 2006). Device subsidence may be related to regional difference in material properties, bone quality, implant size, implant geometry and endplate preparation which can lead to loss of support, progressive deformity and non-union.

*In vitro e*xperimental studies investigating the effect of endplate removal on the vertebral structural properties using compression testing have predominantly relied on measuring the maximum failure load to evaluate subsidence resistance (Closkey et al. 1993; Hollowell et al. 1996; Jost et al. 1998; Lim et al. 2001; Lowe et al. 2004; McBroom et al. 1985; Oxland et al. 2003; Steffen et al. 1998; Steffen et al. 2000), with conflicting evidence on the importance of the endplate for resisting subsidence. Oxland et al. (2003) found a significant decrease in failure load and stiffness for endplate removal using a 3 mm hemispherical indenter. Using an 8 mm indenter, Lim et al. (2001) found a reduction in compressive strength with complete endplate removal. McBroom et al. (1985) related complete endplate removal with a reduction in failure load of ~10% compared to the intact endplate. Lowe et al. (2004) found that mean failure loads for complete endplate removal were significantly lower than partially removed or intact endplates and suggested using larger hollow devices that lie on the endplate periphery. Using full and peripheral support devices, Steffen et al. (2000) found no difference in failure load with intact endplates and removed (device sitting on periphery) endplates and promoted partial endplate removal. According to Hollowell et al. (1996), the endplate may not be thick enough to resist device subsidence and hence complete trabecular-device contact may offer similar compressive strength (Steffen et al. 2000).

2.4 References

Abrate, S. (2008) Criteria for yielding or failure of cellular materials. J Sandw Struct Mater 10 (1):5-51.

Agneskirchner, J., Freiling, D., Hurschler, C., Lobenhoffer, P. (2006) Primary stability of four different implants for opening wedge high tibial osteotomy. Knee Surg Sports Traumatol Arthrosc 14 (3):291-300.

Albrektsson, B. E., Ryd, L., Carlsson, L. V., Freeman, M. A., Herberts, P., Regner, L., Selvik, G. (1990) The effect of a stem on the tibial component of knee arthroplasty. A roentgen stereophotogrammetric study of uncemented tibial components in the freeman-samuelson knee arthroplasty. J Bone Joint Surg Br 72 (2):252-258.

Andriacchi, T. P., Hurwitz, D. E. (1997) Gait biomechanics and the evolution of total joint replacement. 5 (3):256-264.

AOA (2011) Australian orthopaedic association national joint replacement registry. Demographics of knee arthroplasty, supplementary report.

ASTM (2008) Standard specification for rigid polyurethane foam for use as a standard material for testing orthopaedic devices and instruments. ASTM F1839-01. Pennsylvania.

Austin, M. S., Sharkey, P. F., Hozack, W. J., Rothman, R. H. (2004) Knee failure mechanisms after total knee arthroplasty. Tech Knee Surg 3 (1):55.

Bayraktar, H. H., Gupta, A., Kwon, R. Y., Papadopoulos, P., Keaveny, T. M. (2004) The modified super-ellipsoid yield criterion for human trabecular bone. J Biomech Eng 126 (6):677-684.

Bayraktar, H. H., Keaveny, T. M. (2004) Mechanisms of uniformity of yield strains for trabecular bone. J Biomech 37 (11):1671-1678.

Bert, J. M., McShane, M. (1998) Is it necessary to cement the tibial stem in cemented total knee arthroplasty? Clin Orthop 356:73-78.

Bessho, M., Ohnishi, I., Matsuyama, J., Matsumoto, T., Imai, K., Nakamura, K. (2007) Prediction of strength and strain of the proximal femur by a ct-based finite element method. J Biomech 40 (8):1745-1753.

Beutler, W. J., Peppelman, W. C. (2003) Anterior lumbar fusion with paired bak standard and paired bak proximity cages: Subsidence incidence, subsidence factors, and clinical outcome. Spine J 3 (4):289-293.

Boyd, S. K., Müller, R., Zernicke, R. F. (2002) Mechanical and architectural bone adaptation in early stage experimental osteoarthritis. J Bone Miner Res 17 (4):687-694.

Bozic, K. J., Kurtz, S. M., Lau, E., Ong, K., Chiu, V., Vail, T. P., Rubash, H. E., Berry, D. J. (2010) The epidemiology of revision total knee arthroplasty in the united states. Clinical Orthop 468 (1):45-51.

Burstein, A. H., Reilly, D. T., Martens, M. (1976) Aging of bone tissue: Mechanical properties. J Bone Joint Surg Am 58 (1):82.

Carter, D. R., Van der Meulen, M. C. H., Beaupre, G. S. (1996) Mechanical factors in bone growth and development. Bone 18 (1):S5-S10.

Charlebois, M., Jirasek, M., Zysset, P. K. (2010a) A nonlocal constitutive model for trabecular bone softening in compression. Biomech Model Mechanobiol 9 (5):597-611.

Charlebois, M., Pretterklieber, M., Zysset, P. K. (2010b) The role of fabric in the large strain compressive behavior of human trabecular bone. J Biomech Eng 132:1-10.

Chen, L., Yang, H., Tang, T. (2005) Cage migration in spondylolisthesis treated with posterior lumbar interbody fusion using bak cages. Spine 30 (19):2171-2175.

Chevalier, Y., Charlebois, M., Pahr, D., Varga, P., Heini, P., Schneider, E., Zysset, P. (2008) A patient-specific finite element methodology to predict damage accumulation in vertebral bodies under axial compression, sagittal flexion and combined loads. Comput Method Biomech 11 (5):477-487.

Choi, J. Y., Sung, K. H. (2006) Subsidence after anterior lumbar interbody fusion using paired stand-alone rectangular cages. Eur Spine J 15 (1):16-22.

Chong, A. C. M., Miller, F., Buxton, M., Friis, E. A. (2007) Fracture toughness and fatigue crack propagation rate of short fiber reinforced epoxy composites for analogue cortical bone. J Biomech Eng 129 (4):487-493.

CJRR (2008-2009) Hip and knee replacements in canada. Canadian joint replacement registry.

Closkey, R. F., Parsons, J. R., Lee, C. K., Blacksin, M. F., Zimmerman, M. C. (1993) Mechanics of interbody spinal fusion. Analysis of critical bone graft area. Spine 18 (8):1011.

Completo, A., Fonseca, F., Simoes, J. A. (2007a) Finite element and experimental cortex strains of the intact and implanted tibia. J Biomech Eng 129 (5):791-797.

Completo, A., Fonseca, F., Simões, J. A. (2007b) Experimental validation of intact and implanted distal femur finite element models. J Biomech 40 (11):2467-2476.

Completo, A., Fonseca, F., Simões, J. A. (2008) Strain shielding in proximal tibia of stemmed knee prosthesis: Experimental study. J Biomech 41 (3):560-566.

Completo, A., Talaia, P., Fonseca, F., Simões, J. A. (2009) Relationship of design features of stemmed tibial knee prosthesis with stress shielding and end-of-stem pain. Mater Design 30 (4):1391-1397.

Cristofolini, L., Viceconti, M. (2000) Mechanical validation of whole bone composite tibia models. J Biomech 33 (3):279-288.

Cristofolini, L., Viceconti, M., Cappello, A., Toni, A. (1996) Mechanical validation of whole bone composite femur models. J Biomech 29 (4):525-535.

Currey, J. D. (1984) Effects of differences in mineralization on the mechanical properties of bone, vol 304. Philosophical transactions of the royal society of london. Series b, biological sciences, vol 1121. The Royal Society.

Dempster, W. T., Liddicoat, R. T. (1952) Compact bone as a non-isotropic material. Am J Anat 91 (3):331-362.

Derikx, L. C., Vis, R., Meinders, T., Verdonschot, N., Tanck, E. (2011) Implementation of asymmetric yielding in case-specific finite element models improves the prediction of femoral fractures. Comput Method Biomech 14 (02):183-193.

Deyo, R. A., Gray, D. T., Kreuter, W., Mirza, S., Martin, B. I. (2005) United states trends in lumbar fusion surgery for degenerative conditions. Spine 30 (12):1441-1445.

Deyo, R. A., Mirza, S. K., Martin, B. I. (2006) Back pain prevalence and visit rates: Estimates from us national surveys, 2002. Spine 31 (23):2724-2727.

Efe, T., Figiel, J., Danek, S., Tibesku, C. O., Paletta, J. R. J., Skwara, A. (2011) Initial stability of tibial components in primary knee arthroplasty. A cadaver study comparing cemented and cementless fixation techniques. Acta Orthop Belg 29 (15):50.

Feerick, E. M., Kennedy, J., Mullett, H., FitzPatrick, D., McGarry, J. P. (2012) Investigation of metallic and carbon fibre peek fracture fixation devices for three-part proximal humeral fractures. Med Eng Phys In Press.

Fenech, C. M., Keaveny, T. M. (1999) A cellular solid criterion for predicting the axial-shear failure properties of bovine trabecular bone. J Biomech Eng 121 (4):414-422.

Fratzl, P., Weinkamer, R. (2007) Nature's hierarchical materials. Prog Mater Sci 52 (8):1263-1334.

Gandhi, R., Tsvetkov, D., Davey, J. R., Mahomed, N. N. (2009) Survival and clinical function of cemented and uncemented prostheses in total knee replacement: A meta-analysis. 91 (7):889.

Gercek, E., Arlet, V., Delisle, J., Marchesi, D. (2003) Subsidence of stand-alone cervical cages in anterior interbody fusion: Warning. Eur Spine J 12 (5):513-516.

Gibson, L. J. (2005) Biomechanics of cellular solids. J Biomech 38 (3):377-399.

Gibson, L. J., Ashby, M. F. (1999) Cellular solids: Structure and properties. Cambridge Univ Pr.

Goldstein, S. A. (1987) The mechanical properties of trabecular bone: Dependence on anatomic location and function. J Biomech 20 (11-12):1055-1061.

Goldstein, S. A., Wilson, D. L., Sonstegard, D. A., Matthews, L. S. (1983) The mechanical properties of human tibial trabecular bone as a function of metaphyseal location. J Biomech 16 (12):965-969.

Grant, J. P., Oxland, T. R., Dvorak, M. F. (2001) Mapping the structural properties of the lumbosacral vertebral endplates. Spine 26 (8):889-896.

Guillén, T., Zhang, Q. H., Tozzi, G., Ohrndorf, A., Christ, H. J., Tong, J. (2011) Compressive behaviour of bovine cancellous bone and bone analogous materials, microct characterisation and fe analysis. J Mech Behav Biomed Mater 4 (7):1452-1461.

Gupta, A., Bayraktar, H., Fox, J., Keaveny, T., Papadopoulos, P. (2007) Constitutive modeling and algorithmic implementation of a plasticity-like model for trabecular bone structures. Comput Mech 40 (1):61-72.

Gupta, H. S., Zioupos, P. (2008) Fracture of bone tissue: The `hows' and the `whys'. Med Eng Phys 30 (10):1209-1226.

Harrigan, T. P., Jasty, M., Mann, R. W., Harris, W. H. (1988) Limitations of the continuum assumption in cancellous bone. J Biomech 21 (4):269-275.

Harrison, N. M., McDonnell, P., Mullins, L., Wilson, N., O'Mahoney, D., McHugh, P. E. (2012) Failure modelling of trabecular bone using a non-linear combined damage and fracture voxel finite element approach. Biomech Model Mechanobiol:1-17.

Harrison, N. M., McDonnell, P. F., O'Mahoney, D. C., Kennedy, O. D., O'Brien, F. J., McHugh, P. E. (2008) Heterogeneous linear elastic trabecular bone modelling using micro-ct attenuation data and experimentally measured heterogeneous tissue properties. J Biomech 41 (11):2589-2596.

Heiner, A. D. (2008) Structural properties of fourth-generation composite femurs and tibias. J Biomech 41 (15):3282-3284.

Heiner, A. D., Brown, T. D. (2001) Structural properties of a new design of composite replicate femurs and tibias. J Biomech 34 (6):773-781.

Heinlein, B., Kutzner, I., Graichen, F., Bender, A., Rohlmann, A., Halder, A. M., Beier, A., Bergmann, G. (2009) Esb clinical biomechanics award 2008: Complete data of total knee replacement loading for level walking and stair climbing measured in vivo with a follow-up of 6-10 months. Clin Biomech 24 (4):315-326.

Hernandez-Vaquero, D., Garcia-Sandoval, M. A., Fernandez-Carreira, J. M., Gava, R. (2008) Influence of the tibial stem design on bone density after cemented total knee arthroplasty: A prospective seven-year follow-up study. Int Orthop 32 (1):47-51.

Hildebrand, T., Laib, A., Müller, R., Dequeker, J., Rüegsegger, P. (1999) Direct three-dimensional morphometric analysis of human cancellous bone: Microstructural data from spine, femur, iliac crest, and calcaneus. J Bone Miner Res 14 (7):1167-1174.

Hofmann, A. A., Goldberg, T. D., Tanner, A. M., Cook, T. M. (2006) Surface cementation of stemmed tibial components in primary total knee arthroplasty: Minimum 5-year follow-up. J Arthroplasty 21 (3):353-357.

Hollowell, J. P., Vollmer, D. G., Wilson, C. R., Pintar, F. A., Yoganandan, N. (1996) Biomechanical analysis of thoracolumbar interbody constructs: How important is the endplate? Spine 21 (9):1032-1036.

Huiskes, R., Weinans, H., Grootenboer, H. J., Dalstra, M., Fudala, B., Slooff, T. J. (1987) Adaptive bone-remodeling theory applied to prosthetic-design analysis. 20 (11):1135-1150.

Huiskes, R., Weinans, H., Rietbergen, B. (1992) The relationship between stress shielding and bone resorption around total hip stems and the effects of flexible materials. Clin Orthop 274:124.

Jost, B., Cripton, P. A., Lund, T., Oxland, T. R., Lippuner, K., Jaeger, P., Nolte, L. P. (1998) Compressive strength of interbody cages in the lumbar spine: The effect of cage shape, posterior instrumentation and bone density. Eur Spine J 7 (2):132-141.

Keaveny, T. M., Pinilla, T. P., Crawford, P. R., Kopperdahl, D. L., Lou, A. (1997) Systematic and random errors in compression testing of trabecular bone. J Orthop Res 15 (1):101-110.

Keaveny, T. M., Wachtel, E. F., Ford, C. M., Hayes, W. C. (1994) Differences between the tensile and compressive strengths of bovine tibial trabecular bone depend on modulus. J Biomech 27 (9):1137-1146.

Keaveny, T. M., Wachtel, E. F., Kopperdahl, D. L. (1999a) Mechanical behavior of human trabecular bone after overloading. J Orthop Res 17 (3):346-353.

Keaveny, T. M., Wachtel, E. F., Zadesky, S. P., Arramon, Y. P. (1999b) Application of the tsai-wu quadratic multiaxial failure criterion to bovine trabecular bone. J Biomech Eng 121:99.

Keyak, J. H. (2001) Improved prediction of proximal femoral fracture load using nonlinear finite element models. Med Eng Phys 23 (3):165-173.

Keyak, J. H., Rossi, S. A. (2000) Prediction of femoral fracture load using finite element models: An examination of stress- and strain-based failure theories. J Biomech 33 (2):209-214.

Klever, F. J., Klumpert, R., Grootenboer, H. J., van Campen, D. H., Pauly, T. (eds) (1985) Global mechanical properties of trabecular bone: Experimental determination and prediction from a structural model. Biomechanics: Current interdisciplinary research. Martinus Nijhoff, Dordrecht.

Kolisek, F. R., Mont, M. A., Seyler, T. M., Marker, D. R., Jessup, N. M., Siddiqui, J. A., Monesmith, E., Ulrich, S. D. (2009) Total knee arthroplasty using cementless keels and cemented tibial trays: 10-year results. Int Orthop 33 (1):117-121.

Kopperdahl, D. L., Keaveny, T. M. (1998) Yield strain behavior of trabecular bone. J Biomech 31 (7):601-608.

Kurtz, S., Ong, K., Lau, E., Mowat, F., Halpern, M. (2007) Projections of primary and revision hip and knee arthroplasty in the united states from 2005 to 2030. J Bone Joint Surg Am 89 (4):780.

Kurtz, S. M., Ong, K. L., Lau, E., Widmer, M., Maravic, M., Gomez-Barrena, E., de Fatima de Pina, M., Manno, V., Torre, M., Walter, W. L. (2011) International survey of primary and revision total knee replacement. International Orthopaedics 35 (12):1783-1789.

Li, B., Aspden, R., M. (1997) Composition and mechanical properties of cancellous bone from the femoral head of patients with osteoporosis or osteoarthritis. J Bone Miner Res 12 (4):641-651.

Lim, T. H., Kwon, H., Jeon, C. H., Kim, J. G., Sokolowski, M., Natarajan, R., An, H. S., Bj Andersson, G. (2001) Effect of endplate conditions and bone mineral density on the compressive strength of the graft-endplate interface in anterior cervical spine fusion. Spine 26 (8):951-956.

Linde, F., Hvid, I. (1989) The effect of constraint on the mechanical behaviour of trabecular bone specimens. J Biomech 22 (5):485-490.

Linde, F., Hvid, I., Madsen, F. (1992) The effect of specimen geometry on the mechanical behaviour of trabecular bone specimens. J Biomech 25 (4):359-368.

Lonner, J. H., Klotz, M., Levitz, C., Lotke, P. A. (2001) Changes in bone density after cemented total knee arthroplasty: Influence of stem design. J Arthroplasty 16 (1):107-111.

Lowe, T. G., Hashim, S., Wilson, L. A., O'Brien, M. F., Smith, D. A. B., Diekmann, M. J., Trommeter, J. (2004) A biomechanical study of regional endplate strength and cage morphology as it relates to structural interbody support. Spine 29 (21):2389-2394.

Luring, C., Perlick, L., Trepte, C., Linhardt, O., Perlick, C., Plitz, W., Grifka, J. (2006) Micromotion in cemented rotating platform total knee arthroplasty: Cemented tibial stem versus hybrid fixation. Arch Orthop Trauma Surg 126 (1):45-48.

MacNeil, J. A., Boyd, S. K. (2008) Bone strength at the distal radius can be estimated from high-resolution peripheral quantitative computed tomography and the finite element method. Bone 42 (6):1203-1213.

Martin, R. B., Burr, D. B., Sharkey, N. A. (1998) Skeletal tissue mechanics. Springer Verlag.

McBroom, R. J., Hayes, W. C., Edwards, W. T., Goldberg, R. P., White 3rd, A. A. (1985) Prediction of vertebral body compressive fracture using quantitative computed tomography. J Bone Joint Surg Am 67 (8):1206-1214.

McCalden, R. W., McGeough, J. A. (1997) Age-related changes in the compressive strength of cancellous bone. The relative importance of changes in density and trabecular architecture. J Bone Joint Surg 79 (3):421.

McElhaney, J. H. (1966) Dynamic response of bone and muscle tissue. J Appl Physiol 21 (4):1231-1236.

Morgan, E. F., Bayraktar, H. H., Keaveny, T. M. (2003) Trabecular bone modulus-density relationships depend on anatomic site. J Biomech 36 (7):897-904.

Morgan, E. F., Keaveny, T. M. (2001) Dependence of yield strain of human trabecular bone on anatomic site. J Biomech 34 (5):569-577.

Morrison, J. B. (1970) The mechanics of the knee joint in relation to normal walking. 3 (1):51-61.

Mosekilde, L., Danielsen, C. C. (1987) Biomechanical competence of vertebral trabecular bone in relation to ash density and age in normal individuals. Bone 8 (2):79-85.

Müller, R., Rüegsegger, P. (1995) Three-dimensional finite element modelling of non-invasively assessed trabecular bone structures. Med Eng Phys 17 (2):126-133.

Munro, J. T., Pandit, S., Walker, C. G., Clatworthy, M., Pitto, R. P. (2010) Loss of tibial bone density in patients with rotating-or fixed-platform tka. Clin Orthop 468 (3):775-781.

Nagaraja, S., Couse, T. L., Guldberg, R. E. (2005) Trabecular bone microdamage and microstructural stresses under uniaxial compression. J Biomech 38 (4):707-716.

Neilsen, M. K., Krieg, R. D., Schreyer, H. L. (1995) A constitutive theory for rigid polyurethane foam. Polym Eng Sci 35 (5):387-394.

Niebur, G. L., Feldstein, M. J., Keaveny, T. M. (2002) Biaxial failure behavior of bovine tibial trabecular bone. J Biomech Eng 124 (6):699-705.

Niebur, G. L., Feldstein, M. J., Yuen, J. C., Chen, T. J., Keaveny, T. M. (2000) High-resolution finite element models with tissue strength asymmetry accurately predict failure of trabecular bone. J Biomech 33 (12):1575-1583.

Öchsner, A., Ahmed, W. (eds) (2010) Biomechanics of hard tissues. Wiley, Weinheim.

Odgaard, A., Linde, F. (1991) The underestimation of young's modulus in compressive testing of cancellous bone specimens. J Biomech 24 (8):691-698.

Ong, K. L., Day, J. S., Kurtz, S. M., Field, R. E., Manley, M. T. (2009) Role of surgical position on interface stress and initial bone remodeling stimulus around hip resurfacing arthroplasty. J Arthroplasty 24 (7):1137.

Oxland, T. R., Grant, J. P., Dvorak, M. F., Fisher, C. G. (2003) Effects of endplate removal on the structural properties of the lower lumbar vertebral bodies. Spine 28 (8):771-777.

Peters, C. L., Craig, M. A., Mohr, R. A., Bachus, K. N. (2003) Tibial component fixation with cement: Full-versus surface-cementation techniques. Clin Orthop 409:158.

Ramsey, D. K., Wretenberg, P. F. (1999) Biomechanics of the knee: Methodological considerations in the in vivo kinematic analysis of the tibiofemoral and patellofemoral joint. Clin Biomech 14 (9):595-611.

Rand, J. A., Trousdale, R. T., Ilstrup, D. M., Harmsen, W. S. (2003) Factors affecting the durability of primary total knee prostheses. J Bone Joint Surg Am 85 (2):259-265.

Raofi, S., Schappert, S. M. (2006) Medication therapy in ambulatory medical care: United states, 2003-04. (163):1.

Regnér, L. R., Carlsson, L. V., Kärrholm, J. N., Hansson, T. H., Herberts, P. G., Swanpalmer, J. (1999) Bone mineral and migratory patterns in uncemented total knee arthroplasties: A randomized 5-year follow-up study of 38 knees. Acta Orthop Scand 70 (6):603-608.

Reilly, D. T., Burstein, A. H. (1975) The elastic and ultimate properties of compact bone tissue. J Biomech 8 (6):393-396, 397-405.

Rho, J.-Y., Kuhn-Spearing, L., Zioupos, P. (1998) Mechanical properties and the hierarchical structure of bone. Med Eng Phys 20 (2):92-102.

Rincon-Kohli, L., Zysset, P. (2009) Multi-axial mechanical properties of human trabecular bone. Biomech Model Mechanobiol 8 (3):195-208.

Røhl, L., Larsen, E., Linde, F., Odgaard, A., Jørgensen, J. (1991) Tensile and compressive properties of cancellous bone. J Biomech 24 (12):1143-1149.

Saari, T., Li, M. G., Wood, D., Nivbrant, B. (2008) Comparison of cementing techniques of the tibial component in total knee replacement. Int Orthop:1-4.

Schai, P. A., Thornhill, T. S., Scott, R. D. (1998) Total knee arthroplasty with the pfc system. J Bone Joint Surg Br 80:850-858.

Schipplein , O. D., Andriacchi, T. P. (1991) Interaction between active and passive knee stabilizers during level walking.

Seki, T., Bourgeault, C., Chareancholvanich, A. K., Lew, W., Bechtold, J. E., Gustilo, R. B. (1997) Does a central stem affect bone strain and the stability of a cemented tibial tray in primary and revision tka. Trans Orthop Res Soc 22:635.

Sharkey, P. F., Hozack, W. J., Rothman, R. H., Shastri, S., Jacoby, S. M. (2002) Why are total knee arthroplasties failing today? Clinical Orthop 404:7-13.

Simkin, A., Robin, G. (1973) The mechanical testing of bone in bending. J Biomech 6 (1):31-36, IN33, 37-39.

Skwara, A., Figiel, J., Knott, T., Paletta, J. R. J., Fuchs-Winkelmann, S., Tibesku, C. O. (2009) Primary stability of tibial components in tka: In vitro comparison of two cementing techniques. Arthroscopy 17 (10):1199-1205.

Steffen, T., Gagliardi, P., Hurrynag, P., Aebi, M. Optimal implant-endplate interface for interbody spinal fusion devices. In: European Spine Society, Innsbruck, Austria, 1998.

Steffen, T., Tsantrizos, A., Aebi, M. (2000) Effect of implant design and endplate preparation on the compressive strength of interbody fusion constructs. Spine 25 (9):1077-1084.

Szivek, J. A., Thomas, M., Benjamin, J. B. (1993) Technical note. Characterization of a synthetic foam as a model for human cancellous bone. J Appl Biomater 4 (3):269-272.

Tsai, S. W., Wu, E. M. (1971) A general theory of strength for anisotropic materials. J Compos Mater 5 (1):58-80.

Ulrich, D., Van Rietbergen, B., Laib, A. (1999) The ability of three-dimensional structural indices to reflect mechanical aspects of trabecular bone. Bone 25 (1):55-60.

Vaidya, R., Weir, R., Sethi, A., Meisterling, S., Hakeos, W., Wybo, C. D. (2007) Interbody fusion with allograft and rhbmp-2 leads to consistent fusion but early subsidence. J Bone Joint Surg Br 89 (3):342-345.

Van Rietbergen, B., Weinans, H., Huiskes, R., Odgaard, A. (1995) A new method to determine trabecular bone elastic properties and loading using micromechanical finite-element models. J Biomech 28 (1):69-81.

Vanlommel, J., Luyckx, J. P., Labey, L., Innocenti, B., De Corte, R., Bellemans, J. (2011) Cementing the tibial component in total knee arthroplasty: Which technique is the best? J Arthroplasty 26 (3):492-496.

Verhulp, E., Van Rietbergen, B., Müller, R., Huiskes, R. (2008) Micro-finite element simulation of trabecular-bone post-yield behaviour - effects of material model, element size and type. Comput Method Biomech 11 (4):389-395.

Vertical Health, L. (2010) Spine universe. http://www.spineuniverse.com. Accessed 21/09/12 2012

Wachtel, E. F., Keaveny, T. M. (1997) Dependence of trabecular damage on mechanical strain. 15 (5):781-787.

Walker, P. S., Hsu, H. P., Zimmerman, R. A. (1990) A comparative study of uncemented tibial components. J Arthroplasty 5 (3):245.

Wang, X., Nyman, J. S., Dong, X., Leng, H., Reyes, M. (eds) (2010) Fundamental biomechanics in bone tissue engineering, vol 2. Synthesis lectures on tissue engineering, vol 1. Morgan & Claypool Publishers.

Weinans, H., Huiskes, R., Van Rietbergen, B., Sumner, D. R., Turner, T. M., Galante, J. O. (1993) Adaptive bone remodeling around bonded noncemented total hip arthroplasty: A comparison between animal experiments and computer simulation. J Orthop Res 11 (4):500-513.

Wolff, J. (1892) Das gesetz der transformation der knochen.1-139.

Zihlmann, M. S., Stacoff, A., Romero, J., Quervain, I. K.-d., Stüssi, E. (2005) Biomechanical background and clinical observations of rotational malalignment in tka:: Literature review and consequences. Clin Biomech 20 (7):661-668.

Zysset, P., Rincon-Kohli, L. (2006) An alternative fabric-based yield and failure criterion for trabecular bone. In: Holzapfel, G. A., Ogden, R. W. (eds) Mechanics of biological tissue. Springer, Berlin, pp 457-470.

Zysset, P. K., Curnier, A. (1996) A 3d damage model for trabecular bone based on fabric tensors. J Biomech 29 (12):1549-1558.

Chapter 3

Finite Element Theory and Constitutive Formulations

This chapter outlines the finite element theory and constitutive plasticity formulations that are investigated in the current work to capture the inelastic deformation of trabecular bone.

3.1 Continuum Mechanics

3.1.1 Notation

An introduction to the notation used in the current chapter is presented for clarity. As regards notation, capital letters are used for tensors and matrices and small letters are used for vectors. Bold type face font is denoted for vectors, tensors and matrices and their component parts are shown in italics. Index notation is used to illustrate manipulation of these quantities, whereby a repeated index implies a summation. The coordinate system uses the axes x_1, x_2 and x_3 or x_i where $i = 1, 2, 3$ (summation over values of the indices from 1 to 3). For example, index notation summation convention is illustrated below using the dot product (scalar or inner product) of two vectors in 3D ($\mathbf{u}$, $\mathbf{v}$), which is the summation of the component parts

$$\mathbf{u} \cdot \mathbf{v} = u_i v_i = u_1 v_1 + u_2 v_2 + u_3 v_3 \tag{3.1}$$

Second order tensors are represented by nine components in 3D. Each component is denoted by two subscripts that define its location in the tensor. For example, the second order tensor $\mathbf{A}$ in component form is A_{ij}, where the subscripts define the location within the tensor at row i and column j. A fourth order tensor is defined as the linear tensor function of a second order tensor. For example, the linear elastic constitutive law relates the second order stress tensor, $\boldsymbol{\sigma}$, and strain tensor, $\boldsymbol{\varepsilon}$, through the fourth order elastic modulus tensor, $\mathbf{C}$, as follows

$$\boldsymbol{\sigma} = \mathbf{C} : \boldsymbol{\varepsilon} \qquad \sigma_{ij} = C_{ijkl} \varepsilon_{kl} \tag{3.2}$$

3.1.2 Fundamental Principals and Theoretical Formulations

In the computational simulations performed in this work, finite deformation kinematics is assumed. The position vectors, $\mathbf{x}$ and $\mathbf{y}$, define a material point in the undeformed (reference) and deformed (current) configurations, respectively. The displacement vector of the material point is given as

$$\mathbf{u}(\mathbf{x}, \mathrm{t}) = \mathbf{y}(\mathbf{x}, \mathrm{t}) - \mathbf{x} \tag{3.3}$$

The velocity vector is the time derivative of $\mathbf{u}$

$$d\mathbf{u} = \mathbf{v}(\mathbf{x}, \mathrm{t}) = \frac{d\mathbf{u}}{d\mathrm{t}} \tag{3.4}$$

where t is time. The deformation gradient tensor, $\mathbf{F}$, relates the distance between two neighbouring material points to that in the reference configuration.

$$d\mathbf{y} = \mathbf{F} \cdot d\mathbf{x} \qquad \text{and} \qquad \mathbf{F} = \frac{\partial \mathbf{y}}{\partial \mathbf{x}} \tag{3.5}$$

The spatial velocity gradient, $\mathbf{L}$, is calculated from the deformation gradient as

$$\mathbf{L} = \frac{\partial \mathbf{v}}{\partial \mathbf{y}} = d\mathbf{F} \cdot \mathbf{F}^{-1} \tag{3.6}$$

The spatial velocity gradient, $\mathbf{L}$, can be decomposed into a symmetric rate of deformation tensor, $\mathbf{D}$, and an asymmetric spin tensor, $\boldsymbol{\omega}$. The rate of deformation tensor, $\mathbf{D}$, is a measure of the strain rate associated with the deformed configuration and is from the spatial velocity gradient, $\mathbf{L}$, as

$$\mathbf{D} = \mathrm{sym}(\mathbf{L}) = \frac{1}{2}(\mathbf{L} + \mathbf{L}^{\mathbf{T}}) \tag{3.7}$$

$$\boldsymbol{\omega} = \mathrm{asym}(\boldsymbol{\omega}) = (\mathbf{L} - \mathbf{L}^{\mathbf{T}}) \tag{3.8}$$

By integrating the rate of deformation, $\mathbf{D}$, the logarithmic strain tensor, $\boldsymbol{\varepsilon}$, which is a useful finite strain measure and can be calculated

$$\boldsymbol{\varepsilon}(\mathrm{t}) = \int_{\mathbf{0}}^{\boldsymbol{t}} \mathbf{D}\, d\mathrm{t} \tag{3.9}$$

In the present work the Cauchy stress, or true stress, $\boldsymbol{\sigma}$, is the primary measure of stress and is defined as the force per unit area on the current (deformed) configuration.

3.1.3 Elasto-Plasticity

A continuum constitutive plasticity formation is required for trabecular bone that can predict its inelastic deformation under complex loading and boundary conditions. To provide a continuum representation of the material behaviour of trabecular bone, in the present work the material is assumed to be rate independent, homogeneous and elastic-plastic. Further information regarding elasto-plasticity is available in (Abaqus 2011; Abrate 2008; Cvitanic et al. 2008; Khan and Huang 1995; Öchsner and Hosseini 2010).

The common basic assumption of elastic-plastic constitutive formulations, in general, and as used in the present work, is that the deformation can be split up into an elastic part that is recoverable (reversible) and a plastic part that is non-recoverable (irreversible) and permanent. Thus, the total deformation gradient, **F**, can be defined as follows

$$\mathbf{F} = \mathbf{F}^{el} \cdot \mathbf{F}^{pl} \tag{3.10}$$

where $\mathbf{F}^{el}$ is the elastic recoverable part of the deformation and $\mathbf{F}^{pl}$ is the plastic non-recoverable part of the deformation. Equation (3.10) can be approximated in terms of the mechanical strain rates in the system

$$d\boldsymbol{\varepsilon} = d\boldsymbol{\varepsilon}^{el} + d\boldsymbol{\varepsilon}^{pl} \tag{3.11}$$

where $d\boldsymbol{\varepsilon}$ is the total strain rate, $d\boldsymbol{\varepsilon}^{el}$ is the elastic strain rate and, $d\boldsymbol{\varepsilon}^{pl}$ is the plastic strain rate (Abaqus 2011; McGarry et al. 2004). The total strain tensor, $\boldsymbol{\varepsilon}$, calculated by integrating equation (3.11) with respect to time, consists of the elastic strain, $\boldsymbol{\varepsilon}^{el}$, and the plastic strain, $\boldsymbol{\varepsilon}^{pl}$.

$$\boldsymbol{\varepsilon} = \boldsymbol{\varepsilon}^{el} + \boldsymbol{\varepsilon}^{pl} \tag{3.12}$$

For equations (3.11) and (3.12) to be analogous, the elastic response must always be small (Abaqus 2011), which is the case for the elastic strains in trabecular and synthetic bone that are considered in the present work, which are typically less than 1 or 2%. In the elastic region, the relationship between stress and strain is linear and a linear elastic constitutive model can be represented concisely using the generalised Hooke's Law

$$\boldsymbol{\sigma} = \mathbf{C}^{el} : \boldsymbol{\varepsilon}^{el} \tag{3.13}$$

where $\boldsymbol{\sigma}$ is the stress tensor and $\mathbf{C}^{el}$ is a fourth order tensor of elastic moduli that does not depend on the material deformation. When a material body is subjected to external forces it deforms. The three dimensional stress state of a material can be represented by the stress tensor, $\boldsymbol{\sigma}$ (i.e. σ_{ij}).

$$\sigma_{ij} = \begin{bmatrix} \sigma_{11} & \sigma_{12} & \sigma_{13} \\ \sigma_{21} & \sigma_{22} & \sigma_{23} \\ \sigma_{31} & \sigma_{32} & \sigma_{33} \end{bmatrix} \tag{3.14}$$

The stress tensor is symmetric, whereby $\sigma_{ij} = \sigma_{ji}$, therefore only six independent stress components are needed to represent a stress state. The eigenvalue problem $det[\boldsymbol{\sigma} - \lambda \mathbf{I}] = 0$, where $[\mathbf{I}]$ is the 3x3 identity tensor, leads to the characteristic equation

$$\lambda^3 - I_1(\sigma_{ij})\lambda^2 + I_2(\sigma_{ij})\lambda - I_3(\sigma_{ij}) = 0 \tag{3.15}$$

where the invariants of the stress tensor are

$$I_1 = trace(\boldsymbol{\sigma}) = \sigma_{ii} = \sigma_{11} + \sigma_{22} + \sigma_{33} \tag{3.16}$$

$$I_2 = \sigma_{11}\sigma_{22} + \sigma_{22}\sigma_{33} + \sigma_{11}\sigma_{33} - \sigma_{12}^2 - \sigma_{13}^2 - \sigma_{23}^2 \tag{3.17}$$

$$I_3 = det[\sigma_{ij}] = \sigma_{11}\sigma_{22}\sigma_{33} + 2\sigma_{12}\sigma_{23}\sigma_{31} - \sigma_{33}\sigma_{12}^2 - \sigma_{22}\sigma_{13}^2 - \sigma_{11}\sigma_{23}^2 \tag{3.18}$$

Values of stress invariants are independent of the coordinate system used. The invariants of the stress tensor can also be written in terms of the principal stresses σ_1, σ_2 and σ_3 as

$$I_1 = \sigma_1 + \sigma_2 + \sigma_3 \tag{3.19}$$

$$I_2 = \sigma_1\sigma_2 + \sigma_2\sigma_3 + \sigma_3\sigma_1 \tag{3.20}$$

$$I_3 = \sigma_1\sigma_2\sigma_3 \tag{3.21}$$

The associated principal direction for each principal stress, σ_i, can be calculated as

$$\boldsymbol{\sigma} \cdot \mathbf{n}^i = \sigma_i \mathbf{n}^i \tag{3.22}$$

where $\mathbf{n}^i$ is the unit vector in the ith principal direction. The stress state of a material can be determined if the principal stresses and their directions are known. For plasticity theory it is common to express the stress tensor, σ_{ij}, in terms of the deviatoric stress tensor, $\mathbf{S}$, and the hydrostatic stress (mean stress) tensor, σ_{ij}^0, as

$$\begin{aligned}\sigma_{ij} &= S_{ij} + \sigma_{ij}^{0} \\ &= S_{ij} + p\delta_{ij}\end{aligned} \tag{3.23}$$

The hydrostatic stress tensor, σ_{ij}^{0}, controls the portion of the applied stress that changes the volume where δ_{ij} is the Kronecker tensor and p is the equivalent pressure stress (hydrostatic pressure) defined as

$$p = \frac{1}{3}\sigma_{ii} = \frac{I_1}{3} = -\frac{1}{3}trace(\boldsymbol{\sigma}) \tag{3.24}$$

The deviatoric stress tensor, S_{ij}, is the shape changing stress and hence controls the distortion

$$S_{ij} = \begin{bmatrix} S_{11} & S_{12} & S_{13} \\ S_{21} & S_{22} & S_{23} \\ S_{31} & S_{32} & S_{33} \end{bmatrix} \tag{3.25}$$

and is calculated from

$$S_{ij} = \sigma_{ij} - p\delta_{ij} \tag{3.26}$$

In terms of the components the stress tensor in equation (3.23) can be written as

$$\begin{bmatrix} \sigma_{11} & \sigma_{12} & \sigma_{13} \\ \sigma_{21} & \sigma_{22} & \sigma_{23} \\ \sigma_{31} & \sigma_{32} & \sigma_{33} \end{bmatrix} = \begin{bmatrix} S_{11} & S_{12} & S_{13} \\ S_{21} & S_{22} & S_{23} \\ S_{31} & S_{32} & S_{33} \end{bmatrix} + \begin{bmatrix} p & 0 & 0 \\ 0 & p & 0 \\ 0 & 0 & p \end{bmatrix} \tag{3.27}$$

The eigenvalue problem $det[\mathbf{S} - \lambda\mathbf{I}] = 0$ leads to the characteristic equation

$$\lambda^3 - I_1(S_{ij})\lambda^2 + I_2(S_{ij})\lambda - I_3(S_{ij}) = 0 \tag{3.28}$$

where the invariants of the deviatoric stress tensor are

$$J_1 = trace(S_{ij}) = S_{11} + S_{22} + S_{33} = 0 \tag{3.29}$$

$$J_2 = \frac{1}{2}S_{ij}S_{ij} = S_{12}^2 + S_{13}^2 + S_{23}^2 - S_{11}S_{22} - S_{22}S_{33} - S_{11}S_{33} \tag{3.30}$$

$$J_3 = det[S_{ij}] \tag{3.31}$$

The invariants of the deviatoric stress tensor can also be written in terms of the principal components as S_1, S_2 and S_3 as

$$J_1 = trace(S_{ij}) = S_1 + S_2 + S_3 = 0 \tag{3.32}$$

$$J_2 = \frac{1}{2}(S_1^2 + S_2^2 + S_3^2) \tag{3.33}$$

$$J_3 = S_1 S_2 S_3 \tag{3.34}$$

The second and third invariants of the deviatoric stress tensor, S_{ij}, are related to the invariants of the stress tensor, σ_{ij}, by the following equations

$$J_2 = \frac{1}{3}(I_1^2 - 3I_2) \tag{3.35}$$

$$J_3 = \frac{1}{27}(2I_1^3 - 9I_1 I_2 + 27I_3) \tag{3.36}$$

The von Mises equivalent stress (effective stress), q, is commonly used in the elasto-plastic analysis of materials and can be defined as

$$q = \sqrt{\frac{3}{2} S_{ij} S_{ij}} \tag{3.37}$$

or in terms of the second invariant of the deviatoric stress tensor, J_2, as

$$q = \sqrt{3\, J_2} \tag{3.38}$$

As shown in Figure 3-1, the hydrostatic axis in principal stress space starts at the origin and makes equal angles with the coordinate axes $(\sigma_1, \sigma_2, \sigma_3)$. At all points along the hydrostatic axis

$$\sigma_1 = \sigma_2 = \sigma_3 = \frac{1}{3} I_1 \tag{3.39}$$

$$S_1 = S_2 = S_3 = 0 \tag{3.40}$$

Any plane perpendicular to the hydrostatic axis is called an octahedral (deviatoric) plane, which is represented by

$$\sigma_1 + \sigma_2 + \sigma_3 = \mathrm{C} = \sqrt{3d} \tag{3.41}$$

where d is the distance from the origin to the plane and C is a constant. The plane is termed the π-plane when $d = 0$. For a stress state the hydrostatic part is represented by a vector along the hydrostatic axis. The deviatoric part is represented by a vector on the deviatoric plane which is perpendicular to the hydrostatic axis (Figure 3-1) (Khan and Huang 1995; Öchsner and Hosseini 2010).

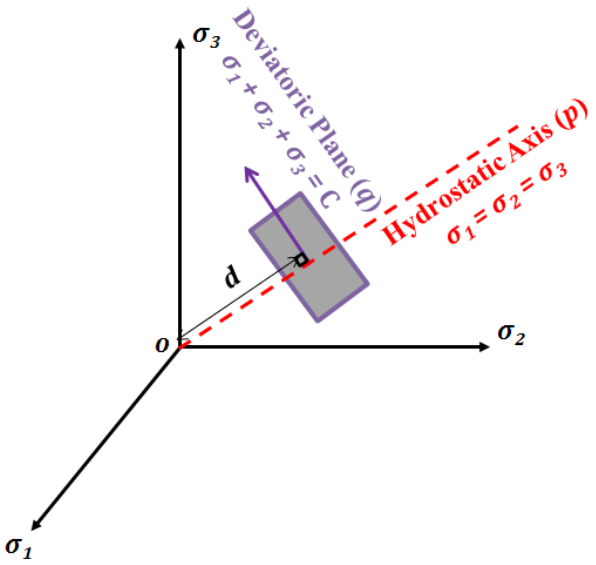

Figure 3-1 Principal stress space showing the hydrostatic axis and the deviatoric stress plane (Khan and Huang 1995).

The strain tensor, $\boldsymbol{\varepsilon}$, is symmetric whereby $\varepsilon_{ij} = \varepsilon_{ji}$ and can be written as

$$\varepsilon_{ij} = \begin{bmatrix} \varepsilon_{11} & \varepsilon_{12} & \varepsilon_{13} \\ \varepsilon_{21} & \varepsilon_{22} & \varepsilon_{23} \\ \varepsilon_{31} & \varepsilon_{32} & \varepsilon_{33} \end{bmatrix} \tag{3.42}$$

The eigenvalue problem $det[\boldsymbol{\varepsilon} - \lambda \mathbf{I}] = 0$ leads to the characteristic equation

$$\lambda^3 - I_1(\varepsilon_{ij})\lambda^2 + I_2(\varepsilon_{ij})\lambda - I_3(\varepsilon_{ij}) = 0 \tag{3.43}$$

where the invariants of the strain tensor are

$$I_1 = trace(\boldsymbol{\varepsilon}) = \varepsilon_{ii} = \varepsilon_{11} + \varepsilon_{22} + \varepsilon_{33} \tag{3.44}$$

$$I_2 = \varepsilon_{12}^2 + \varepsilon_{13}^2 + \varepsilon_{23}^2 - \varepsilon_{11}\varepsilon_{22} - \varepsilon_{22}\varepsilon_{33} - \varepsilon_{11}\varepsilon_{33} \tag{3.45}$$

$$I_3 = det[\varepsilon_{ij}] \tag{3.46}$$

Similar to the stress tensor, the strain tensor can be written in terms of the deviatoric strain tensor, ε'_{ij}, and the volumetric strain tensor, ε^0_{ij}, as

$$\varepsilon_{ij} = \varepsilon'_{ij} + \varepsilon^0_{ij} \tag{3.47}$$

$$= \varepsilon'_{ij} + \varepsilon_{vol}\delta_{ij} \tag{3.48}$$

where ε_{vol} is the volumetric strain calculated as

$$\varepsilon_{vol} = \varepsilon_{11} + \varepsilon_{22} + \varepsilon_{33} = \frac{1}{3} trace(\boldsymbol{\varepsilon}) \tag{3.49}$$

In terms of model definition, the elasticity is considered to be isotropic and linear (in terms of finite deformation quantities) and, therefore, the elastic component of the deformation can be defined in terms of two material constants. The bulk modulus, K, and the shear modulus, G, can be calculated using the Young's modulus, E, and the elastic Poisson's ratio, ν_e.

$$\mathrm{K} = \frac{\mathrm{E}}{3(1 - 2\nu_e)} \tag{3.50}$$

$$\mathrm{G} = \frac{\mathrm{E}}{2(1 + \nu_e)} \tag{3.51}$$

If a material is compressed along its axial direction the Poisson's ratio,ν_e, can be calculated as

$$\nu_e = -\frac{\varepsilon_{trans}}{\varepsilon_{axial}} \tag{3.52}$$

where ε_{trans} is the transverse strain and ε_{axial} is the axial strain. The plastic Poisson's ratio, ν_p, can also be calculated in the same manner.

3.1.3.1 Yield Criterion, Plastic Flow and Hardening Rule

To describe the post yield behaviour of a material the yield criterion, flow rule and hardening rule are required. The yield criterion relates the stress state of the material to the onset of plastic yielding. When plastic flow of the material occurs, the flow rule relates the stress state to the corresponding increment (rate) of plastic strain. The hardening rule describes how the yield criterion is modified by straining beyond the initial yield (Abrate 2008; Khan and Huang 1995; Öchsner and Hosseini 2010).

The yield surface (or failure surface) is the boundary in stress space between the elastic and plastic components. The shape, size and orientation of the yield surface is important as the stress-strain relationship is different for elastic and plastic deformation. When a material deforms elastically its current stress state lies within the yield surface and the yield criterion can be defined as follows

$$F(\boldsymbol{\sigma}) < 0 \tag{3.53}$$

Yielding occurs if the stress state of a material falls on the yield surface

$$F(\boldsymbol{\sigma}) = 0 \tag{3.54}$$

For an isotropic material, plastic yielding is only dependent on the magnitude of the principal stresses and not on the direction. The yield criterion for a plasticity formulation can be graphically represented as a 3D surface in principal stress space, as described in later sections for each plasticity formulation considered. For yield criteria that depend only on the deviatoric stress (pressure independent), the shape of the yield surface is constant along the hydrostatic axis. If the yield criterion depends only on J_2, the yield surface is a constant diameter along the hydrostatic axis and circle in the deviatoric plane around the hydrostatic axis. If the yield criterion is dependent on the third invariant of the deviatoric stress tensor, J_3, the yield surface can deviate from a circle in the deviatoric plane. If the yield criterion is pressure dependent (I_1 invariant) the diameter along the hydrostatic axis may change but remains a circle in the deviatoric plane (Öchsner and Hosseini 2010).

The yield surface definition depends on the stress variables in addition to the plastic strain and hardening parameters. As the material is additionally loaded, the stress state must stay on the yield surface with $F = 0$, as the yield function for a rate independent model can not have a positive value, although the yield surface can

move and change shape as the equivalent (effective) plastic strain, $\boldsymbol{\varepsilon}^{pl}$, varies. The yield function can be expressed as a function of the true Cauchy stress components and the equivalent plastic strain

$$F(\boldsymbol{\sigma}, \boldsymbol{\varepsilon}^{pl}) = 0 \tag{3.55}$$

When the stress state reaches the failure surface further loading induces plastic flow**,** the onset of plastic flow occurring when $F(\boldsymbol{\sigma}) = 0$.

For isotropic hardening, when plastic flow is induced the shape of the yield surface changes uniformly in all directions. It should be noted that although it is referred to as a "hardening" model, strain softening or a combination of softening and hardening can be defined. Isotropic hardening is considered suitable for quasi-static analysis as the material is deformed plastically past the initial yield state where the Bauschinger effect is noticeable (Abaqus 2011; Rice 1975). A general form of the yield criterion, F, for an isotropic hardening material can be defined as

$$F = f(\boldsymbol{\sigma}) - \kappa(\bar{\varepsilon}^{pl}) = 0 \tag{3.56}$$

where $\bar{\varepsilon}^{pl}$ is a hardening parameter and $\kappa(\bar{\varepsilon}^{pl})$ represents the stress-strain relation (Cvitanic et al. 2008). The hardening parameter defines the way in which the yield surface and/or flow potential definitions change as plastic deformation occurs. The hardening parameter, $\bar{\varepsilon}^{pl}$ is termed the work equivalent plastic strain as it is considered as an equivalent plastic strain that obeys the principal of plastic work conjugacy equivalence as defined by

$$f(\boldsymbol{\sigma}) d\bar{\varepsilon}^{pl} = \boldsymbol{\sigma} : d\boldsymbol{\varepsilon}^{pl} \tag{3.57}$$

The flow rule is usually stated in terms of the flow potential, g, as a function of stress. The flow rule governs the way the increment of plastic strain is computed. For the non-associated flow rule, the plastic part of the deformation is governed by

$$d\boldsymbol{\varepsilon}^{pl} = d\lambda \frac{\partial \mathrm{g}(\boldsymbol{\sigma})}{\partial \boldsymbol{\sigma}} \tag{3.58}$$

where λ is a positive scalar called a plastic multiplier or consistency parameter measuring the amount of plastic flow rate.

The flow rule is referred to as the associated flow rule (or normality rule) if the plastic flow potential, g, and the yield function, f, are identical and equation (3.58) becomes

$$f(\boldsymbol{\sigma}) = \mathrm{g}(\boldsymbol{\sigma}) \quad \text{i.e.} \quad \frac{\partial \mathrm{g}}{\partial \boldsymbol{\sigma}} = \frac{\partial f}{\partial \boldsymbol{\sigma}} \tag{3.59}$$

In this case, as the material yields the plastic strain rate is normal to the yield surface in principal stress space. Hence the plastic deformation is volume invariant.

In the present work, material hardening behaviour is defined from uniaxial compression experimental data. For most formulations the isotropic hardening data inputted into Abaqus in tabular form in a piecewise linear hardening curve in terms of the true Cauchy stress versus axial logarithmic plastic strain. The plastic strain data corresponds to the onset of plasticity i.e., the initial plastic strain input must be zero. The hardening curve for each plasticity formulation is described in the subsequent sections.

Perfectly plastic material behaviour is the simplest plasticity model which contains no hardening parameters, therefore, the model does not evolve during deformation and the material can exhibit unlimited plastic flow. The material undergoes irrecoverable deformation without an increase in stress.

3.2 Constitutive Plasticity Formulations

The following six constitutive plasticity formulations are investigated in the present work: von Mises; Hill; Mohr-Coulomb; Drucker-Prager; crushable foam with isotropic hardening; and crushable foam with volumetric hardening. Each model is inbuilt into the Abaqus code and has been developed within the framework of elasto-plasticity as described previously. The elastic behaviour for each constitutive formulation is modelled as linear elastic. The main features of each of the plasticity formulations are described in the following sections.

3.2.1 Von Mises Plasticity Formulation

The von Mises plasticity formulation (von Mises 1913), also known as the J_2 plasticity or flow theory, is isotropic and predicts equal yield strengths in compression and tension. For the von Mises plasticity formulation, plastic yielding is considered to be independent of the equivalent pressure stress, p, hence the plastic component of the deformation is incompressible.

Yield Criterion:

$$F = J_2 - \kappa^2 = 0 \tag{3.60}$$

where κ is a constant and J_2 is the second invariant of deviatoric stress tensor as given in equation (3.30). By assuming the material is under uniaxial stress, the uniaxial yield stress of the material can be defined as $\sigma_y = \sqrt{3}\kappa$. By substituting in equation (3.60) for J_2 and κ, the definition of the yield criterion can be rewritten in terms of stress components as

$$F = \frac{3}{2} S_{ij} S_{ij} - \sigma_y^2 = 0 \tag{3.61}$$

$$F = q - \sigma_y = 0 \tag{3.62}$$

where q is the von Mises equivalent stress as shown in equation (3.38). The von Mises plasticity formulation represents a cylinder in principal stress space that is parallel to the hydrostatic stress axis, as shown in Figure 3-2.

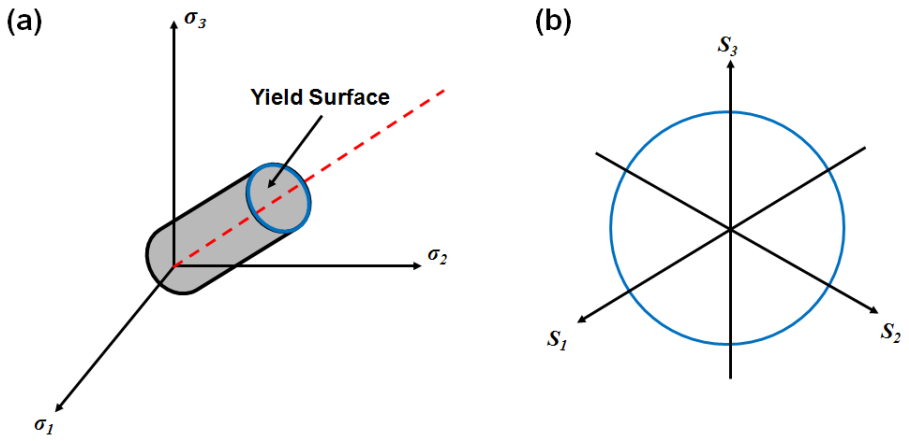

Figure 3-2 (a) In principal stress space the von Mises plasticity formulation represents a cylinder (b) The yield surface in the deviatoric plane (Abaqus 2011)

Flow Rule: The flow is associated flow and the equivalent plastic strain rate, $d\boldsymbol{\varepsilon}^{pl}$, is defined as

$$d\boldsymbol{\varepsilon}^{pl} = S_{ij}\frac{3}{2}\frac{d\bar{\varepsilon}^{pl}}{q} \tag{3.63}$$

Hardening: The isotropic hardening data for the von Mises plasticity formulation is defined from uniaxial compression experimental data and is inputted in tabular form in a piecewise linear hardening curve in terms of the true Cauchy stress versus axial logarithmic plastic strain.

3.2.2 Hill Plasticity Formulation

The anisotropic Hill plasticity formulation, which was proposed by Hill (Hill 1948), is a generalisation of the isotropic von Mises plasticity formulation. Hence, it assumes that yielding is independent of the equivalent pressure stress, p, and that the plastic component of the deformation is incompressible. It assumes symmetric behaviour in tension and compression and accounts for anisotropic behaviour by predicting different yield stresses in the three principal directions.

Yield Criterion:

$$F = \sqrt{\mathrm{L}(\sigma_2 - \sigma_3)^2 + \mathrm{M}(\sigma_3 - \sigma_1)^2 + \mathrm{N}(\sigma_1 - \sigma_2)^2 + 2\mathrm{T}\tau_{23}^2 + 2\mathrm{U}\tau_{31}^2 + 2\mathrm{V}\tau_{12}^2} \quad (3.6$$

$$\mathrm{L} = \frac{\sigma_0^2}{2}\left(\frac{1}{\bar{\sigma}_2^2} + \frac{1}{\bar{\sigma}_3^2} - \frac{1}{\bar{\sigma}_1^2}\right) \quad (3.65)$$

$$\mathrm{M} = \frac{\sigma_0^2}{2}\left(\frac{1}{\bar{\sigma}_3^2} + \frac{1}{\bar{\sigma}_1^2} - \frac{1}{\bar{\sigma}_2^2}\right) \quad (3.66)$$

$$\mathrm{N} = \frac{\sigma_0^2}{2}\left(\frac{1}{\bar{\sigma}_1^2} + \frac{1}{\bar{\sigma}_2^2} - \frac{1}{\bar{\sigma}_3^2}\right) \quad (3.67)$$

$$\mathrm{T} = \frac{3}{2}\left(\frac{\tau_0}{\bar{\tau}_{23}}\right) \qquad \mathrm{U} = \frac{3}{2}\left(\frac{\tau_0}{\bar{\tau}_{13}}\right) \qquad \mathrm{V} = \frac{3}{2}\left(\frac{\tau_0}{\bar{\tau}_{12}}\right) \quad (3.68)$$

Where L, M, N, T, U and V are material constants, σ_i are the direct stress components in the principal directions of anisotropy, τ_{ij} are the shear stress components, $\bar{\sigma}_i$ are the uniaxial yield stresses in the principal directions of anisotropy and $\bar{\tau}_{ij}$ are the shear yield stresses with respect to the axis of anisotropy.

Flow and Hardening: The flow is associated and in the present work and perfect plasticity is assumed for the Hill plasticity formulation.

3.2.3 Mohr-Coulomb Plasticity Formulation

The Mohr-Coulomb plasticity formulation used in the present work is an extension of the classical Mohr-Coulomb failure criterion which includes an isotropic cohesion hardening law and flow rule. The Mohr-Coulomb plasticity formulation is pressure dependent and can be written in terms of three stress invariants, q, p and J_3.

Yield Criterion:

$$F = R_{mc}q - p\mathrm{Tan}\varphi - \mathrm{c} = 0 \tag{3.69}$$

where φ is the friction angle of the material, c is the cohesion yield stress of the material and R_{mc} is the Mohr-Coulomb deviatoric stress measure defined as

$$R_{mc} = \frac{1}{\sqrt{3}\mathrm{Cos}\varphi}\mathrm{Sin}\left(\Theta + \frac{\pi}{3}\right) + \frac{1}{3}\mathrm{Cos}\left(\Theta + \frac{\pi}{3}\right)\mathrm{Tan}\varphi \tag{3.70}$$

and Θ is the deviatoric polar angle (Chen and Han 2008) defined as

$$\mathrm{Cos}(3\Theta) = \left(\frac{J_3}{q}\right)^3 \tag{3.71}$$

where J_3 is the third invariant of the deviatoric stress tensor.

In the meridional plane the friction angle, φ, determines the slope of the yield surface (Figure 3-3). For a friction angle of 0°, the Mohr-Coulomb plasticity formulation reduces to the Tresca model. Unlike the classical Mohr-Coulomb plasticity formulation, the Mohr-Coulomb plasticity formulation used by Menétrey and Willam (1995), has no corners in the deviatoric stress space. This provides a smooth flow potential and hence a unique definition of the plastic flow direction.

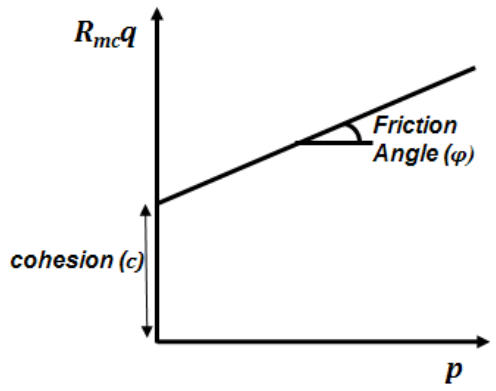

Figure 3-3 The yield criterion for the Mohr-Coulomb plasticity formulation in the meridional $p - R_{mc}q$ plane (Abaqus 2011).

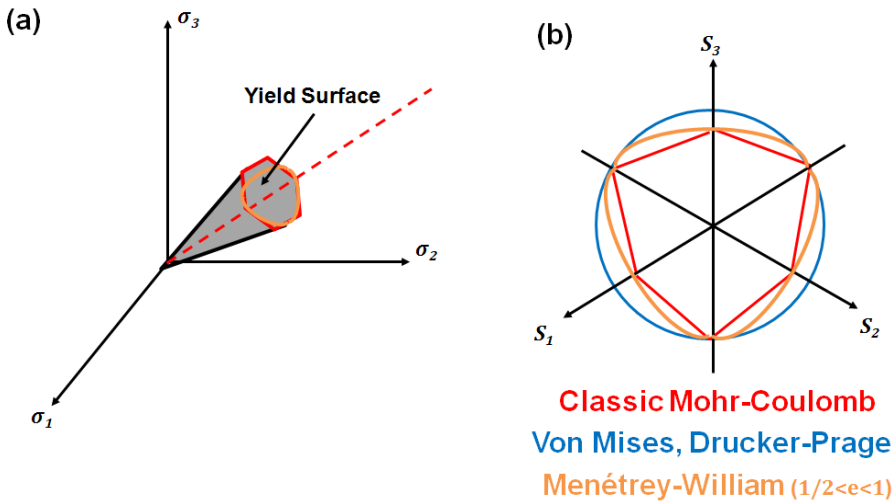

Figure 3-4 (a) The yield surface in principal stress space for the Mohr-Coulomb plasticity formulation (b) The von Mises, classic Mohr-Coulomb (and Menétrey and Willam (1995)), and Drucker-Prager plasticity formulations in the deviatoric stress plane.

Flow Potential:

$$\mathrm{g} = \sqrt{(\epsilon \mathrm{c}|_0 \mathrm{Tan}\psi)^2 + (R_{mw} q)^2} - p\mathrm{Tan}\psi \tag{3.72}$$

$$R_{mw} = \frac{4(1-e^2)\mathrm{Cos}^2\Theta + (2e-1)^2}{2(1-e^2)\mathrm{Cos}\Theta + (2e-1)\sqrt{4(1-e^2)\mathrm{Cos}^2\Theta + 5e^2 - 4e}} R_{mc} \tag{3.73}$$

$$e = \frac{3 - Sin\varphi}{6Cos\varphi} \tag{3.74}$$

where ϵ is the meridional eccentricity, $\mathrm{c}|_0$ is the initial cohesion yield stress where $\boldsymbol{\varepsilon}^{pl} = 0$, ψ is the dilation angle measured in the $p - R_{mw}q$ plane, R_{mw} is the smooth elliptical function in the deviatoric stress plane used by Menétrey and Willam (1995) (Figure 3-5) and e is the "out of roundness" parameter which is determined by matching the flow potential to the yield surface in triaxial compression and triaxial tension in the deviatoric stress plane.

Flow Rule: The flow is non-associated flow and the equivalent plastic strain rate, $d\boldsymbol{\varepsilon}^{pl}$, is defined as

$$d\boldsymbol{\varepsilon}^{pl} = \frac{d\bar{\varepsilon}^{pl}}{g} \frac{\partial \mathrm{g}}{\partial \boldsymbol{\sigma}} \tag{3.75}$$

where

$$g = \frac{1}{\mathrm{c}}\boldsymbol{\sigma}:\frac{\partial \mathrm{g}}{\partial \boldsymbol{\sigma}} \tag{3.76}$$

and the equivalent plastic strain rate, $d\boldsymbol{\varepsilon}^{pl}$, is defined by the work conjugacy expression as

$$\mathrm{c}d\bar{\varepsilon}^{pl} = \boldsymbol{\sigma}: d\boldsymbol{\varepsilon}^{pl} \tag{3.77}$$

In the meridional plane the flow can be close to associated if the friction angle, φ, and the dilation angle, ψ, are equal and the eccentricity parameter, ϵ, is small.

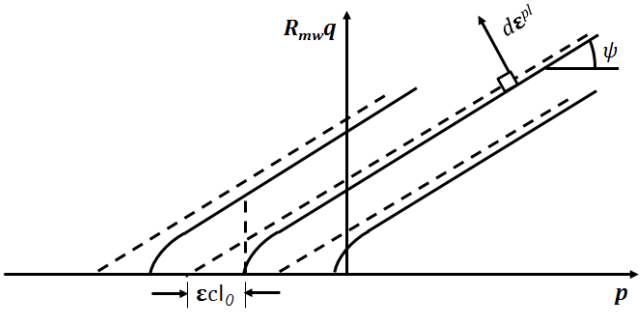

Figure 3-5 The flow potential for the Mohr-Coulomb plasticity formulation has a hyperbolic shape in the meridional ($p - R_{mw}q$) stress plane. The eccentricity, ϵ, defines the rate at which the function approaches the asymptote, provided that the flow potential tends to a straight line as the eccentricity tends to zero (Abaqus 2011).

Hardening: The isotropic cohesion hardening law is implemented in tabular form where the hardening parameter, the cohesion yield stress c, is dependent on the equivalent plastic strain.

3.2.4 Drucker-Prager Plasticity Formulation

The Drucker-Prager plasticity formulation was introduced by Drucker and Prager (1951). A modified form of the original Drucker-Prager plasticity formulation is used in the present work. It incorporates pressure dependent and asymmetric yielding, as it allows different yield stresses in triaxial tension and compression. The von Mises equivalent stress, q, is a linear function of the hydrostatic pressure, p, hence the failure surface is a straight line in the meridional $(q - p)$ plane (Figure 3-6). This linear form of the Drucker-Prager plasticity formulation is most suitable for the application used in the present work, where the stresses are mostly compressive (Abaqus 2011). The Drucker-Prager plasticity formulation is similar to the Mohr-Coulomb plasticity formulation but attempts to provide a smoother yield surface.

Yield Criterion:

$$F = t - p\mathrm{Tan}\beta - d = 0 \tag{3.78}$$

where

$$t = \frac{q}{2}\left[1 + \frac{1}{K_{DP}} - \left(1 - \frac{1}{K_{DP}}\right)\left(\frac{J_3}{q}\right)^3\right] \tag{3.79}$$

$$d = \left(1 - \frac{1}{3}\mathrm{Tan}\beta\right)\sigma_c \tag{3.80}$$

where t is the Drucker-Prager deviatoric stress measure, β is the friction angle of the material, d is the cohesion yield stress, K_{DP} is flow stress ratio, J_3 is the third invariant of deviatoric stress tensor, σ_c is the uniaxial compression yield stress.

The friction angle, β, defines the slope of the linear yield surface in the $p - t$ plane (Figure 3-6). Due to the linear yield surface, higher stresses are required to result in further plastic deformation. The flow stress ratio, K_{DP}, is the ratio of the yield stress in triaxial tension to the yield stress in triaxial compression. The classical Drucker-Prager plasticity formulation is obtained for $K_{DP} = 1$, whereby the yield stresses in triaxial tension and triaxial compression are equal which implies that $t = q$.

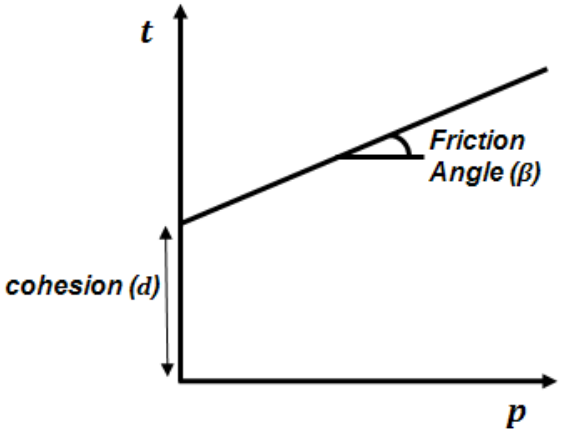

Figure 3-6 The yield criterion for the Drucker-Prager plasticity formulation in the meridional plane (Abaqus 2011).

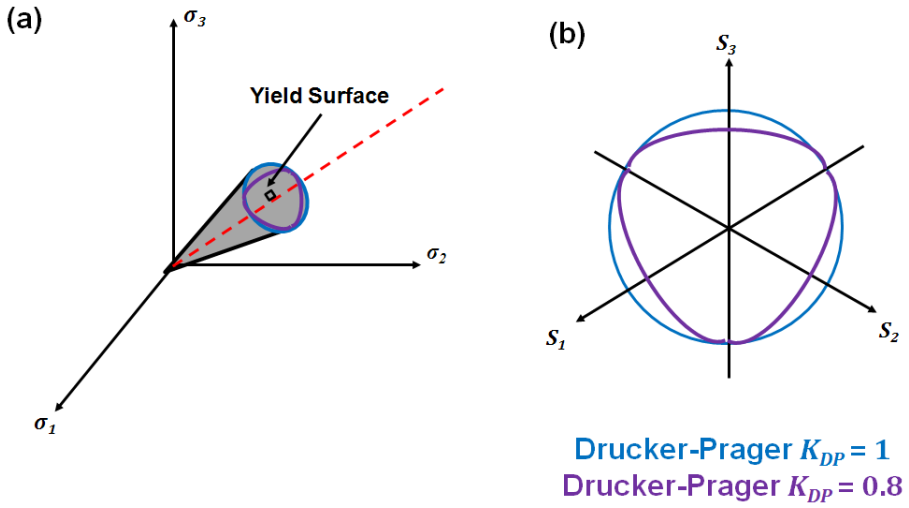

Figure 3-7 (a) The yield surface in principal stress space for the Drucker-Prager plasticity formulation (b) The yield surface for the Drucker-Prager plasticity formulation in the deviatoric plane. The yield surface is convex for $0.778 < K_{DP} < 1$ (Abaqus 2011).

Flow Potential:

$$g = t - p\mathrm{Tan}\psi \tag{3.81}$$

where ψ is the dilation angle of the material in the $p - t$ stress plane. The inelastic deformation of the material is incompressible and no dilation occurs for $\psi = 0$, whereas, for positive values of ψ the material dilates.

Flow Rule: In the deviatoric plane the flow is associated as both the yield surface and flow potential have the same dependence on deviatoric stress measure, t, as

evident in equations (3.78) and (3.81). The flow is non-associated in the meridional $(p-t)$ plane, and the equivalent plastic strain rate, $d\boldsymbol{\varepsilon}^{pl}$, is defined as

$$d\boldsymbol{\varepsilon}^{pl} = \frac{d\bar{\varepsilon}^{pl}}{\mathrm{c}} \frac{\partial \mathrm{g}}{\partial \boldsymbol{\sigma}} \tag{3.82}$$

when hardening is defined in uniaxial compression

$$\mathrm{c} = \left(1 - \frac{1}{3}\mathrm{Tan}\psi\right) \tag{3.83}$$

The flow in the meridional plane reduces to associated flow when $\psi = \beta$, and hence reduces to the original Drucker-Prager plasticity formulation.

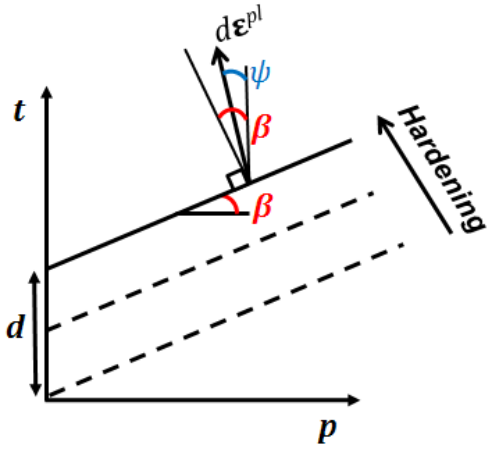

Figure 3-8 The yield surface and flow direction in the meridional $p-t$ plane (Abaqus 2011).

Hardening: The isotropic hardening data is defined from uniaxial compression experimental data and is inputted in tabular form in a piecewise linear hardening curve in terms of the true Cauchy stress versus axial logarithmic plastic strain.

3.2.5 Crushable Foam Plasticity Formulations

Two crushable foam plasticity formulations are considered in the present work and are referred to as the crushable foam with isotropic hardening (CFI) plasticity formulation and the crushable foam with volumetric hardening (CFV) plasticity formulation. Both yield surfaces are isotropic and have an elliptical dependence of the von Mises equivalent stress, q, on the equivalent pressure stress, p. A detailed description of both crushable foam plasticity formulations is given below and further information is available from (Abaqus 2008; Deshpande and Fleck 2000; Tita 2012). Under mostly compressive loading both plasticity formulations predict similar behaviour. For both the CFI and CFV plasticity formulations, the yield surface is a von Mises circle in the deviatoric stress plane and an ellipse in the meridional (q-p) stress plane.

3.2.5.1 Crushable Foam with Isotropic Hardening

The CFI plasticity formulation was developed by (Deshpande and Fleck 2000) and assumes symmetric behaviour under hydrostatic tension and hydrostatic compression. It assumes an isotropic yield surface in addition to isotropic hardening.

Yield Criterion:

$$F = \sqrt{q^2 + \alpha^2 p^2} - B = 0 \tag{3.84}$$

where

$$B = \alpha p_c \tag{3.85}$$

$$\alpha = \frac{3K}{\sqrt{9 - K^2}} \tag{3.86}$$

$$K = \frac{\sigma_c^0}{p_c^0} \tag{3.87}$$

where α is the shape of the yield ellipse, B is the size of the yield ellipse, p_c is the yield stress in hydrostatic compression, K is the compression yield stress ratio, σ_c^0 is the initial yield stress in uniaxial compression and p_c^0 is the initial yield stress in hydrostatic compression.

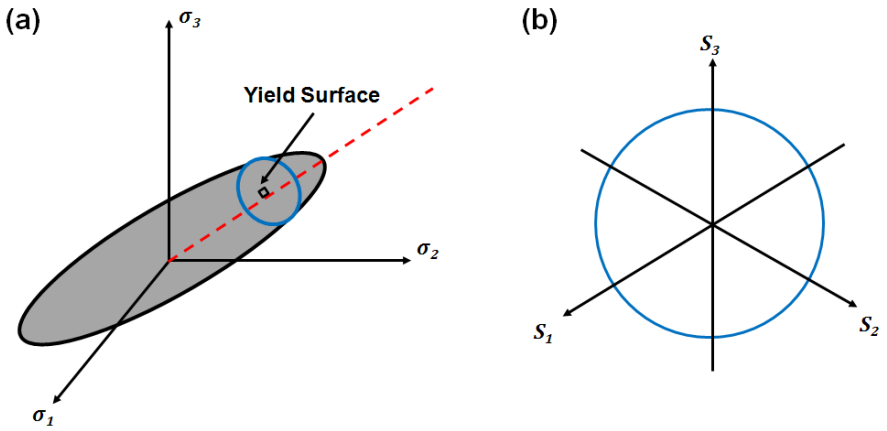

Figure 3-9 (a) The yield surface in principal stress space for the crushable foam with isotropic hardening (CFI) plasticity formulation (b) The yield surface for the CFI plasticity formulation in the deviatoric plane, which is a von Mises circle.

In the meridional $(q - p)$ stress plane the isotropic yield surface is an ellipse centred at the origin (Figure 3-10(a)) and evolves in uniformly on all loading paths. The shape of the yield ellipse, α, is defined using the parameter K. When $K = 0$, it reduces to the von Mises circle.

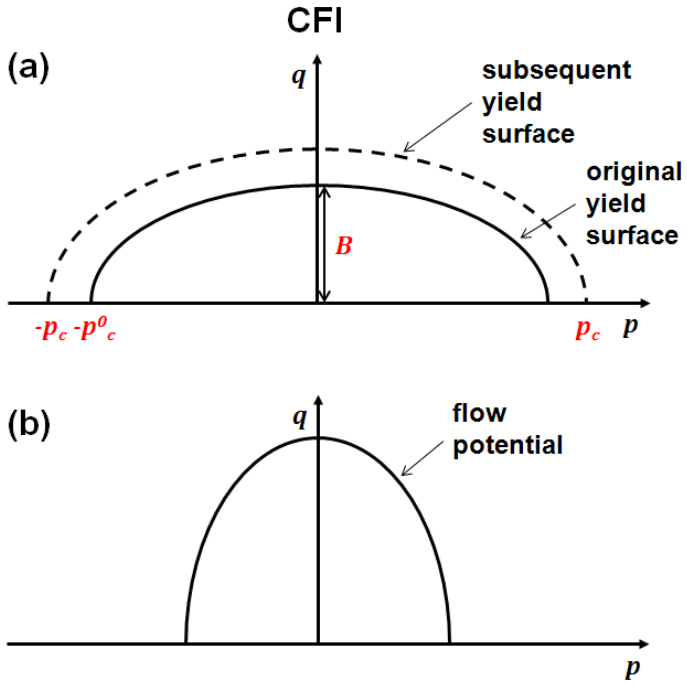

Figure 3-10 (a) The yield surface and yield surface evolution and (b) flow potential for the crushable foam with isotropic hardening (CFI) plasticity formulation in the meridional $q - p$ stress plane (Abaqus 2011).

Flow Potential:

$$\mathrm{g} = \sqrt{q^2 + \beta^2 p^2} \tag{3.88}$$

where β is the shape of the ellipse for the flow potential which is controlled by plastic Poisson's ratio ν_p as

$$\beta = \frac{3}{\sqrt{2}} \sqrt{\frac{1 - 2\nu_p}{1 + \nu_p}} \tag{3.89}$$

The plastic Poisson's ratio, ν_p, is determined under uniaxial compression and is the ratio of the transverse to the longitudinal plastic strain. For a $\nu_p = 0.5$, the plastic flow is incompressible.

Flow Rule: The flow is non-associated flow which allows independent calibration of the yield surface shape and the plastic Poisson's ratio, ν_p. The equivalent plastic strain rate, $\boldsymbol{\varepsilon}^{pl}$, is defined as

$$d\boldsymbol{\varepsilon}^{pl} = d\bar{\varepsilon}^{pl} \frac{\partial \mathrm{g}}{\partial \boldsymbol{\sigma}} \tag{3.90}$$

and the equivalent plastic strain rate, $d\boldsymbol{\varepsilon}^{pl}$, is defined by the work conjugacy expression as

$$\sigma_c d\bar{\varepsilon}^{pl} = \boldsymbol{\sigma} : d\boldsymbol{\varepsilon}^{pl} \tag{3.91}$$

where σ_c is the yield stress under uniaxial compression. When $\alpha = \beta$, the flow is associated.

Hardening: The isotropic hardening data is defined from uniaxial compression experimental data and is inputted in tabular form in a piecewise linear hardening curve in terms of the true Cauchy stress versus axial logarithmic plastic strain.

3.2.5.2 Crushable Foam with Volumetric Hardening

The CFV plasticity formulation accounts for different material responses in hydrostatic tension and compression. It is motivated by the fact that cellular foams generally have higher yield stress under hydrostatic compression than under hydrostatic tension. Under tension, cellular materials are more brittle and the cell walls break more readily than under compression. Under compressive loading cellular materials deform volumetrically due to the buckling of the cell walls (Gibson 1985; Gibson 2005; Gibson and Ashby 1982, 1999). The CFV plasticity formulation assumes that the deformation cannot be recovered instantaneously and, therefore, is assumed plastic for small time periods.

Yield Criterion:

$$F = \sqrt{q^2 + \alpha^2 (p - p_0)^2} - B = 0 \tag{3.92}$$

where

$$\alpha = \frac{3K}{\sqrt{(3K_t + K)(3 - K)}} \tag{3.93}$$

$$B = \alpha \frac{p_c + p_t}{2} \tag{3.94}$$

$$K = \frac{\sigma_c^0}{p_c^0} \tag{3.95}$$

$$K_t = \frac{p_t}{p_c^0} \tag{3.96}$$

where α is the shape of the yield ellipse, p_0 is the centre of the yield ellipse on the p-axis, B is the size of the yield ellipse, K is the compression yield stress ratio, K_t is the hydrostatic yield stress ratio, p_c is the yield stress in hydrostatic compression, p_t is the yield stress in hydrostatic tension, σ_c^0 is the initial yield stress in uniaxial compression and p_c^0 is the initial yield stress in hydrostatic compression.

The shape of the elliptical yield surface is defined by the parameters K and K_t. The von Mises circle is recovered when $\alpha = 0$. The value of K_t does not largely effect the results unless the material is loaded under hydrostatic tension.

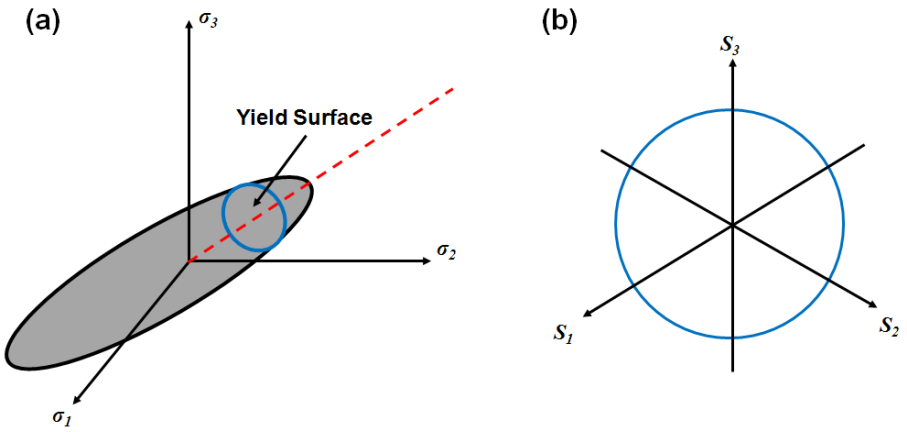

Figure 3-11 The yield surface in principal stress space for the crushable foam with isotropic hardening (CFI) plasticity formulation (b) The yield surface for the CFI plasticity formulation in the deviatoric plane is a von Mises circle.

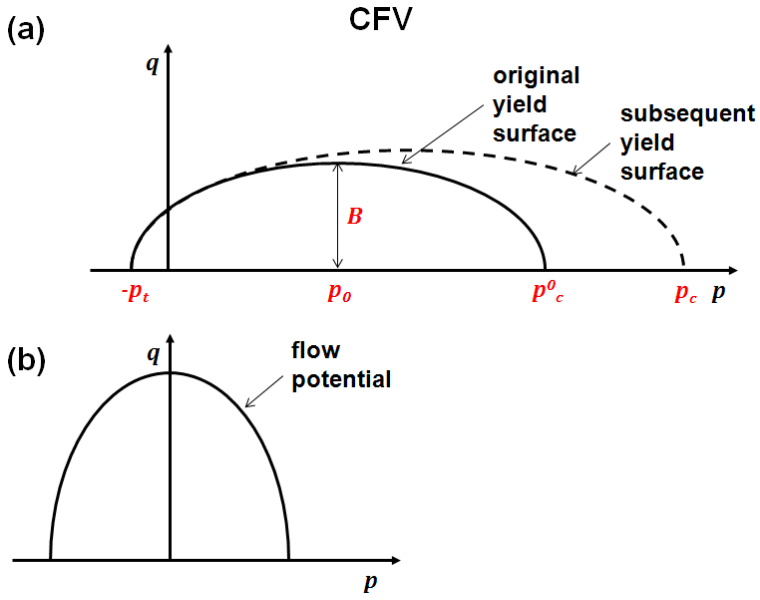

Figure 3-12 (a) The yield surface and yield surface evolution and (b) flow potential for the crushable foam with volumetric hardening (CFV) constitutive plasticity formulation in the meridional $q - p$ stress plane (Abaqus 2011).

Flow Potential:

$$g = \sqrt{q^2 + \frac{9}{2}p^2} \tag{3.97}$$

The flow potential for the CFV plasticity formulation is shown in Figure 3-12(b). Unlike the CFI plasticity formulation, no control over the flow potential is available for the CFV plasticity formulation and a plastic Poisson's ratio, ν_p, of zero is

assumed. Under pure shear or hydrostatic tension loading (zero or negative pressure stress) no yielding occurs, the value of p_t is fixed during plastic deformation, and perfect plasticity is assumed (Figure 3-12(a)). For compressive loading (positive pressure stress) hardening occurs and the yield surface evolves to the right of the $q-p$ stress plane according to the hydrostatic compression yield stress, p_c, as shown in Figure 3-12(a).

Flow Rule: The flow is non-associative and the equivalent plastic strain rate, $d\boldsymbol{\varepsilon}^{pl}$, is defined as

$$d\boldsymbol{\varepsilon}^{pl} = d\bar{\varepsilon}^{pl}\frac{\partial \mathrm{g}}{\partial \boldsymbol{\sigma}} \tag{3.98}$$

and the equivalent plastic strain rate, $d\boldsymbol{\varepsilon}^{pl}$, is defined by the work conjugacy expression as

$$\mathrm{g}d\bar{\varepsilon}^{pl} = \boldsymbol{\sigma}\colon d\boldsymbol{\varepsilon}^{pl} \tag{3.99}$$

The equivalent plastic strain rate is related to the axial plastic strain rate, ε_{axial}^{pl}, under uniaxial compression by

$$d\bar{\varepsilon}^{pl} = \sqrt{\frac{2}{3}d\varepsilon_{axial}^{pl}} \tag{3.100}$$

Hardening: Volumetric hardening is assumed for the CFV plasticity formulation where the hardening data is defined from the uniaxial compression experimental data and the value of the volumetric compression stress, p_c.

The yield surface evolves according to the volumetric compression stress, p_c, as a function of the volumetric plastic strain, ε_{vol}^{pl}, due to compaction (density increase) or dilation (density reduction) of the material

$$p_c\left(\varepsilon_{vol}^{pl}\right) = \frac{\sigma_c\left(\varepsilon_{vol}^{pl}\right)\left[\sigma_c\left(\varepsilon_{vol}^{pt}\right)\left(\frac{1}{\alpha^2}+\frac{1}{9}\right)+\frac{p_t}{3}\right]}{p_t+\frac{\sigma_c\left(\varepsilon_{vol}^{pl}\right)}{3}} \tag{3.101}$$

In order to calibrate the hardening curve with the uniaxial compression experimental data, equation (3.101) is determined by applying the yield criterion in equation (3.92) to a uniaxial compression test and isolating p_c. The hardening data is inputted in tabular form in a piecewise linear hardening curve in terms of the Cauchy stress

versus axial logarithmic plastic strain, ε_{axial}^{pl}. As the $\nu_p = 0$, under uniaxial compression the axial plastic strain is

$$\varepsilon_{axial}^{pl} = \varepsilon_{vol}^{pl}$$

3.2.6 Summary of Plasticity Formulations

Table 3-1 outlines the material parameters required for calibration of each constitutive plasticity formulation.

Table 3-1Summary of the constitutive plasticity formulations

Plasticity Formulation	Pressure Dependence	Material Parameters	Hardening
Von Mises	Pressure independent	σ_y	Isotropic
Mohr-Coulomb	Linear function of q and p	σ_y, φ, c, ψ	Isotropic cohesion
Drucker-Prager	Linear function of q and p	σ_y, β, K_{DP}, ψ	Isotropic
Crushable Foam -isotropic	Elliptical dependence of q on p	σ_y, K, ν_p	Isotropic
Crushable Foam -volumetric	Elliptical dependence of q on p	σ_y, K, K_t	Volumetric

3.3 Finite Element Solution Methods

In the present work two finite element numerical approaches are used, Abaqus/Standard and Abaqus/Explicit (Dassault Systémes Simulia Corp. Providence, RI, USA) to solve boundary value problems. The implicit general purpose finite element solver code Abaqus/Standard is used to solve a range of linear and non-linear problems. The explicit code Abaqus/Explicit is used for solving transient dynamic problems due to its efficiency in solving highly non-linear problems and complex contact conditions. In this section, a summary of the fundamental equations upon which both codes are based are presented. Further information on the explicit and implicit finite element theory can be found in (Abaqus 2011; Fagan 1992).

The finite element method solves boundary value problems by dividing a body into subsections called elements which are connected together at nodes (points). The group of nodes and elements which represent the material body, V, is called a finite element mesh. The governing constitutive equations, which are calculated for each discrete element, assemble to form a system equation to describe the behaviour in the material body as a whole. By applying boundary conditions to the system equation, stress and strain can be calculated for each increment in an incremental manner.

3.3.1 Implicit Finite Element Solution Method

A range of implicit solution procedures are available depending on the analysis type. In the present work which analyses quasi-static structural problems, Abaqus/Standard uses a form of the Newton-Raphson iterative solution procedure which solves the discrete method incrementally from time t to time $t + \Delta t$. To determine a solution, iteration and convergence is required and the state at $t + \Delta t$ is determined based on information at time $t + \Delta t$. The form presented here is in vector matrix notation is the small strain case for simplicity. To solve a quasi-static boundary condition the principle of virtual work is applied as

$$\int_V \delta\boldsymbol{\varepsilon}^T \boldsymbol{\sigma} dV = \int_S \delta\mathbf{u}^T \mathbf{t} dS \tag{3.102}$$

where equilibrium is enforced on the reference volume, V, bound by a surface, S. $\boldsymbol{\sigma}$ is the stress vector, $\mathbf{t}$ is the surface traction vector, $\delta\boldsymbol{\varepsilon}$ is the virtual strain vector and

$\delta\mathbf{u}$ is the virtual displacement vector. The integrals of equation (3.102) are taken over a finite element mesh with individual elements "e" of volume V_e and surface S_e and are evaluated using

$$\delta\boldsymbol{\varepsilon} = \mathbf{B}_e \delta\mathbf{u}_e \tag{3.103}$$

$$\delta\mathbf{u} = \mathbf{N}_e \delta\mathbf{u}_e \tag{3.104}$$

where $\mathbf{N}_e$ is the element shape function matrix and $\mathbf{B}_e$ is the element shape function gradient matrix. The following expression is obtained if equations (3.103) and (3.102) are substituted into equation (3.102)

$$\sum_e \int_{V_e} \delta\mathbf{u}_e^T \mathbf{B}_e^T \boldsymbol{\sigma}(\mathbf{u}_e) dV = \sum_e \int_{S_e} \delta\mathbf{u}_e^T \mathbf{N}_e^T \mathbf{t} dS \tag{3.105}$$

where the summation is over all elements "e" in the finite element mesh. The stress matrix is dependent on the elemental vector of nodal displacements, $\mathbf{u}_e$. Performing the summation, which in effect means assembling elemental quantities into global quantities, and eliminating the arbitrary virtual quantities yields the following global expression

$$\int_V \mathbf{B}^T \boldsymbol{\sigma}(\mathbf{u}) dV = \int_S \mathbf{N}^T \mathbf{t} dS \tag{3.106}$$

where $\mathbf{u}$ is the global nodal displacement vector for the finite element mesh. A set of global equations in $\mathbf{u}$ for the out of balance force, $\mathbf{G}$, can then be assembled and solved as

$$\mathbf{G}(\mathbf{u}) = \int_V \mathbf{B}^T \boldsymbol{\sigma}(\mathbf{u})\, dV - \int_S \mathbf{N}^T \mathbf{t} dS = 0 \tag{3.107}$$

In general for non-linear problems involving non-linear constitutive laws and/or non-linear boundary conditions, equation (3.107) is non-linear, and is usually solved by incremental methods, where loads/displacements are applied in time steps, Δt, up to an ultimate time, t_{final}. Within each increment, the state of the analysis is updated iteratively using the Newton-Raphson method from time t to time $t + \Delta t$ to solve for $\mathbf{u}^{t+\Delta t}$. An estimation of the roots of equation (3.105) is made using the Newton-Raphson formula, such that for the i^{th} iteration

$$\delta\mathbf{u}_{i+1} = \mathbf{u}_{i+1}^{t+\Delta t} - \mathbf{u}_{i}^{t+\Delta t} = -\left(\frac{\partial \mathbf{G}(\mathbf{u}_{i}^{t+\Delta t})}{\partial \mathbf{u}}\right)\mathbf{G}(\mathbf{u}_{i}^{t+\Delta t}) \qquad (3.108)$$

where $\mathbf{u}_{i}^{t+\Delta t}$ is the vector of nodal displacements for the i^{th} iteration at time $t+\Delta t$ and $\mathbf{u}_{i+1}^{t+\Delta t}$ is an improved estimate of the nodal displacements relative to $\mathbf{u}_{i}^{t+\Delta t}$. The partial derivative on the right hand side of the equation is known as the Jacobian matrix of the governing equations and can also be referred to as the global stiffness matrix, $\mathbf{K}_G$. Equation (3.108) is manipulated and inverted to produce a system of linear equations

$$\mathbf{K}_{\mathrm{G}}(\mathbf{u}_{i}^{t+\Delta t})\delta\mathbf{u}_{i+1} = -\mathbf{G}(\mathbf{u}_{i}^{t+\Delta t}) \qquad (3.109)$$

The equation above must be solved, for each iteration, for the change in incremental displacements, $\delta\mathbf{u}_{i+1}$. In order to solve for $\delta\mathbf{u}_{i+1}$ the global stiffness matrix, $\mathbf{K}_{\mathrm{G}}$, must be inverted. Although this is more computationally expensive than the explicit solution method, it ensures accuracy of the solution using a relatively large time increment.

Following iteration i, $\delta\mathbf{u}_{i+1}$ has been determined and a better approximation of the solution has been made, $\mathbf{u}_{i+1}^{t+\Delta t}$, through equation (3.108). This in turn is used as the current approximation to the solution for the subsequent iteration $(i+1)$. The accuracy of the solution is also dictated by the convergence criterion where the updated value for $\mathbf{G}$ must be less than a tolerance value. Complications can arise in an analysis that has a highly non-linear stress-strain response or where there is contact and sliding between two surfaces. In such cases many iterations are usually needed to solve for an increment leading to progressively smaller time steps being used. If large nonlinearities are encountered, convergence may be impossible to achieve in practical terms. In contrast to the implicit method, the explicit method does not involve iteration and hence convergence issues are not an issue.

3.3.2 Explicit Finite Element Solution Method

For the explicit solution method accelerations and velocities at a particular point in time, t, are assumed to be constant and are used to solve for the next point in time, i.e. it solves for $t+\Delta t$ based on information at time t. The central difference integration scheme is used (Abaqus 2011)

$$\mathbf{u}^{i+1} = \mathbf{u}^{i} + \Delta\mathbf{t}^{i+1}\dot{\mathbf{u}}^{i+\frac{1}{2}} \tag{3.110}$$

$$\dot{\mathbf{u}}^{i+\frac{1}{2}} = \dot{\mathbf{u}}^{i-\frac{1}{2}} + \frac{\Delta\mathbf{t}^{i+1} + \Delta\mathbf{t}^{i}}{2}\ddot{\mathbf{u}}^{i} \tag{3.111}$$

where $\mathbf{u}$ is the displacement vector and the superscripts refer to the time increment. In the explicit method iteration is not performed and i refers to the time increment number (unlike the implicit method described previously where i refers to the iteration number within a certain time increment). The accelerations are computed at the start of the increment by

$$\ddot{\mathbf{u}}^{i} = \mathbf{M}^{-1}\left(\mathbf{F}^{i} - \mathbf{I}^{i}\right) \tag{3.112}$$

where $\mathbf{M}$ is the lumped mass matrix

$$\mathbf{M} = \int_{V} \rho\mathbf{N}\, dV \tag{3.113}$$

and $\mathbf{I}^{i}$ is the vector of internal element forces given by

$$\mathbf{I}^{i} = \int_{V} \mathbf{B}^{T}\boldsymbol{\sigma}^{i}\, dV \tag{3.114}$$

and $\mathbf{F}^{i}$ is the vector of externally applied forces

$$\mathbf{F}^{i} = \int_{S} \mathbf{N}^{\mathrm{T}}\,\mathbf{t}^{i} dS + \int_{V} \mathbf{N}^{T}\,\mathbf{P}^{i} dV \tag{3.115}$$

where $\mathbf{P}^{i}$ is the vector of nodal forces and ρ denotes the current material density. All other quantities are defined through equation (3.106). Equation (3.112), rearranged as $\mathbf{M}\ddot{\mathbf{u}} = (\mathbf{F} - \mathbf{I})$, is analogous to the system of linear equations in the implicit method, equation (3.112). Each time increment is computationally efficient to solve as the lumped mass matrix $\mathbf{M}$ is diagonalised and therefore easily inverted, unlike the global stiffness matrix $\mathbf{K}_{\mathrm{G}}$ in the implicit method.

For the explicit method, as the solution progresses through the increments, and as the displacement vector $\mathbf{u}^{i}$ is updated for each increment, it is necessary to calculate the stresses $\boldsymbol{\sigma}^{i}$ to form equation (3.112) which necessitates an accurate stress update algorithm. A stability limit determines the size of the time increment

$$\Delta t \leq \frac{2}{\omega_{max}} \tag{3.116}$$

where ω_{max} is the maximum element eigenvalue. A conservative and practical way of implementing the inequality in the equation above is

$$\Delta t = min\left(\frac{L^e}{c^d}\right) \tag{3.117}$$

where L^e is the characteristic element length and c^d is the dilatational wave speed

$$c^d = \sqrt{\frac{\lambda + 2\mu}{\rho}} \tag{3.118}$$

And λ and μ are the Lamé elastic constants. As shown above, there is a linear relationship between the size of the model and the solution time, as dictated by the characteristic element length L^e and the number of elements in the model. However, in order to obtain an accurate solution, changes in acceleration between subsequent time increments must be small. Using the explicit method, although the incremental solution is easy to obtain, a quasi-static analysis can therefore often take up to 100,000 increments to solve due to an extremely small time increment. To ensure efficiency of the analysis it is important to ensure the element size is as regular as possible so that a single element doesn't reduce the time increment for the whole model. Due to the large runtime it is often impractical to run quasi-static analysis using its true time scale. A number of methods can be used to artificially reduce the run time of the simulation including speeding up the applied deformation or loading rate and scaling the material density in the model. When performing a quasi-static simulation, in order to prevent unrealistic dynamic results it is important that the internal forces do not affect the mechanical response. It is recommended that the ratio of kinetic energy to total internal strain energy in the model is less than 5% in order to ensure dynamic effects are negligible in quasi-static analysis (Choi et al. 2002; Chung et al. 1998).

3.4 Computational Details of Model Construction

3.4.1 Continuum and Microstructural Based Computational Models

In the present work the whole bone geometry for the continuum finite element models are based on 1 mm sliced computed tomography (CT) scans of the synthetic tibiae (Chapters 4 and 7). The microstructural based finite models in Chapter 6 use

geometry based on micro-computed tomography (μCT) scans with a resolution of 72μm resolution (μCT 40, Scanco Medical AG, Basserdorf, Switzerland). The μCT technique enables a three dimensional visualisation and characterisation of the trabecular bone microarchitecture. In the present work the continuum and microstructural based finite element models are generated using the 3D reconstruction software Simpleware (Simpleware LTD., Exeter, UK) and Mimics/3Matic (Materialise, Leuven, Belgium) (Figure 3-13). In the 3D reconstruction software an appropriate threshold value is selected to create distinct masks of the cortical and trabecular bone. Morphological filters and paint algorithms are applied to these masks to refine the data. In order to reduce computational power and reduce the simulation run time, the CT data may be down-sampled (increase the pixel spacing) to reduce the number of elements created.

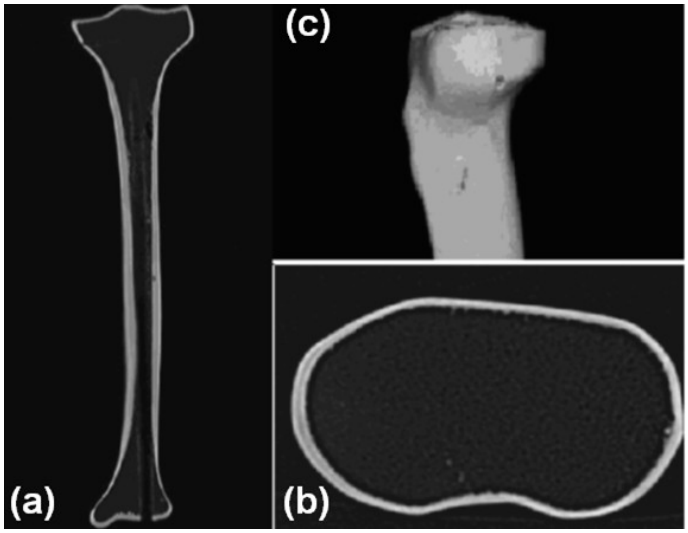

Figure 3-13 (a,b) 2D computed tomography (CT) images of a synthetic sawbone tibia. (c) The CT images are used to generate 3D finite element models.

3.4.2 Loading Configurations

In the present study the following loading configurations were considered: uniaxial compression; confined compression; hydrostatic compression. The boundary conditions for the loading configurations considered in the present work for cubic specimens of natural and synthetic trabecular bone are described in this section using a hexahedral representative volume element (RVE) (Figure 3-14). Symmetric boundary conditions were implemented for the μCT based models in Chapter 6 and for the continuum models in Chapters 5-7. For symmetry boundary conditions the

sides of the RVE must remain planar (orthogonal) during loading and also must observe mirror symmetry. To achieve this, the nodal displacements on a given face of the finite element mesh are coupled to a master node in the direction normal to that face (Mullins et al. 2007). In a given direction of the RVE, the average stress, **σ**, is calculated as the reaction force of the master node (node 7 in Figure 3-15) divided by the cross sectional area of the RVE ($A = lxl = l^2$). The apparent Young's modulus, E, is the average stress divided by the applied strain.

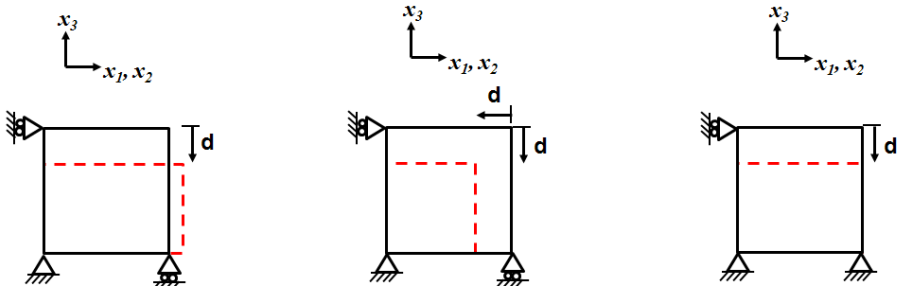

Figure 3-14 Loading and boundary conditions for compression testing: (a) uniaxial compression; (b) hydrostatic compression; (c) confined compression.

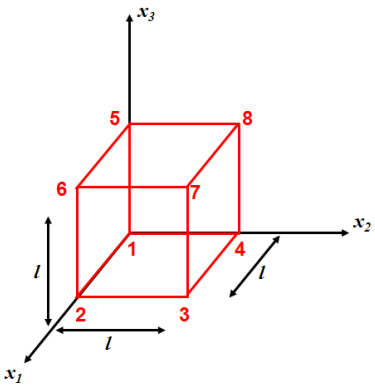

Figure 3-15 Schematic for implementation of boundary conditions for the finite element models.

3.5 References

Abaqus (2008) Analysis user's manual.

Abaqus (2011) Analysis theory manual.

Abrate, S. (2008) Criteria for yielding or failure of cellular materials. J Sandw Struct Mater 10 (1):5-51.

Chen, W. F., Han, D. J. (2008) Plasticity for structural engineers. Springer Verlag, New York.

Choi, H. H., Hwang, S. M., Kang, Y. H., Kim, J., Kang, B. S. (2002) Comparison of implicit and explicit finite-element methods for the hydroforming process of an automobile lower arm. Int J Adv Manuf Tech 20 (6):407-413.

Chung, W. J., Cho, J. W., Belytschko, T. (1998) On the dynamic effects of explicit fem in sheet metal forming analysis. 15 (6):750-776.

Cvitanic, V., Vlak, F., Lozina, Z. (2008) A finite element formulation based on non-associated plasticity for sheet metal forming. Int J Plasticity 24 (4):646-687.

Deshpande, V. S., Fleck, N. A. (2000) Isotropic constitutive models for metallic foams. J Mech Phys Solids 48 (6-7):1253-1283.

Drucker, D. C., Prager, W. (1951) Soil mechanics and plastic analysis or limit design. Division of Applied Mathematics, Brown University, Brown University. Division of Applied, Mathematics United States. Office of Naval, Research.

Fagan, M. J. (1992) Finite element analysis: Theory and practice. Longman Scientific & Technical.

Gibson, L. J. (1985) The mechanical behaviour of cancellous bone. J Biomech 18 (5):317-328.

Gibson, L. J. (2005) Biomechanics of cellular solids. J Biomech 38 (3):377-399.

Gibson, L. J., Ashby, M. F. (1982) The mechanics of three-dimensional cellular materials. 382 (1782):43-59.

Gibson, L. J., Ashby, M. F. (1999) Cellular solids: Structure and properties. Cambridge Univ Pr.

Hill, R. (1948) A theory of the yielding and plastic flow of anisotropic metals. Proc Roy Soc London 193 (1033):281-297.

Khan, A. S., Huang, S. (1995) Continuum theory of plasticity. John Wiley, New York.

McGarry, J. P., O'Donnell, B. P., McHugh, P. E., McGarry, J. G. (2004) Analysis of the mechanical performance of a cardiovascular stent design based on micromechanical modelling. Comp Mater Sci 31 (3-4):421-438.

Menétrey, P., Willam, K. J. (1995) Triaxial failure criterion for concrete and its generalization. ACI Struct J 92 (3).

Mullins, L. P., McGarry, J. P., Bruzzi, M. S., McHugh, P. E. (2007) Micromechanical modelling of cortical bone. Comput Method Biomec 10 (3):159-169.

Öchsner, A., Hosseini, S. M. H. (2010) Constitutive modeling of the mechanical behavior of trabecular bone-continuum mechanical approaches. In: Öchsner, A., Ahmed, W. (eds) Biomechanics of hard tissues. Wiley, Weinheim, pp 159-191.

Rice, J. R. (ed) (1975) Continuum mechanics and thermodynamics of plasticity in relation to microscale deformation mechanisms. Constitutive equations in plasticity. MIT Press, Cambridge, Massachusetts, USA.

Tita, V. (2012) Numerical simulation of anisotropic polymeric foams. Lat Am J Solids Stru 9 (2):259.

von Mises, R. (1913) Mechanik der festen körper im plastisch deformablen zustand. Göttin Nachr Math Phys 1:582-592.

Chapter 4

Full and Surface Tibial Cementation in Total Knee Arthroplasty: A Biomechanical Investigation of Stress Distribution and Remodelling in the Tibia

Abstract

Aseptic tibial component loosening remains a major cause of total knee arthroplasty failure. The cementation technique used to achieve fixation may play a major role in loosening. Despite this, the optimum technique remains unanswered. This study aims to investigate stress and strain distributions in the proximal tibia for full cementation and surface cementation of the Genesis II tibial component. Principal cortical bone strains were measured experimentally in intact, surface cemented and fully cemented synthetic tibiae using strain gauges. Both axial and 15° flexion loading were considered. Finite element models were used to assess both cortical and trabecular bone stresses and strains. Using a bone remodelling algorithm potential sites of bone formation and resorption were identified post-implantation. Principal cortical bone strain results demonstrate strong correlations between the experimental and finite element analyses ($R^2 \geq 0.81$, $RMSE(\%) \leq 17.5\%$). Higher cortical strains are measured for surface cementation, as full cementation creates a stiffer proximal tibial structure. Simulations reveal that both cementation techniques result in lower trabecular stresses under the baseplate compared to the intact tibia, with greater reductions being computed for full cementation. The surface cementation model displays the closest trabecular stress distribution to the intact model. In addition, bone remodelling simulations predict more extensive bone resorption under the baseplate for full cementation (43%) than for surface cementation (29%). Full cementation results in greater stress reduction under the tibial baseplate than surface cementation, suggesting that surface cementation will result in less proximal bone resorption, thus reducing the possibility of aseptic loosening.

4.1 Introduction

Total knee arthroplasty (TKA) is an established treatment option for end-stage degenerative knee joint disease. With revision or loosening as the endpoint, survivorship of greater than 93.7% at 15 years has been reported for cemented implants (Ito et al. 2003; Keating et al. 2002). Successive arthroplasty registers have noted aseptic loosening as the most common cause of failure (38%-44%) (Graves et al. 2004; Registry 2003; Robertsson et al. 2001). Demand in the US for TKA revision surgery is set to increase by 601% between 2005 and 2030 (Kurtz et al. 2007). Cementless implants have not demonstrated superior survivorship to cemented TKA (Baker et al. 2007; Gandhi et al. 2009). The underlying mechanisms of aseptic loosening are not known and are considered to have a multi-factorial aetiology. Due to component implantation, tibial load transfer is altered and may result in peri-prosthetic bone remodelling and subsequent stress shielding. Aseptic tibial component loosening may be attributed to such changes in bone morphology post-implantation.

Implant fixation is paramount in achieving long-term stability and is still a major issue concerning primary TKA. Tibial cementation techniques include full cementation (FC) and surface cementation (SC). FC involves cementing the tibial cut surface and stem. SC implies the application of cement across the tibial cut surface leaving the stem uncemented. FC and SC tibial component cementation techniques in primary TKA have widely been debated however no optimum technique has been determined. Advocates of SC claim sufficient component stability and maintenance of the underlying BMD thus leaving the bone less vulnerable to stress shielding (Hofmann et al. 2006; Kolisek et al. 2009; Seki et al. 1997; Skwara et al. 2009). Advocates of FC claim better fixation as well as a lower potential for early micromotion thus creating a stronger construct for long-term stability (Bert and McShane 1998; Luring et al. 2006).

Micromotion, assessed clinically through roentgen stereophotogrammetric analysis (RSA), has not shown significant differences between the two techniques (Saari et al. 2008). Experimentally, only micromotion has been evaluated via cyclic point loading as an end-point for comparing SC and FC and has shown conflicting results between the two techniques (Bert and McShane 1998; Luring et al. 2006; Peters et al. 2003; Seki et al. 1997; Skwara et al. 2009). Cement penetration has been highlighted as

playing a key role in implant stability between the two techniques (Bert and McShane 1998; Hofmann et al. 2006; Peters et al. 2003). The extent to which the tibial cut surface is cemented is dependent on the operator, bone and implant. Cortical bone strains have also been used to assess cementation technique in primary (Seki et al. 1997) and revision TKA (Completo et al. 2007a; Completo et al. 2008; Seki et al. 1997). However the role of the stem in revision TKA is different to primary TKA. Revision TKA is frequently complicated by poor quality proximal tibial bone, requiring diaphyseal stem fixation, in which the stem used to stabilise the tibial component is considerably longer than that used in primary TKA implants. Regardless of cementation technique the revision stem engages the cortices of the more distal tibial diaphysis. Therefore due to the key differences in bone quality, stem length, cortical contact and load transfer, investigation of primary and revision TKA cementation techniques must be considered separately. Clinical cohorts have not provided conclusive direction on the optimal cementation method (Hofmann et al. 2006; Ito et al. 2003; Kolisek et al. 2009; Schai et al. 1998; Sharkey et al. 2002). Only Schai et al. (1998) compared clinical survivorship for FC and SC in primary TKA, with a survival rate of 90% at 10 years from a series of 235 patients of which 226 were cemented (144 FC, 82 SC).

To date no biomechanical study has considered the trabecular bone stresses/strains or bone remodelling due to FC or SC of primary TKA, despite the clinical evidence of stress shielding in the proximal trabecular bone (Lonner et al. 2001). The aim of this study is to experimentally and computationally investigate primary tibial component TKA cementation techniques; FC and SC. This study hypothesises that SC of the tibial component in primary TKA results in less stress shielding directly under the baseplate than FC. To test this hypothesis cortical bone strains are experimentally measured in intact, FC and SC tibiae at axial and 15º flexion loading. Experimental results are then used to validate finite element (FE) simulations, which offer an insight into the trabecular stress and strain distributions for FC and SC. Using an established bone remodelling algorithm (Huiskes et al. 1992; Ong et al. 2009) regions of bone resorption and formation are computed for both FC and SC.

4.2 Methods

4.2.1 Experimental Testing

Six pairs of 4th generation synthetic composite tibiae (#3402, 10 pcf cellular rigid, Sawbones, Malmö, Sweden) were implanted with the Genesis II Total Knee System (Smith & Nephew, Memphis, TN, USA). Six models per group each tested 4 times provided statistical significance. All stages of tibial preparation were performed by an orthopaedic resident (DTC) under the supervision of a consultant orthopaedic surgeon (FJS). Cutting, drilling and punching were standardised to ensure identical preparation was achieved with all tibiae. The tibiae were cemented at room temperature with PMMA bone cement (Simplex P, Stryker-Howmedica, NJ, USA), 6 FC and 6 SC. The polyethylene insert and femoral component were used to load the tibiae. Eight stacked triaxial (45°) strain gauge rosettes (KFG-3-120-D17-11L3M2S, Kyowa Electronic Instruments, Tokyo, Japan) were applied to each tibia at the antero-medial (AM), lateral (L) and posterior (P) aspects at 5 mm, 30 mm and 50 mm below the proximal tibial cut surface Figure 4-1. Gauge positions are referred to as AM5 (antero-medial gauge at 5 mm), L5, P50 etc.. P5 gauges were not considered due to cement overspill at this location during implantation. In order to obtain consistent strain gauge placement a vernier height gauge (Mitutoyo Corporation, Tokyo, Japan) was used. A reference axis was marked on the cortex and each gauge was aligned and positioned accordingly. The middle strain gauge was aligned with the vertical axis of the tibia.

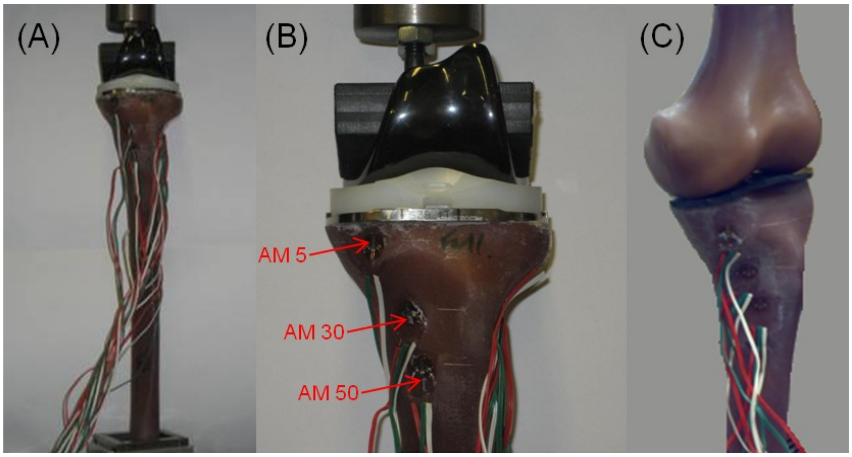

Figure 4-1 Experimental loading set-up. (A) Implanted tibia with femoral component articulation proximally and rigid constraint distally. (B) Proximal implanted tibia with strain gauges placed at 3 levels (5 mm, 30 mm and 50 mm) from the tibial cut surface. (C) Intact loading configuration.

The tibia was rigidly fixed at the distal end and placed in a universal testing machine (Model 4467, Instron, MA, USA). The femoral component was constrained so that a 60:40 medial:lateral (Completo et al. 2007a; Halloran et al. 2005) load distribution was implemented. A load of 2060 N (3x70 kg BW) was applied. Both axial and 15° flexion loading of the tibia were implemented. An intact tibia was also tested to 2060 N for comparison with the implanted tibiae (Figure 4-1(C)). A pressure pad was used at the joint line to monitor contact stresses so that native joint loading contact conditions could be replicated. Maximum principal (ε_{max}) and minimum principal (ε_{min}) cortical strains were calculated based on three strains measured with tri-axial rosettes using a data acquisition system (National Instruments, TX, USA) at the eight gauge locations, with four test replicates. Null calibration was performed at the outset, and shunt calibration was performed with each adjustment of position (standard of error <0.2%). One-way analysis of variance (ANOVA) was applied to test for the effect of cement on the measured variable strain using statistical software (v.15, Minitab Inc., State College, PA, USA). Pairwise post-hoc analyses were performed using the General Linear Model with a Tukey significant difference test. Significance was determined at $\alpha<0.05$.

4.2.2 Finite Element Modelling

One millimetre slice CT images of a sawbone tibia (#3402, 10 pcf) were utilised to create solid computational models of intact and implanted tibiae. Virtual surgery was performed on the tibia to align and implant replica models of the Genesis II and bone cement (v3.2 Simpleware LTD, Exeter, UK). FE software (Abaqus, v6.8-1 Dassault Systemes, RI, USA) was utilised to create 3D multi-component computational models (~1×10^6 mixed four noded tetrahedral and eight noded hexahedral elements). The components were modelled as homogenous, linear elastic and isotropic. Material properties (Table 4-1), boundary conditions, loading and positional parameters were applied in order to replicate the experimental set-up. At both loading positions a 2060 N load (60:40 medial:lateral) was delivered through implant articulation.

Table 4-1 Material properties of the computational models.

Part	Young's Modulus E (MPa)	Poisson's Ratio ν_e
Cortical Bone	16,700	0.26
Trabecular Bone	23	0.3
Tibial Component	112,000	0.3
Polyethylene Insert	500	0.3
Cement	2,280	0.3
Trabecular Bone-Cement Composite	2,050	0.3

A cement penetration depth of ~2 mm in the closed cell foam was observed in preliminary experimental tests and upon excision of the implants. Similar penetration depths have also been observed clinically (Hofmann et al. 2006; Kolisek et al. 2009). The FC and SC models contained a trabecular bone-cement composite layer of ~2 mm (Figure 4-2(A)). This interdigitated layer was assigned a Young's modulus of 2050 MPa based on a specified 10% trabecular bone volume ratio (Sawbones, personal communication). The FC model contained a 2 mm interdigitated trabecular bone-cement composite layer below the baseplate and surrounding the stem and fins. This layer was rigidly bonded to the implant and peri-prosthetic bone. The reduced diameter of the distal stem (30-50 mm) resulted in a space between this layer and the stem created by drilling and punching. This space was filled with cement, which was rigidly bonded to the stem and interdigitated layer. The SC model also had a 2 mm rigidly bonded interdigitated composite layer below the baseplate. Frictionless contact was defined between the stem and surrounding bone. The distal SC stem did not contact the surrounding bone due to its reduced diameter. ε_{max} and ε_{min} were determined at locations on the tibiae corresponding to the experimental locations.

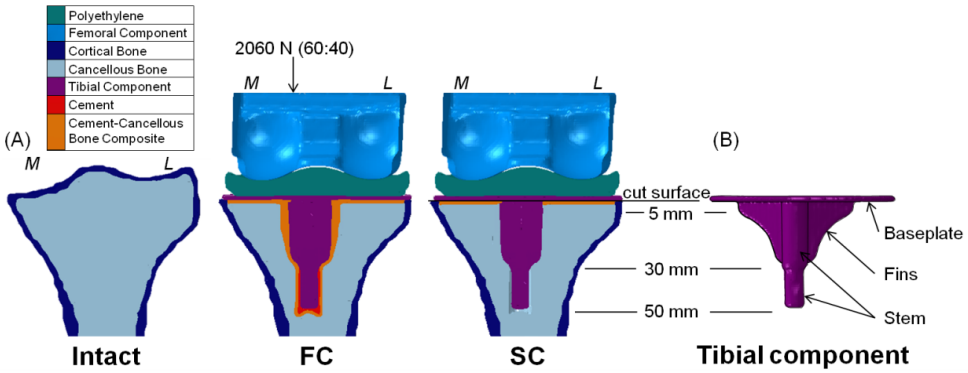

Figure 4-2 (A) Proximal tibial coronal section views of the computational models: intact model, FC model, SC model (*M* = medial, *L* = lateral). (B) Computational tibial component.

FE results were input into a well established bone remodelling algorithm in order to predict regions of bone resorption and formation following implantation (Huiskes et al. 1992; Ong et al. 2009). Relative changes in strain energy density (SED) from the intact distribution were computed for both FC and SC. The mechanical stimulus, s, is related to the resultant remodelling through the equations

$$(1-s)S_{ref} <= S_{post} <= (1+s)S_{ref}$$

where $s = 0.75$, S_{ref} is the SED for the intact bone and S_{post} is the SED for the bone post-arthroplasty. A lazy zone, where no remodelling occurs, is the region between $(1-s)S_{ref}$ and $(1+s)S_{ref}$. An increase in SED≥75% at any point in the tibia resulted in bone formation whereas a decrease in SED≤75% resulted in bone resorption. The rate of change of density is linearly related to the SED stimulus and the Young's modulus is related to the remodelled bone density using the relationship $E = c\rho^3$ where $c = 3790\ MPa/(g/cm^3)^3$ (Huiskes et al. 1992). Remodelling is considered over a period of 24 months based on the observations of (Weinans et al. 1993).

Experimental and computational cortical strain correlation was established by performing regression analysis with good agreement indicated by a correlation coefficient (R^2) approaching 1. Additionally the root-mean-square-error (*RMSE* (%)) was calculated and expressed as a percentage of the measured peak strains. A mesh sensitivity study revealed that a ~33% increase in the number of elements (from ~1×10^6 to ~1.5×10^6) resulted in changes in computed stress of less than 1.5%.

4.3 Results

4.3.1 Cortical Strain: Experimental Testing and Computational Prediction

Experimentally, both axial (Figure 4-3) and 15° flexion loading result in statistically significant differences ($P < 0.05$) between FC and SC for 8 out of 16 measurements. Statistically significant results ($P < 0.05$) display higher strain magnitudes for SC than FC, except for AM50 ε_{max}. Principal strain trends computed by our FE models for FC and SC are similar to those observed experimentally (Figure 4-3). Higher strain magnitudes are computed for SC than for FC at all locations at which statistically higher SC strain magnitudes are observed experimentally ($P < 0.05$). While computed differences between FC and SC strain magnitudes are less pronounced than experimentally observed differences, it should be noted that good experimental and computational correlation is observed (axial $R^2 \geq 0.85$, $P < 0.05$; flexion $R^2 \geq 0.81$, $P < 0.05$). An acceptable RMSE of 15.6-17.5% is also observed that is in a similar range to that reported in previous studies (Completo et al. 2007b). Full details are presented in Table 4-2. Computational models without an interdigitated layer resulted in a decrease in experimental-computational correlation (R^2) by up to 5%. Statistically significant differences are obtained between the axial FC and intact strains for 9 of 16 measurements, compared to only 5 of 16 for SC ($P < 0.05$). Again an excellent correlation is obtained for the intact model ($R^2 = 0.89$, $P < 0.05$).

Table 4-2 Experimental and computational cortical bone strain linear regression correlation results for axial and 15° flexion loading of the intact, full cementation (FC) and surface cementation (SC) models.

Model	Loading	R^2	Slope	*RMSE* (%)
Intact	Axial	0.89	0.83	17.5
FC	Axial	0.85	1.08	16.1
SC	Axial	0.89	1.17	16.1
FC	15° flexion	0.81	1.03	16.8
SC	15° flexion	0.87	1.11	15.6

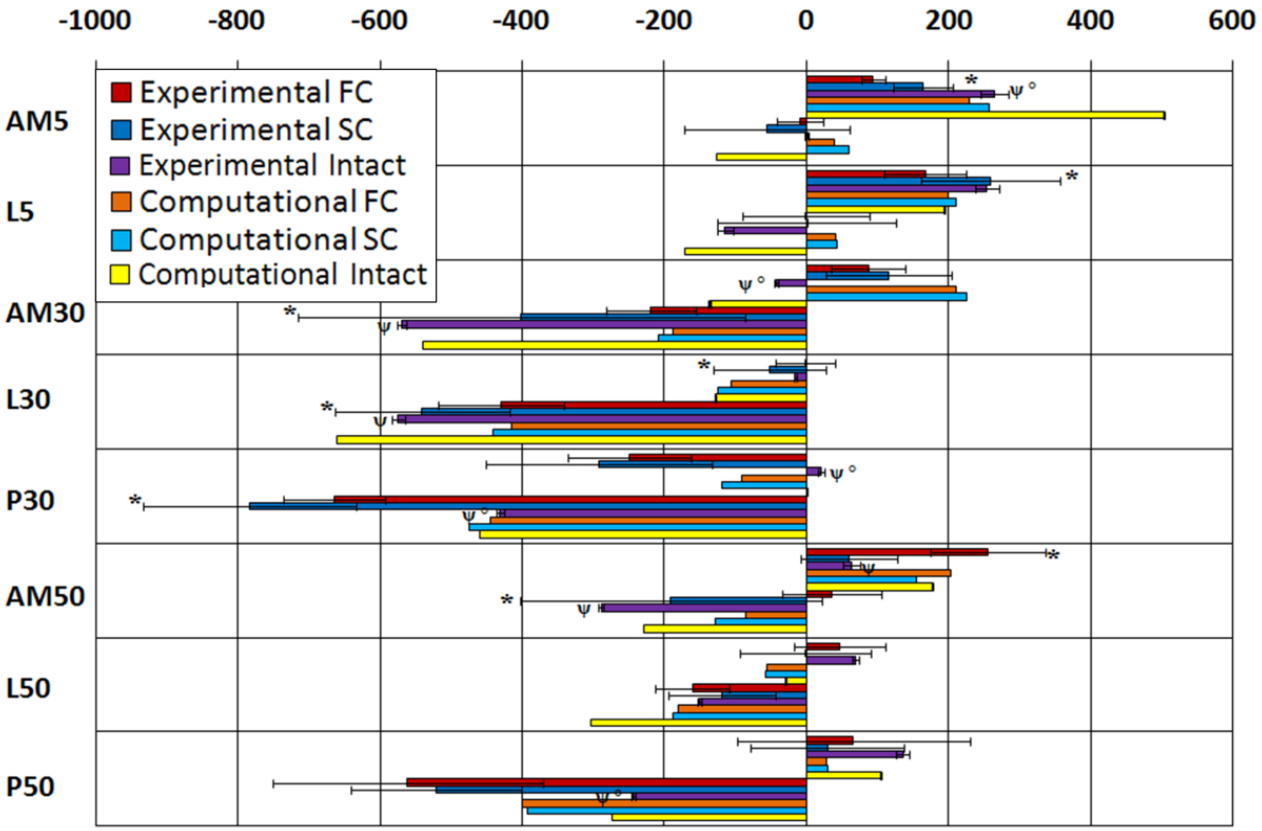

Figure 4-3 Experimental and computational maximum (ε_{max}) and minimum (ε_{min}) principal cortical bone strain ($\mu\varepsilon$) results for the intact model, FC model and SC model under axial loading. The mean (SD) of the results are displayed for each strain gauge, where AM5 refers to the antero-medial strain gauge at 5 mm from the proximal tibial cut surface etc. Statistical differences of P <0.05 are denoted by: * between the FC and SC experimental models; ψ between the intact and FC experimental models; ° between the intact and SC experimental models.

4.3.2 Computationally Simulated Strain and Stress in the Trabecular Bone

Having established a strong correlation between experimental and FE results for cortical strain, we now consider FE predictions of trabecular stress and strain distributions for intact, FC and SC. Principal strains in the peri-prosthetic trabecular bone (3 mm from the tibial stem on the anterior and posterior aspects) are presented in Figure 4-4. At 50 mm higher strain magnitudes are computed for FC, with values being up to 16 times greater than the SC and intact results. At 5 mm both implanted models predict lower strain magnitudes than the intact model. In general, differences between computed FC and SC trabecular strains (Figure 4-4) are more pronounced than computed differences between FC and SC cortical strains (Figure 4-3).

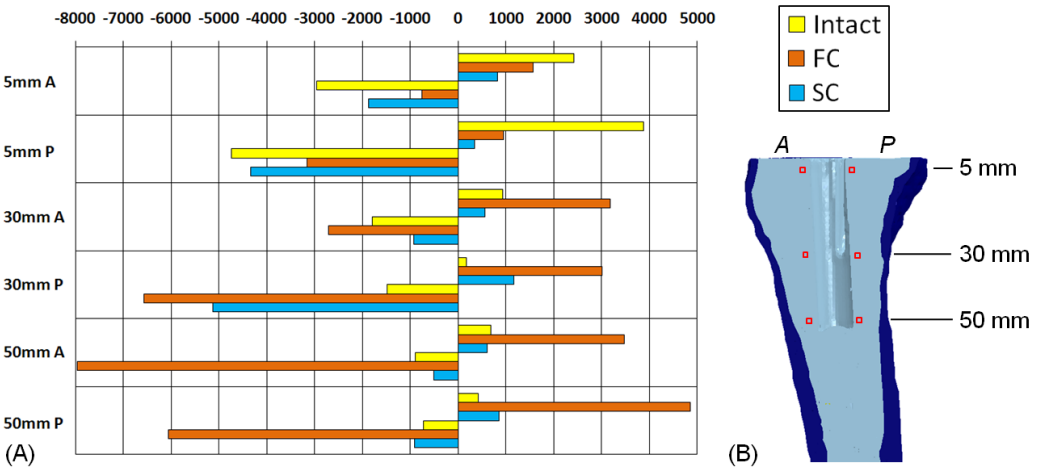

Figure 4-4 (A) Computational results showing the maximum and minimum principal axial peri-prosthetic trabecular bone strains ($\mu\varepsilon$) taken at 5 mm, 30 mm and 50 mm from the tibial cut surface at 3 mm from the tibial component stem on the anterior and posterior aspects for the intact, FC and SC models. (B) Schematic of trabecular bone strain measurement locations. (*A* = anterior, *P* = posterior).

Trabecular von Mises stress distributions are shown in Figure 4-5 for axial loading. In the FC (Figure 4-5 (B, E)), significant stresses are transferred to the trabecular bone from the proximal implant stem and fins to the distal stem tip area, where maximum stresses are computed. This is in sharp contrast to the intact where the highest trabecular stresses are computed beneath the tibial plateau (Figure 4-5(A)). For the SC (Figure 4-5(C, F)), localised stress concentrations surround the fins, where normal contact tractions lead to load transfer. Low trabecular stresses are computed around the SC stem as implant-trabecular load transfer via shear tractions

is dramatically reduced by the absence of cement. Importantly, very low stresses are computed in proximal trabecular bone below the cut surface for both FC and SC. FC stresses are distinctly lower than SC stresses in this region, with the latter providing a better approximation of the intact stress distribution. Very similar trends are computed for 15° flexion loading. In addition to von Mises stress distributions, pressure distributions results are shown in Figure 4-7 (Appendix B) in order to provide a complete characterisation of the trabecular stress state.

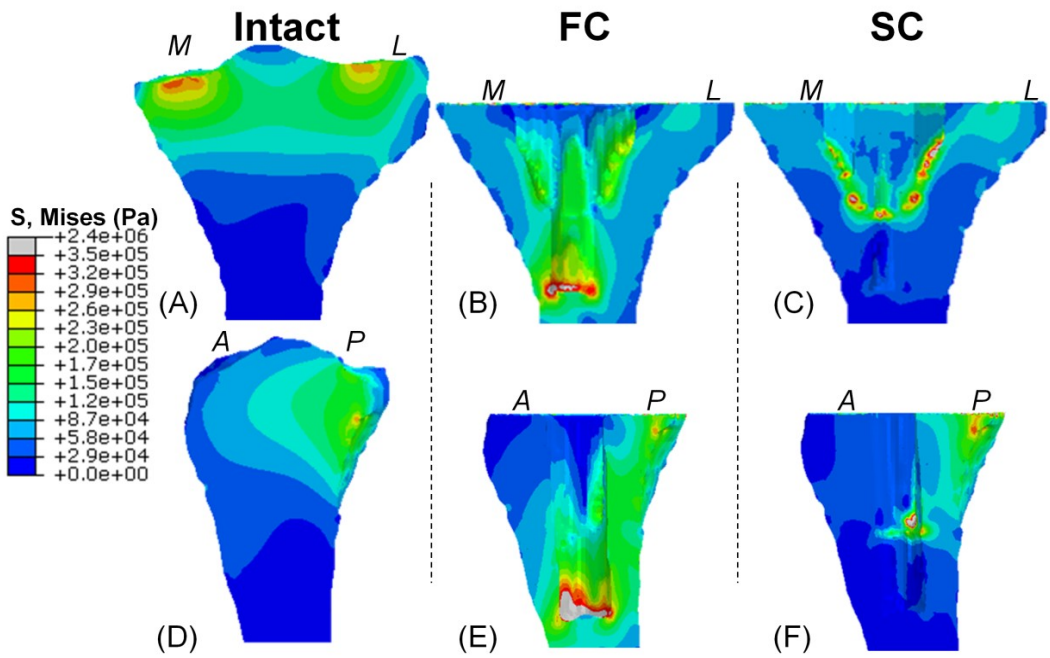

Figure 4-5 Contour plots showing coronal (A-C) and sagittal (D-F) section views of von Mises trabecular bone stress results in Pa for the axial models. The cortical bone, implant components, interdigitated layer and cement volume are removed for clarity leaving only the trabecular bone. (*M* = medial, *L* = lateral, *A* = anterior, *P* = posterior).

4.3.3 Prediction of Bone Remodelling Following FC and SC

Contour plots of bone remodelling predictions for the axial model (Figure 4-6) demonstrate potential bone remodelling throughout the cortical and trabecular bone, with a trend of bone resorption proximally and formation distally. At 2 mm (just below the interdigitated composite layer) bone resorption is predicted antero-medially in both FC (43% of section area) and SC (29% of section area). A similar trend is evident at 5 mm. At 30 mm and 50 mm bone formation is envisaged posteriorly and around the stem in both models, which is more pronounced in the

FC. The implementation of long term bone remodelling incorporates an inhomogeneous bone distribution for both cementation techniques due to the reduction in density and therefore a subsequent reduction in modulus for the cortical and trabecular bone. Very similar trends are observed for a homogeneous and inhomogeneous distribution and these trends do not alter the trends reported in Figure 4-5 where higher stresses are computed at the distal stem for FC in addition to greater stress reductions directly under the baseplate in comparison to SC.

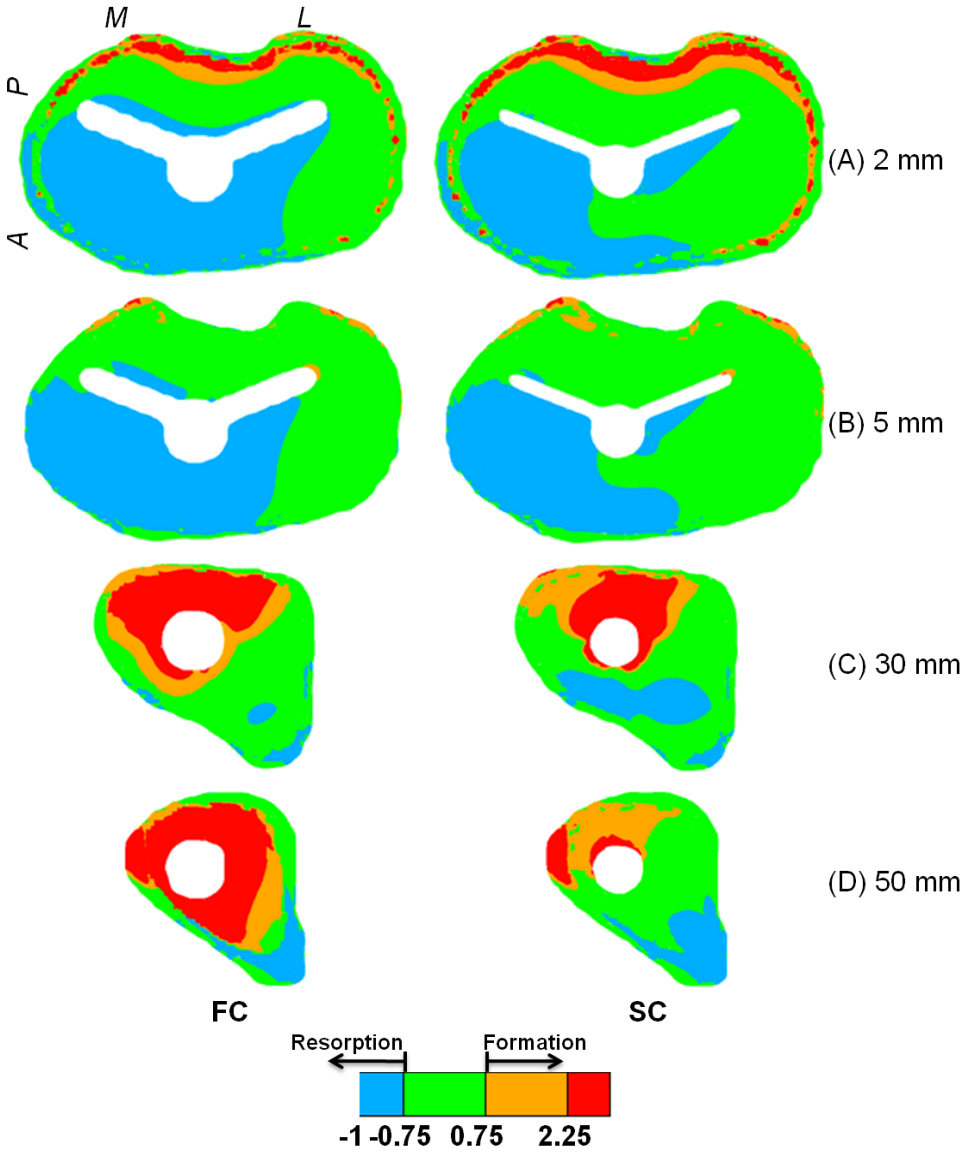

Figure 4-6 Axial section views of the proximal tibial cortical and trabecular bone showing the bone remodelling predictions using adaptive bone remodelling theory in the FC and SC computational models under axial loading at: (A) The interdigitated bone-cement interface at 2 mm from the cut surface, (B) 5 mm level, (C) 30 mm level, (D) 50 mm level. The interdigitated trabecular bone-cement layer is removed and therefore a larger void is seen in the FC model sections. (*M* = medial, *L* = lateral, *A* = anterior, *P* = posterior).

4.4 Discussion

The present study examined proximal tibial bone stresses and strains for the intact and implanted tibia to investigate tibial component cementation techniques (FC and SC) used in primary TKA. Due to clinical evidence of stress shielding (Lonner et al. 2001) and aseptic tibial loosening (Sharkey et al. 2002), stresses and strains were measured both experimentally and computationally in the intact and implanted models to gain insight into the potential for remodelling and risk of implant failure.

Assessment of experimental composite tibiae, implanted with the Genesis II implant, measure statistically different ($P < 0.05$) cortical strains for FC and SC at half of the gauge locations for axial and 15° flexion loading. Higher strains are measured for SC than FC at 5 mm for both loading positions. These differences can be attributed to the fact that FC creates a stiffer structure than SC as a result of: (a) bonding of the stem and fins to the surrounding trabecular bone; and (b) cement interdigitation into the bone surrounding the stem and fins, creating a stiffer composite material. At 50 mm statistically significant differences in cortical strain for FC and SC are only measured antero-medially for both positions ($P < 0.05$). This can be attributed to load transfer at this location from the distal stem to the cortex via surrounding interdigitated cement. While both cementation techniques yield principal strains that differ from that of an intact tibia at several locations, fewer statistically significant differences from the intact case are determined for SC ($P < 0.05$).

Our computational models predict a similar pattern of cortical strains to those measured experimentally, with a reasonably strong correlation being demonstrated. Following this validation of our FE simulations, stress and strain distributions in the trabecular bone were then analysed. Firstly, it reveals that differences in FC and SC trabecular strains are far more pronounced than for cortical strains. This is particularly evident at 50 mm where FC trabecular strains are up to 16 times higher than SC and intact strains. This suggests that experimental measurement of cortical strains for assessment of device performance offers limited insight into the stress/strain state in the underlying peri-prosthetic trabecular bone unless it is performed in parallel with FE simulation. Experimental proximal tibial cortical strains have been measured solely at 1 mm below the baseplate for primary FC and SC (Seki et al. 1997). Greater reductions in principal strain were noted for FC than SC, which is in agreement with our results at 5 mm.

Examination of trabecular stress distributions show similarities between the intact and SC models in the stem tip region where low stresses are computed. In contrast, high stresses are computed for FC in this region due to the bonding of the stem tip to the surrounding interdigitated cement and cement penetration into the bone and consequent creation of a stiff composite material. For the Genesis II tibial component, the hole drilled and punched to accommodate the stem is 11 mm in diameter, hence the proximal 30 mm of the stem is press-fit and the distal 20 mm of the stem does not contact the bone directly. Consequently there is no stress transfer to this region of trabecular bone for SC. An equivalent SC stress distribution could be achieved by shortening the stem length, which would also facilitate a reduction of the volume of trabecular bone removed during TKA due to a reduction in the depth of the drilled and punched hole. Overall the SC model displays the closest trabecular stress distribution to the intact model.

While both FC and SC result in reduced stresses under the baseplate when compared to the intact case, the greatest stress reductions are predicted for FC due to shear stress transfer from the proximal trabecular bone to the bone surrounding the distal stem. Such shear transfer does not occur for SC due to the non-contacting stem tip that results in less significant reductions in stress under the baseplate, similar to the intact case. This would suggest that more extensive bone resorption will occur beneath the tibial baseplate for FC than SC.

To support our suggestion that greater stress reduction under the baseplate in FC could lead to aseptic loosening we implemented a bone remodelling algorithm. Results suggest that resorption will occur more extensively for FC than for SC in the bone immediately below the interdigitated bone-cement interface, with 43% and 29% resorption occurring respectively. Our predictions are supported by a clinical study where BMD was observed 7 years post-arthroplasty under the tibial plateau for a pegged stemless implant and a FC stemmed implant (Lonner et al. 2001). Significant loss of BMD was observed proximally for the FC stemmed implant compared to the non-operated contralateral knee. Significant bone loss was not observed for the unstemmed implant. It can be concluded that, similar to our predictions, load transfer to the bone surrounding the distal cemented stem results in the reduced proximal BMD in the study of Lonner et al. (2001). Regnér et al. (1999) demonstrated that a hydroxyapatite coated stem resulted in a 36% decrease in BMD

under the medial plateau compared to 15% for a smooth uncoated stem. The authors hypothesised that the hydroxyapatite coating resulted in bony apposition around the stem, thus leading to a transfer of stress to the distal trabecular bone and consequent resorption of proximal trabecular bone. Our computed stress distributions suggest that this is indeed the case. A study by Felix et al. (1997) revealed that peri-prosthetic fractures following TKA are most likely to occur at the tibial plateau, and not more distally along the stem. Again, our predictions suggest that this phenomenon can be explained by reduced stress in this region and consequent bone resorption. Our prediction that greater bone resorption occurs under the medial plateau is supported by the clinical study of Hernandez-Vaquero et al. (2008). The finding by Munro et al. (2010) that BMD reduction is more pronounced in trabecular than in cortical bone following TKA is also consistent with our computations.

SC displays less bone formation and greater bone resorption than the FC at 30 mm and 50 mm below the cut surface. However, these regions of resorption do not extend to the bone-implant interface, suggesting that distal remodelling is not expected to have a negative effect on implant stability. As discussed above, the implant considered in our study does not contact the trabecular bone along the distal stem for the SC case. It is therefore reasonable to expect that proximal remodelling should be the primary determinant of aseptic loosening for SC.

The argument that FC provides a more stable construct than SC has been examined in several biomechanical studies whereby micromotion between the baseplate and cut surface has been recorded during cyclic point loading (Bert and McShane 1998; Luring et al. 2006; Peters et al. 2003; Seki et al. 1997; Skwara et al. 2009). Micromotion has also been assessed clinically through RSA, and has not shown significant differences between FC and SC (Saari et al. 2008). Also using RSA Ryd et al. (1999) found no mechanical loosening for SC and indicated that the SC stem may not promote bone ingrowth. However FC was not investigated. Using the same implant as the present study Efe et al. (2011) found greater failure in cementless (8/10 cases) than SC (2/10 cases) using RSA after 10000 cycles. In comparison to a penetration of 1 mm, Bert and McShane (1998) demonstrated no difference in lift-off with penetration greater than 3 mm using synthetic tibiae. Using sawbones Luring et al. (2006) demonstrated a significantly higher lift-off rate with SC. Using cadaveric tibiae Peters et al., (2003) reported no difference in lift-off between FC and SC after

6000 cycles with a cement penetration of 3.6 mm. Seki et al. (1997) found no significant differences in micromotion between FC and SC. Using the Genesis II implant considered in the present study, Skwara et al. (2009) found no significant difference in micromotion, with more migration being observed for FC. This clearly demonstrates that the non-contacting region of the distal stem in SC does not compromise the initial stability of the implant. Our finding that SC reduces stress shielding and bone resorption in the proximal peri-prosthetic bone, along with the finding of Skwara et al. (2009) that SC does not compromise initial implant stability, provides a very strong case for SC over FC. Additionally the finding of Skwara et al. (2009) further reinforces our suggestion that the Genesis II would be equally effective under SC if the non-contacting distal stem was removed.

To our knowledge, our study is the first experimental-FE investigation of alterations in tibial stress and strain for primary FC and SC TKA. While our results provide insight into the stress alterations in the proximal tibia for both cementation techniques, a further validation of our experimental results using cadaveric specimens would be desirable. The synthetic tibiae have a closed cell trabecular structure and a relatively homogenous porosity unlike cadaveric specimens. Following bone remodelling leading to an inhomogeneous stiffness distribution, the same trends are observed with much higher distal stresses and strains being computed for FC than SC. This suggests that the correct representation of cementation technique is a far more dominant factor than the issue of trabecular bone inhomogeneity. Synthetic tibiae were chosen for the current study in order to provide maximal reproducibility in terms of specimen size, material properties and cement penetration depth. In our study a low standard deviation was noted for repeated testing of the same implanted bone that is in line with previous studies (Completo et al. 2007a; Completo et al. 2008), demonstrating the reliability of our test methods. However, as we tested six bones per technique our overall standard deviations are understandably higher. A consistent method for strain gauge positioning was followed, however some errors may have resulted during application to the predetermined position. Errors may also be due in part to the inconsistent cortical thickness observed in our specimens. Inconsistent cortical thickness and the local structural stiffness of the proximal synthetic tibia have also been reported as reasons for experimental and computational errors (Completo et al. 2007a). Precise and

reproducible sample preparation, cementation and implantation were performed under the supervision of a consultant arthroplasty surgeon, strictly following manufacturer protocols. We therefore do not expect that our implantation techniques contributed significantly to any experimental error encountered. While only one implant design is considered in this study it should be noted that the tibial component is reflective of a standard metal backed baseplate with a central finned or winged stem used in primary TKA, similar to most models in contemporary use.

The maximum trabecular stresses reported in the study are close to the reported yield stress of the material, raising the important issue of plasticity and damage in TKA. However, this was beyond the scope of the present study. To our knowledge this is the first study to include a representation of cement penetration of trabecular bone in a computational model. Inclusion of this interdigitated bone-cement offered improved correlation, highlighting the importance of incorporating a representation of cement penetration in computational models. Previous studies have highlighted the importance of cement penetration (Bert and McShane 1998; Hofmann et al. 2006; Peters et al. 2003) and the present study went to considerable length to incorporate this both experimentally and computationally. Trabecular results are higher than cortical results, highlighting the importance of this joint experimental computational investigation.

4.5 Conclusions

Experimental cortical bone strains result in significant differences ($P < 0.05$) between FC and SC TKA, with lower strains measured for FC. In comparison to the intact results, our FE simulations compute greater reduction in trabecular stress under the baseplate for FC than SC due to the presence of cement at the stem resulting in stress transfer to the distal trabecular bone. This higher level of proximal stress shielding for FC is predicted to result in a higher area of bone resorption under the baseplate. This suggests that SC reduces the contribution of proximal bone resorption to aseptic loosening of the tibial component.

Appendices

Appendix A

Table 4-3 Experimental *P*-values for each strain gauge between the full and surface cementation models for axial and 15° flexion loading (* denotes *P*<0.05)

Gauge	Axial		Flexion	
	ε_{max}	ε_{min}	ε_{max}	ε_{min}
AM5	0.000*	0.139	0.000*	0.923
L5	0.000*	0.999	0.000*	0.999
AM30	0.360	0.016*	0.445	0.013*
L30	0.020*	0.002*	0.004*	0.004*
P30	0.454	0.002*	0.198	0.019*
AM50	0.000*	0.000*	0.000*	0.000*
L50	0.089	0.062	0.198	0.785
P50	0.612	0.636	0.847	0.993

Appendix B Supplementary Data to Journal Publication

In the axial intact case (Figure 4-7(A, D)) trabecular pressures are primarily compressive (positive). Comparable regions of tensile (negative) pressure (shown in black in the contour plots) are computed anteriorly in the intact and SC case (Figure 4-7(D, F)). However, a significantly increased region of anterior tensile pressure is computed for FC (Figure 4-7(E)). Both cementation techniques produce increased compressive pressures posteriorly compared to the intact case. Flexion loading produces similar trends, with a slightly reduced regions of negative pressure anteriorly and compressive pressures posteriorly for both implanted models (Figure 4-4(G, H)).

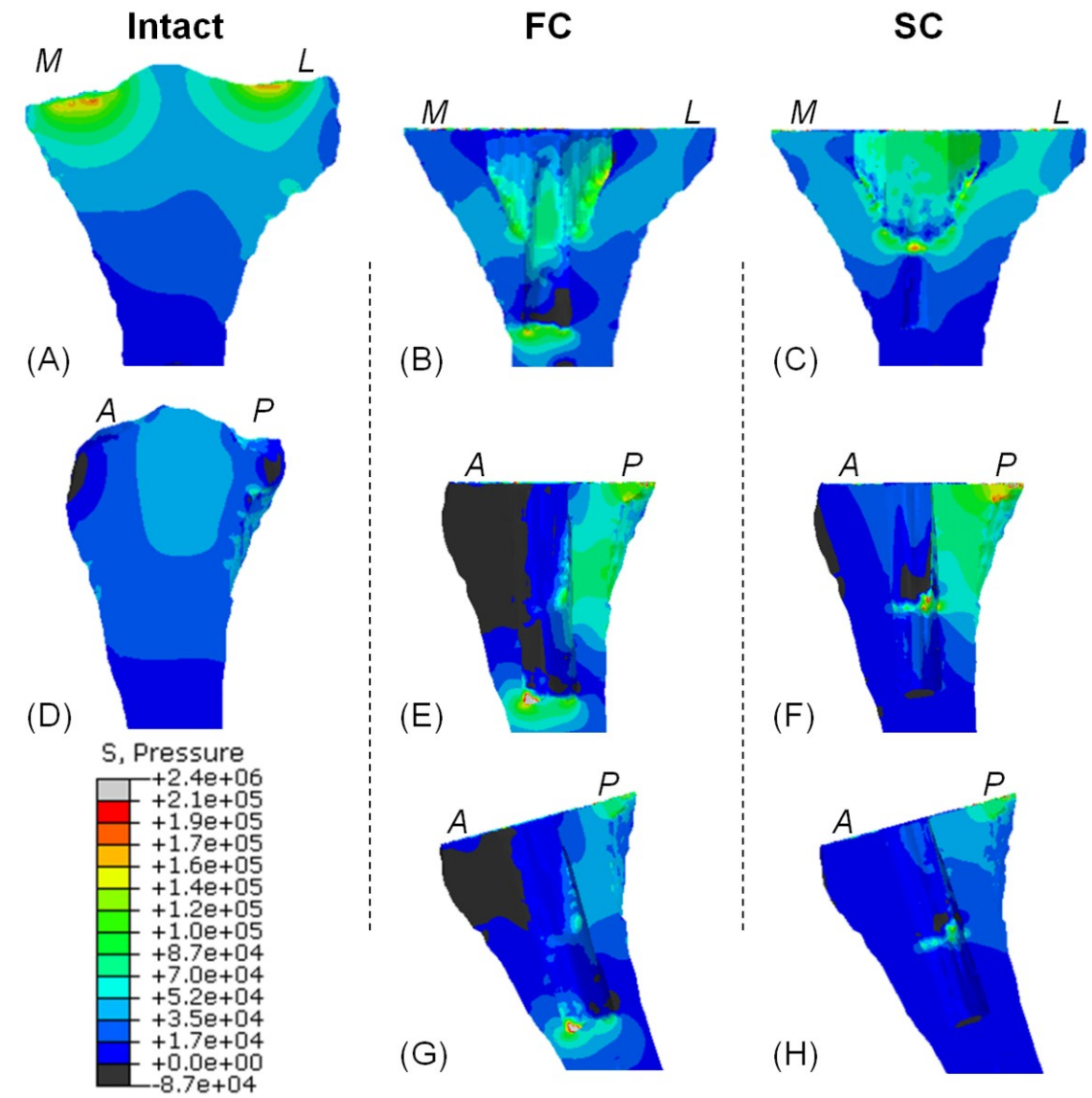

Figure 4-7 Contour plots showing coronal (A-C) and sagittal (D-H) section views of trabecular bone pressure results in Pa for the axial models (A-F) and 15° flexion models (G, H). The cortical bone, implant components, interdigitated layer and cement volume are removed for clarity leaving only the trabecular bone. Positive pressure values in the legend denote compression whereas negative values denote tension (shown in black). (*M* = medial, *L* = lateral, *A* = anterior, *P* = posterior).

Appendix C Strain Gauge Measurements

The triaxial strain gauge rosettes contain three gauges aligned at 45° apart. Measurement of independent strains for each gauge allows for the calculation of principal strains and principal directions with respect to the rosette gauge. The stacked grid formation of the gauges allows for accurate measurements in areas of high-gradients.

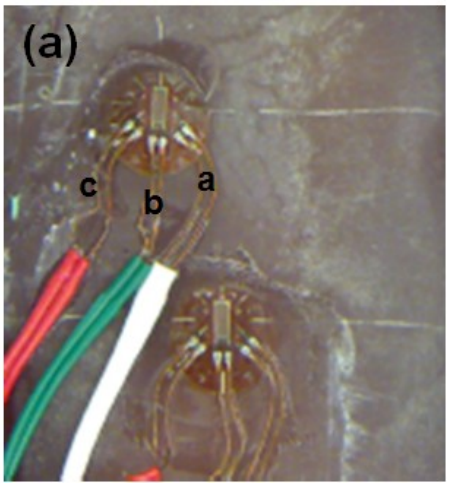

Figure 4-8 (a) Triaxial strain gauge rosettes.

For illustration purposes as shown in Figure 4-8, the gauges are labelled as a, b and c. If the principal strains are oriented at an angle θ to gauge b axis the strains in each rosette can be calculated in terms of the principal strains and the angle, θ_p. The maximum principal strain, ε_{max}, and minimum principal strain, ε_{min}, can be calculated as follows

$$\varepsilon_{max} = \frac{\varepsilon_a + \varepsilon_c}{2} + \frac{\sqrt{(\varepsilon_a - \varepsilon_c)^2 + (2\varepsilon_b - \varepsilon_c - \varepsilon_a)^2}}{2} \tag{4.1}$$

$$\varepsilon_{min} = \frac{\varepsilon_a + \varepsilon_c}{2} - \frac{\sqrt{(\varepsilon_a - \varepsilon_c)^2 + (2\varepsilon_b - \varepsilon_c - \varepsilon_a)^2}}{2} \tag{4.2}$$

where ε_a, ε_b and ε_c are the strain values for the strain gauges at 0°, 45° and 90° respectively. The principal direction for each rosette can be calculated as

$$\theta_p = \frac{1}{2} Tan^{-1}\left(\frac{2\varepsilon_b - \varepsilon_a - \varepsilon_c}{\varepsilon_a - \varepsilon_c}\right) \tag{4.3}$$

4.6 References

Baker, P. N., Khaw, F. M., Kirk, L. M. G., Esler, C. N. A., Gregg, P. J. (2007) A randomised controlled trial of cemented versus cementless press-fit condylar total knee replacement: 15-year survival analysis. J Bone Joint Surg Br 89 (12):1608.

Bert, J. M., McShane, M. (1998) Is it necessary to cement the tibial stem in cemented total knee arthroplasty? Clin Orthop 356:73-78.

Completo, A., Fonseca, F., Simoes, J. A. (2007a) Finite element and experimental cortex strains of the intact and implanted tibia. J Biomech Eng 129 (5):791-797.

Completo, A., Fonseca, F., Simões, J. A. (2007b) Experimental validation of intact and implanted distal femur finite element models. J Biomech 40 (11):2467-2476.

Completo, A., Fonseca, F., Simões, J. A. (2008) Strain shielding in proximal tibia of stemmed knee prosthesis: Experimental study. J Biomech 41 (3):560-566.

Efe, T., Figiel, J., Danek, S., Tibesku, C. O., Paletta, J. R. J., Skwara, A. (2011) Initial stability of tibial components in primary knee arthroplasty. A cadaver study comparing cemented and cementless fixation techniques. Acta Orthop Belg 29 (15):50.

Felix, N. A., Stuart, M. J., Hanssen, A. D. (1997) Periprosthetic fractures of the tibia associated with total knee arthroplasty. Clin Orthop 345:113.

Gandhi, R., Tsvetkov, D., Davey, J. R., Mahomed, N. N. (2009) Survival and clinical function of cemented and uncemented prostheses in total knee replacement: A meta-analysis. J Bone Joint Surg Br 91 (7):889.

Graves, S. E., Davidson, D., Ingerson, L., Ryan, P., Griffith, E. C., McDermott, B. F. J., McElroy, H. J., Pratt, N. L. (2004) The australian orthopaedic association national joint replacement registry. The Australian Orthopaedic Association National Joint Replacement Registry 180 (5):31.

Halloran, J. P., Petrella, A. J., Rullkoetter, P. J. (2005) Explicit finite element modeling of total knee replacement mechanics. J Biomech 38 (2):323-331.

Hernandez-Vaquero, D., Garcia-Sandoval, M. A., Fernandez-Carreira, J. M., Gava, R. (2008) Influence of the tibial stem design on bone density after cemented total knee arthroplasty: A prospective seven-year follow-up study. Int Orthop 32 (1):47-51.

Hofmann, A. A., Goldberg, T. D., Tanner, A. M., Cook, T. M. (2006) Surface cementation of stemmed tibial components in primary total knee arthroplasty: Minimum 5-year follow-up. J Arthroplasty 21 (3):353-357.

Huiskes, R., Weinans, H., Rietbergen, B. (1992) The relationship between stress shielding and bone resorption around total hip stems and the effects of flexible materials. Clin Orthop 274:124.

Ito, J., Koshino, T., Okamoto, R., Saito, T. (2003) 15-year follow-up study of total knee arthroplasty in patients with rheumatoid arthritis. J Arthroplasty 18 (8):984-992.

Keating, E. M., Meding, J. B., Faris, P. M., Ritter, M. A. (2002) Long-term followup of nonmodular total knee replacements. Clin Orthop 404:34.

Kolisek, F. R., Mont, M. A., Seyler, T. M., Marker, D. R., Jessup, N. M., Siddiqui, J. A., Monesmith, E., Ulrich, S. D. (2009) Total knee arthroplasty using cementless keels and cemented tibial trays: 10-year results. Int Orthop 33 (1):117-121.

Kurtz, S., Ong, K., Lau, E., Mowat, F., Halpern, M. (2007) Projections of primary and revision hip and knee arthroplasty in the united states from 2005 to 2030. J Bone Joint Surg Am 89 (4):780.

Lonner, J. H., Klotz, M., Levitz, C., Lotke, P. A. (2001) Changes in bone density after cemented total knee arthroplasty: Influence of stem design. J Arthroplasty 16 (1):107-111.

Luring, C., Perlick, L., Trepte, C., Linhardt, O., Perlick, C., Plitz, W., Grifka, J. (2006) Micromotion in cemented rotating platform total knee arthroplasty: Cemented tibial stem versus hybrid fixation. Arch Orthop Trauma Surg 126 (1):45-48.

Munro, J. T., Pandit, S., Walker, C. G., Clatworthy, M., Pitto, R. P. (2010) Loss of tibial bone density in patients with rotating-or fixed-platform tka. Clin Orthop 468 (3):775-781.

Ong, K. L., Day, J. S., Kurtz, S. M., Field, R. E., Manley, M. T. (2009) Role of surgical position on interface stress and initial bone remodeling stimulus around hip resurfacing arthroplasty. J Arthroplasty 24 (7):1137.

Peters, C. L., Craig, M. A., Mohr, R. A., Bachus, K. N. (2003) Tibial component fixation with cement: Full-versus surface-cementation techniques. Clin Orthop 409:158.

Registry, C. J. R. (2003) Canadian joint replacement registry (cjrr) 2003 report: Total hip and total knee replacements in canada. Canadian Institute for Health Information.

Regnér, L. R., Carlsson, L. V., Kärrholm, J. N., Hansson, T. H., Herberts, P. G., Swanpalmer, J. (1999) Bone mineral and migratory patterns in uncemented total knee arthroplasties: A randomized 5-year follow-up study of 38 knees. Acta Orthop Scand 70 (6):603-608.

Robertsson, O., Knutson, K., Lewold, S., Lidgren, L. (2001) The swedish knee arthroplasty register 1975-1997: An update with special emphasis on 41,223 knees operated on in 1988-1997. Acta Orthop Scand 72 (5):503-513.

Ryd, L., Hansson, U., Blunn, G., Lindstrand, A., Toksvig-Larsen, S. (1999) Failure of partial cementation to achieve implant stability and bone ingrowth: A long-term roentgen stereophotogrammetric study of tibial components. J Orthop Res 17 (3):311-320.

Saari, T., Li, M. G., Wood, D., Nivbrant, B. (2008) Comparison of cementing techniques of the tibial component in total knee replacement. Int Orthop:1-4.

Schai, P. A., Thornhill, T. S., Scott, R. D. (1998) Total knee arthroplasty with the pfc system. J Bone Joint Surg Br 80:850-858.

Seki, T., Bourgeault, C., Chareancholvanich, A. K., Lew, W., Bechtold, J. E., Gustilo, R. B. (1997) Does a central stem affect bone strain and the stability of a cemented tibial tray in primary and revision tka. Trans Orthop Res Soc 22:635.

Sharkey, P. F., Hozack, W. J., Rothman, R. H., Shastri, S., Jacoby, S. M. (2002) Why are total knee arthroplasties failing today? Clinical Orthop 404:7-13.

Skwara, A., Figiel, J., Knott, T., Paletta, J. R. J., Fuchs-Winkelmann, S., Tibesku, C. O. (2009) Primary stability of tibial components in tka: In vitro comparison of two cementing techniques. Arthroscopy 17 (10):1199-1205.

Weinans, H., Huiskes, R., Van Rietbergen, B., Sumner, D. R., Turner, T. M., Galante, J. O. (1993) Adaptive bone remodeling around bonded noncemented total hip arthroplasty: A comparison between animal experiments and computer simulation. J Orthop Res 11 (4):500-513.

Chapter 5

Experimental and Numerical Characterisation of the Elasto-Plastic Properties of Bovine Trabecular Bone and a Trabecular Bone Analogue

Abstract

The inelastic pressure dependent compressive behaviour of bovine trabecular bone is investigated through experimental and computational analysis. Two loading configurations are implemented, uniaxial and confined compression, providing two distinct loading paths in the von Mises-pressure stress ($q-p$) plane. Experimental results reveal distinctive yielding followed by a constant nominal stress plateau for both uniaxial and confined compression. Computational simulation of the experimental tests using the Drucker-Prager and Mohr-Coulomb plasticity models fails to capture the confined compression behaviour of trabecular bone. The high pressure developed during confined compression does not result in plastic deformation using these formulations, and a near elastic response is computed. In contrast, the crushable foam plasticity models provide accurate simulation of the confined compression tests, with distinctive yield and plateau behaviour being predicted. The elliptical yield surfaces of the crushable foam formulations in the $q-p$ stress plane accurately characterise the plastic behaviour of trabecular bone. Results reveal that the hydrostatic yield stress is equal to the uniaxial yield stress for trabecular bone, demonstrating the importance of accurate characterisation and simulation of the pressure dependent plasticity. It is also demonstrated that cellular PU, a synthetic bone analogue, exhibits similar pressure dependent yield behaviour to trabecular bone despite having a lower strength and stiffness. The present study provides novel insight into the pressure dependent yield behaviour of trabecular bone, demonstrating the inadequacy of uniaxial testing alone. For the first time, crushable foam plasticity formulations are implemented for trabecular bone. The enhanced understanding of the inelastic behaviour of trabecular bone established will allow for more realistic simulation of orthopaedic device implantation and failure.

5.1 Introduction

Trabecular bone is a highly porous cellular structure composed of a complex interconnected network of rods and plates called trabeculae. Its material properties are dependent on many factors including density, age, sex, species, geometry and anatomic site (Goldstein 1987; Keaveny et al. 1993b; Morgan et al. 2003). Both cellular rigid and solid rigid polyurethane foam (PU), commercially available trabecular bone analogue materials (Sawbones, Pacific Research Labs, Malmö, Sweden), have been widely used as trabecular bone substitutes in biomechanical testing (Agneskirchner et al. 2006; Poukalova et al. 2010). A range of rigid closed cell PU foams (grades 5-50, $\rho = 0.08\text{-}0.8$ g/cm^3) have been identified in ASTM F1839-08 (ASTM 2008). This artificial bone material has become an attractive alternative over cadaveric bone due to its availability, uniformity, low inter-specimen variability, reproducibility and clean testing environment. It has a similar cellular structure and many of its elastic properties are of the same order of magnitude as trabecular bone (Patel et al. 2008; Thompson et al. 2003). Due to its intricate porous lattice-like structure, the mechanical response of cellular foams and trabecular bone during uniaxial compressive loading is complex. The stress-strain curve of a cellular material typically displays three phase deformation behaviour. An initial linear elastic region occurs due to elastic cell bending which is followed by material yield causing collapse of the cell walls under constant load. An inelastic section follows where a constant stress plateau occurs due to progressive cell wall damage, breakage and buckling under increased loading. A steep stiffness increase called densification occurs when the cell material consolidates due to cells collapsing and contacting (Gibson 2005; Goldstein 1987; Neilsen et al. 1995; Szivek et al. 1993). Due to its widespread use as a trabecular bone substitute material for biomechanical applications, grade 20 cellular rigid closed cell PU was used in this study. Additionally, grade 50 solid rigid PU foam is also considered.

Knowledge of the complex deformation behaviour of trabecular bone is important at a clinical and biomechanical level. Previous studies investigating non-linear trabecular bone mechanics have uncovered viscoelastic, damage and elasto-plastic behaviour (Keaveny et al. 1999; Linde 1994; Moore and Gibson 2002). The present study focuses on elasto-plastic behaviour, in particular focusing on the role of pressure (hydrostatic stress) in the yield behaviour of trabecular bone. Inelastic

deformation can occur due to excessive loading or fatigue and may lead to microdamage, fracture, compaction and crushing of trabecular bone (Moore and Gibson 2002). Inelastic loading also occurs during the subsidence of prostheses, such as vertebral fusion devices and the implantation of press-fit prostheses in total joint arthroplasty (Taylor et al. 1998). As trabecular bone is naturally confined by stiff cortical bone it is reasonable to suggest that high pressures will occur during such inelastic deformation. Despite this, the pressure dependent plastic yielding of trabecular bone has not previously been investigated.

Previous continuum level finite element studies characterising the elasto-plastic behaviour of bone have focused primarily on cortical bone. Several studies have considered von Mises plasticity which neglects pressure dependent yield (Adam and Swain 2011; Keyak 2001; Keyak and Rossi 2000; Lotz et al. 1991; Mullins et al. 2009). Additionally, several studies have focused on the Drucker-Prager (DP) (Adam and Swain 2011; Bessho et al. 2007; Carnelli et al. 2010; Carnelli et al. 2011; Mercer et al. 2006; Mullins et al. 2009) and Mohr-Coulomb (MC) (Tai et al. 2006; Wang et al. 2008) constitutive formulations. Through the definition of a friction angle the DP and MC models allow for an increasing yield stress for increasing pressure. Comparing the von Mises and DP models for the simulation of cortical bone nanoindentation, Mullins et al. (2009) suggested that a pressure dependent yield criterion should be used when modelling the post yield behaviour of cortical bone due to frictional mechanisms.

Cortical and trabecular bone have different microarchitecture (Keaveny et al. 2001) and therefore the plasticity mechanisms of both materials may be very different. The inelastic behaviour of cellular materials, such as trabecular bone and PU foam, are related to the microstructural level deformation. At the level of single trabeculae, Wang et al. (2008) used the MC model to simulate nanoindentation. While DP and MC type material behaviour may be appropriate for cortical bone and for individual trabeculae, the suitability of such plasticity models has not previously been investigated for macroscale behaviour of trabecular bone. Inelastic continuum material models have also been proposed that can account for trabecular bone morphology (Charlebois et al. 2010a; Rincon-Kohli and Zysset 2009; Zysset and Rincon-Kohli 2006; Zysset and Curnier 1996). Due to the experimental evidence that at the apparent level trabecular bone yields at a nearly constant strain within an

anatomic site (Bayraktar and Keaveny 2004; Chang et al. 1999; Kopperdahl and Keaveny 1998; Morgan and Keaveny 2001), strain-based inelastic material models have been developed and implemented for trabecular bone (Cowin and He 2005). In contrast, trabecular bone yield stress and elastic modulus are not uniform within an anatomic site (Chang et al. 1999; Morgan and Keaveny 2001). van Rietbergen et al. (1996) and van Rietbergen et al. (1998) demonstrated that a uniform uniaxial yield strain exists for trabecular bone that is independent of the direction of loading. Microarchitecture based high resolution FE models have been used to investigate trabecular bone behaviour (Bayraktar et al. 2004; Guillén et al. 2011; Harrison et al. 2008; Mc Donnell et al. 2009; Niebur et al. 2002; Niebur et al. 2000). Detailed reconstruction of the trabecular bone microarchitecture allows for the simulation of non-linear behaviour while using simplified material constitutive laws, however, microstructural based FE models are of limited use for macroscale simulation of orthopaedic device performance. In contrast, the macroscale inelastic behaviour of trabecular bone can be modelled using continuum constitutive models that are less complex and less computationally expensive than microstructural based models. Continuum models are investigated in the current study in an attempt to phenomenologically replicate the complex inelastic material behaviour of trabecular bone and may potentially be applied to macroscale trabecular bone applications involving inelastic deformation.

The current study involves a detailed experimental and numerical investigation of the elasto-plastic macroscale behaviour of PU and bovine trabecular bone (BTB). Both uniaxial and confined compression tests are performed in order to identify two distinct loading paths on the von Mises-pressure stress ($q - p$) plane. The main aim of the study is to investigate, for the first time, the pressure dependent yield behaviour of trabecular bone under confined compression and to determine a constitutive formulation that best captures this behaviour. Due to widespread use of cellular and solid rigid PU foams as trabecular bone analogues for biomechanical testing our secondary aim is to compare the pressure dependent plasticity of such foams to that of trabecular bone. The following pressure dependent constitutive formulations are investigated: DP; MC; isotropic crushable foam (CFI); volumetric crushable foam (CFV).

5.2 Methods

5.2.1 Experimental

Cubic specimens of 8 mm of grade 20 cellular rigid closed cell PU foam (ρ = 0.32 g/cm^3) and grade 50 solid rigid closed cell PU foam (ρ = 0.80 g/cm^3, E = 1148 MPa, ~99.9% closed cell) by Sawbones (Pacific Research Labs, Malmö, Sweden) and BTB were cut using a bandsaw (Jubilee VBS 360, Addison Saws Ltd., West Midlands, UK). For the remainder of this document the grade 20 cellular rigid PU will be referred to as "cellular PU" and the grade 50 solid rigid PU will be referred to as "solid PU". It should be noted that only one density of each foam type has been tested and therefore the results apply only to these particular density foams. The BTB specimens were prepared from the proximal tibia of a single bovine steer under 30 months obtained from a local abattoir and stored at 4°C prior to testing. BTB specimens were kept hydrated in phosphate buffer solution (PBS) with the marrow *in situ* at all times, including during mechanical testing, and were tested with their principal trabecular orientation approximately aligned parallel to the axis of loading. BTB was chosen for the experimental study over cadaveric bone due to the size and availability of specimens and its similarity to human trabecular bone.

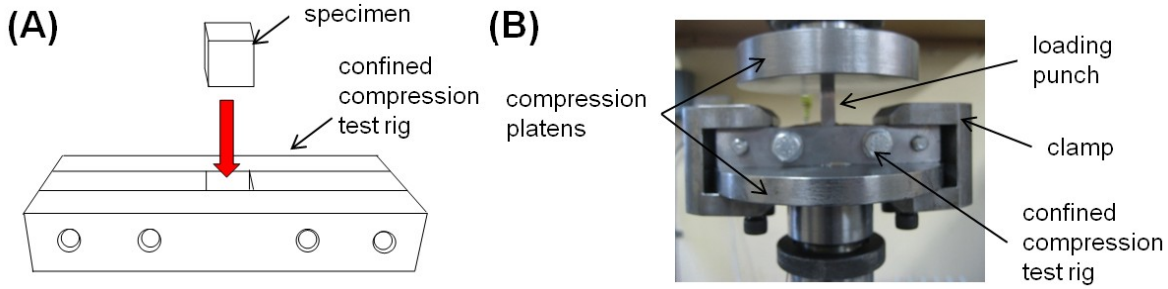

Figure 5-1(A) Schematic of experimental rig used for confined compression testing. (B) Confined compression experimental set-up on an Instron testing machine.

Plano-parallel specimen ends were produced using sandpaper. The PU and BTB specimen dimensions were taken as an average of four measurements with a digital vernier calliper before testing to account for the inhomogeneity of the samples and were randomly assigned to experimental groups. Two different loading configurations were investigated; uniaxial compression and confined compression. Compression is a dominant *in vivo* loading mode for trabecular bone and confined

compression is appropriate as trabecular bone is typically confined by a hard cortical shell. Destructive static compression tests were performed on the cellular PU and BTB at room temperature on a servo hydraulic testing machine (model 8500, Instron Corp., Canton, MA, USA) equipped with a 100 kN load cell (n = 9/group). 36 tests were performed in total; nine specimens were tested for the each specimen type (cellular PU and BTB) and for each test configuration (uniaxial and confined). Uniaxial compression was performed using the conventional platens test and the specimens were placed between polished parallel hardened steel platens. The confined compression tests were performed on a custom made confinement rig (Figure 5-1) which prevented lateral displacement of the specimen during loading. The test specimens were placed in a hole in the rig which was the same size as the specimens. The rig was then secured between the two loading platens using clamps, as shown in Figure 5-1(B). A loading punch with a cross-sectional area of 8 x 8 mm was used to load the specimen via the compression platens. For both uniaxial and confined compression testing, a 5-10 N compressive preload was applied and the specimens were loaded at a constant strain rate of 5 mm/min to 60% strain. Air exposure was kept to a minimum during BTB testing. Additional uniaxial (n = 5) and confined (n = 5) compression testing was also performed on the solid PU to elucidate any pressure dependent behaviour of the ~99.9% closed cell foam. Preliminary uniaxial compression testing was performed on five cellular PU specimens in each of the three loading directions (n = 15 in total). Two sample t-tests were performed to determine statistical significance between the three uniaxial loading directions. Significance was determined at $p<0.05$.

Nominal stress-nominal strain curves were constructed based on undeformed specimen dimensions. The apparent compressive Young's modulus (E) was computed as the slope of the uniaxial nominal stress-nominal strain curve between 30% and 70% of the ultimate stress (Keaveny et al. 1993a, 1993b; Turner 1989). The yield stress (σ_y) was determined using the 0.2% offset method. The elastic Poisson's ratio (ν_e) and plastic Poisson's ratio (ν_p) were measured using a video extensometer (ME 46, Messphysik, Fürstenfeld, Austria).

5.2.2 Material Model Calibration

Finite element simulations (Abaqus v6.8 Dassault Systemes, RI, USA) were performed in order to establish suitable elasto-plastic constitutive formulations for both PU and BTB. Both materials were both treated as a homogenous continuum and modelled using each of the aforementioned elasto-plastic material models: DP; MC; CFI; CFV. Using 3D continuum elements, boundary conditions were applied to replicate the uniaxial and confined compression experimental tests. Both the PU and BTB were compressed to 60% strain. Each of the elasto-plastic material models was used in combination with an isotropic, linear elastic material model where a value of E and ν_e were required. A hardening curve, describing the uniaxial compressive yield stress as a function of the corresponding plastic strain, determined from the mean uniaxial experimental nominal stress-nominal strain curve for PU and BTB, were used to describe the inelastic behaviour. Material parameter calibration was conducted for each constitutive model to identify an accurate numerical solution for the experimental results under uniaxial compression. Following model calibration under uniaxial compression, parameter variation under confined compression was simulated in order to investigate the pressure dependent plastic behaviour of each material model. The computed response was compared to experimental confined compression data. The yield surface and flow potential of all four constitutive models considered in the study are governed by the von Mises equivalent stress (q) and the equivalent pressure stress (p) where

$$q = \sqrt{\frac{3}{2} S_{ij} S_{ij}} \qquad\qquad p = -\frac{1}{3} trace(\boldsymbol{\sigma})$$

and S_{ij} is the stress deviator.

The stress state in uniaxial compression (Figure 5-2(A)) is expressed in terms of a single principal stress component in the loading direction (σ_{33}). It therefore follows that $q/p = 3$ for uniaxial tests, independent of ν_e. In confined compression three principal stress components exist (σ_{11}, σ_{22}, σ_{33}) when load is applied axially (direction 3), and lateral deformation of the specimens is prevented in the other two directions (whereby $\varepsilon_{11} = \varepsilon_{22} = 0$, $\sigma_{11} = \sigma_{22}$) (Figure 5-2(B)). Using Hooke's law for an isotropic elastic material, it is trivial to determine the ratio of von Mises stress to pressure as a function of ν_e (Figure 5-2(B, C)). As an illustrative example, for a ν_e = 0.3, q/p = 0.92 for a confined compression test. Therefore, by performing both

uniaxial and confined compression tests up to yielding in tandem, two distinct points on a yield surface in the $q-p$ plane can be established as shown in Figure 5-3. Examples of the yield surface calibration of a DP or MC type material and a crushable foam type material are shown in Figure 5-3(B, C).

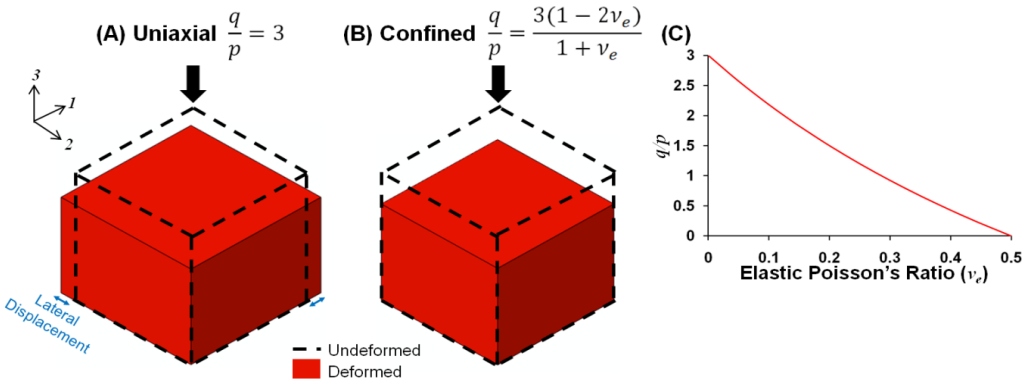

Figure 5-2 (A) Schematic of uniaxial compression for an elastic Poisson's ratio, ν_e, of 0.3. (B) Schematic of confined compression. (C) Relationship between the ratio q/p (von Mises stress/pressure stress) and the elastic Poisson's ratio (ν_e) for confined compression of an isotropic elastic material.

The DP and MC plasticity models are very similar; their yield surfaces are represented by a straight line in the $q-p$ plane (Figure 5-3(B)). The DP criterion was introduced by Drucker and Prager (1951) and was traditionally used to model soils. Both the DP and MC models have previously been calibrated for cortical bone (Mercer et al. 2006; Mullins et al. 2009; Tai et al. 2006), where a high friction angle results in an increased von Mises yield stress with increasing pressure as shown in Figure 5-3(B). Refer to Chapter 3 for further information on the DP and MC formulations.

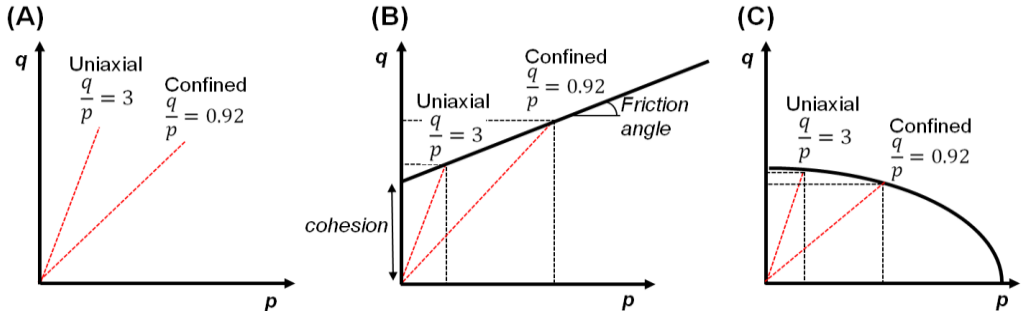

Figure 5-3 (A) Schematic of the loading path for uniaxial compression and confined compression for an elastic material in the $q-p$ plane; (B) Schematic of a Drucker-Prager or Mohr-Coulomb type yield surface; (C) Schematic of a crushable foam type yield surface. q = von Mises stress, p = pressure.

Crushable foam plasticity models can phenomenologically represent the buckling of cell walls under compression of a cellular material. The crushable foam yield surface is an ellipse in the $q-p$ plane (Figure 5-3(C), Figure 5-4). An increase in pressure leads to a lower von Mises stress at yield for the CFI and CFV models, in contrast to DP and MC plasticity. The CFI model is based on a model by Deshpande and Fleck (2000) assumes symmetric behaviour in tension and compression and the yield ellipse is centred at the origin of the $q-p$ plane (Figure 5-4(A)).

The yield criterion for the CFI model is given by:

$$F = \sqrt{q^2 + \alpha^2 p^2} - B = 0$$

where

$$B = \alpha p_c$$

$$\alpha = \frac{3K}{\sqrt{9 - K^2}}$$

$$K = \frac{\sigma_c^0}{p_c^0}$$

The flow potential for the CFI model is given by:

$$\mathrm{g} = \sqrt{q^2 + \beta^2 p^2}$$

where

$$\beta = \frac{3}{\sqrt{2}} \sqrt{\frac{1 - 2\nu_p}{1 + \nu_p}}$$

where α is the shape of the yield ellipse in the $q-p$ stress plane, B is the size of the yield ellipse, p_c is the yield strength in hydrostatic compression, K is the compression yield stress ratio, σ_c^0 is the initial yield strength in uniaxial compression, p_c^0 is the initial yield strength in hydrostatic compression, β is the ellipse for the potential flow and ν_p is the plastic Poisson's ratio.

The yield ellipse progression is governed by the equivalent plastic strain (Deshpande and Fleck 2000). In contrast to the CFI model, the CFV model allows for asymmetric compression-tension behaviour. The CFV yield ellipse is not centred at the origin and during plastic deformation the hydrostatic tension strength is assumed

fixed (Figure 5-4(B)). The yield stress in uniaxial compression evolves due to an increase (compaction) or decrease (dilation) in material density.

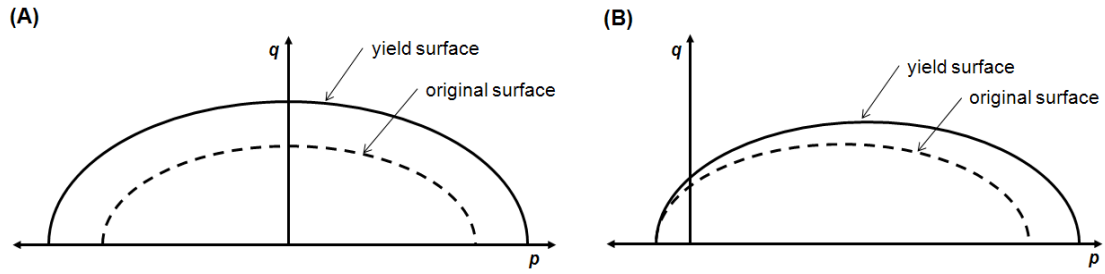

Figure 5-4 The yield surface and yield surface evolution for: (A) CFI model; (B) CFV model.

The yield criterion for the CFV foam model is given by:

$$F = \sqrt{q^2 + \alpha^2 (p - p_0)^2} - B = 0$$

where

$$\alpha = \frac{3K}{\sqrt{(3K_t + K)(3 - K)}}$$

$$K = \frac{\sigma_c^0}{p_c^0}$$

$$K_t = \frac{p_t}{p_c^0}$$

The flow potential for the CFV model is given by:

$$\mathrm{g} = \sqrt{q^2 + \frac{9}{2} p^2}$$

Where p_0 is the centre of the yield ellipse, K_t is the hydrostatic yield stress ratio and p_t is the yield strength in hydrostatic tension.

The CFV yield ellipse progression is governed by the volumetric compacting plastic strain. Given the large deformations that occur during mechanical testing, with plastic strains exceeding 50%, finite deformation kinematics was implemented in all models. However, for convenience, both experimental and computational results are plotted in terms of nominal stress and nominal strain.

5.3 Results

5.3.1 Experimental

Experimentally measured nominal stress-nominal strain plots for the uniaxial and confined compression testing of the cellular PU and the proximal tibial BTB are illustrated in Figure 5-5 and Figure 5-6, respectively. All experimental testing involved strain beyond the yield point and in all cases permanent plastic deformation was observed. The specimens undergo permanent plastic deformation with a very small amount of elastic recovery upon load removal. The elasto-plastic behaviour of cellular PU and BTB exhibit distinctive yielding.

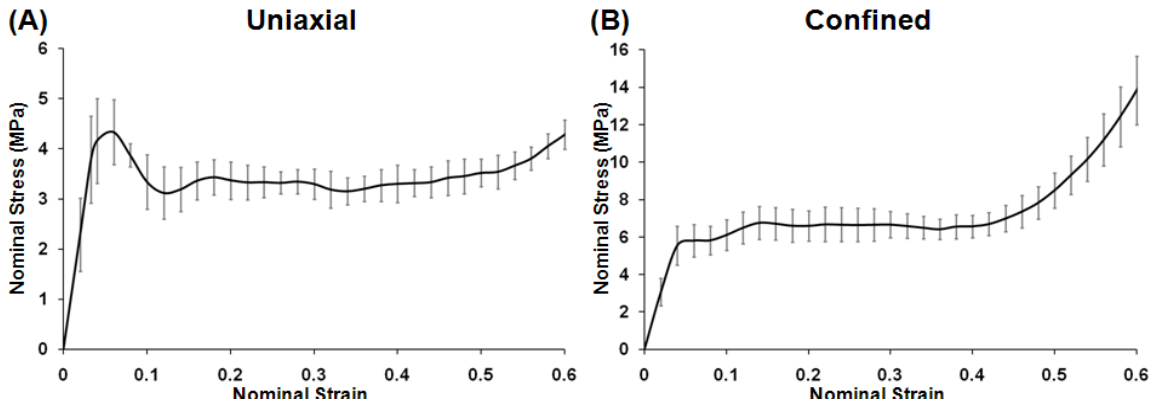

Figure 5-5 Grade 20 cellular rigid polyurethane foam experimental results: (A) mean ± SD for uniaxial compression; (B) mean ± SD for confined compression.

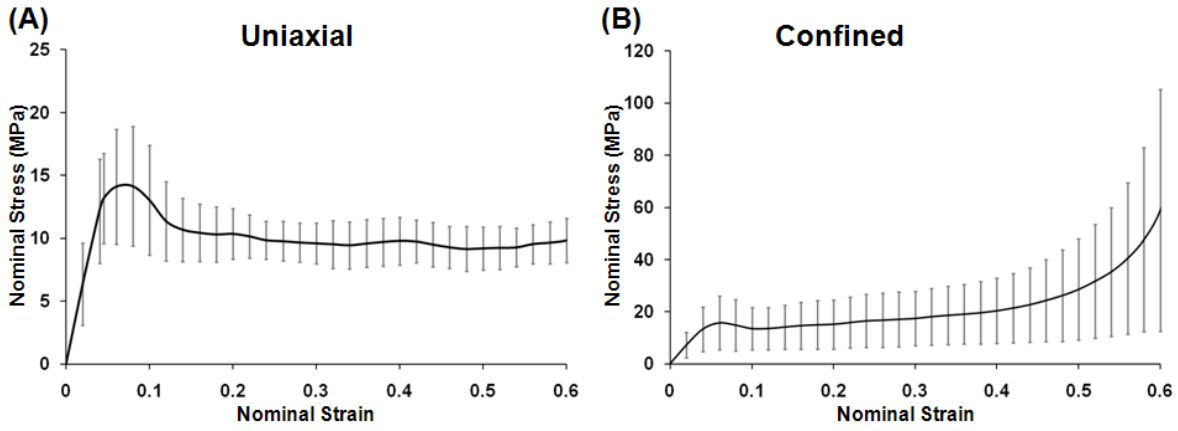

Figure 5-6 Bovine trabecular bone experimental results: (A) mean ± SD for uniaxial compression; (B) mean ± SD for confined compression.

Material properties experimentally measured for both specimen types (mean ± SD (range)) under uniaxial compression are shown in Table 5-1. The magnitudes of the mean measured values of E and σ_y for cellular PU under uniaxial compression are 141.3 ± 40.9 MPa and 3.8 ± 0.7 MPa respectively. Under uniaxial compression, the magnitudes of the mean E and σ_y for BTB are 381.7 ± 181.9 MPa and 13.2 ± 3.6 MPa respectively. Regarding the uniaxial compression data (Figure 5-5(A), Figure 5-6(A), Table 5-1), the cellular PU and BTB specimens show a similar nominal stress-nominal strain response. Under uniaxial compression the measured σ_y for BTB (13.2 MPa) is greater than the cellular PU (3.8 MPa) by a factor of 3.5. Also the measured E for BTB (381.7 MPa) is a factor of 2.7 greater than the cellular PU (141.3 MPa). A similar uniaxial compressive mean v_e is measured for cellular PU (0.20 ± 0.06) and BTB (0.16 ± 0.05). Despite quantitative differences measured for cellular PU and BTB, qualitatively similar inelastic deformation characteristics are observed. A plateau region of nearly constant stress is observed post yield at ~3.5 MPa and ~10 MPa for the cellular PU and BTB respectively. This is followed by material densification occurring at ~50% strain for the cellular PU. Regarding the confined compression results, the nominal stress (in the loading direction) exhibits distinctive yield behaviour for the cellular PU (Figure 5-5(B)) and BTB (Figure 5-6(B)). Most importantly, both specimen types exhibit a flat nominal stress-nominal strain curve following the initial yielding, resembling a perfect-plasticity nominal stress-nominal strain curve. An increase in nominal stress at higher strains occurs at ~40% strain for both specimen types.

Table 5-1 Experimentally measured material properties for cellular polyurethane foam and bovine trabecular bone under uniaxial compression. Results are reported as mean ± SD (range).

	Young's Modulus, E (MPa)	Yield Stress, σ_y (MPa)	Elastic Poisson's Ratio, ν_e	Plastic Poisson's Ratio, ν_p
PU Foam (grade 20)	141.3 ± 40.9 (76.4-165.9)	3.8 ± 0.7 (2.8-4.6)	0.20 ± 0.06 (0.14-0.28)	0.23 ± 0.08 (0.13-0.36)
BTB	381.7 ± 181.9 (168.5-798.4)	13.2 ± 3.6 (9.2-20.9)	0.16 ± 0.05 (0.12-0.2)	0.29 ± 0.20 (0.17-0.47)

5.3.2 Material Model

The four aforementioned plasticity formulations (DP, MC, CFI and CFV) are calibrated to replicate the cellular PU and BTB experimental data for uniaxial compression as shown in Figure 5-7. Each formulation is capable of capturing the inelastic behaviour under uniaxial compression conditions, including the yield, peak, plateau and densification.

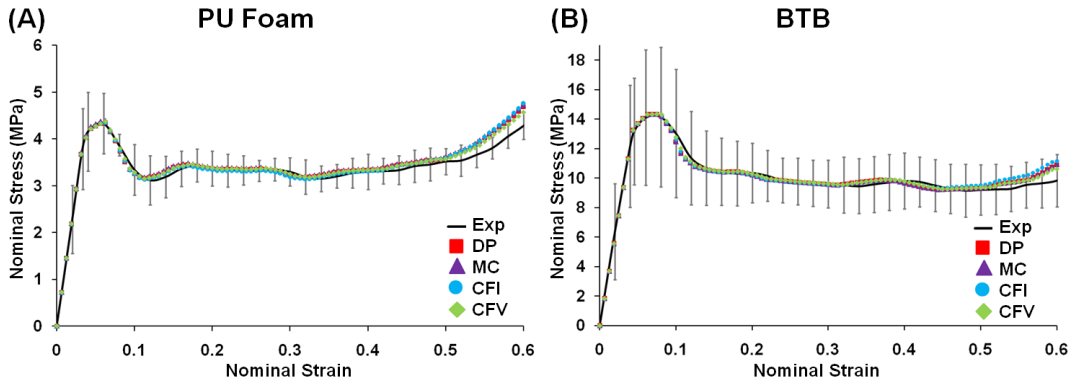

Figure 5-7 Uniaxial compression Drucker-Prager (DP), Mohr-Coulomb (MC), isotropic crushable foam (CFI), volumetric crushable foam (CFV) and experimental (mean ± SD) results: (A) cellular PU foam; (B) BTB.

Next, using the material parameters calibrated from the uniaxial compression test, confined compression is simulated using the four plasticity formulations (Figure 5-8). Firstly, it should be noted that the initial elastic response in confined compression is accurately simulated (for each model) using the mean experimentally measured E for both cellular PU and BTB and by performing a parametric study of ν_e. A computed ν_e of 0.28 for the cellular PU and 0.16 for the BTB respectively give a very good fit to our confined experimental data. These values lie in the range of the ν_e reported in Table 5-1, measured using video extensometry. Next focusing on the plastic response under confined compression, it is shown in Figure 5-8 that the DP and MC material models cannot replicate the experimental nominal stress-nominal strain data. For both the DP and MC models a friction angle $\beta = 0°$ and a dilation angle $\psi = 0°$ provide the closest match to the confined experimental results for both specimen types. In contrast to the DP and MC models, the CFI and CFV models accurately capture the initial yield behaviour of both the cellular PU and BTB under confined compression (Figure 5-8). A best fit is obtained with a uniaxial to hydrostatic yield stress ratio of $K = 0.7$ for PU and $K = 1$ for BTB, illustrating the

significant role played by pressure stress in the onset of plastic behaviour for both materials. Plateau behaviour is computed for both materials following initial yielding, similar to that observed experimentally, however, under predicting the experimental results. Predicted stresses lie within the experimental standard deviations for BTB up to a nominal strain of 0.42. For the CFI model K = 1 and ν_p = 0.19 provides the best fit for BTB. This value of ν_p falls within the experimentally measured range for BTB (Table 5-1). For the cellular PU K = 0.7 and ν_p = 0.36 provides the best match. Again, ν_p is within the measured range (Figure 5-8(A), Table 5-1). While identical K values are determined for the CFI and CFV models, providing accurate initial yield predictions, the CFV model offers limited ability to calibrate peak stress under confined compression and lateral deformation under compression. In contrast, calibration of ν_p in the CFI model allows for accurate simulation of peak stress and lateral deformation.

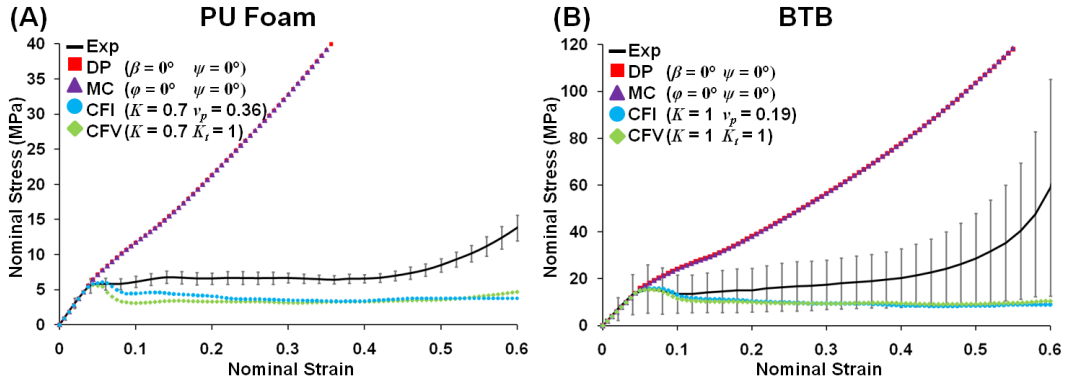

Figure 5-8 Confined compression Drucker-Prager (DP), Mohr-Coulomb (MC), isotropic crushable foam (CFI), volumetric crushable foam (CFV) and experimental (mean ± SD) results: (A) cellular PU foam; (B) BTB.

In order to further illustrate the fundamental differences between the predicted behaviour for linear yield surfaces (DP and MC models) and elliptical yield surfaces (CFI and CFV models), Figure 5-9 plots the evolution of von Mises stress and pressure predicted for uniaxial (Figure 5-9(A)) and confined (Figure 5-9(B)) compression. In the case of uniaxial compression, there is only one non-zero stress component, which is equal to the von Mises stress. The pressure is at all times equal to one third of this stress, so no notable differences exist between the DP and crushable foam models. For confined compression, in addition to the stress component in the loading direction, lateral stress components also exist and the

pressure is no longer simply given as $p = q/3$. As shown in Figure 5-9(B), even though the von Mises stress follows a yield criterion, no pressure dependent yield is computed for the DP model, with the computed pressure being equal to the elastic solution. As a result, the nominal stress in the loading direction does not exhibit the required yield behaviour, as is evident from Figure 5-9. In contrast, for the crushable foam models, both the von Mises stress and pressure stress follow a yield criterion, thus resulting in a pronounced yield in the predicted nominal stress.

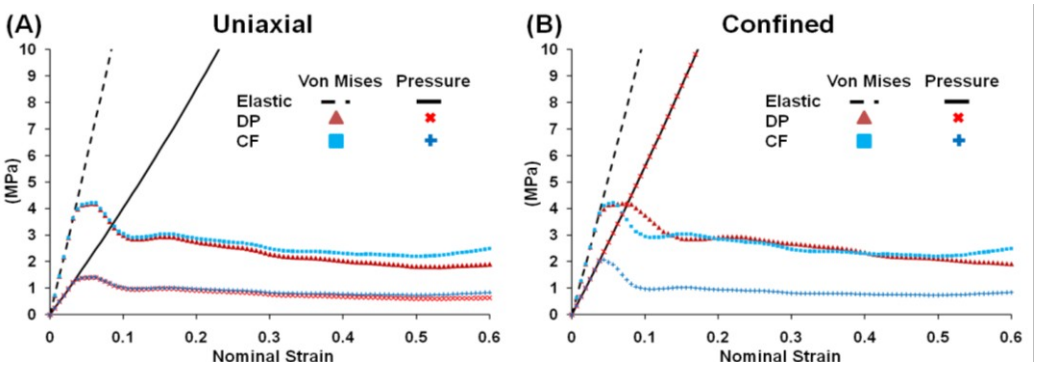

Figure 5-9 Schematic of the contribution of pressure stress and von Mises stress for an elastic, Drucker-Prager (DP) and crushable foam (CF) simulation: (A) a uniaxial compression test; (B) a confined compression test.

To gain further insight, parametric studies are presented in Figure 5-10 for the DP and CFI models for BTB. A range of ν_p and K values are considered for the CFI model. As previously shown, K = 1 and ν_p = 0.19 provides the best fit for the experimentally observed initial yield. A decrease in K (as shown for K = 0.7 and K = 0.5) in Figure 5-10(A, B)) results in a slightly over predicted yield stress and peak stress. A lower value of K reduces the pressure dependent yield, thus increasing the stress at which plasticity initiates. As expected, the ν_p has no effect on the initial yield. Increasing the ν_p (from 0.19 to 0.3) generally results in an increase in both the peak stress (Figure 5-10(B)) and the plateau (Figure 5-10(A, C)). It was not possible to accurately predict the plateau stress at high nominal strains (> 0.15) without significantly over predicting the initial yield and peak stresses. As previously noted, however, the CFI model provides the best prediction of experimental test data for PU and BTB. Also shown in Figure 5-10 for the DP model, increasing the friction angle of the DP or MC models (from 0° to 20°) results in even more inaccurate predictions**,** as expected, with higher friction angles further delaying the onset of yield.

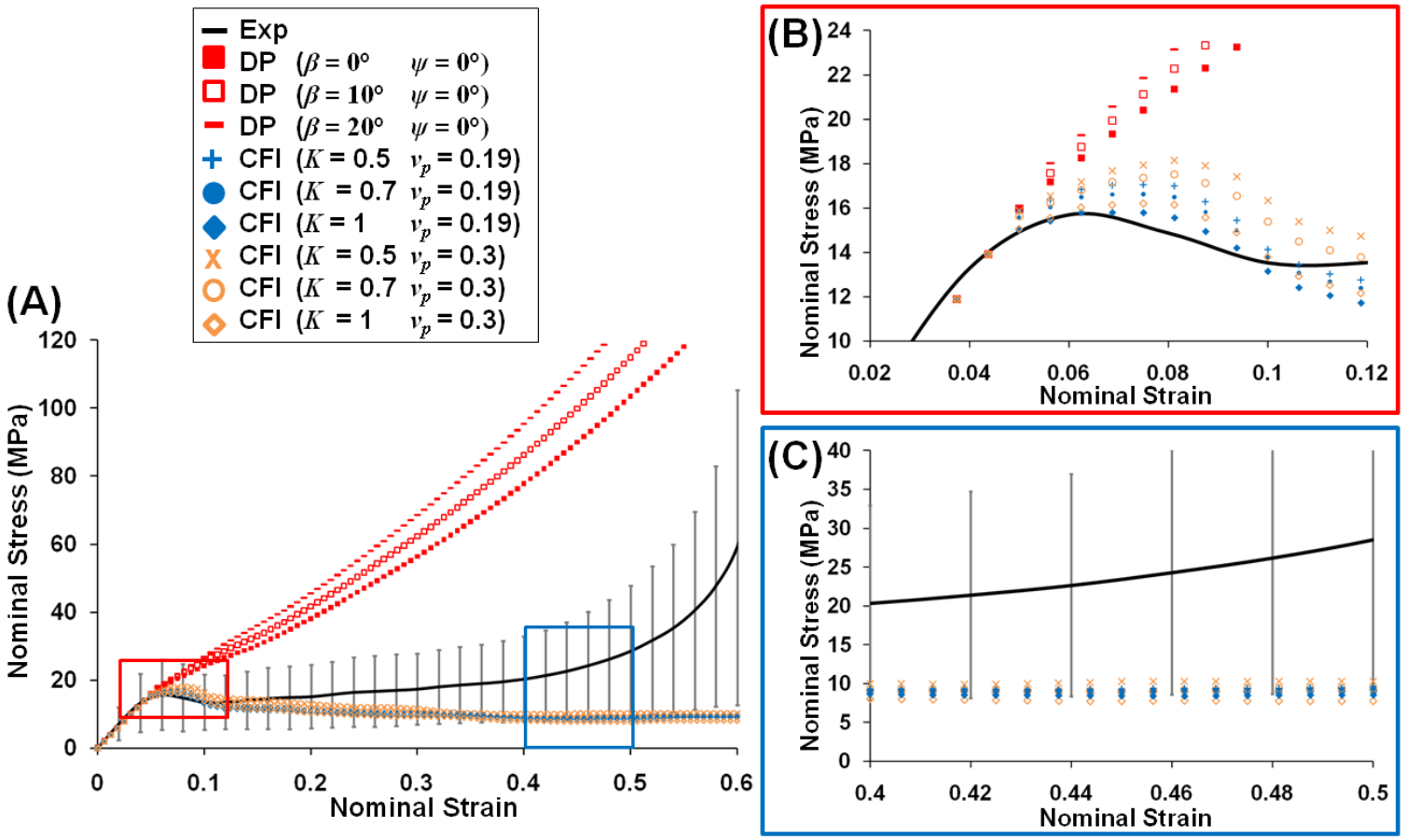

Figure 5-10 (A) Confined compression experimental BTB results (mean ± SD) and BTB parametric study results for the Drucker-Prager (DP) and isotropic crushable foam (CFI) material models; (B) Yield and peak stress behaviour; (C) Plateau stress behaviour for a nominal strain of 0.4 to 0.5.

The experimental (mean ± SD) and computational (von Mises plasticity model) uniaxial and confined compression testing results for the solid PU are shown in Figure 5-11. Under uniaxial compression, yield is followed by a plateau region and then densification, which is similar to the cellular PU and BTB (Figure 5-5(A) and Figure 5-6(A) respectively). No distinct yield is apparent under confined compression for the solid PU which is in stark contrast to the cellular PU and BTB (Figure 5-5(B) and Figure 5-6(B) respectively). The uniaxial and confined compressive behaviour of the solid PU is captured by a perfectly plastic von Mises plasticity model (Figure 5-11), in which yielding is independent of hydrostatic stress. This simple model is equivalent to a DP model with a frication angle of 0°. Despite the yield curve in uniaxial compression, the solid PU does not yield in confined compression, where an increase in pressure leads to increased elastic strain, as illustrated in Figure 5-9. Preliminary uniaxial compression testing of the cellular PU in the three loading directions showed no statistical difference $(p < 0.05)$ for σ_y or at 40% strain. No significant cellular PU anisotropy was evident from these macroscale results, providing justification for the use of isotropic constitutive models for these PU foams.

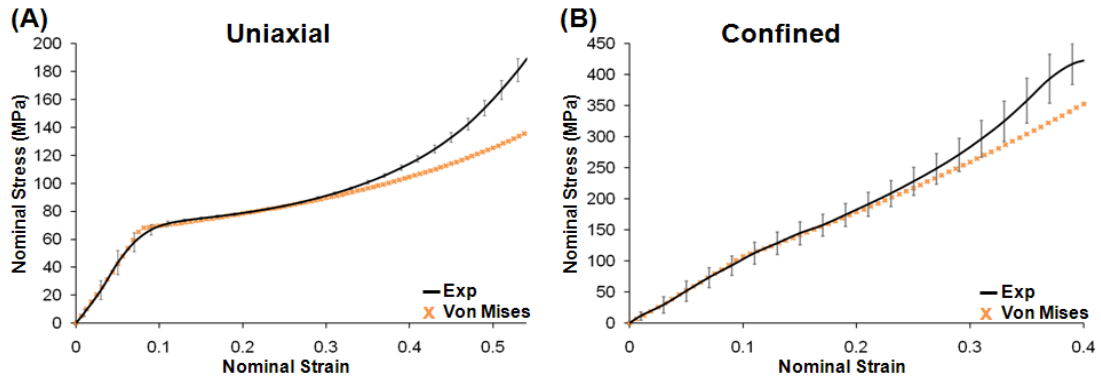

Figure 5-11 (A) Experimental and computational (von Mises plasticity) uniaxial compression testing results (mean ± SD) for grade 50 solid rigid PU foam. (B) Experimental and computational (von Mises plasticity) confined compression testing results (mean ± SD) for grade 50 solid rigid PU foam.

5.4 Discussion

The inelastic pressure dependent compressive behaviour of BTB is investigated through experimental and computational analysis. Two loading configurations are implemented, uniaxial and confined compression, providing two distinct loading paths in the $q-p$ plane. Experimental results reveal distinctive yielding followed by a constant nominal stress plateau for both uniaxial and confined compression. Computational simulation of the experimental tests using the DP and MC plasticity models fails to capture the confined compression behaviour of BTB. The high pressure developed during confined compression does not result in plastic deformation using these formulations, and a near elastic response is computed. In contrast, crushable foam plasticity models provide accurate simulation of confined compression tests, with distinctive yield and plateau behaviour being predicted. The elliptical yield surfaces of these formulations in the $q-p$ plane accurately characterise the plastic behaviour of BTB. It is also demonstrated that cellular PU exhibits similar pressure dependent yield behaviour, despite having a lower stiffness and strength than trabecular bone, supporting the use of cellular PU as a biomechanical test substitute material for trabecular bone applications involving multiaxial loading.

Several attempts have been made previously to calibrate constitutive plasticity models for cortical bone under different loading conditions. The DP and MC models have been successfully calibrated for cortical bone (Mercer et al. 2006; Mullins et al. 2009; Tai et al. 2006). Using the MC model for cortical bone Tai et al. (2006) calibrated a friction angle of 15°. Mullins et al. (2009) and Mercer et al. (2006) calibrated the DP model for cortical bone with values of (β = 46°, K_{DP} = 1, ψ = 0°) and (β = 43.5°, K_{DP} = 1) respectively. Few plasticity models have been calibrated for trabecular bone. Wang et al. (2008) calibrated the MC model with a friction angle of 12.9° for canine vertebral trabecular bone. However, this nanoindentation study probed individual trabeculae and is not reflective of the macroscale inelastic behaviour of the porous trabecular bone structure. To our knowledge the present study is the first attempt to characterise the pressure dependent yield behaviour of trabecular bone. We demonstrate that for DP and MC plasticity sufficient yielding is prevented at higher pressures in confined compression. In contrast, the crushable foam models better represent the inelastic behaviour of cellular PU and BTB,

predicting a plateau region post yield for confined compression due to significant pressure dependent yielding. Results suggest that a ratio of uniaxial to hydrostatic yield stress K = 1 provides a good fit for BTB, with a slightly lower ratio being computed for cellular PU (K = 0.7), indicating the importance of modelling pressure dependent yield for both materials (K = 0 represents a standard von Mises type plasticity formulation). For the crushable foam models considered in the present study the computed plateau stress at high levels of deformation in the confined compression tests is lower than that observed experimentally. This suggests that a crushable foam plasticity model in which the ratio of uniaxial to pressure yield stress changes with plastic strain may provide further improvements in accuracy. The CFI and CFV plasticity models have previously been applied to cellular foams (Flores-Johnson et al. 2008; Rizov et al. 2005), however to our knowledge they have never been applied to trabecular bone.

Strain-based plasticity models that neglect pressure dependent yield, have been developed and implemented for trabecular bone (Cowin and He 2005) and cortical bone (Natali et al. 2008). There are plausible reasons for adopting strain based yield criterion for trabecular bone given the experimental evidence that within an anatomic site trabecular bone yield strains are more constant than the corresponding yield stresses and Young's moduli site (Chang et al. 1999; Morgan and Keaveny 2001). Based on the anisotropic elastic characterisation of trabecular bone by van Rietbergen et al. (1996, 1998), Cowin and He (2005) proposed a yield criterion based on a uniform yield stress, i.e. an anisotropic yield stress is determined from the elastic constants. A multiaxial strain-based criterion proposed by Natali et al. (2008) has been applied to cortical bone and uses an effective strain quantity to define a yield criterion. This effective strain is a strain-based version of the von Mises stress, so is constructed from the deviatoric strain tensor. It is important to note that, similar to von Mises plasticity, this yield criterion does not allow for any yielding due to volumetric strain (strain based criterion) or hydrostatic stress (stress based criterion). Based on the results of the present study under confined compression, we have demonstrated that yielding associated with hydrostatic stress or volumetric strain is an essential feature of the inelastic behaviour of trabecular bone. Based on the encouraging application of crushable foam models to trabecular bone in the current study, coupled with previous experimental evidence of consistent strain for

trabecular bone within anatomic site, the authors suggest that future work should entail the development of a multiaxial strain based yield criterion that includes yield due volumetric strain for trabecular bone. However further extensive multiaxial experimental tests under different q/p ratios will be required to develop such a yield criterion.

Solid PU and cellular PU are commonly used to synthesise trabecular bone for the biomechanical testing of implants (Agneskirchner et al. 2006; Poukalova et al. 2010). An accurate representation of its elasto-plastic behaviour is essential in assessing its suitability as a test material substitute for trabecular bone for applications in which large deformation occurs (e.g. bone fracture, press-fit implantation in total joint arthroplasty). The cellular PU exhibits similar pressure dependent yield behaviour to BTB, despite this density of foam having a lower Young's modulus and uniaxial yield stress than BTB. However, qualitatively similar elasto-plastic behaviour is observed for cellular PU and BTB with flat plateau regions evident under confined compression. In stark contrast to the cellular PU and BTB, the solid PU does not display pressure dependent yield in confined compression due to its near solid structure. A simple von Mises perfectly plastic material model, in which yielding is independent of hydrostatic stress, predicts the solid PU uniaxial and confined data very well. The results of the present study demonstrate the influence of the cellular PU structure in replicating the inelastic behaviour of trabecular bone under confined compression.

Previous studies have primarily relied on uniaxial testing to characterise elastic properties of trabecular bone (Goldstein 1987; Kopperdahl and Keaveny 1998; Røhl et al. 1991) and PU trabecular bone analogue (Calvert et al. 2010; Johnson and Keller 2008; Patel et al. 2008; Thompson et al. 2003). In terms of elastic properties, the mean Young's modulus of grade 20 cellular PU measured in this study (141.3 MPa) is very close to the value of 137 MPa reported by the manufacturer and in previous studies (Patel et al. 2008; Thompson et al. 2003). Regarding trabecular bone, previous studies reported a similar mean (485 ± 333 MPa) and range (1.4-552 MPa) of Young's modulus values for human proximal tibial trabecular bone (Goldstein 1987; Kopperdahl and Keaveny 1998; Røhl et al. 1991). Our BTB yield stress of 13.2 ± 3.6 MPa is comparable with reported values by Morgan and Keaveny (2001) for the human proximal tibia (5.83 ± 3.42 MPa) and femoral neck

(17.45 ± 6.15 MPa). Our measured BTB elastic Poisson's ratio is within the range reported for the human proximal tibia of 0.07-0.65 (Klever et al. 1985). The large experimental standard deviations reported are in line with previous uniaxial compressive testing of trabecular bone (Kopperdahl and Keaveny 1998; Morgan and Keaveny 2001; Røhl et al. 1991). Larger standard deviations exist for BTB than PU which is attributed to the inherent inconsistent properties of trabecular bone. The BTB specimens were taken from a single bovine tibia from the same anatomical location (proximal tibia) and were tested along their principal loading axis. Despite this, variation in the structural conformation of specimens is likely to have contributed to the scatter evident in the experimental results. Morgan and Keaveny (2001) performed on-axis uniaxial compression testing on trabecular bone specimens from the vertebrae, proximal tibia, femoral neck and greater trochanter and measured a large scatter in data for the different anatomical locations and within anatomical site. Material properties measured from uniaxial compressive testing of proximal tibial trabecular specimens taken from various locations can vary by up to two orders of magnitude (Goldstein et al. 1983). In the present study, testing multiple specimens from the proximal tibial accounted for the inherent biological heterogeneity of trabecular bone within a single anatomic site. Although the cellular PU and BTB have a similar cellular structure, there are some distinct differences between the two materials. In addition to the lack of bone marrow, closed cell PU foams lack the open cell structure of trabecular bone. Despite such differences, qualitatively similar stress-strain curves are evident for the two cellular materials under both loading modes.

Very few studies have considered the confined compression behaviour of trabecular bone (Charlebois et al. 2010b; Linde and Hvid 1989) despite the fact that this loading mode is physiologically relevant, given that *in vivo* trabecular bone is confined by a stiff cortical shell. The studies of Gibson (2005) and Szivek et al. (1993) reported the three phase uniaxial stress-strain behaviour of trabecular bone but did not implement confined compression testing. Charlebois et al. (2010b) performed an investigation of the role of morphological measures determined from micro computed tomography (μCT) scans, namely volume fraction and a fabric tensor, in the elastic and post yield behaviour of trabecular bone under uniaxial and confined conditions. An earlier study Linde and Hvid (1989) investigated the elastic

behaviour of trabecular bone using both uniaxial and confined compression testing, however plasticity was not considered. Due to the lack of experimental data, the confined compression results could not be compared to previous studies.

Like cellular foams, the failure mechanisms of trabecular bone are highly influenced by its cellular structure. The combination of rod and plate like trabeculae as well as the horizontal and vertical composition vary with anatomic site and are affected by numerous factors. Gibson (1985) proposed three failure modes for cellular solids: elastic buckling; plastic hinging; brittle fracture. Under progressive compressive loading cellular materials absorb large amounts of energy and the trabeculae undergo a combination of these failure modes simultaneously. While slender rod like trabeculae may be buckling, stouter rod or plate like trabeculae may be yielding. Micro-compression tests have predicted the failure of rod like trabeculae to occur due to bending and buckling which is followed by trabecula collapse when overloaded (Müller et al. 1998). Bending or buckling was not predicted for plate-like trabeculae and instantaneous failure occurred (Müller et al. 1998). An experimental and numerical investigation by Deshpande and Fleck (2000) showed a pressure dependent yield in the yield surface of open cell and closed cell metallic foams. Using the crushable foam model developed by Deshpande and Fleck (2000) to represent the crushing and buckling behaviour of cellular foams, the present study uncovered similar pressure dependent yield behaviour for BTB and cellular PU in confined compression.

The intrinsic material properties and structural composition of trabeculae play a fundamental role in trabecular bone failure mechanisms. Macroscale inelastic continuum material models have been proposed that represent the trabecular bone morphology (Charlebois et al. 2010a; Rincon-Kohli and Zysset 2009; Zysset and Rincon-Kohli 2006; Zysset and Curnier 1996) where fabric based tensors and volume fraction describe the material heterogeneity and anisotropy respectively. Such models include information on the structural conformation of the trabeculae from the analysis of 3D reconstructions. However, the importance of pressure dependent yield has not been considered. Microarchitecture based FE models, based on high resolution images such as μCT data, explicitly represent individual trabecular geometries (Bayraktar et al. 2004; Guillén et al. 2011; Harrison and McHugh 2010; Mc Donnell et al. 2010; Niebur et al. 2002; Niebur et al. 2000).

Niebur et al. (2002) performed biaxial testing and investigated the influence of the trabecular structure on yield. Similar to other studies (Bayraktar et al. 2004; Guillén et al. 2011; Niebur et al. 2000), a bilinear asymmetric material model that neglects pressure dependent yield was used to describe the yield behaviour. These bilinear models offer limited capability of matching the post yield behaviour as they rely on a reduction of the material stiffness post yield to 5% when the critical principal strain is exceeded, an assumption that is based on post yield testing of cortical bone specimens. The microscale pressure dependent yield behaviour of trabecular bone could not be exposed due to the constant q/p ratio for all simulations. Such microstructural based FE models require considerable effort in relation to mesh generation and computational expense which limits their use for macroscale trabecular bone applications. However, the present continuum approach provides a phenomenological representation of the mechanical response due to the buckling and crushing of trabeculae that does not depend on the structural conformation of the material. In addition to the uniaxial testing already performed, further multiaxial testing in confined compression is required to phenomenologically capture the relationship between trabecular bone microarchitecture and multiaxial plastic deformation. Such testing as well as high resolution imaging of trabecular specimens would allow for the development of more sophisticated continuum models that incorporate microstructural descriptors.

Trabecular bone has an aligned composite porous microstructure and is both inhomogeneous and anisotropic (Hodgskinson and Currey 1990; Townsend et al. 1975; Williams and Lewis 1982). Solely on-axis uniaxial and confined compression testing was performed for BTB therefore the anisotropy of the trabecular specimens could not be determined. A significant limitation of the present study is that trabecular bone is modelled as an isotropic material. The current study took a significant step in uncovering the pressure dependent yield behaviour of trabecular bone at the macroscale. We demonstrate that crushable foam plasticity models with elliptical yield surfaces in the $q-p$ plane capture this behaviour reasonably well. Although not tested in the present study, it is expected that a similar pressure dependent yield should occur regardless of the direction of loading, following from the fact that pressure is a stress invariant. However an extensive series of uniaxial, multiaxial and confined compression testing must be performed on trabecular bone

to uncover the manner in which the ratio of uniaxial to pressure dependent yield should vary as a function of the material anisotropy. Pressure increase under confined compression is a function of Poisson's ratio, which will depend on the loading direction for an anisotropic material. Follow on studies should involve the extension of the phenomenological CFI and CFV models to include additional features such as material anisotropy and trabecular architecture.

A number of limitations and sources of error should be noted for the present study. The accuracy of the experimental testing directly influences the results obtained. As trabecular bone is naturally confined by cortical bone, confined compression testing was performed as an approximation of the *in vivo* situation. Purely hydrostatic loading would have been desirable and may be investigated in a future study. BTB was used over cadaveric specimens for its similarity to human trabecular bone. The focus of this study was on the inelastic behaviour of trabecular bone and it is expected that similar pressure dependent yield behaviour would be evident for cadaveric specimens taken from various anatomical locations. Standard experimental errors due to friction, damage and machine compliance have been previously reported for compression testing of trabecular bone and should be noted in the present study also (Keaveny et al. 1993a, 1993b; Linde and Hvid 1989; Linde et al. 1992; Odgaard and Linde 1991). Although unavoidable for the test methods employed damage artifacts due to specimen machining interrupting the natural trabecular network have also been previously reported (Keaveny et al. 1997; Linde et al. 1992; Odgaard and Linde 1991). Additionally frictional artifacts at the compression platens represent a further source of test error (Brown and Ferguson 1980; Odgaard and Linde 1991). Errors due to specimen alignment with the platens, pre-existing specimen damage and off-axis specimens would have also induced approximations in the experimental results. Due care was taken during the preparation, alignment and testing of all specimens to minimise any possible errors. No creep recovery was observed following load removal, indicating that viscoelasticity is not a dominant mechanism. All testing was performed at a constant strain rate, eliminating the introduction of any strain rate sensitivity in the yield behaviour. Although not investigated, strain rate effects have been shown to influence trabecular bone compressive behaviour (Galante et al. 1970; Linde et al. 1991). Further experimental testing and application of the CFI and CFV material

models to trabecular bone loading at various strain rates is desirable. Damage models were not investigated but may be able to capture the inelastic behaviour observed experimentally for BTB. We suggest that, similar to the yield function in the CF plasticity models, an appropriate damage model should include a damage component driven by hydrostatic stress.

Whole bone fracture, the implantation of press-fit devices and subsidence of prostheses involve multiaxial loading and inelastic deformation that lead to significant hydrostatic stresses due to naturally confined nature of trabecular bone. The findings of the present study will allow for improved prediction of trabecular bone plasticity in such a complex environment.

5.5 Conclusions

In order to investigate the inelastic behaviour of trabecular bone both uniaxial and confined compression were performed, representing two different loading paths in the $q-p$ plane and elucidating for the first time the pressure dependent yield behaviour. An assessment of established plasticity constitutive formulations revealed that trabecular bone is best represented by an elliptical yield surface in the $q-p$ plane, characteristic of crushable foam plasticity. In contrast, plasticity models typically used for cortical bone, such as the DP or MC formulations are unsuitable for trabecular bone, given that a pressure increase leads to a reduced plastic deformation in such models. We also demonstrate that cellular PU synthetic bone analogue exhibits similar pressure dependent yield behaviour to trabecular bone, despite having a lower strength and stiffness. In contrast, solid PU does not exhibit pressure dependent yield in confined compression due to its near solid structure. The enhanced understanding of the inelastic behaviour of trabecular bone provided by this study will allow for more realistic simulation of the performance of implant devices. Specifically, ongoing work entails further experimental testing and model development to assess the inelastic deformation of trabecular bone during the implantation of press-fit total arthroplasty components.

Appendix A

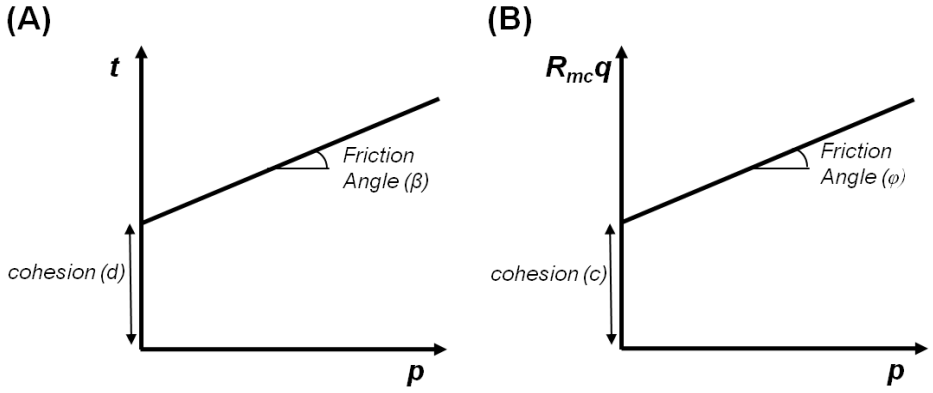

Figure 5-12 (A) Drucker-Prager yield criterion. (B) Mohr-Coulomb yield criterion.

Appendix B Supplementary Data to Journal Publication

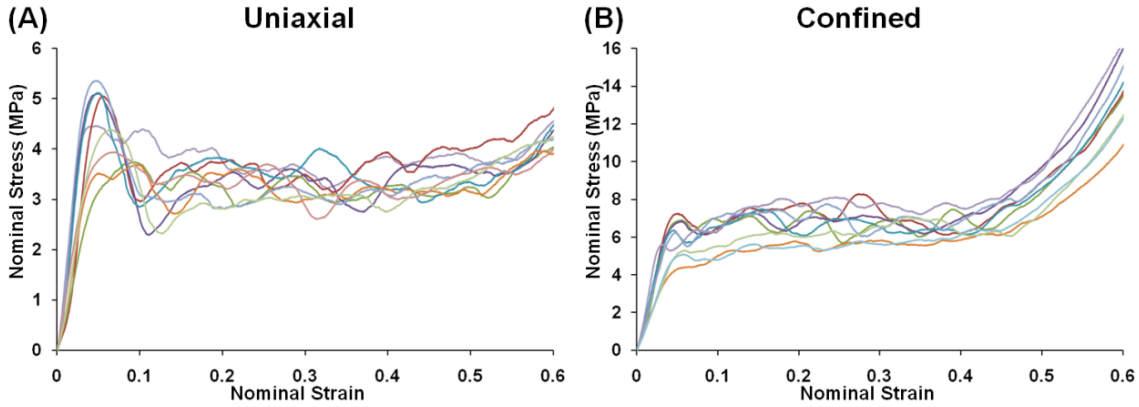

Figure 5-13 Grade 20 cellular rigid polyurethane foam experimental results: (A) uniaxial compression; (B) confined compression.

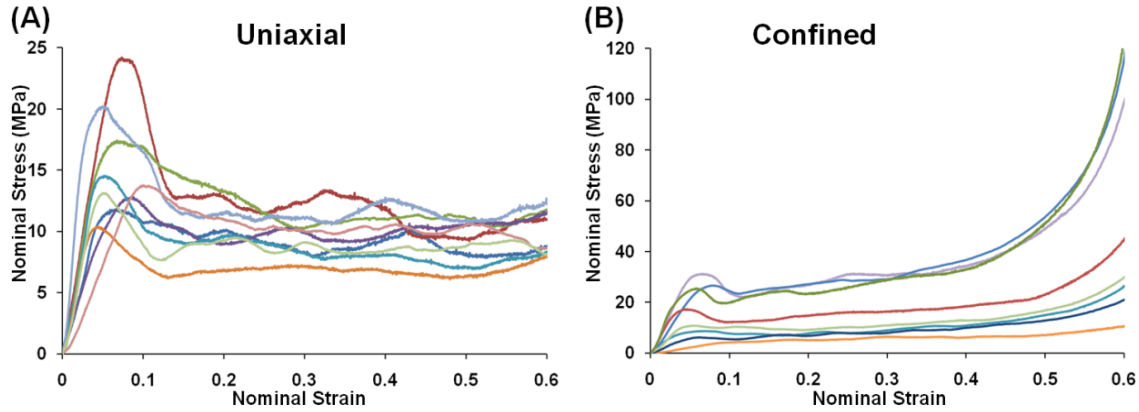

Figure 5-14 Bovine trabecular bone experimental results: (A) uniaxial compression; (B) confined compression.

Appendix C

For an isotropic material the material properties are independent of direction and have only two independent variables (elastic constants) which can be expressed in terms of E and v_e. Hooke's Law for an isotropic material can be expressed in terms of the two elastic constants, Young's modulus, E, and elastic Poisson's ratio, ν_e, as

$$\boldsymbol{\varepsilon} = \frac{1}{\mathrm{E}}\boldsymbol{\sigma} - \frac{\nu_e}{\mathrm{E}}(trace(\boldsymbol{\sigma})\mathbf{I} - \boldsymbol{\sigma}) \quad 5.1$$

where $\boldsymbol{\varepsilon}$ is the strain tensor, $\boldsymbol{\sigma}$ is the stress tensor and $\mathbf{I}$ is the identity matrix.

In expanded form

$$\varepsilon_{11} = \frac{1}{\mathrm{E}}(\sigma_{11} - \nu_e(\sigma_{22} + \sigma_{33})) \quad 5.2$$

$$\varepsilon_{22} = \frac{1}{\mathrm{E}}(\sigma_{22} - \nu_e(\sigma_{11} + \sigma_{33})) \quad 5.3$$

$$\varepsilon_{33} = \frac{1}{\mathrm{E}}(\sigma_{33} - \nu_e(\sigma_{11} + \sigma_{22})) \quad 5.4$$

$$\varepsilon_{12} = \frac{1}{2\mathrm{G}}\sigma_{12} \quad 5.5$$

$$\varepsilon_{13} = \frac{1}{2\mathrm{G}}\sigma_{13} \quad 5.6$$

$$\varepsilon_{23} = \frac{1}{2\mathrm{G}}\sigma_{23} \quad 5.7$$

Under confined compression loading three principal stress components exist $(\sigma_{11}, \sigma_{22}, \sigma_{33})$. Under an axial load (3 direction) where lateral deformation is prevented in the other two directions $(1, 2)$ whereby

$$\varepsilon_{11} = \varepsilon_{22} = 0 \quad 5.8$$

$$\sigma_{11} = \sigma_{22} \quad 5.9$$

and no shear components exist

$$\varepsilon_{12} = \varepsilon_{13} = \varepsilon_{23} = 0 \quad 5.10$$

$$\sigma_{11} = \frac{\nu_e \sigma_{33}}{1 - \nu_e} \quad 5.11$$

Confined compression expressed in terms of the von Mises equivalent stress, q and the hydrostatic stress, p, as

$$p = -\frac{\sigma_{33}}{3}\left(\frac{1+\nu_e}{1-\nu_e}\right) \quad 5.12$$

$$q = \sigma_{33}\left(\frac{2\nu_e - 1}{1-\nu_e}\right) \quad 5.13$$

Therefore the ratio of von Mises equivalent stress, q, to hydrostatic stress, p, as a function of ν_e is

$$\frac{q}{p} = \frac{3(1-2\nu_e)}{1+\nu_e} \quad 5.14$$

5.6 References

Adam, C. J., Swain, M. V. (2011) The effect of friction on indenter force and pile-up in numerical simulations of bone nanoindentation. J Mech Behav Biomed Mater 4 (7):1554-1558.

Agneskirchner, J., Freiling, D., Hurschler, C., Lobenhoffer, P. (2006) Primary stability of four different implants for opening wedge high tibial osteotomy. Knee Surg Sports Traumatol Arthrosc 14 (3):291-300.

ASTM (2008) Standard specification for rigid polyurethane foam for use as a standard material for testing orthopaedic devices and instruments. ASTM F1839-01. Pennsylvania.

Bayraktar, H. H., Gupta, A., Kwon, R. Y., Papadopoulos, P., Keaveny, T. M. (2004) The modified super-ellipsoid yield criterion for human trabecular bone. J Biomech Eng 126 (6):677-684.

Bayraktar, H. H., Keaveny, T. M. (2004) Mechanisms of uniformity of yield strains for trabecular bone. J Biomech 37 (11):1671-1678.

Bessho, M., Ohnishi, I., Matsuyama, J., Matsumoto, T., Imai, K., Nakamura, K. (2007) Prediction of strength and strain of the proximal femur by a ct-based finite element method. J Biomech 40 (8):1745-1753.

Brown, T. D., Ferguson, A. B. (1980) Mechanical property distributions in the cancellous bone of the human proximal femur. Acta Orthop 51 (1-6):429-437.

Calvert, K. L., Trumble, K. P., Webster, T. J., Kirkpatrick, L. A. (2010) Characterization of commercial rigid polyurethane foams used as bone analogs for implant testing. J Mater Sci: Mater Med 21 (5):1453-1461.

Carnelli, D., Gastaldi, D., Sassi, V., Contro, R., Ortiz, C., Vena, P. (2010) A finite element model for direction-dependent mechanical response to nanoindentation of cortical bone allowing for anisotropic post-yield behavior of the tissue. J Biomech Eng 132:1-10.

Carnelli, D., Lucchini, R., Ponzoni, M., Contro, R., Vena, P. (2011) Nanoindentation testing and finite element simulations of cortical bone allowing for anisotropic elastic and inelastic mechanical response. J Biomech 44 (10):1852-1858.

Chang, W. C. W., Christensen, T. M., Pinilla, T. P., Keaveny, T. M. (1999) Uniaxial yield strains for bovine trabecular bone are isotropic and asymmetric. J Orthop Res 17 (4):582-585.

Charlebois, M., Jirasek, M., Zysset, P. K. (2010a) A nonlocal constitutive model for trabecular bone softening in compression. Biomech Model Mechanobiol 9 (5):597-611.

Charlebois, M., Pretterklieber, M., Zysset, P. K. (2010b) The role of fabric in the large strain compressive behavior of human trabecular bone. J Biomech Eng 132:1-10.

Cowin, S. C., He, Q. C. (2005) Tensile and compressive stress yield criteria for cancellous bone. J Biomech 38 (1):141-144.

Deshpande, V. S., Fleck, N. A. (2000) Isotropic constitutive models for metallic foams. J Mech Phys Solids 48 (6-7):1253-1283.

Drucker, D. C., Prager, W. (1951) Soil mechanics and plastic analysis or limit design. Division of Applied Mathematics, Brown University, Brown University. Division of Applied, Mathematics United States. Office of Naval, Research.

Flores-Johnson, E. A., Li, Q. M., Mines, R. A. W. (2008) Degradation of elastic modulus of progressively crushable foams in uniaxial compression. J Cell Plast 44 (5):415.

Galante, J., Rostoker, W., Ray, R. D. (1970) Physical properties of trabecular bone. Calcif Tissue Int 5 (1):236-246.

Gibson, L. J. (1985) The mechanical behaviour of cancellous bone. J Biomech 18 (5):317-328.

Gibson, L. J. (2005) Biomechanics of cellular solids. J Biomech 38 (3):377-399.

Goldstein, S. A. (1987) The mechanical properties of trabecular bone: Dependence on anatomic location and function. J Biomech 20 (11-12):1055-1061.

Goldstein, S. A., Wilson, D. L., Sonstegard, D. A., Matthews, L. S. (1983) The mechanical properties of human tibial trabecular bone as a function of metaphyseal location. J Biomech 16 (12):965-969.

Guillén, T., Zhang, Q. H., Tozzi, G., Ohrndorf, A., Christ, H. J., Tong, J. (2011) Compressive behaviour of bovine cancellous bone and bone analogous materials, microct characterisation and fe analysis. J Mech Behav Biomed Mater 4 (7):1452-1461.

Harrison, N., McHugh, P. (2010) Comparison of trabecular bone behavior in core and whole bone samples using high-resolution modeling of a vertebral body. Biomech Model Mechanobiol 9 (4):469-480.

Harrison, N. M., McDonnell, P. F., O'Mahoney, D. C., Kennedy, O. D., O'Brien, F. J., McHugh, P. E. (2008) Heterogeneous linear elastic trabecular bone modelling using micro-ct attenuation data and experimentally measured heterogeneous tissue properties. J Biomech 41 (11):2589-2596.

Hodgskinson, R., Currey, J. D. (1990) The effect of variation in structure on the young's modulus of cancellous bone: A comparison of human and non human material. Proc Inst Mech Eng 204 (28):115-121.

Johnson, A. E., Keller, T. S. (2008) Mechanical properties of open-cell foam synthetic thoracic vertebrae. J Mater Sci: Mater Med 19 (3):1317-1323.

Keaveny, T. M., Borchers, R. E., Gibson, L. J., Hayes, W. C. (1993a) Theoretical analysis of the experimental artifact in trabecular bone compressive modulus. J Biomech 26 (4-5):599-607.

Keaveny, T. M., Borchers, R. E., Gibson, L. J., Hayes, W. C. (1993b) Trabecular bone modulus and strength can depend on specimen geometry. J Biomech 26 (8):991-1000.

Keaveny, T. M., Morgan, E. F., Niebur, G. L., Yeh, O. C. (2001) Biomechanics of trabecular bone. Annu Rev Biomed Eng 3 (1):307-333.

Keaveny, T. M., Pinilla, T. P., Crawford, P. R., Kopperdahl, D. L., Lou, A. (1997) Systematic and random errors in compression testing of trabecular bone. J Orthop Res 15 (1):101-110.

Keaveny, T. M., Wachtel, E. F., Kopperdahl, D. L. (1999) Mechanical behavior of human trabecular bone after overloading. J Orthop Res 17 (3):346-353.

Keyak, J. H. (2001) Improved prediction of proximal femoral fracture load using nonlinear finite element models. Med Eng Phys 23 (3):165-173.

Keyak, J. H., Rossi, S. A. (2000) Prediction of femoral fracture load using finite element models: An examination of stress- and strain-based failure theories. J Biomech 33 (2):209-214.

Klever, F. J., Klumpert, R., Grootenboer, H. J., van Campen, D. H., Pauly, T. (eds) (1985) Global mechanical properties of trabecular bone: Experimental determination and prediction from a structural model. Biomechanics: Current interdisciplinary research. Martinus Nijhoff, Dordrecht.

Kopperdahl, D. L., Keaveny, T. M. (1998) Yield strain behavior of trabecular bone. J Biomech 31 (7):601-608.

Linde, F. (1994) Elastic and viscoelastic properties of trabecular bone by a compression testing approach. Dan Med Bull 41 (2):119.

Linde, F., Hvid, I. (1989) The effect of constraint on the mechanical behaviour of trabecular bone specimens. J Biomech 22 (5):485-490.

Linde, F., Hvid, I., Madsen, F. (1992) The effect of specimen geometry on the mechanical behaviour of trabecular bone specimens. J Biomech 25 (4):359-368.

Linde, F., Norgaard, P., Hvid, I., Odgaard, A., Soballe, K. (1991) Mechanical properties of trabecular bone. Dependency on strain rate. J Biomech 24 (9):803-809.

Lotz, J. C., Cheal, E. J., Hayes, W. C. (1991) Fracture prediction for the proximal femur using finite element models: Part i—linear analysis. J Biomech Eng 113:353.

Mc Donnell, P., Harrison, N., Liebschner, M. A. K., Mc Hugh, P. E. (2009) Simulation of vertebral trabecular bone loss using voxel finite element analysis. J Biomech 42 (16):2789-2796.

Mc Donnell, P., Harrison, N., McHugh, P. E. (2010) Investigation of the failure behaviour of vertebral trabecular architectures under uni-axial compression and wedge action loading conditions. Med Eng Phys 32 (6):569-576.

Mercer, C., He, M. Y., Wang, R., Evans, A. G. (2006) Mechanisms governing the inelastic deformation of cortical bone and application to trabecular bone. Acta Biomater 2 (1):59-68.

Moore, T. L. A., Gibson, L. J. (2002) Microdamage accumulation in bovine trabecular bone in uniaxial compression. J Biomech Eng 124 (1):63-71.

Morgan, E. F., Bayraktar, H. H., Keaveny, T. M. (2003) Trabecular bone modulus-density relationships depend on anatomic site. J Biomech 36 (7):897-904.

Morgan, E. F., Keaveny, T. M. (2001) Dependence of yield strain of human trabecular bone on anatomic site. J Biomech 34 (5):569-577.

Müller, R., Gerber, S. C., Hayes, W. C. (1998) Micro-compression: A novel technique for the nondestructive assessment of local bone failure. Technol Health Care 6 (5-6):433-444.

Mullins, L. P., Bruzzi, M. S., McHugh, P. E. (2009) Calibration of a constitutive model for the post-yield behaviour of cortical bone. J Mech Behav Biomed Mater 2 (5):460-470.

Natali, A. N., Carniel, E. L., Pavan, P. G. (2008) Constitutive modelling of inelastic behaviour of cortical bone. 30 (7):905-912.

Neilsen, M. K., Krieg, R. D., Schreyer, H. L. (1995) A constitutive theory for rigid polyurethane foam. Polym Eng Sci 35 (5):387-394.

Niebur, G. L., Feldstein, M. J., Keaveny, T. M. (2002) Biaxial failure behavior of bovine tibial trabecular bone. J Biomech Eng 124 (6):699-705.

Niebur, G. L., Feldstein, M. J., Yuen, J. C., Chen, T. J., Keaveny, T. M. (2000) High-resolution finite element models with tissue strength asymmetry accurately predict failure of trabecular bone. J Biomech 33 (12):1575-1583.

Odgaard, A., Linde, F. (1991) The underestimation of young's modulus in compressive testing of cancellous bone specimens. J Biomech 24 (8):691-698.

Patel, P. S. D., Shepherd, D. E. T., Hukins, D. W. L. (2008) Compressive properties of commercially available polyurethane foams as mechanical models for osteoporotic human cancellous bone. BMC Musculoskelet Disord 9 (1):137.

Poukalova, M., Yakacki, C. M., Guldberg, R. E., Lin, A., Saing, M., Gillogly, S. D., Gall, K. (2010) Pullout strength of suture anchors: Effect of mechanical properties of trabecular bone. J Biomech 43 (6):1138-1145.

Rincon-Kohli, L., Zysset, P. (2009) Multi-axial mechanical properties of human trabecular bone. Biomech Model Mechanobiol 8 (3):195-208.

Rizov, V., Shipsha, A., Zenkert, D. (2005) Indentation study of foam core sandwich composite panels. Comp Struct 69 (1):95-102.

Røhl, L., Larsen, E., Linde, F., Odgaard, A., Jørgensen, J. (1991) Tensile and compressive properties of cancellous bone. J Biomech 24 (12):1143-1149.

Szivek, J. A., Thomas, M., Benjamin, J. B. (1993) Technical note. Characterization of a synthetic foam as a model for human cancellous bone. J Appl Biomater 4 (3):269-272.

Tai, K., Ulm, F.-J., Ortiz, C. (2006) Nanogranular origins of the strength of bone. Nano Lett 6 (11):2520-2525.

Taylor, M., Tanner, K. E., Freeman, M. A. R. (1998) Finite element analysis of the implanted proximal tibia: A relationship between the initial cancellous bone stresses and implant migration. J Biomech 31 (4):303-310.

Thompson, M. S., McCarthy, I. D., Lidgren, L., Ryd, L. (2003) Compressive and shear properties of commercially available polyurethane foams. J Biomech Eng 125 (5):732-734.

Townsend, P. R., Raux, P., Rose, R. M., Miegel, R. E., Radin, E. L. (1975) The distribution and anisotropy of the stiffness of cancellous bone in the human patella. J Biomech 8 (6):363-364.

Turner, C. H. (1989) Yield behavior of bovine cancellous bone. J Biomech Eng 111 (3):256-260.

van Rietbergen, B., Odgaard, A., Kabel, J., Huiskes, R. (1996) Direct mechanics assessment of elastic symmetries and properties of trabecular bone architecture. J Biomech 29 (12):1653-1657.

van Rietbergen, B., Odgaard, A., Kabel, J., Huiskes, R. (1998) Relationships between bone morphology and bone elastic properties can be accurately quantified using high resolution computer reconstructions. J Orthop Res 16 (1):23-28.

Wang, X., Allen, M. R., Burr, D. B., Lavernia, E. J., Jeremic, B., Fyhrie, D. P. (2008) Identification of material parameters based on mohr-coulomb failure criterion for bisphosphonate treated canine vertebral cancellous bone. Bone 43 (4):775-780.

Williams, J. L., Lewis, J. L. (1982) Properties and an anisotropic model of cancellous bone from the proximal tibial epiphysis. J Biom Eng 104:50.

Zysset, P., Rincon-Kohli, L. (2006) An alternative fabric-based yield and failure criterion for trabecular bone. In: Holzapfel, G. A., Ogden, R. W. (eds) Mechanics of biological tissue. Springer, Berlin, pp 457-470.

Zysset, P. K., Curnier, A. (1996) A 3d damage model for trabecular bone based on fabric tensors. J Biomech 29 (12):1549-1558.

Chapter 6

An Experimental and Computational Investigation of the Post-Yield Behaviour of Trabecular Bone during Vertebral Device Subsidence

Abstract

Interbody fusion device subsidence has been reported clinically. An enhanced understanding of the mechanical behaviour of the surrounding bone would allow for accurate predictions of vertebral subsidence. The multiaxial inelastic behaviour of trabecular bone is investigated at a microscale and macroscale level. The post-yield behaviour of trabecular bone under hydrostatic and confined compression is investigated using micro-computed tomography derived microstructural models, elucidating a mechanism of pressure dependent yielding at the macroscopic level. Specifically, microstructural trabecular simulations predict a distinctive yield point in the apparent stress-strain curve under uniaxial, confined and hydrostatic compression. Such distinctive apparent stress-strain behaviour results from localised stress concentrations and material yielding in the trabecular microstructure. This phenomenon is shown to be independent of the plasticity formulation employed at a trabecular level. The distinctive response can be accurately captured by a continuum model using a crushable foam plasticity formulation in which pressure dependent yielding occurs. Vertebral device subsidence experiments are also performed, providing measurements of the trabecular plastic zone. It is demonstrated that a pressure dependent plasticity formulation must be used for continuum level macroscale models of trabecular bone in order to replicate the experimental observations, further supporting the microscale investigations. Using a crushable foam plasticity formulation in the simulation of vertebral subsidence, it is shown that the predicted subsidence force and plastic zone size correspond closely with the experimental measurements. In contrast, the use of von Mises, Drucker-Prager and Hill plasticity formulations for continuum trabecular bone models lead to over prediction of the subsidence force and plastic zone.

6.1 Introduction

Low back pain is a major health care problem, and an interbody fusion device (IFD) endeavours to replace a damaged or diseased intervertebral disc. IFDs often contain bone graft material to promote rigid fixation of the adjacent vertebrae. The metallic IFDs are significantly stiffer than the natural intervertebral disc and do not mimic the natural disc geometry. A range of IFD subsidence rates (3-76.7%) have been reported clinically (Beutler and Peppelman 2003; Chen et al. 2005; Choi and Sung 2006). The vertebral endplates, the superior and inferior surfaces of the vertebral body, are composed of cortical bone. Various IFD designs require different bony endplate preparation techniques: intact; partial removal; complete removal. Removal of the stiffer cortical endplate exposes a host bed of bleeding trabecular bone (potentially osteogenic cells) which is advantageous from a biological point of view allowing bone fusion with the graft material. A number of *in vitro* investigations into the effect of endplate removal on the vertebral subsidence force have provided conflicting recommendations including endplate preservation (Lim et al. 2001; Oxland et al. 2003); partial endplate removal (Lowe et al. 2004; Steffen et al. 2000); and complete endplate removal (Closkey et al. 1993; Hollowell et al. 1996). Regardless of the endplate preparation technique, the insertion of a stiff metallic IFD will induce significant stress concentrations in the surrounding bone. An enhanced understanding of the mechanical behaviour of the surrounding bone would allow for accurate predictions of vertebral subsidence, ultimately leading to improved IFD design and a reduced risk of subsidence.

The present study investigates vertebral device subsidence into the underlying trabecular bone that entails finite deformation and inelastic material behaviour. A complex stress state occurs due to the natural confinement of trabecular bone by a stiff cortical shell leading to significant pressure stress and large inelastic deformation. This suggests that it is essential to correctly model the multiaxial yield behaviour of trabecular bone to accurately predict subsidence. The importance of using an appropriate continuum constitutive plasticity formulation for an accurate prediction of the macroscale plastic deformation of trabecular bone during vertebral subsidence is, therefore, investigated.

To characterise the mechanical properties of trabecular bone, previous studies have primarily relied on uniaxial compression testing of representative samples of trabecular bone (Goldstein 1987; Keaveny et al. 1993; Keyak et al. 1996; Kopperdahl and Keaveny 1998; Morgan and Keaveny 2001; Røhl et al. 1991). Few studies have performed confined compression testing (Charlebois et al. 2010b; Linde and Hvid 1989) or multiaxial compression testing (Fenech and Keaveny 1999; Keaveny et al. 1999; Rincon-Kohli and Zysset 2009) although trabecular bone is naturally constrained *in vivo* by the surrounding cortex. Complex loading configurations such as hydrostatic and confined compression, which involve the development of high trabecular pressures, should be considered to elucidate the multiaxial yield behaviour of trabecular bone. Recently published experiments demonstrate that confined compression (Charlebois et al. 2010b) and multiaxial compression (Rincon-Kohli and Zysset 2009) loading of trabecular bone lead to apparent stress-strain curves that exhibit a distinctive yield point. Further, in Chapter 5 it is demonstrated that simulation of this apparent response to confined compression using a continuum model requires the use of a pressure dependent yield formulation (i.e., a formulation in which a purely hydrostatic stress state can result in material yielding, unlike the conventional pressure independent von Mises (VM) plasticity formulation).

In addition to the macroscale investigation of vertebral subsidence, a microstructural analysis of trabecular bone plasticity is also performed. Micro-computed tomography (μCT) based finite element (FE) models provide an accurate representation of the trabecular microarchitecture, however, due to high computational expense they are usually limited in terms of contact conditions, material behaviour and deformation. The use of microstructural models of representative trabecular bone samples to elucidate the inelastic behaviour can lead to the development of accurate continuum models, as demonstrated in the present study which may be used for macroscale applications with complex boundary and contact conditions, finite deformation and non-linear material behaviour.

Using microstructural voxel based trabecular geometry with linear elastic material models, several studies have simulated the response of representative samples of trabecular bone to uniaxial compression (Harrison et al. 2008; Müller and Rüegsegger 1995; Nagaraja et al. 2005; Van Rietbergen et al. 1995). A number of

studies have simulated non-linear trabecular behaviour by reducing the elastic modulus of the trabecular material when the principal strain at a material point exceeds a predefined value (Bayraktar et al. 2004; Bayraktar and Keaveny 2004; Guillén et al. 2011; Niebur et al. 2002; Niebur et al. 2000; Verhulp et al. 2008). Verhulp et al. (2008) simulated uniaxial compression using μCT based trabecular geometry with a perfectly-plastic VM plasticity formulation, while Harrison et al. (2012) simulated material damage and fracture in the trabecular microarchitecture, also under uniaxial compression. Apart from the studies of Niebur et al. (2002) and Bayraktar et al. (2004), in which biaxial (triaxial stress) and axial-shear testing was simulated using the principal strain based modulus reduction model, none of these μCT studies has investigated the role of microstructural architecture in the multiaxial yielding of trabecular bone at the apparent level by considering loading configurations other than uniaxial compression. Van Rietbergen et al. (1995) and Boyd et al. (2002) considered confined compression of microstructural trabecular specimens, which were restricted to the elastic regime with maximum apparent strains of 1%, again assuming linear elastic material behaviour.

The present study provides a link between the microscale (trabeculae) and macroscale inelastic behaviour of trabecular bone. The first objective of the study is to implement uniaxial, hydrostatic and confined compression for microstructural based models of a representative sample of the trabecular bone microstructure in order to predict multiaxial apparent yield behaviour. Specifically, the following issue is investigated: if a pressure independent plasticity formulation is used to represent the material behaviour of individual trabeculae in a μCT model, will the predicted apparent stress-strain curves for hydrostatic and confined compression exhibit distinctive yielding? The second objective is to investigate the importance of using an appropriate continuum constitutive plasticity formulation for an accurate prediction of the macroscale plastic deformation of trabecular bone in order to accurately simulate the experimental subsidence of a vertebral IFD.

6.2 Methods

To reflect the two aforementioned objectives of the study, the materials and methods are separated into two distinct parts. Part A describes the creation of the μCT based models and the implementation of apparent level uniaxial, hydrostatic and confined compression loading configurations. Part B describes the experimental vertebral subsidence testing and the development of macroscale models to replicate the experiments.

6.2.1 Part A - Computational Modelling of a Trabecular Bone Sample

In order to investigate the roles of trabecular bone microstructure on apparent yielding, 3D 8 mm cube FE models of the trabecular bone microstructure were created from a lumbar ovine vertebra obtained from the PRTLI 'Bone for Life' project (Prendergast and McHugh 2004) using μCT images at 72 μm resolution (μCT 40, Scanco Medical AG, Basserdorf, Switzerland) consisting of approximately 270,000 four noded tetrahedral elements (v14.11 Mimics and v6.0 3matic, Materialise, Leuven, Belgium) (Figure 6-1). An elastic perfectly-plastic VM plasticity formulation was implemented, which does not include any pressure dependent yielding in the trabecular material. Three different simulations were performed: uniaxial compression; hydrostatic compression; confined compression. The tests were simulated in the superior-inferior direction where the specimens were oriented parallel to the axis of loading (on-axis). Apparent stress-strain curves were created for each loading configuration. The simulations investigated whether apparent yielding of trabecular bone (as demonstrated in Chapter 5) can be captured using a simple VM plasticity formulation in addition to an explicit representation of the trabecular bone microarchitecture. Simulations were also performed in which the Drucker-Prager (DP) plasticity formulation was used to model the trabecular material. Based on nanoindentation results from individual ovine vertebral trabeculae (Harrison et al. 2008), a local trabecular tissue Young's modulus (E_{LOC}) of 4 GPa was assumed. A local trabecular yield stress (σ_{yLOC}) of 66 MPa and elastic Poisson's ratio (v_e) of 0.3 were also assumed (Harrison et al. 2008). Symmetric boundary conditions were imposed at the apparent level to simulate each loading configuration ensuring the specimen edges remained planar during loading and each model was loaded to 5% apparent strain (v6.11 Abaqus Standard, Dassault Systémes Simulia Corp. Providence, RI).

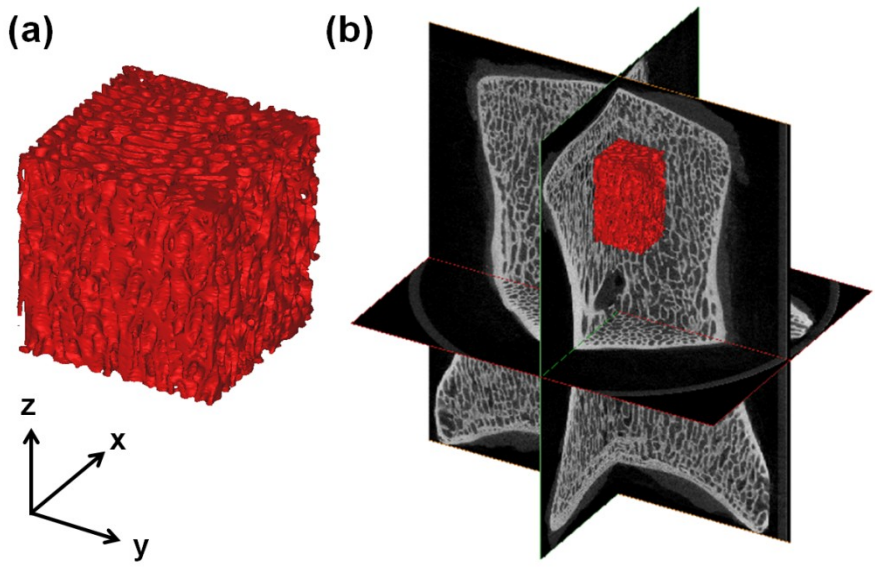

Figure 6-1 (a) 8 mm trabecular bone µCT based cube model. The z-direction is the superior-inferior (on-axis) loading direction. (b) L6 vertebra with the 8 mm cube of trabecular bone taken from the superior region of the vertebra.

In addition to µCT models, continuum models of the trabecular bone were also investigated in order to replicate the material behaviour. Uniaxial, confined and hydrostatic compression loading were implemented to 5% apparent strain, noting that the $q-p$ ratio differs for each loading case (where q denotes the von Mises equivalent stress and p is the pressure (hydrostatic) stress, refer to Chapter 3). The VM, crushable foam with isotropic hardening (CFI) and crushable foam with volumetric hardening (CFV) plasticity formulations are considered (v6.11 Abaqus Standard). All three plasticity formulations were calibrated in uniaxial compression to the µCT based models and the ability of each formulation to replicate the hydrostatic and confined compression behaviour of the µCT models was investigated. For the CFI and CFV plasticity formulations, the compression yield stress ratio (K), the ratio of the uniaxial to the hydrostatic yield stress, was determined from the µCT results. A plastic Poisson's ratio (ν_p) of 0.29 was assumed (Chapter 5). Parameter calibration was performed to identify an accurate solution for ν_e under hydrostatic compression.

6.2.2 Part B - Macroscale Vertebral Punch Indentation

Mechanical testing of IFD subsidence was performed by indenting an 8 mm diameter punch into a lumbar ovine vertebral body, referred to as a full vertebral test (FVT). In order to visualise the trabecular deformation that occurs during the mechanical testing, testing was also performed on ovine vertebral bodies dissected in the sagittal plane and indented using a half punch, referred to as a vertebral visualisation test (VVT). Eight L6 ovine vertebrae obtained from the PRTLI 'Bone for Life' project were frozen at -20°C and thawed at 4°C in phosphate buffer solution (PBS) for 24 hours prior to mechanical testing. The transverse processes were removed at approximately 5 mm from where they joined the vertebral body using a bandsaw under constant irrigation (Jubilee VBS 360, Addison Saws Ltd., West Midlands, UK). The superior intervertebral discs were dissected using a scalpel and care was taken not to damage the vertebral endplate.

For the FVTs (n = 5) each vertebra was secured in a custom made rig ensuring the superior endplate remained parallel to the test direction (Figure 6-2). The inferior endplate was potted to a depth of approximately 19 mm in a rig using a low melting point alloy. An 8 mm diameter slot drill was used to remove approximately 1 mm of the cortical bone from the central portion of the superior endplate until a complete surface of underlying trabecular bone was observed. The potted specimens were mounted in a testing machine with a 30 kN load cell (model 4467, Instron Corp., Canton, MA, USA). To approximate an IFD, an 8 mm diameter solid cylindrical aluminium punch was used to apply an axial compressive load to the specimens at a rate of 5 mm/min to an indentation depth of 10 mm. One FVT specimen experienced significant modulus reduction during testing and was excluded, leaving four specimens for analysis.

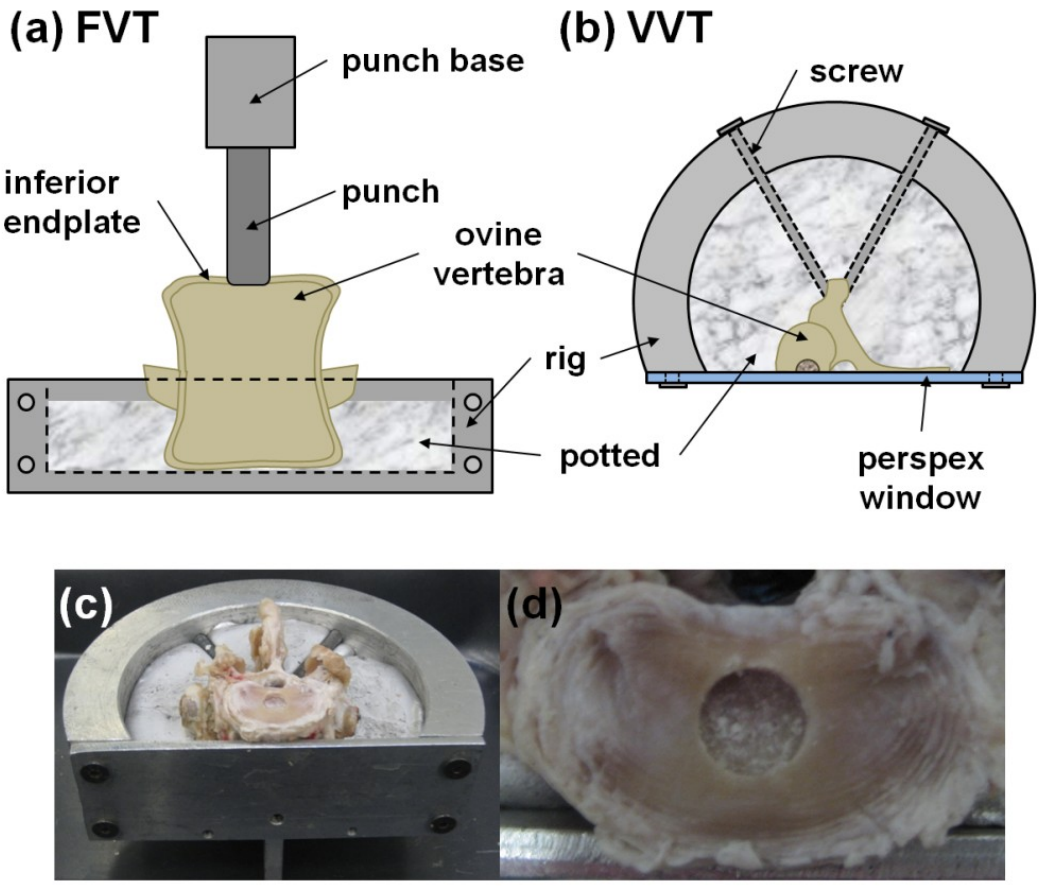

Figure 6-2 Experimental testing (a) Front view schematic of a full vertebral test (FVT) specimen potted in the testing rig. (b) Plan view schematic of a vertebral visualisation test (VVT) specimen potted in the testing rig. (c) FVT specimen potted in the testing rig. (d) FVT specimen with drilled hole in the central vertebral endplate exposing the trabecular bone.

For the VVTs (n = 5) (Figure 6-2(b)) the vertebral bodies were cut in the sagittal plane using a bandsaw. An 8 mm diameter slot drill was used to create a semi-circular hole with a radius of 4 mm and a depth of approximately 1 mm at the centre of the endplate. A small brush and water hose were used to remove the excess marrow at the cut surface to expose the external trabecular bone struts. The vertebral cut surface was placed against a perspex window in a custom made rig, creating a symmetry boundary condition, and was potted (~19 mm) in the rig and mounted on the Instron (Figure 6-2(b)). The specimens were loaded in axial compression using a semi-circular punch (radius = 4 mm) also at a rate of 5 mm/min and to an indentation depth of 10 mm. In tandem with the mechanical tests, 2D video imaging of each VVT was performed using a camera. The experimental whitening regions were measured from selected frames at 4 to 8 mm indentation. Force-indentation curves

were plotted for each specimen. The maximum force was defined as the maximum load following the linear portion of the force-indentation curve.

A macroscale continuum 2D axisymmetric FE model of an ovine lumbar vertebra was created consisting of approximately 375,000 linear triangular and quadrilateral elements (v6.11 Abaqus Explicit). The metallic punch was modelled as a rigid body as it is several orders of magnitude stiffer than the trabecular bone. The cortical bone was assumed to be homogenous, isotropic and linear elastic with an apparent Young's modulus (E_{APP}) of 22 GPa and an ν_e of 0.3 (Reilly and Burstein 1974). The trabecular bone was assumed to be homogenous and was modelled using five different plasticity formulations: VM; DP; CFI; CFV; Hill. Following initial yield, perfectly-plastic behaviour (no strain hardening) was assumed for all formulations. Material parameter calibration was performed for the trabecular bone E_{APP} and apparent yield stress (σ_{yAPP}) to determine an accurate numerical solution for the experimental results. The ν_e was based on the microstructural results. For the DP plasticity formulation, a friction angle (β) of 2°, a flow stress ratio (K_{DP}), the ratio of the yield stress in triaxial tension to the yield stress in triaxial compression, of 1 and a dilation angle (ψ) of 0° were assumed. For the crushable foam plasticity formulations, the value of K was based on the microstructural results. A ν_p of 0.29 for the CFI plasticity formulation was assumed (Chapter 5). For the anisotropic Hill plasticity formulation, the yield stress ratios in the two transverse directions were based on testing of the μCT models in the two transverse loading directions. Details of the five plasticity formulations are provided in Chapter 3. Loads and boundary conditions were applied to replicate the experimental set-up. A frictionless surface-to-surface penalty contact algorithm was implemented between the punch and bone. An adaptive remeshing rule was used due to the large deformations that occur during loading.

6.3 Results

The results are subdivided into two distinct parts. Part A outlines the results of the microstructural and continuum based models. Part B outlines the results of the experimental testing and computational simulation of the indentation of an IFD into ovine vertebrae.

6.3.1 Part A - Computational Results of a Trabecular Bone Sample

The computed apparent stress-strain curves of the μCT based trabecular bone models under uniaxial, hydrostatic and confined compression for a VM plasticity formulation are shown in Figure 6-3(a-c) (black lines). The stress results in Figure 6-3 are normalised, whereby the apparent stress (σ) is divided by the σ_{yAPP}. For the μCT model under uniaxial compression, a distinct apparent yield point is followed by a stress plateau (Figure 6-3(a)). A ratio of the E_{APP} to the σ_{yAPP} of 79 is computed under uniaxial compression. The E_{APP} and σ_{yAPP} results are in agreement with previously reported experimental uniaxial compression results on ovine lumbar trabecular bone (Harrison et al. 2008). For confined compression, a very similar apparent stress-strain curve is computed for the μCT model, with a slightly higher σ_{yAPP} (Figure 6-3(c)). The computed uniaxial and confined compression apparent stress-strain curves are similar to previous experimental results in Chapter 5. Under hydrostatic compression, similar yield behaviour is also computed for the μCT models with slight strain hardening evident post-yield (Figure 6-3(b)). For the μCT models with a DP plasticity formulation assumed for the trabecular material, incorporating a friction angle (β = 4°; K_{DP} = 1; ψ = 0°) and strength asymmetry (β = 0°; K_{DP} = 0.8; ψ = 0°), similar yield points in the apparent stress-strain curve are predicted for hydrostatic and confined compression (Appendix , Figure 6-14(a)) to that predicted for a VM plasticity formulation.

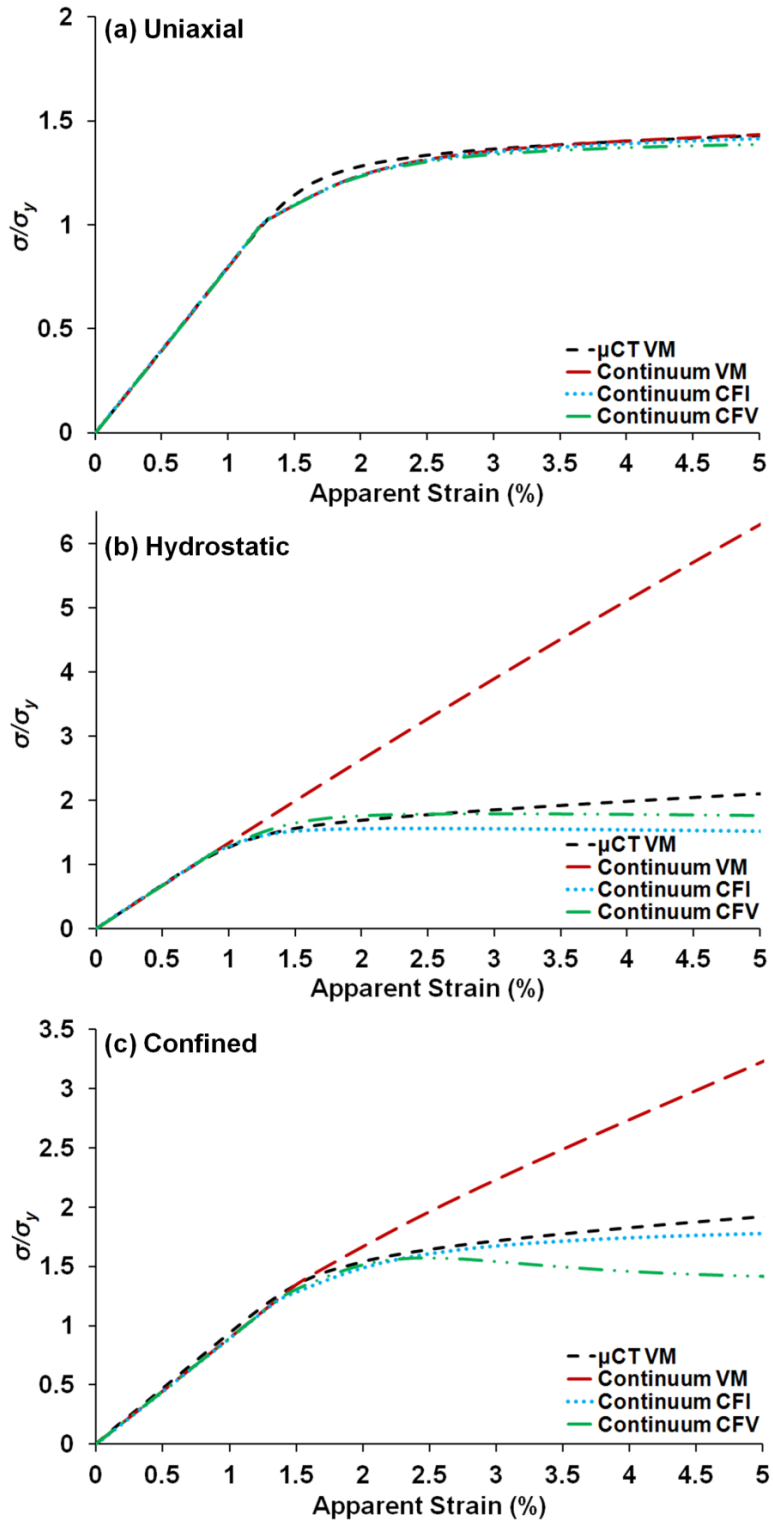

Figure 6-3 Computational results of the µCT based models and continuum based models for the von Mises (VM), crushable foam with isotropic hardening (CFI) and crushable foam with volumetric hardening (CFV) plasticity formulations under (a) uniaxial compression, (b) hydrostatic compression and (c) confined compression.

At an apparent strain of 2%, trabecular yielding is evident in all three compression loading configurations, whereas at 5% strain, near perfectly-plastic behaviour with little strain hardening is computed for the μCT models with a VM plasticity formulation for the trabecular material (Figure 6-3). In Figure 6-4 and Figure 6-5, the local behaviour of individual trabeculae are shown at an apparent strain of 2 and 5% for the μCT models under all three compression loading configurations. The computed contour plot results of equivalent plastic strain, von Mises equivalent stress (q) and pressure stress (p) are detailed. For all three loading configurations, the applied apparent strains result in non-uniform localised yielding of the trabeculae (Figure 6-4(a-c), Figure 6-5(a-c)), which are more pronounced under hydrostatic compression. At both 2 and 5% strain, greater local magnitudes and distributions of equivalent plastic strain, von Mises equivalent stress and pressure are predicted for hydrostatic compression (Figure 6-4(b, e, h) Figure 6-5(b, e, h). It is critical to note that, although the apparent boundary conditions are hydrostatic compression and the material behaviour of individual trabeculae are the simplistic pressure independent VM plasticity formulation, extensive localised plastic yielding and plasticity occur due to the complex trabecular architecture (Figure 6-4(b), Figure 6-5(b)). At 2 and 5% strain, the plastic strain regions (Figure 6-4(a-c), Figure 6-5(a-c)) correspond to comparable regions of high von Mises equivalent stress (Figure 6-4(d-f), Figure 6-5(d-f)). It is clear from the μCT results that despite implementing a simplistic VM plasticity formulation for the trabecular material, the complex microarchitecture of the trabeculae causes a distinct yield point in the apparent stress-strain curve under all three compression loading configurations.

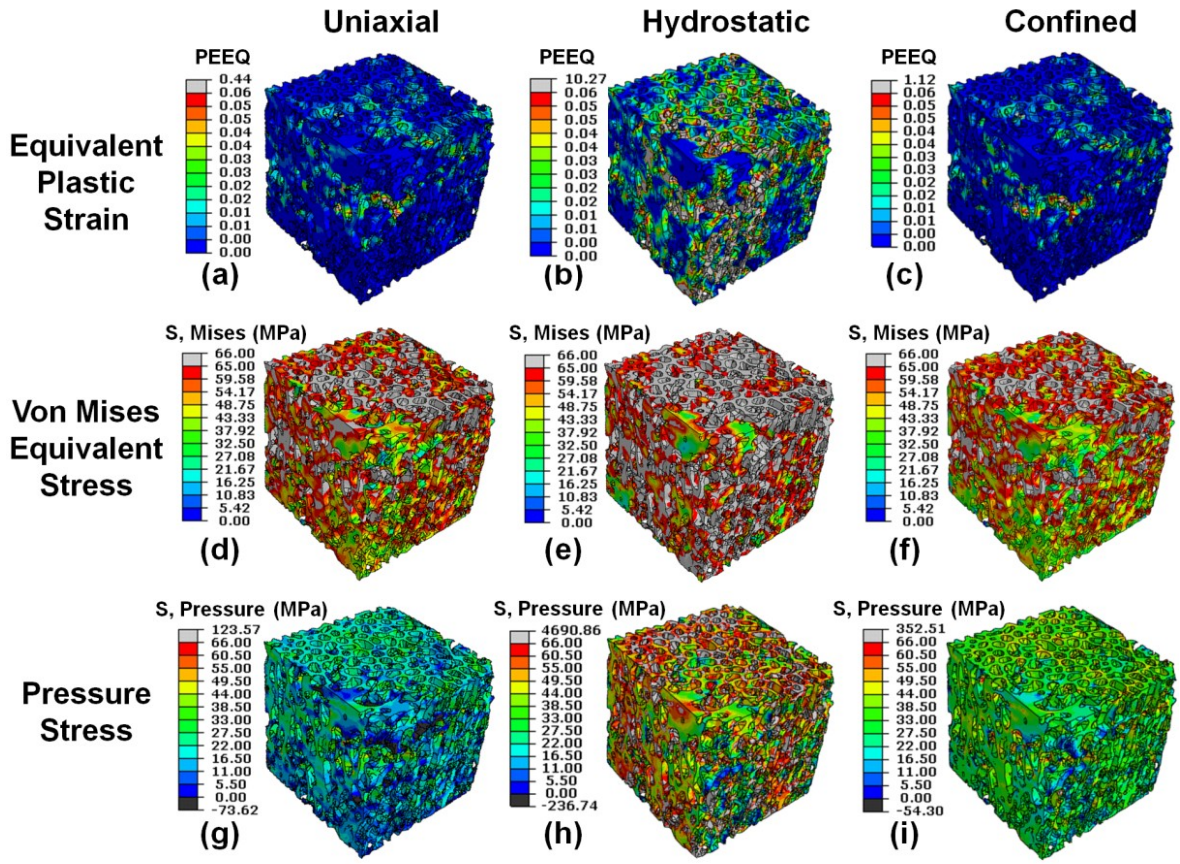

Figure 6-4 Computational local equivalent plastic strain, von Mises equivalent stress and pressure stress results at an apparent strain of 2% for the μCT based models for uniaxial, hydrostatic and confined compression using a von Mises plasticity formulation.

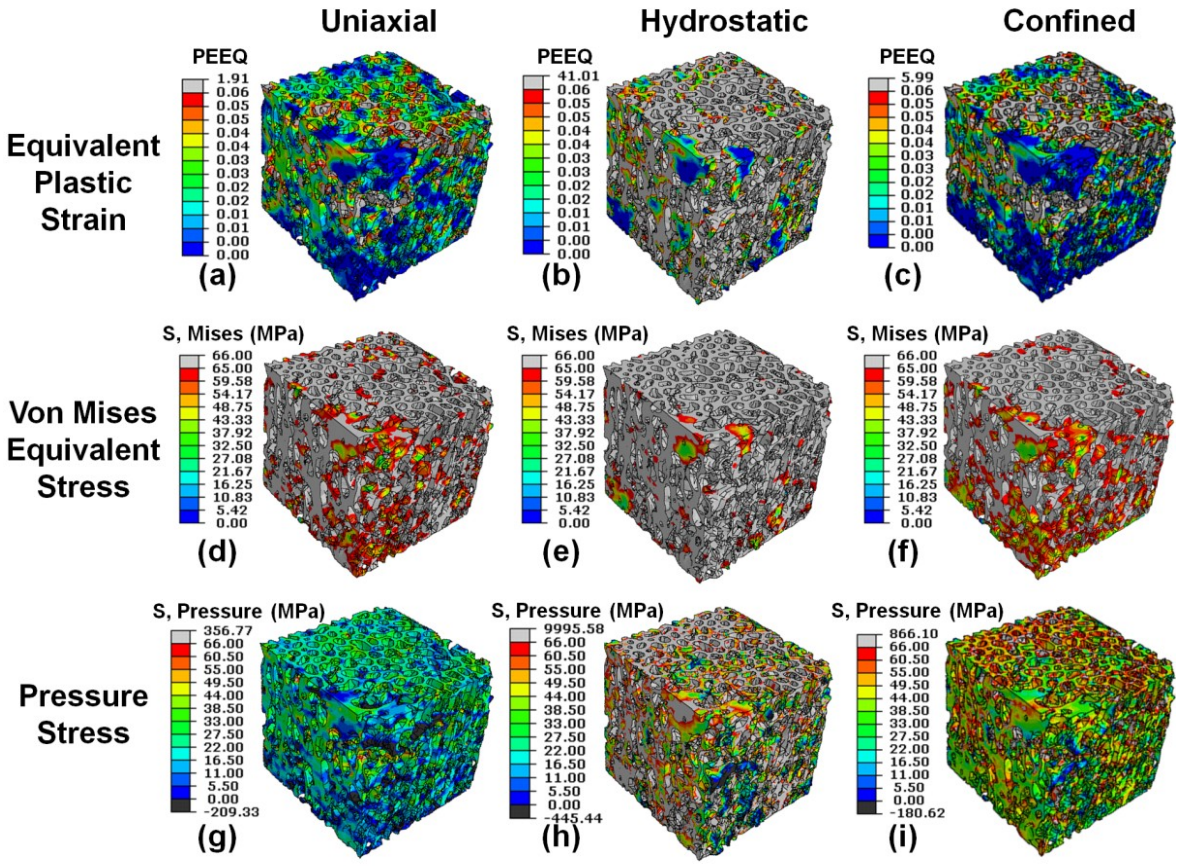

Figure 6-5 Computational local equivalent plastic strain, von Mises equivalent stress and pressure stress results at an apparent strain of 5% for the μCT based models for uniaxial, hydrostatic and confined compression using a von Mises plasticity formulation.

The ability of a continuum model of the trabecular bone with a VM plasticity formulation to replicate the μCT based apparent level stress-strain curves is also considered in Figure 6-3 (red lines). Under uniaxial compression, the continuum VM plasticity formulation is calibrated to the μCT results, where a distinctive yield point is followed by a stress plateau (Figure 6-3(a)). Under hydrostatic compression, a ν_e of 0.21 is computed, which replicates the initial elastic behaviour very well (Figure 6-3(b)). The continuum VM plasticity formulation cannot replicate the μCT results under hydrostatic compression and no yield is computed (by definition). A continuum based VM plasticity formulation cannot achieve apparent yield under hydrostatic loading; therefore, a plasticity formulation that incorporates pressure dependent yielding is necessary for a continuum based representation of trabecular bone. Under confined compression, slight plastic deformation occurs for the

continuum VM plasticity formulation and a poor match to the μCT results is achieved (Figure 6-3(c)). For the continuum VM plasticity formulation, the apparent stresses at 5% apparent strain are over predicted by a factor of 6.3 and 3.2 under hydrostatic and confined compression, respectively, when compared to the μCT results. A continuum model with a DP plasticity formulation does not have the ability to capture the yield behaviour of the μCT models under hydrostatic or confined compression due to its linear yield surface in the $q - p$ plane and would produce similar over predicted results under hydrostatic compression to the continuum VM plasticity formulation.

Additionally, the ability of a continuum model with the CFI and CFV plasticity formulations to capture the μCT based apparent level stress-strain curves is considered in Figure 6-3 (blue and green lines). The CFI and CFV plasticity formulations were calibrated under uniaxial compression to the μCT results (Figure 6-3(a)). For the crushable foam plasticity formulations, K was computed as 0.85 based on the μCT results. In contrast to the continuum VM plasticity formulation, a distinctive yield point is predicted for the CFI and CFV plasticity formulations under hydrostatic compression, approximating the μCT results very well (Figure 6-3(b)). Although the stresses for the CFI and CFV plasticity formulations are slightly under predicted at higher strains for hydrostatic loading, they provide superior matches to the μCT results than the continuum VM plasticity formulation. As a validation, confined compression was performed and the CFI and CFV plasticity formulations predict the microstructural yield stress and post-yield behaviour quite well (Figure 6-3(c)). The CFI plasticity formulation provides a better correlation with the μCT results under confined compression than the CFV plasticity formulation. For the CFV plasticity formulation, a hydrostatic yield stress ratio (K_t) of 0.5 (i.e., the ratio of the yield stress in hydrostatic tension to the initial yield stress in hydrostatic compression) provides a reasonable match to the μCT results under all three loading configurations. The continuum CFI and CFV plasticity formulations, which permit pressure dependent yielding, replicate the μCT based apparent stress-strain curves very well under all three loading configurations.

The μCT models reveal that when a pressure independent VM plasticity formulation is assumed, the apparent yield behaviour of the trabecular bone is pressure dependent due to local yielding of trabeculae. The development of stress concentrations lead to

localised yielding of trabeculae due to the microarchitecture. The VM plasticity formulation can predict apparent trabecular yielding under hydrostatic and confined compression loading only if the trabecular microstructure is considered concurrently. However, for a continuum representation of trabecular bone under hydrostatic or confined compression, it is essential to implement a constitutive formulation, such as a crushable foam plasticity formulation, that has the ability to capture the pressure dependent yield behaviour of the trabecular bone. Unlike VM (and DP) plasticity, for an increase in pressure, the crushable foam plasticity formulations lead to a lower von Mises equivalent stress at yield due to the elliptical yield surface in the $q - p$ plane.

6.3.2 Part B - Macroscale Vertebral Punch Indentation Results

The experimental force-indentation curves for the macroscale indentation of a punch into vertebral trabecular bone specimens are shown in Figure 6-6. The FVT and VVT results are shown in Figure 6-6(a, b) where distinctive yielding is followed by a stress plateau. As only half vertebrae are tested, the mean VVT force results in Figure 6-6(c) are multiplied a factor of two, therefore comparing directly with the mean FVT results. Similar mean experimental results are measured for the FVTs and VVTs (scaled results) where yielding occurs at approximately 3 and 2.5 kN, respectively. Experimental (mean±SD) maximum force results of 3.1±0.7 and 1.5±0.1 kN (scaled 3.0±0.1 kN) are measured for the FVTs and VVTs.

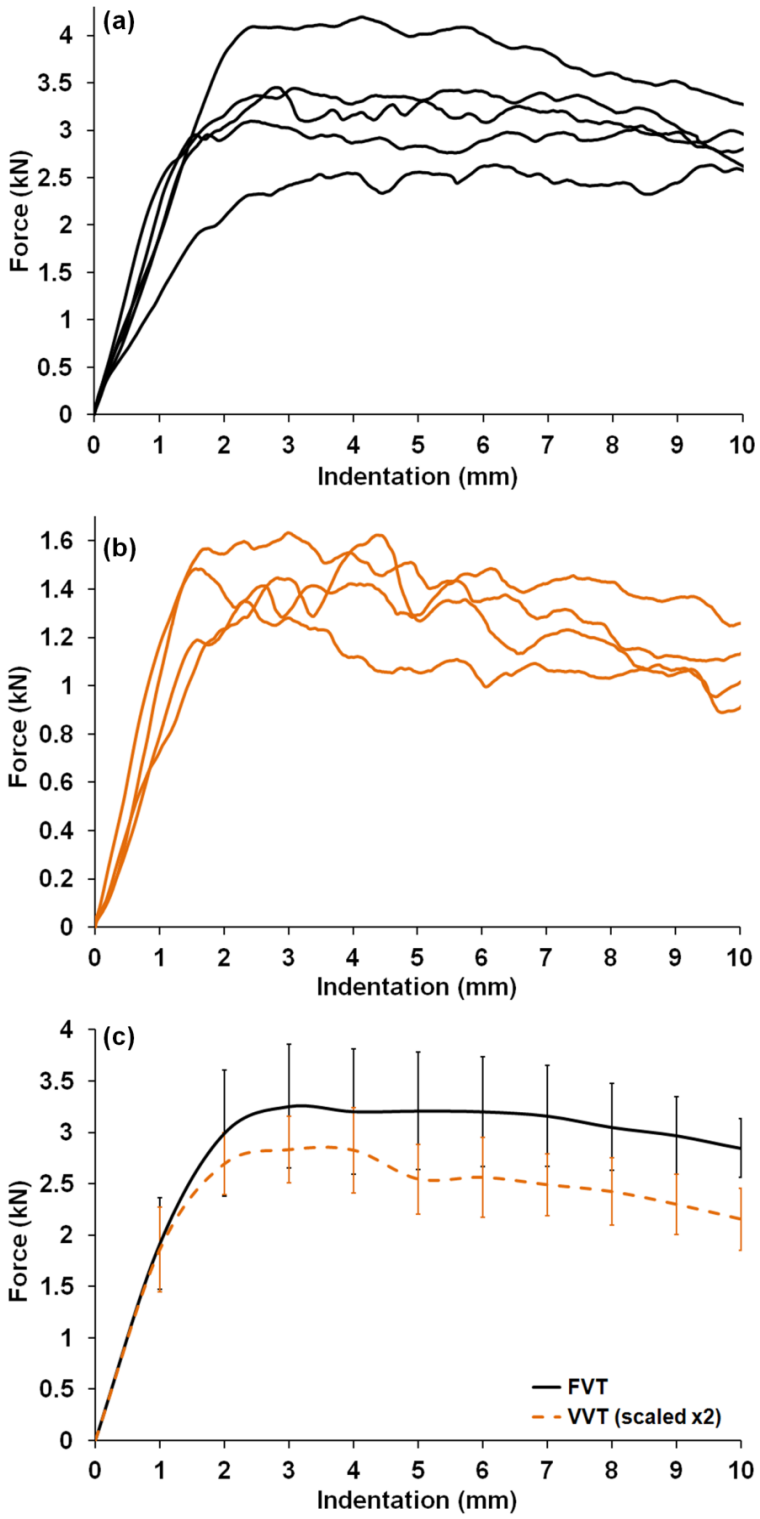

Figure 6-6 (a) Experimental full vertebral test (FVT) results. (b) Experimental vertebral visualisation test (VVT) results. (c) Experimental results (mean±SD) of the VVTs and FVTs. For purposes of comparison with FVT results, the VVT force results are scaled by a factor of two as only half of each vertebral specimen was tested.

The results of a VVT at indentation depths of 0, 2, 4, 6, 8 and 10 mm are shown in Figure 6-7 where localised regions of trabecular bone whitening are observed directly below the punch. Whitening of trabecular bone has been shown to be evidence of localised plastic deformation, crushing and microdamage of trabeculae (Jungmann et al. 2011; Thurner et al. 2007; Thurner et al. 2006) and is clearly evident below the punch at indentation depths of 2-10 mm. At 2 mm indentation, a whitened trabecular region is evident immediately below the punch, extending 3.2±0.9 mm from the punch-bone interface (Figure 6-7(b)). With increased indentation from 4 to 8 mm, the whitened trabecular region that advances below the punch does not increase substantially, extending 3.2±0.4, 3.3±0.6 and 3.4±0.7 mm below the interface, respectively (Figure 6-7(c-e)).

The macroscale computational predictions for punch indentation depths of 2-10 mm are shown in Figure 6-8. The trabecular bone was modelled as a continuum and the material behaviour was modelled using the VM, DP, Hill, CFI and CFV plasticity formulations. The experimental FVT results (mean±SD) are also shown in Figure 6-8 for comparison. For the trabecular bone, an E_{APP} of 170 MPa and a ν_e of 0.21 replicate the initial pre-yield portion of the experimental results very well. With a trabecular bone $\sigma_{yAPP}$of 50 MPa the VM plasticity formulation accurately predicts the initial yield behaviour; however, it cannot capture the experimental force plateau post-yield. Very similar results are also computed for the DP plasticity formulation (σ_{yAPP} = 50 MPa; β = 2°; K_{DP} = 1; ψ = 0°). At an indentation of over 3 mm, the forces for the VM and DP plasticity formulations exceed the experimental standard deviations, overestimating the force required to achieve punch indentation by 73% and 65%, respectively. The anisotropic Hill plasticity formulation, with yield stress ratios in the transverse directions of 0.52 and 0.57 of the axial σ_{yAPP}, captures the initial yield behaviour very well. However, an over predicted force plateau is computed from 4 to 10 mm indentation that is outside the experimental standard deviations. The experimental yield and force plateau behaviour are captured very well by the CFI plasticity formulation (σ_{yAPP} = 50 MPa; K = 0.85; ν_p = 0.29) which are within the experimental standard deviations. For a CFV plasticity formulation (σ_{yAPP} = 50 MPa; K = 0.85; K_t = 0.5) the initial yield and force plateau are slightly under predicted, but computed force values are within the standard deviations of the experimental results. When compared to the mean experimental FVT results,

maximum errors in the force predictions of 32%, 8% and 17% occur for the Hill, CFI and CFV plasticity formulations, respectively.

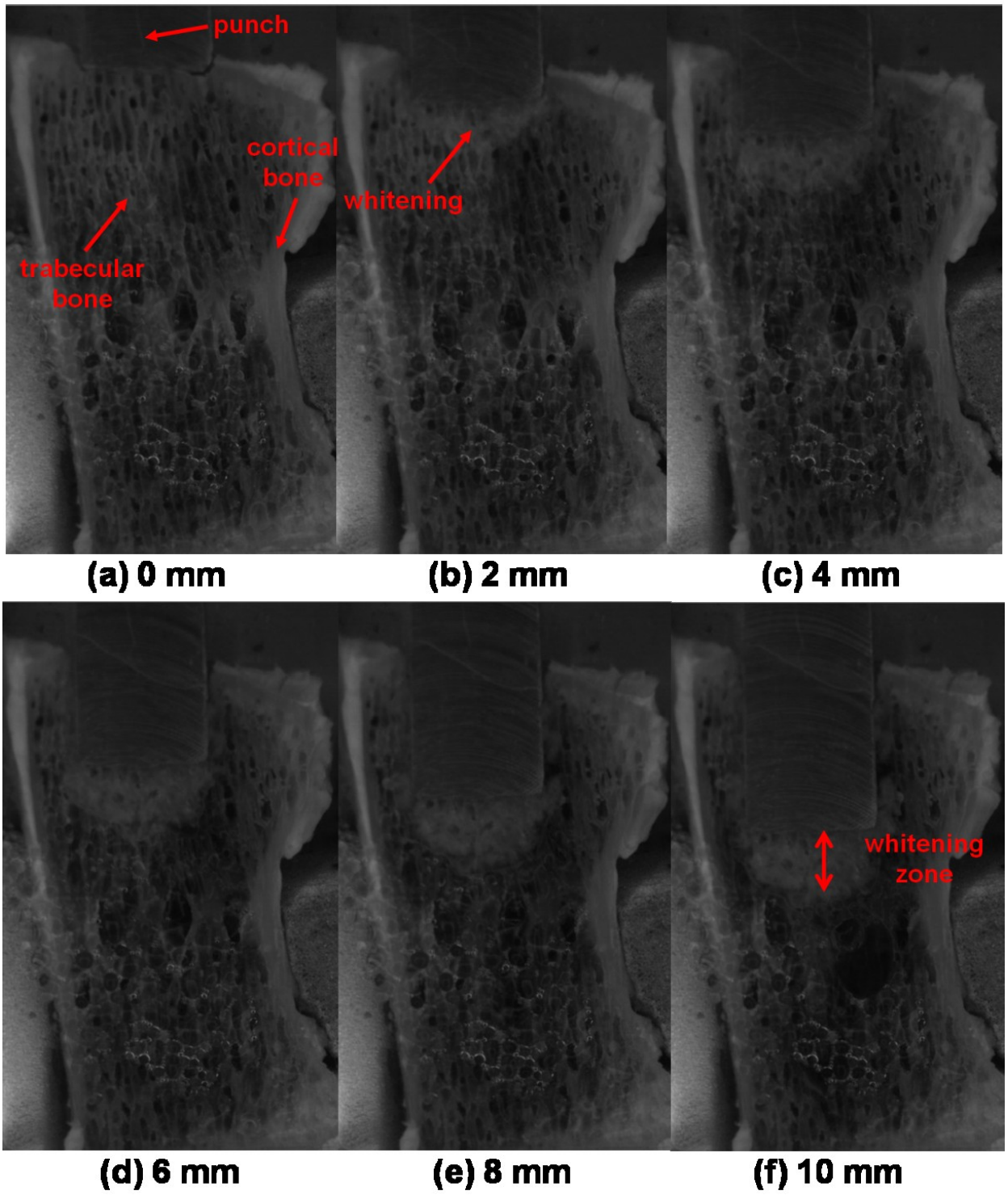

Figure 6-7 Experimental images of a vertebral visualisation test (VVT) specimen captured at indentation depths of: (a) 0 mm (b) 2 mm; (c) 4 mm; (d) 6 mm; (e) 8 mm; (f) 10 mm. A localised zone of trabecular bone whitening, indicating plastic deformation and damage, can be observed directly under the punch during subsidence.

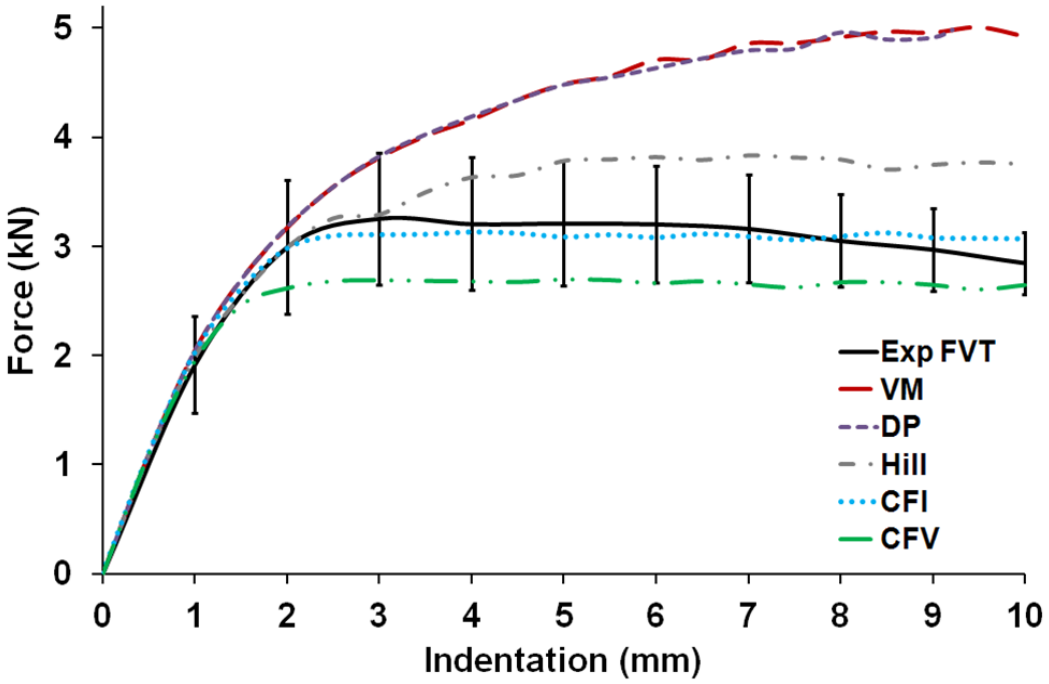

Figure 6-8 Macroscale experimental and computational results of the full vertebra with 10 mm punch indentation for five different plasticity formulations: von Mises (VM); Drucker-Prager (DP); Hill; crushable foam with isotropic hardening (CFI); crushable foam with volumetric hardening (CFV).

Computational contour plot results of the equivalent plastic strain, von Mises equivalent stress and pressure of the punch indentation into the vertebral trabecular bone are depicted in Figure 6-9, Figure 6-10 and Figure 6-11 respectively for the VM, Hill, CFI and CFV plasticity formulations. Due to the similarity with the VM plasticity formulation results, contour plot predictions for the DP plasticity formulation are not presented. At a punch indentation depth of 2 mm, similar stress and strain results are evident for the VM, Hill, CFI and CFV plasticity formulations (Figure 6-9(a), Figure 6-10(a) and Figure 6-11(a)). In addition to the qualitative results in Figure 6-9, Figure 6-10 and Figure 6-11, quantitative results are presented in Figure 6-12 where the depths the plastic zone regions extend below the punch-bone interface are shown for all five plasticity formulations at 4, 6 and 8 mm punch indentation. In Figure 6-12 the plastic regions are also compared to the experimentally (mean±SD) observed whitening regions at the same indentation depths. As shown in Figure 6-9 and Figure 6-12, greater regions of equivalent plastic strain are computed for the VM and Hill plasticity formulations at 4-10 mm indentation than for the CFI and CFV plasticity formulations where the strains are

much more localised. For VM plasticity, a non-yielding region (black in contour plot) is evident directly below the punch-bone interface at 4-10 mm indentation (Figure 6-9(b-e)). In contrast, localised plastic yielding is evident directly below the interface for the CFI plasticity formulation in Figure 6-9(b-e) which extends 3.1, 3.2, 3.1 and 3.1 mm from the interface at 4-10 mm indentation, respectively (Figure 6-12). Whitening of the trabecular bone at the region immediately below the punch-bone interface is also observed experimentally (Figure 6-7), with very similar regions and depths of whitening and plastic strain observed experimentally and for the CFI plasticity formulation (Figure 6-12). Similar plastic strain depths are also predicted for the CFV plasticity formulation (Figure 6-9(b-e), Figure 6-12); however, non-yielding regions are evident, which are not observed experimentally. An over predicted zone of plastic yielding is evident for the VM plasticity formulation (Figure 6-9(b-e)) that enlarges below the punch with increased indentation, extending 5.1-6.3 mm from the interface at 4-10 mm indentation (Figure 6-12). The Hill plasticity formulation over predicts the region of plastic yielding, which a maximum depth of 5.9 mm at 8 mm indentation (Figure 6-9, Figure 6-12). A larger plastic yielding region lateral to the punch is also predicted for the Hill plasticity formulation (Figure 6-9). Experimental images reveal that such whitening is not evident lateral to the punch (Figure 6-7).

At 4-10 mm indentation in Figure 6-10(b-e), distinct localised regions of high von Mises equivalent stress (shown in red and grey) are evident for the CFI and CFV plasticity formulations in contrast to the VM and Hill plasticity formulations where a much greater area of increased stress is computed. Although the peak von Mises equivalent stress is similar for all of the plasticity formulations, the regions of high stress increase in depth with increased punch indentation for the VM in comparison with CFI and CFV plasticity formulations where the regions remain nearly constant. In contrast to the von Mises equivalent stress results in Figure 6-10, the magnitudes of the peak compressive pressure (+*ve*) in Figure 6-11 are much greater for the VM and Hill plasticity formulations than for the CFI and CFV plasticity formulations. At 4-10 mm indentation, peak compressive pressures of 74-126 MPa and 99-101 MPa occur for VM and Hill plasticity, respectively, in comparison with 52-55 MPa and 54-59 MPa for the CFI and CFV plasticity formulations, respectively (Figure 6-11(b-e)). At 4-10 mm indentation (Figure 6-11(b-e)), localised high pressures (>50 MPa,

shown in grey) are evident for CFI and CFV plasticity extending 0.5-0.7 mm and 0.2-1.0 mm from the punch-bone interface, respectively. In contrast to the crushable foam plasticity formulation results, high interface pressures in the VM and Hill plasticity formulations are more pronounced extending 1.8-3.5 mm and 3.2-3.7 mm, respectively, below the punch at 4-10 mm indentation (Figure 6-11(b-e)). Interestingly, for VM plasticity, the high interface pressures (Figure 6-11(b-e)) contrast with the plastic strain results where a non-yielding region is predicted immediately below the punch (Figure 6-9(b-e)).

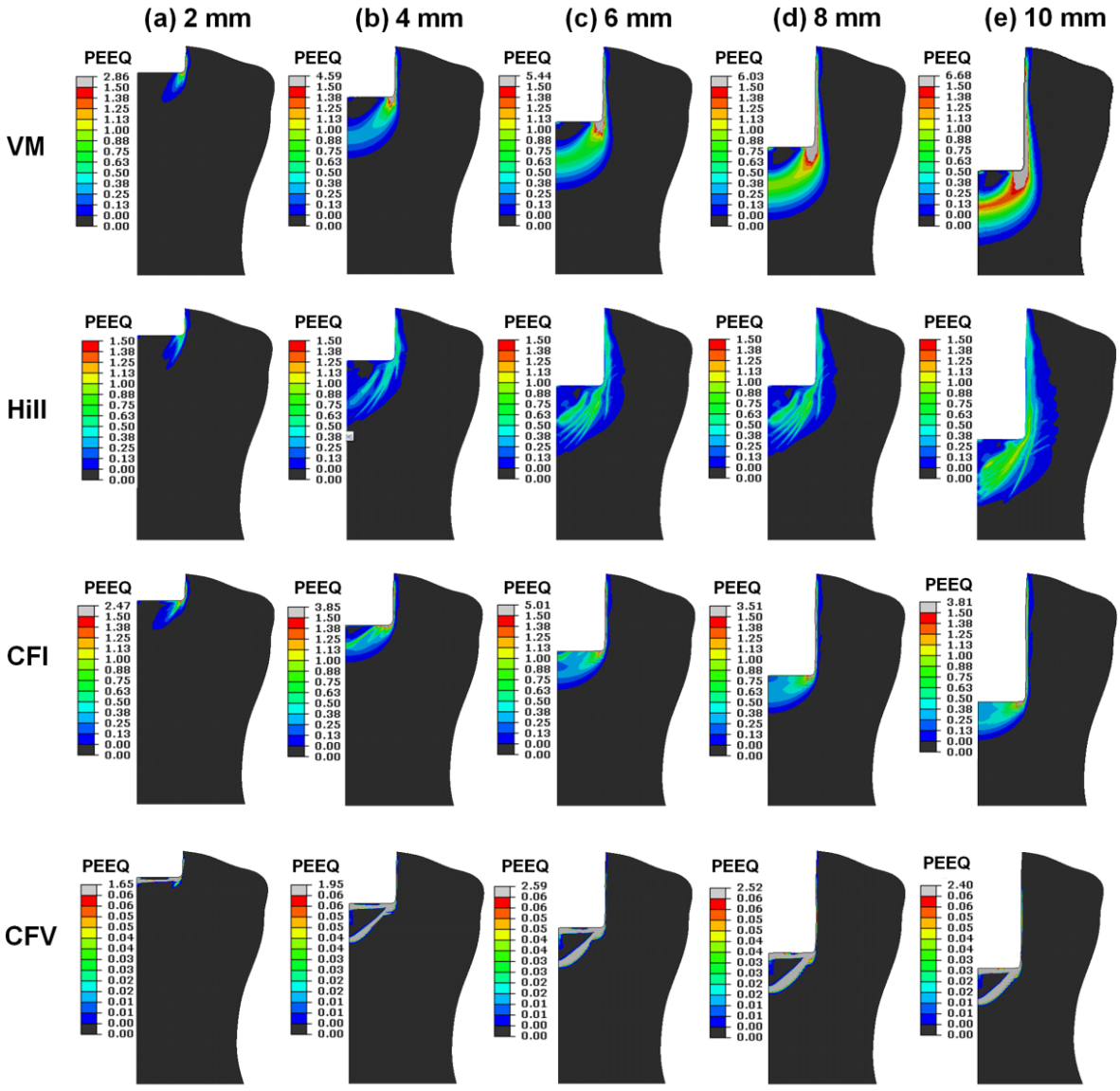

Figure 6-9 Computational equivalent plastic strain contour plots of the macroscale vertebral models at a indentation depth of 2, 4, 6, 8 and 10 mm for trabecular bone with the von Mises (VM), Hill and crushable foam (CFI, CFV) plasticity formulations. The cortical bone and punch are removed for clarity.

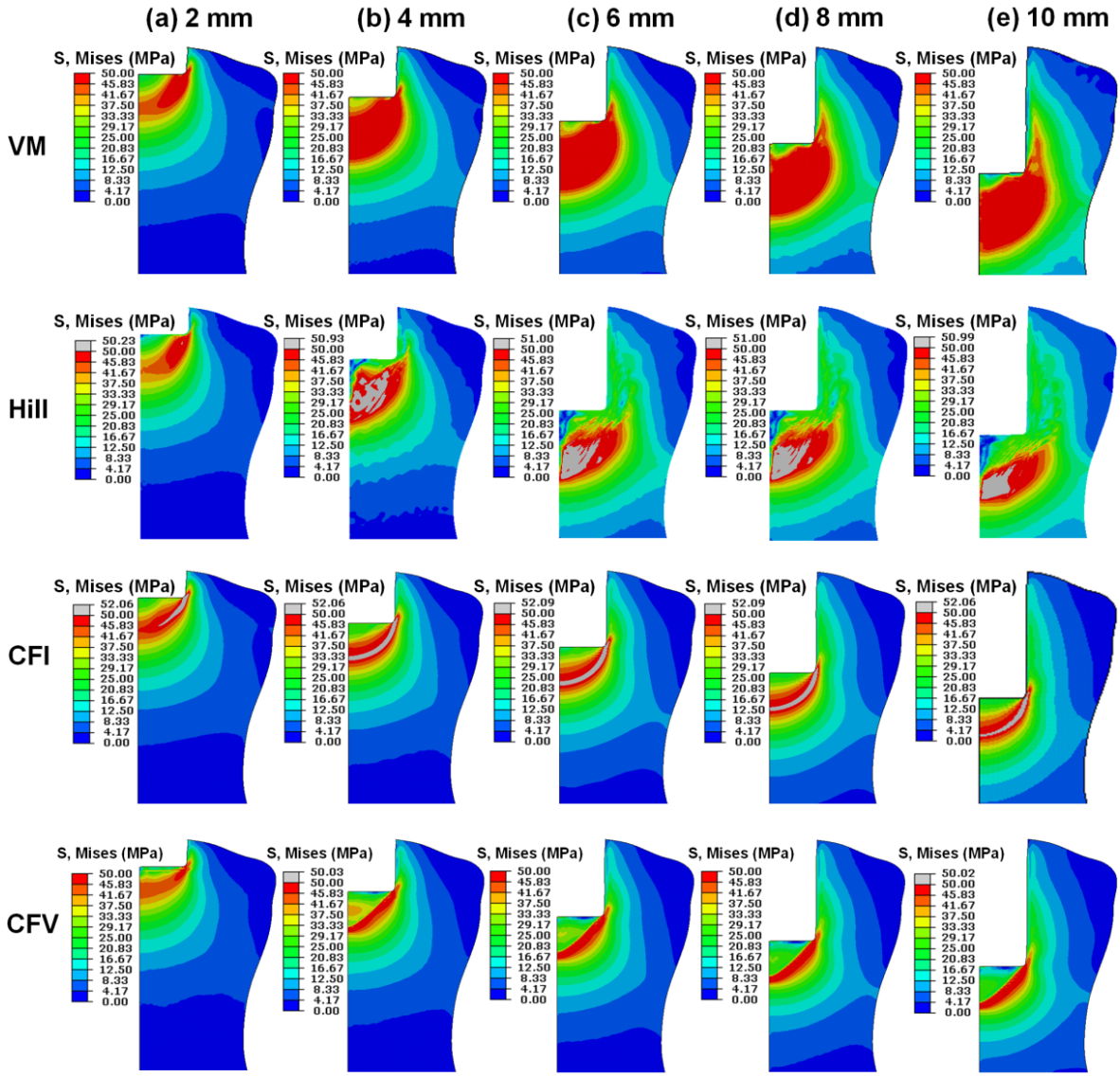

Figure 6-10 Computational von Mises equivalent stress contour plots of the macroscale vertebral models at a indentation depth of 2, 4, 6, 8 and 10 mm for trabecular bone with the von Mises (VM), Hill and crushable foam (CFI, CFV) plasticity formulations. The cortical bone and punch are removed for clarity.

The VM plasticity formulation results in large over predicted distributions of both pressure and von Mises equivalent stress (Figure 6-10, Figure 6-11) and the resulting indentation forces are hence over predicted (Figure 6-8). Similarly over predicted distributions of pressure and von Mises equivalent stress are evident for the Hill plasticity formulation (Figure 6-10, Figure 6-11) and the indentation forces are not within the experimental standard deviations (Figure 6-8). In contrast to the VM and Hill results, plasticity in the CFI and CFV plasticity formulations are concentrated at the interface (Figure 6-4) due to the fact an increase in pressure leads to a lower von

Mises equivalent stress at yield for crushable foam plasticity. For the CFI plasticity formulation, the high interface pressures correspond to a comparable area of plasticity (Figure 6-11).

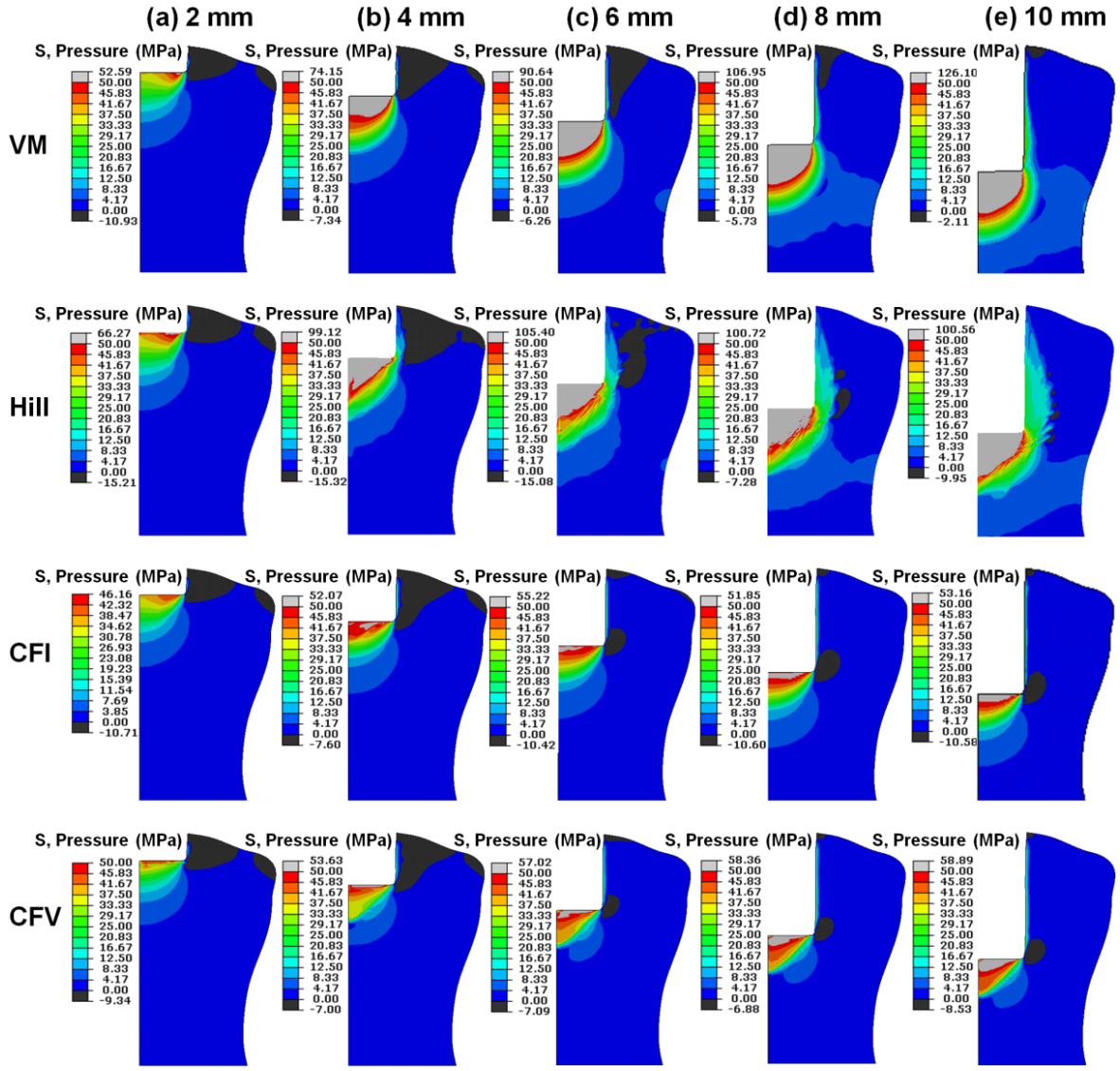

Figure 6-11 Computational pressure stress contour plots of the macroscale vertebral models at a indentation depth of 2, 4, 6, 8 and 10 mm for trabecular bone with the von Mises (VM), Hill and crushable foam (CFI, CFV) plasticity formulations. The cortical bone and punch are removed for clarity.

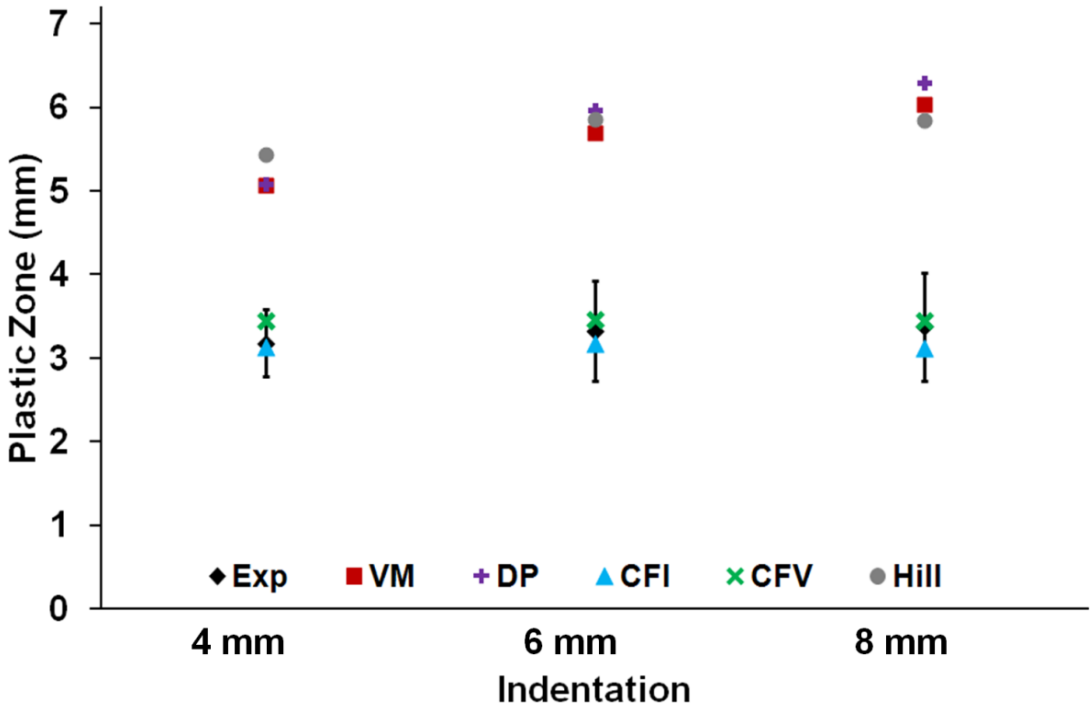

Figure 6-12 Mean (±SD) of plastic regions extending from the punch-bone interface in the experimental VVTs and macroscale computational models at 4, 6 and 8 mm trabecular indentation with the von Mises (VM), Drucker-Prager (DP) ($\beta = 2°$; $K_{DP} = 1$; $\psi = 0°$), Hill, crushable foam with isotropic hardening (CFI) ($K = 0.85$; $v_p = 0.29$) and crushable foam with volumetric hardening (CFV) ($K = 0.85$; $K_t = 0.5$) plasticity formulations.

6.4 Discussion

The microstructural FE simulations of trabecular bone reveal a distinctive yield point at the apparent level under uniaxial, hydrostatic and confined compression. Simulations reveal that under hydrostatic compression, localised stress concentrations occur at a microscale (trabeculae level), resulting in a distinctive yield point in the apparent stress-strain curve. This distinctive response at the apparent level can be accurately captured by a continuum model using a pressure dependent CFI or CFV plasticity formulation. At the macroscale, the vertebral subsidence experiments quantify localised regions of whitened trabecular bone directly under the punch, which remain approximately constant in size with increased indentation. Macroscale vertebral IFD subsidence simulations further emphasise the importance of implementing an appropriate pressure dependent plasticity formulation (with an elliptical yield surface in the $q-p$ plane) in macroscale continuum models of trabecular bone. The CFI plasticity formulation provides accurate predictions of subsidence force in addition to computation of a highly localised region of plastic deformation of trabecular bone directly under the punch, correlating strongly with experimentally observed whitening zones.

In the microstructural models, the trabecular material is modelled using a simple pressure independent VM plasticity formulation; hence, yielding in the trabecular microstructure occurs due to concentrations of the von Mises equivalent stress and not due to localised hydrostatic stress in the trabecular material. However, when apparent hydrostatic compression is applied to a μCT model, a distinctive yield point is observed in the apparent stress-strain curve, similar to the multiaxial compression results of Rincon-Kohli and Zysset (2009). This clearly demonstrates that the apparent pressure dependent yielding of trabecular bone, observed in Chapter 5, can occur as a result of localised stress concentrations and yielding in the trabeculae at a microstructural level without the requirement that the localised yield is pressure dependent. This distinctive yield and plateau behaviour are also observed under hydrostatic compression for a μCT model with a DP plasticity formulation. This demonstrates that the link between localised microstructural yielding and the macroscopic behaviour of trabecular bone is not dependent on the specific plasticity formulation implemented at the microstructural level. Its is also demonstrated that to capture reported differences in tensile and compressive yield stress using a μCT

model, a plasticity formulation that incorporates this strength asymmetry must be used at a material level. It is revealed that the inclusion of the trabecular microarchitecture in the μCT models is a more dominant factor in predicting apparent yield behaviour than the specific form of the plasticity formulation used to represent the material behaviour of the trabecular microstructure. For example, a μCT model with a simplistic VM plasticity formulation at the trabecular material level is sufficient to elucidate the experimentally observed apparent level pressure dependent yielding of trabecular bone. As experimental validation of pure hydrostatic compression is not available, confined compression simulations are also performed using the microstructural geometry. Predicted apparent stress-strain curves under confined compression exhibit a distinctive yield point followed by a stress plateau, similar to the experimental results in Chapter 5 and of Charlebois et al. (2010b).

Previous microstructural voxel based FE models have focused on the simulation of uniaxial compression of trabecular bone using linear elastic material models (Harrison et al. 2008; Mc Donnell et al. 2010; Müller and Rüegsegger 1995; Nagaraja et al. 2005; Van Rietbergen et al. 1995). The non-linear behaviour of microstructural trabecular bone models has also been modelled by reducing the elastic modulus of the trabecular material to 5% when critical principal strain is computed at a material point (Bayraktar et al. 2004; Bayraktar and Keaveny 2004; Guillén et al. 2011; Harrison et al. 2012; Niebur et al. 2002; Niebur et al. 2000; Verhulp et al. 2008). Niebur et al. (2000) based such criteria on macroscopic testing of cortical bone by Reilly and Burstein (1975). Under uniaxial compression Harrison et al. (2012) incorporated material damage using the principal strain based criterion and fracture through element removal and cohesive forces in the trabecular microarchitecture. Also based on the testing of cortical bone specimens, Verhulp et al. (2008) implemented the principal strain based criterion in addition to a perfectly-plastic VM plasticity formulation for the uniaxial compression testing of trabecular bone. Van Rietbergen et al. (1995) and Boyd et al. (2002) considered confined compression loading that was limited to the linear elastic regime, hence offering no insight into multiaxial yield behaviour. Using the principal strain based criterion at a trabecular level, biaxial compression strain and normal-shear strain of μCT based trabecular specimens have been simulated (Bayraktar et al. 2004; Niebur et al. 2002).

Niebur et al. (2002) proposed a multiple-surface yield criterion with two intersecting yield ellipses for the on-axis and transverse yield points, whereas Bayraktar et al. (2004) proposed a modified super-ellipsoid yield criterion. The present study provides predictions of the apparent yield behaviour of microstructural models of trabecular bone under confined and hydrostatic compression. As trabecular bone is naturally constrained by the surrounding cortex, multiaxial loading configurations such as hydrostatic and confined compression are particularly relevant and should be carefully characterised in order to provide accurate predictions of *in vivo* trabecular bone behaviour.

Complex multiaxial loading of trabecular bone is encountered during bone fracture, screw pullout and press-fit device implantation in addition to vertebral IFD subsidence as demonstrated in the present study. Despite this, a relatively small number of experimental studies have performed confined or multiaxial compression testing of trabecular bone specimens. Linde and Hvid (1989) performed confined compression solely in the elastic regime, Charlebois et al. (2010b) performed confined compression post-yield to large inelastic strains. The triaxial compression (Keaveny et al. 1999; Rincon-Kohli and Zysset 2009) and axial-shear strength (Fenech and Keaveny 1999) of trabecular bone have also been investigated. The current study highlights the need for extensive further multiaxial experimental testing and corresponding microstructural computational simulations to further elucidate the inelastic behaviour of trabecular bone under complex loading configurations.

Microstructural based trabecular bone geometries have been applied to macroscale applications of trabecular bone. Microstructural voxel based geometries of vertebrae have been investigated assigning identical linear elastic material properties to the cortex and trabeculae (Eswaran et al. 2006; Harrison and McHugh 2010). Significant limitations are associated with such an approach given the high computational expense. Using idealised microstructural trabecular geometry (lattice beam elements) inside simplified vertebral geometry, McDonald et al. (2010) implemented a VM plasticity formulation for the trabecular microstructure. The present study demonstrates that simulation of multiaxial loading of representative samples of trabecular bone microstructure can inform the development of more accurate

continuum models that can then be used for macroscale applications with finite deformation, accurate contact conditions and complex non-linear material behaviour.

The μCT models in the present study elucidate that localised stress concentrations and yielding in the trabecular microstructure affect the apparent level pressure dependent plasticity of trabecular bone observed experimentally in Chapter 5. A continuum representation of trabecular bone using the CFI or CFV plasticity formulations replicates the apparent stress-strain curve predicted by the μCT models. Under confined compression, the crushable foam plasticity formulations accurately capture the apparent yield point and post-yield behaviour of trabecular bone predicted by the μCT models and observed experimentally in Chapter 5. The crushable foam plasticity formulations capture the apparent pressure dependent yield observed under hydrostatic compression in the μCT models. In the triaxial compression loading of Rincon-Kohli and Zysset (2009), an increase in radial compressive stress results in a decrease in the axial stress required to cause yield. A piecewise yield surface was experimentally uncovered by Rincon-Kohli and Zysset (2009) in which the compressive quadrant is qualitatively similar to the crushable foam plasticity formulation. The predicted compression yield stress ratio, K, of 0.85 for the crushable foam plasticity formulations in the present study for ovine trabecular bone is comparable to the previously reported value of 1 for bovine tibial trabecular bone in Chapter 5.

As expected, a continuum VM plasticity formulation cannot capture the pressure dependent yield behaviour of trabecular bone under hydrostatic or confined compression. Despite this, continuum pressure independent plasticity formulations have been widely used for trabecular bone including the VM (Keyak 2001; Keyak and Falkinstein 2003) and strain based plasticity formulations (Cowin and He 2005; Gupta et al. 2007). The present study has shown that a continuum based pressure dependent DP plasticity formulation is also inadequate in capturing the inelastic trabecular behaviour although previously implemented for trabecular bone (Bessho et al. 2007; Derikx et al. 2011). Chapter 5 and the present study have demonstrated that continuum based plasticity formulations such as the DP and Mohr-Coulomb formulations that have linear yield surfaces in the $q - p$ plane are inappropriate for modelling trabecular bone, although they have been shown to capture the inelastic behaviour of cortical bone (Feerick and McGarry 2012; Mullins et al. 2009).

Plasticity formulations such as the modified super-ellipsoid yield criterion (Bayraktar et al. 2004), the Tsai-Wu plasticity formulation (Fenech and Keaveny 1999; Keaveny et al. 1999) and a cellular solid criterion (Fenech and Keaveny 1999) have also been proposed to describe the multiaxial yielding of trabecular bone. The Tsai-Wu plasticity formulation has been shown to reasonably predict the combined axial-shear strength (Fenech and Keaveny 1999) and to poorly predict the triaxial compressive stress (Keaveny et al. 1999) of trabecular bone. Representing trabecular bone morphology, Zysset and co-workers employed inelastic continuum material models where fabric tensors and volume fraction describe the heterogeneity and anisotropy of the bone, respectively (Charlebois et al. 2010a; Charlebois et al. 2010b; Chevalier et al. 2008; Rincon-Kohli and Zysset 2009; Zysset and Rincon-Kohli 2006; Zysset and Curnier 1996). Although such fabric based models have the advantage of incorporating trabecular inhomogeneity and anisotropy, they require microstructural properties of the trabeculae derived from methods such as μCT data.

In the present study, the video imaging of the macroscale VVTs reveals regions of localised trabecular whitening immediately adjacent to the punch, which remain almost constant with increased indentation. Such whitening regions signify localised plastic deformation, crushing and microdamage of trabeculae (Jungmann et al. 2011; Thurner et al. 2007; Thurner et al. 2006). The experimental yield type force-indentation curves are captured very well using the CFI plasticity formulation. Additionally, the CFI plasticity formulation predicts localised trabecular bone yield regions immediately below the punch that correlate closely with the experimentally measured whitening regions. The force-indentation curves and plastic zone size are also reasonably captured by a CFV plasticity formulation that incorporates asymmetric behaviour in hydrostatic tension and compression. However, non-yielding regions are predicted for the CFV plasticity formulation that are not observed experimentally. The VM, DP and Hill plasticity formulations over predict the experimental forces required to resist subsidence. In comparison with the experimental measurements, the VM, DP and Hill plasticity formulations also predict excessively large plastic zones that further enlarge with increased indentation. The Hill plasticity formulation, an extension of the VM plasticity formulation that incorporates anisotropic yield behaviour, cannot replicate the experimental results. The DP plasticity formulation cannot predict the correct

subsidence force or plastic zone size due to its linear yield surface in the $q - p$ plane that results in an increased yield stress with increased pressure. The VM plasticity formulation also predicts non-yielding regions at the punch-bone interface, which do not correlate with the experimentally observed whitening regions. The experimental study of Warden and Davy (2010), investigating trabecular damage after mechanical testing of IFDs to 1 and 2.5% strain, reports localised histologic damage and permanent deformation close to the implant-bone interface. The localised plastic zone reported by Warden and Davy (2010) supports our macroscale experimental results and CFI plasticity formulation predictions. The present study highlights the importance of implementing a pressure dependent plasticity formulation with an elliptical yield surface in the $q - p$ plane, such as the crushable foam plasticity formulations, when investigating continuum macroscale inelastic behaviour of trabecular bone, leading to accurate prediction of subsidence force and plastic zone size. As revealed in the present study, the VM, DP and Hill plasticity formulations will over predict the subsidence force and the plastic zone size.

The current study has some limitations that should be addressed in future work. In the macroscale experimental testing, only one indenter geometry was investigated. Further experimental studies with various endplate preparation techniques, IFD geometries and strain rates would be advantageous to further investigate the mechanics of vertebral subsidence. It is possible that the stress concentrations induced due to IFD implantation may result in remodelling of the underlying bone, which could alter the mechanics of subsidence. A 2D axisymmetric model was used for the macroscale computational analysis. A fully 3D geometry proved to be excessively computationally demanding due to the large inelastic deformation requiring the use of a remeshing algorithm. The predicted anisotropic behaviour of the μCT trabecular models was incorporated into the macroscale indentation simulations using a continuum based Hill plasticity formulation. Unlike the CFI and CFV plasticity formulations, a continuum based Hill plasticity formulation is limited in replicating the experimentally observed trabecular behaviour as it does not incorporate pressure dependent yielding. While the current study demonstrates the advantages of using a crushable foam plasticity formulation over the VM, DP and Hill plasticity formulations for predicting macroscale vertebral subsidence force and plastic zone size, the authors suggest that ongoing work should entail the simulation

of subsidence using alternative plasticity formulations proposed for trabecular bone such as the fabric based models of Zysset and co-workers, the modified super-ellipsoid yield criterion (Bayraktar et al. 2004), the Tsai-Wu plasticity formulation (Fenech and Keaveny 1999; Keaveny et al. 1999) or a plasticity formulation that incorporates pressure dependent yield, anisotropic yield and strength asymmetry. The incorporation of such a plasticity formulation that includes damage and fracture may also lead to enhanced results and may be a focus of a future study.

The present study provides a significant advance in the simulation of macroscale vertebral IFD subsidence. To the authors knowledge, the current study is the first to investigate the pressure dependent inelastic deformation of trabecular bone during vertebral device subsidence. Additionally, the study provides a correlation between trabecular whitening and regions of plastic deformation during vertebral device subsidence. The plastic zone regions predicted using the CFI plasticity formulation correlate well with the experimental whitening regions, which remain approximately constant in size with increased subsidence. Previous continuum based macroscale studies provide extremely limited predictions of subsidence as they have relied on linear elastic models material models (Lim et al. 2001; Polikeit et al. 2003a; Polikeit et al. 2003b). The present study demonstrates the importance of representing pressure dependent plasticity in continuum models of trabecular bone in order to accurately simulate vertebral subsidence.

Experimental studies on subsidence have predominantly focused on endplate preparation and implant geometry with the maximum failure load being measured to evaluate subsidence resistance (Closkey et al. 1993; Hollowell et al. 1996; Lim et al. 2001; Lowe et al. 2004; Oxland et al. 2003; Steffen et al. 2000). Oxland et al. (2003) found a significant decrease in failure load and stiffness for endplate removal. Lowe et al. (2004) found that mean failure loads for complete removal were significantly lower than partially removed or intact endplates. Using full and peripheral support devices, Steffen et al. (2000) found no difference in failure loads with intact endplates and removed (device sitting on periphery) endplates. Lim et al. (2001) found a reduction in compressive strength with complete endplate removal. According to Hollowell et al.(1996), the endplate thickness may not be sufficient to resist subsidence. The current study provides significant insight into trabecular bone plasticity and demonstrates that the pressure dependent crushable foam plasticity

formulations provide accurate macroscale continuum simulation of vertebral IFD subsidence. In particular, the current study demonstrates that the crushable foam plasticity formulations provide a reasonable representation of the multiaxial behaviour predicted by a μCT model of the trabecular microstructure, while also providing a close correlation with macroscale experimentation. It is therefore suggested that the crushable foam plasticity formulations could be used to accurately model the inelastic behaviour of trabecular bone for macroscale applications in which an explicit representation of the microstructure is not computationally feasible. Such accurate macroscale continuum models could be used to improve the design of IFDs and help guide clinical issues such as endplate preparation and device selection.

6.5 Conclusions

In summary, the μCT models elucidate that localised stress concentrations and yielding in the trabecular microstructure affect the apparent level pressure dependent plasticity of trabecular bone. It is demonstrated that simulation of multiaxial loading of representative samples of the trabecular bone microstructure can inform the development of accurate continuum models that can then be used for macroscale applications. The crushable foam plasticity formulations provide a reasonable link between the microscale and macroscale behaviour of trabecular bone. The multiaxial behaviour of a representative sample of trabecular bone microstructure is accurately replicated by crushable foam plasticity formulations. When applied to a macroscale study of vertebral device subsidence, the crushable foam plasticity formulations provide an accurate prediction of the experimental behaviour. Experimental trabecular whitening during vertebral device subsidence is quantified, and it is demonstrated that it is critically important to use a continuum plasticity formulation that replicates the inelastic pressure dependent behaviour of trabecular bone in order to accurately simulate the experimental behaviour. Unlike the VM, DP and Hill plasticity formulations, continuum based CFI and CFV plasticity formulations capture the macroscale inelastic pressure dependent yield behaviour of trabecular bone leading to the accurate prediction of subsidence force and plastic zone size during vertebral device subsidence. In conclusion, the study provides insight into the role of the trabecular microarchitecture in the macroscale multiaxial behaviour of trabecular bone. Furthermore, correct simulation of the pressure dependent yield behaviour of trabecular bone in a continuum model of vertebral subsidence is shown to provide strong agreement with experimental observations.

Appendix A Supplementary Images to Journal Publication

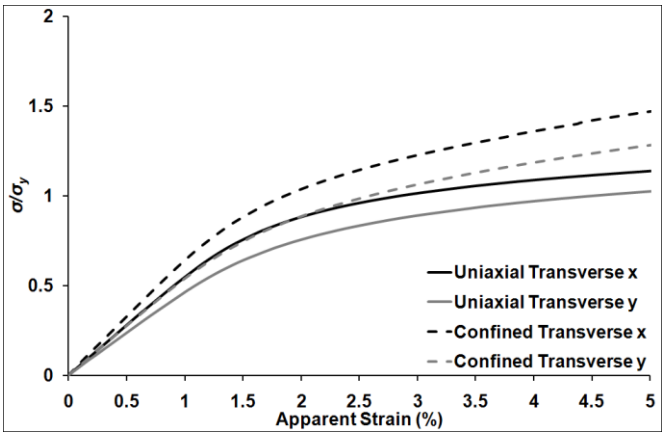

Figure 6-13 Computational results of the µCT based models under uniaxial and confined compression in the transverse loading directions for a perfectly-plastic von Mises (VM) plasticity formulation.

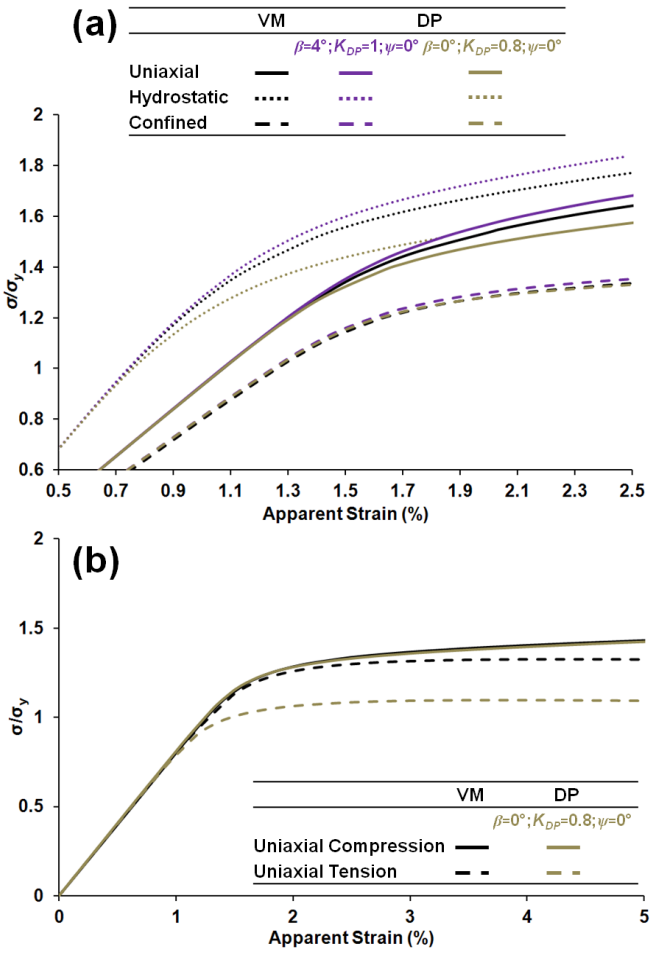

Figure 6-14 Computational results of the µCT based models for: (a) a von Mises (VM) and Drucker-Prager (DP) plasticity formulation under uniaxial compression, hydrostatic compression and confined compression (b) a VM plasticity formulation and a DP ($\beta = 0°$, $K_{DP} = 0.8$, $\psi = 0°$) plasticity formulation under uniaxial compression and uniaxial tension.

6.6 References

Bayraktar, H. H., Gupta, A., Kwon, R. Y., Papadopoulos, P., Keaveny, T. M. (2004) The modified super-ellipsoid yield criterion for human trabecular bone. J Biomech Eng 126 (6):677-684.

Bayraktar, H. H., Keaveny, T. M. (2004) Mechanisms of uniformity of yield strains for trabecular bone. J Biomech 37 (11):1671-1678.

Bessho, M., Ohnishi, I., Matsuyama, J., Matsumoto, T., Imai, K., Nakamura, K. (2007) Prediction of strength and strain of the proximal femur by a ct-based finite element method. J Biomech 40 (8):1745-1753.

Beutler, W. J., Peppelman, W. C. (2003) Anterior lumbar fusion with paired bak standard and paired bak proximity cages: Subsidence incidence, subsidence factors, and clinical outcome. Spine J 3 (4):289-293.

Boyd, S. K., Müller, R., Zernicke, R. F. (2002) Mechanical and architectural bone adaptation in early stage experimental osteoarthritis. J Bone Miner Res 17 (4):687-694.

Charlebois, M., Jirasek, M., Zysset, P. K. (2010a) A nonlocal constitutive model for trabecular bone softening in compression. Biomech Model Mechanobiol 9 (5):597-611.

Charlebois, M., Pretterklieber, M., Zysset, P. K. (2010b) The role of fabric in the large strain compressive behavior of human trabecular bone. J Biomech Eng 132:1-10.

Chen, L., Yang, H., Tang, T. (2005) Cage migration in spondylolisthesis treated with posterior lumbar interbody fusion using bak cages. Spine 30 (19):2171-2175.

Chevalier, Y., Charlebois, M., Pahr, D., Varga, P., Heini, P., Schneider, E., Zysset, P. (2008) A patient-specific finite element methodology to predict damage accumulation in vertebral bodies under axial compression, sagittal flexion and combined loads. Comput Method Biomech 11 (5):477-487.

Choi, J. Y., Sung, K. H. (2006) Subsidence after anterior lumbar interbody fusion using paired stand-alone rectangular cages. Eur Spine J 15 (1):16-22.

Closkey, R. F., Parsons, J. R., Lee, C. K., Blacksin, M. F., Zimmerman, M. C. (1993) Mechanics of interbody spinal fusion. Analysis of critical bone graft area. Spine 18 (8):1011.

Cowin, S. C., He, Q. C. (2005) Tensile and compressive stress yield criteria for cancellous bone. J Biomech 38 (1):141-144.

Derikx, L. C., Vis, R., Meinders, T., Verdonschot, N., Tanck, E. (2011) Implementation of asymmetric yielding in case-specific finite element models improves the prediction of femoral fractures. Comput Method Biomech 14 (02):183-193.

Eswaran, S. K., Gupta, A., Adams, M. F., Keaveny, T. M. (2006) Cortical and trabecular load sharing in the human vertebral body. J Bone Miner Res 21 (2):307-314.

Feerick, E. M., McGarry, J. P. (2012) Cortical bone failure mechanisms during screw pullout. J Biomech 45 (9):1666-1672.

Fenech, C. M., Keaveny, T. M. (1999) A cellular solid criterion for predicting the axial-shear failure properties of bovine trabecular bone. J Biomech Eng 121 (4):414-422.

Goldstein, S. A. (1987) The mechanical properties of trabecular bone: Dependence on anatomic location and function. J Biomech 20 (11-12):1055-1061.

Guillén, T., Zhang, Q. H., Tozzi, G., Ohrndorf, A., Christ, H. J., Tong, J. (2011) Compressive behaviour of bovine cancellous bone and bone analogous materials, microct characterisation and fe analysis. J Mech Behav Biomed Mater 4 (7):1452-1461.

Gupta, A., Bayraktar, H., Fox, J., Keaveny, T., Papadopoulos, P. (2007) Constitutive modeling and algorithmic implementation of a plasticity-like model for trabecular bone structures. Comput Mech 40 (1):61-72.

Harrison, N., McHugh, P. (2010) Comparison of trabecular bone behavior in core and whole bone samples using high-resolution modeling of a vertebral body. Biomech Model Mechanobiol 9 (4):469-480.

Harrison, N. M., McDonnell, P., Mullins, L., Wilson, N., O'Mahoney, D., McHugh, P. E. (2012) Failure modelling of trabecular bone using a non-linear combined damage and fracture voxel finite element approach. Biomech Model Mechanobiol:1-17.

Harrison, N. M., McDonnell, P. F., O'Mahoney, D. C., Kennedy, O. D., O'Brien, F. J., McHugh, P. E. (2008) Heterogeneous linear elastic trabecular bone modelling using micro-ct attenuation data and experimentally measured heterogeneous tissue properties. J Biomech 41 (11):2589-2596.

Hollowell, J. P., Vollmer, D. G., Wilson, C. R., Pintar, F. A., Yoganandan, N. (1996) Biomechanical analysis of thoracolumbar interbody constructs: How important is the endplate? Spine 21 (9):1032-1036.

Jungmann, R., Szabo, M. E., Schitter, G., Yue-Sing Tang, R., Vashishth, D., Hansma, P. K., Thurner, P. J. (2011) Local strain and damage mapping in single trabeculae during three-point bending tests. J Mech Behav Biomed Mater 4 (4):523-534.

Keaveny, T. M., Borchers, R. E., Gibson, L. J., Hayes, W. C. (1993) Trabecular bone modulus and strength can depend on specimen geometry. J Biomech 26 (8):991-1000.

Keaveny, T. M., Wachtel, E. F., Zadesky, S. P., Arramon, Y. P. (1999) Application of the tsai-wu quadratic multiaxial failure criterion to bovine trabecular bone. J Biomech Eng 121:99.

Keyak, J. H. (2001) Improved prediction of proximal femoral fracture load using nonlinear finite element models. Med Eng Phys 23 (3):165-173.

Keyak, J. H., Falkinstein, Y. (2003) Comparison of in situ and in vitro ct scan-based finite element model predictions of proximal femoral fracture load. Med Eng Phys 25 (9):781-787.

Keyak, J. H., Lee, I. Y., Nath, D. S., Skinner, H. B. (1996) Postfailure compressive behavior of tibial trabecular bone in three anatomic directions. J Biomed Mater Res 31 (3):373-378.

Kopperdahl, D. L., Keaveny, T. M. (1998) Yield strain behavior of trabecular bone. J Biomech 31 (7):601-608.

Lim, T. H., Kwon, H., Jeon, C. H., Kim, J. G., Sokolowski, M., Natarajan, R., An, H. S., Bj Andersson, G. (2001) Effect of endplate conditions and bone mineral density on the compressive strength of the graft-endplate interface in anterior cervical spine fusion. Spine 26 (8):951-956.

Linde, F., Hvid, I. (1989) The effect of constraint on the mechanical behaviour of trabecular bone specimens. J Biomech 22 (5):485-490.

Lowe, T. G., Hashim, S., Wilson, L. A., O'Brien, M. F., Smith, D. A. B., Diekmann, M. J., Trommeter, J. (2004) A biomechanical study of regional endplate strength and cage morphology as it relates to structural interbody support. Spine 29 (21):2389-2394.

Mc Donnell, P., Harrison, N., McHugh, P. E. (2010) Investigation of the failure behaviour of vertebral trabecular architectures under uni-axial compression and wedge action loading conditions. Med Eng Phys 32 (6):569-576.

McDonald, K., Little, J., Pearcy, M., Adam, C. (2010) Development of a multi-scale finite element model of the osteoporotic lumbar vertebral body for the investigation of apparent level vertebra mechanics and micro-level trabecular mechanics. Med Eng Phys 32 (6):653-661.

Morgan, E. F., Keaveny, T. M. (2001) Dependence of yield strain of human trabecular bone on anatomic site. J Biomech 34 (5):569-577.

Müller, R., Rüegsegger, P. (1995) Three-dimensional finite element modelling of non-invasively assessed trabecular bone structures. Med Eng Phys 17 (2):126-133.

Mullins, L. P., Bruzzi, M. S., McHugh, P. E. (2009) Calibration of a constitutive model for the post-yield behaviour of cortical bone. J Mech Behav Biomed Mater 2 (5):460-470.

Nagaraja, S., Couse, T. L., Guldberg, R. E. (2005) Trabecular bone microdamage and microstructural stresses under uniaxial compression. J Biomech 38 (4):707-716.

Niebur, G. L., Feldstein, M. J., Keaveny, T. M. (2002) Biaxial failure behavior of bovine tibial trabecular bone. J Biomech Eng 124 (6):699-705.

Niebur, G. L., Feldstein, M. J., Yuen, J. C., Chen, T. J., Keaveny, T. M. (2000) High-resolution finite element models with tissue strength asymmetry accurately predict failure of trabecular bone. J Biomech 33 (12):1575-1583.

Oxland, T. R., Grant, J. P., Dvorak, M. F., Fisher, C. G. (2003) Effects of endplate removal on the structural properties of the lower lumbar vertebral bodies. Spine 28 (8):771-777.

Polikeit, A., Ferguson, S. J., Nolte, L. P., Orr, T. E. (2003a) Factors influencing stresses in the lumbar spine after the insertion of intervertebral cages: Finite element analysis. Eur Spine J 12 (4):413-420.

Polikeit, A., Ferguson, S. J., Nolte, L. P., Orr, T. E. (2003b) The importance of the endplate for interbody cages in the lumbar spine. Eur Spine J 12 (6):556-561.

Prendergast, P. J., McHugh, P. E. Topics in bio-mechanical engineering. In: Proceeding of the 1st symposium on Biomechanical Engineering, Ireland, 2004. Trinity Centre for Bio-Engineering, pp 58-93.

Reilly, D. T., Burstein, A. H. (1974) The mechanical properties of cortical bone. J Bone Jt Surg Am 56 (5):1001-1022.

Reilly, D. T., Burstein, A. H. (1975) The elastic and ultimate properties of compact bone tissue. J Biomech 8 (6):393-396, 397-405.

Rincon-Kohli, L., Zysset, P. (2009) Multi-axial mechanical properties of human trabecular bone. Biomech Model Mechanobiol 8 (3):195-208.

Røhl, L., Larsen, E., Linde, F., Odgaard, A., Jørgensen, J. (1991) Tensile and compressive properties of cancellous bone. J Biomech 24 (12):1143-1149.

Steffen, T., Tsantrizos, A., Aebi, M. (2000) Effect of implant design and endplate preparation on the compressive strength of interbody fusion constructs. Spine 25 (9):1077-1084.

Thurner, P. J., Erickson, B., Jungmann, R., Schriock, Z., Weaver, J. C., Fantner, G. E., Schitter, G., Morse, D. E., Hansma, P. K. (2007) High-speed photography of compressed human trabecular bone correlates whitening to microscopic damage. Eng Fract Mech 74 (12):1928-1941.

Thurner, P. J., Erickson, B., Schriock, Z., Langan, J., Scott, J., Zhao, M., Weaver, J. C., Fantner, G. E., Turner, P., Kindt, J. H. (2006) High-speed photography of the development of microdamage in trabecular bone during compression. J Mater Res 21 (5):1093-1100.

Van Rietbergen, B., Weinans, H., Huiskes, R., Odgaard, A. (1995) A new method to determine trabecular bone elastic properties and loading using micromechanical finite-element models. J Biomech 28 (1):69-81.

Verhulp, E., Van Rietbergen, B., Müller, R., Huiskes, R. (2008) Micro-finite element simulation of trabecular-bone post-yield behaviour - effects of material model, element size and type. Comput Method Biomech 11 (4):389-395.

Warden, K. E., Davy, D. T. (2010) Localized trabecular damage adjacent to interbody fusion devices. Spine 35 (8):874-880.

Zysset, P., Rincon-Kohli, L. (2006) An alternative fabric-based yield and failure criterion for trabecular bone. In: Holzapfel, G. A., Ogden, R. W. (eds) Mechanics of biological tissue. Springer, Berlin, pp 457-470.

Zysset, P. K., Curnier, A. (1996) A 3d damage model for trabecular bone based on fabric tensors. J Biomech 29 (12):1549-1558.

Chapter 7

An Investigation of the Inelastic Behaviour of Trabecular Bone during the Press-fit Implantation of a Tibial Component in Total Knee Arthroplasty

Abstract

The stress distribution and plastic deformation of peri-prosthetic trabecular bone during press-fit tibial component implantation in total knee arthroplasty is investigated using experimental and finite element techniques. It is revealed that the computed stress distribution, implantation force and plastic deformation in the trabecular bone is highly dependent on the plasticity formulation implemented. By incorporating pressure dependent yielding using a crushable foam plasticity formulation to simulate the trabecular bone during implantation, highly localised stress concentrations and plastic deformation are computed at the bone-implant interface. If the pressure dependent yield is neglected using a traditional von Mises plasticity formulation, a significantly different stress distribution and implantation force is computed in the peri-prosthetic trabecular bone. The results of the study highlight the importance of: (i) simulating the insertion process of press-fit stem implantation; (ii) implementing a pressure dependent plasticity formulation, such as the crushable foam plasticity formulation, for the trabecular bone; (iii) incorporating friction at the implant-bone interface during stem insertion. Simulation of the press-fit implantation process and with an appropriate pressure dependent plasticity formulation should be implemented in the design and assessment of arthroplasty prostheses.

7.1 Introduction

Aseptic loosening is one of the most common cause of total hip and knee arthroplasty revision surgery, accounting for 16.1-41.5% of total knee arthroplasty (TKA) revision procedures (AOA 2011; Bozic et al. 2010; CJRR 2008-2009; Sharkey et al. 2002). Typically, surface cemented and uncemented TKA tibial components in are press-fit into the tibial metaphysis to achieve initial primary fixation. The effect of implantation on the surrounding trabecular bone is of great importance in understanding the mechanics of press-fit total arthroplasty components. During press-fit implantation the trabecular bone undergoes multiaxial loading, high confinement pressures and inelastic deformation at large strains. Stresses sufficiently high to cause inelastic deformation of trabecular bone can also be generated during the press-fit implantation of acetabular cups (Souffrant et al. 2012) and femoral stems (Taylor et al. 1995) in total hip arthroplasty. Despite this, biomechanical studies of total joint arthroplasty largely focus on the comparison of the pre-implanted intact bone with the post-implanted bone (Au et al. 2007; Au et al. 2005; Completo et al. 2007; Completo et al. 2006; Feerick et al. 2012), neglecting the effect of the inelastic deformation of the trabecular bone during surgical implantation. Previous finite element studies investigating press-fit implantation of total arthroplasty stems have used linear elastic material models (Monea et al. 2012). To the authors' knowledge, a plasticity formulation that includes pressure dependent yielding of the trabecular bone or PU, a synthetic trabecular bone analogue material, has not been considered for the implantation of a press-fit stem in total knee or hip arthroplasty.

Chapter 5 investigated the inelastic deformation of samples of bovine tibial trabecular bone and polyurethane foam (PU) under uniaxial and confined compression loading to large inelastic strains. Pressure dependent yield behaviour of trabecular bone under confined compression was uncovered and it was demonstrated that a crushable foam with isotropic hardening (CFI) plasticity formulation reasonably predicts the inelastic behaviour of both bovine trabecular bone and PU trabecular bone analogue (Chapter 5). The objective of the current study is to demonstrate the importance of using a crushable foam plasticity formulation to capture the inelastic pressure dependent behaviour of the trabecular material during the macroscale press-fit implantation of a TKA tibial component. The study also

investigates the potential inaccuracies that result from the commonly adopted von Mises (VM) plasticity formulation to model the inelastic behaviour of the trabecular bone. Experimental implantation of a tibial component into a synthetic sawbone tibia is also performed and the results are compared to the computed results for both plasticity formulations.

7.2 Methods

7.2.1 Macroscale Press-fit Tibial Component Implantation

Seven synthetic composite tibiae (#3402, 10 pcf PU) by sawbones (Pacific Research Labs, Malmö, Sweden) were used in the present study (Figure 7-1). All stages of tibial preparation were performed in accordance with the manufacturer's instructions by an orthopaedic resident (DTC) under the supervision of a consultant orthopaedic surgeon (FJS). The distal end of the tibia was potted. A tibial component of the Genesis II Total Knee System (Smith & Nephew, Memphis, TN, USA) was implanted into seven synthetic tibiae using an Instron testing machine (Model 4467, Instron Corp., Canton, MA, USA) under displacement control at a constant rate of 20 mm/min. The proximal ~30 mm of the tibial component has a diameter of 12 mm and the distal ~20 mm has a diameter of 10 mm (Figure 7-1). The punched hole has a constant diameter of 11 mm. Hence, the proximal ~30 mm of the tibial component is press-fit to achieve initial implant stability, with an interference of 1 mm. Force-displacement data was recorded for each tibial implantation.

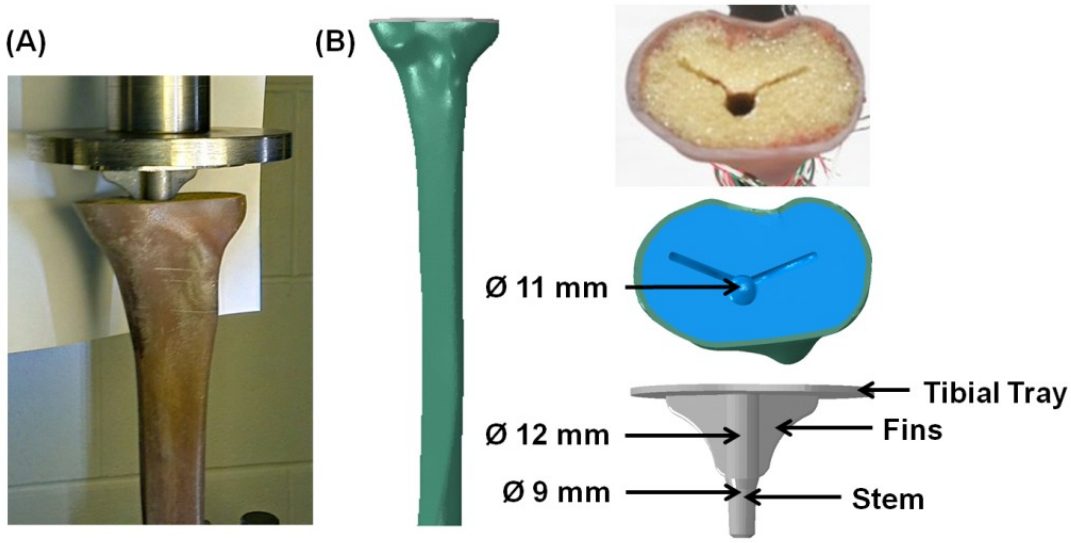

Figure 7-1 Experimental and computational models of the sawbone tibia and the tibial component of the Genesis II Total Knee System.

Computed tomography images (1 mm slice) of the composite tibial sawbone (#3402, 10 pcf PU) and replica models of the Genesis II tibial punch and tibial component were utilized to create 3D models of the experimental set-up (Figure 7-1). The proximal tibia was prepared as per the experimental testing using the

software Mimics (v14.11, Materialise, Leuven, Belgium). A 3D continuum finite element model of the prepared sawbone tibia was created (v6.0 3-Matic, Materialise, Leuven, Belgium) consisting of ~445,000 four noded linear tetrahedral elements and exported into the finite element solver Abaqus (v6.11 Abaqus Explicit, Dassault Systémes, Providence, RI, USA). Loads and boundary conditions were applied to replicate the experimental set-up. The distal end of the tibia was constrained in all directions. To achieve the press-fit implantation a displacement boundary condition was applied to the tibial tray in the axial direction (along the stem axis). The titanium tibial component was treated as a rigid body as it is several orders of magnitude stiffer than the trabecular bone. The cortical bone (short fiber glass epoxy resin) has an apparent Young's modulus (E) of 16.7 GPa and an elastic Poisson's ratio (ν_e) of 0.26 (according to the manufacturer (Sawbones Europe 2012)) and was assumed linear elastic, homogenous and isotropic. The synthetic trabecular material, PU, was assumed homogenous and isotropic and was modelled in separate analyses using a VM plasticity formulation and a CFI plasticity formulation (Figure 7-2). The elastic, yield and strain hardening material parameters for the PU were based on the uniaxial and confined compression testing of individual samples of PU as described in section 7.2.2. A surface-to-surface penalty contact algorithm was implemented between the implant and the bone. The effect of friction at the bone-implant interface was also investigated parametrically, varying the coulomb friction coefficient (μ) between 0 and 0.3 (Monea et al. 2012; Taylor et al. 1995). Stress distributions are shown at coronal and transverse sections through the depth of the proximal tibia as detailed in Figure 7-3.

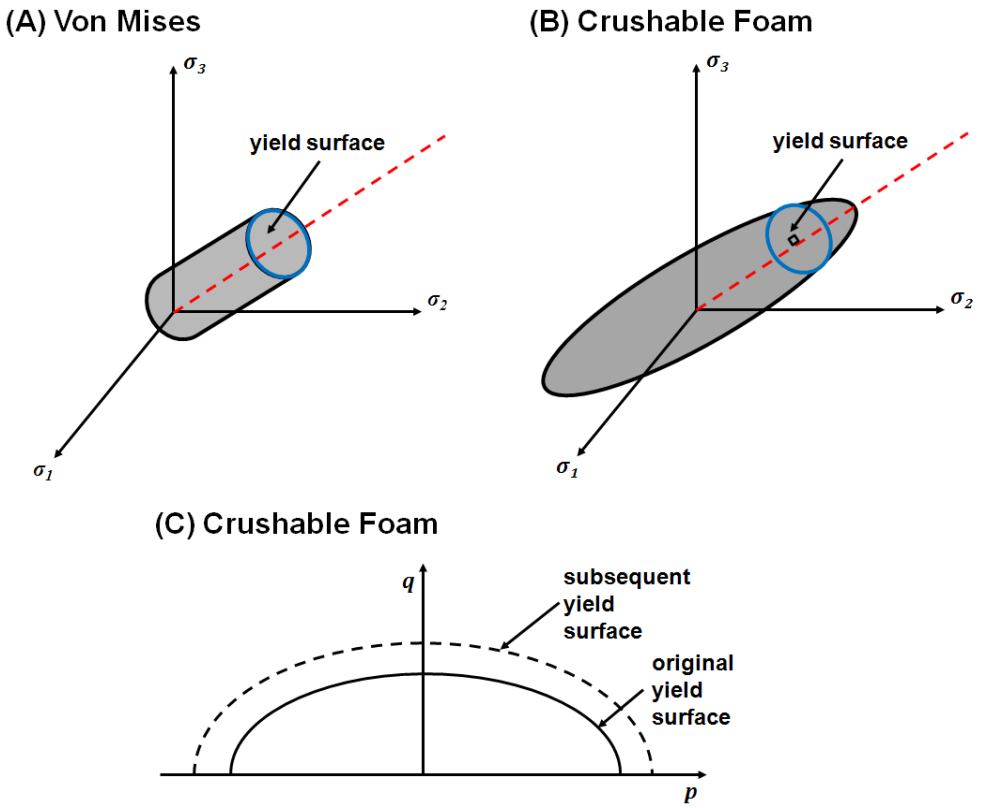

Figure 7-2 (a) The yield surface in principal stress space for the von Mises plasticity formulation (b) The yield surface in principal stress space for the crushable foam with isotropic hardening (CFI) plasticity formulation (c) The yield surface for the CFI plasticity formulation in the meridional $q - p$ stress plane

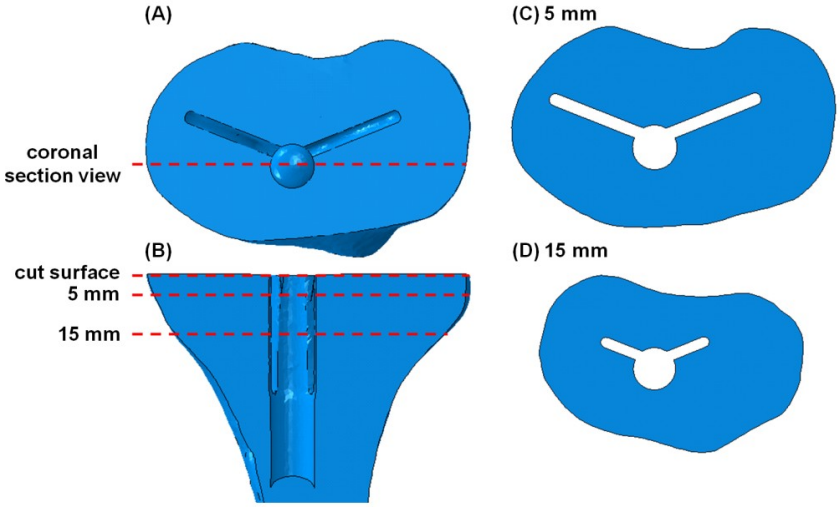

Figure 7-3 (A) Transverse view of the tibial cut surface detailing the coronal section view. (B) Coronal view of the proximal tibia detailing the transverse section view taken at 5 mm and 15 mm from the tibial cut surface. (C) Transverse section of the proximal tibia taken at 5 mm from the tibial cut surface. (D) Transverse section of the proximal tibia taken at 15 mm from the tibial cut surface.

7.2.2 Characterisation of Polyurethane Material Behaviour

In order to accurately simulate the implantation process of the tibial component, as described above, it is first important to characterise the multiaxial elasto-plastic behaviour of the PU. The method of testing the individual PU samples has been detailed for a different density of PU (20 pcf) in Chapter 5 and is briefly summarised in this section. Cubic samples of 15 mm ($n = 10$) of grade 10 cellular rigid closed cell PU (10 pcf, $\rho = 0.16$ g/cm^3) by sawbones (Pacific Research Labs, Malmö, Sweden) were cut using a bandsaw (Jubilee VBS 360, Addison Saws Ltd., West Midlands, UK). Uniaxial compression testing ($n = 5$) was performed using the standard platens test and confined compression testing ($n = 5$) was performed on a custom made confinement rig, preventing lateral displacement and generating a multiaxial stress state. A mechanical test machine was used to load under displacement control at a constant rate of 5 mm/min up to 60% nominal strain in the axis of loading (Instron Corp., Canton, MA, USA). The VM and CFI plasticity formulations were implemented in order to investigate their ability to replicate the inelastic behaviour of the PU under uniaxial and confined compression loading configurations.

7.3 Results

The results of this study are presented into two sections. In section 7.3.1, the material properties of the PU are characterised and the ability of the VM and CFI plasticity formulations to replicate the experimental behaviour is investigated. In section 7.3.2, the experimental and computational macroscale implantation of a TKA tibial component into synthetic tibiae is performed. The trabecular material (PU) is modelled using the VM and CFI plasticity formulations.

7.3.1 Results of Characterisation of Polyurethane Material Behaviour

The results of the characterisation of the individual samples of PU under uniaxial and confined compression loading are shown in Figure 7-4. A mean E of 39.13±5.90 MPa and a mean yield stress (σ_y) of 1.35±0.16 MPa are measured under uniaxial compression where the PU undergoes distinctive yielding followed by a stress plateau and densification at approximately 50% strain (Figure 7-4(A)). Under uniaxial compression loading both the VM and CFI plasticity formulations are calibrated to the experimental results (Figure 7-4(A)). However, under confined compression loading the VM plasticity formulation greatly over predicts the stresses post yield, as an increase in pressure does not result in material yielding (Figure 7-4(B)). In contrast, the CFI plasticity formulation accurately predicts the PU behaviour under confined compression for a uniaxial compression to hydrostatic compression yield stress ratio of K = 0.7 and a plastic Poisson's ratio of ν_p = 0.23 (Figure 7-4(B)).

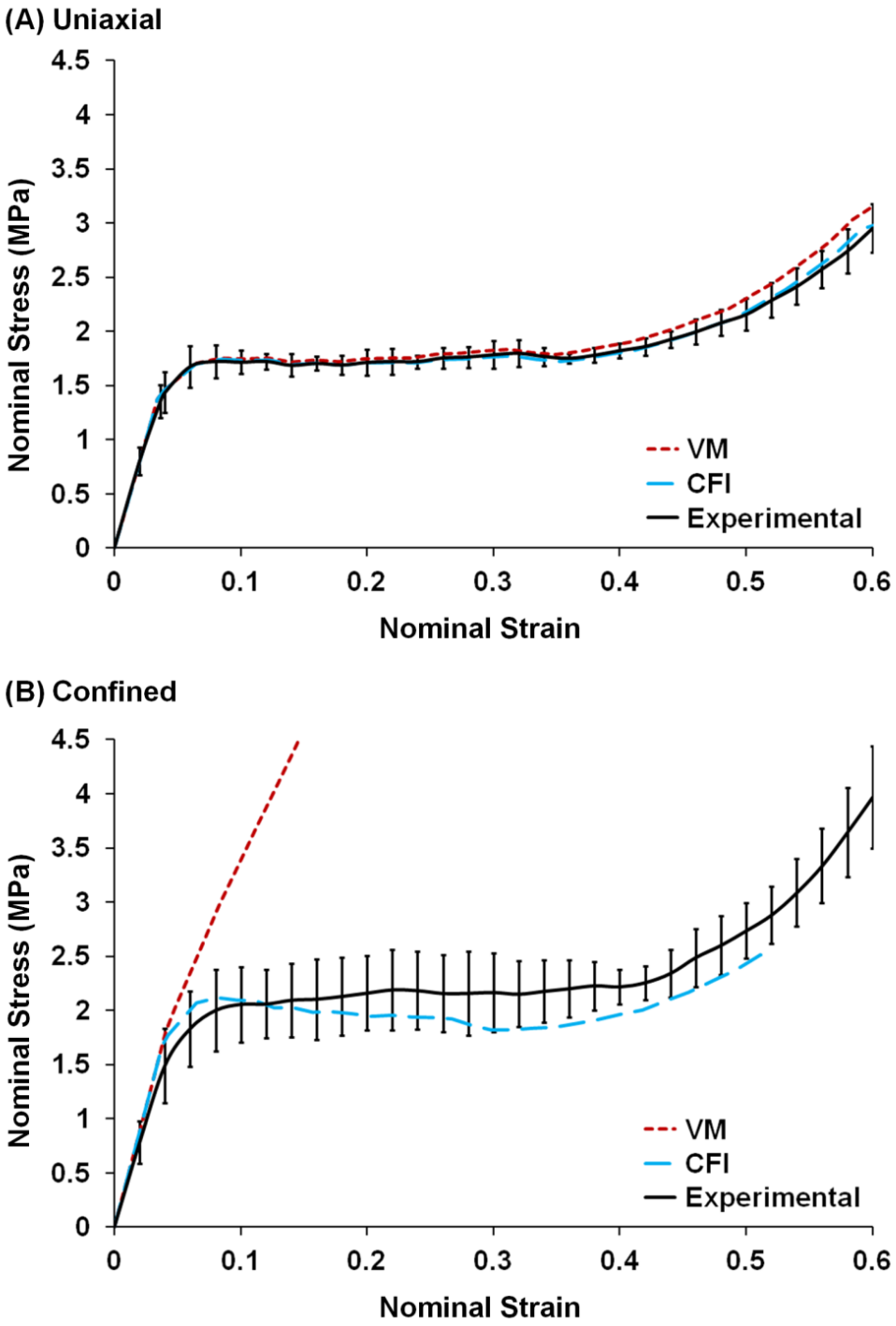

Figure 7-4 Experimental results (mean±SD) of the samples of polyurethane foam (PU), a synthetic trabecular bone analogue material, under uniaxial compression and confined compression loading configurations. Predicted behaviour for the von Mises (VM) plasticity formulation and crushable foam with isotropic hardening (CFI) plasticity formulation are also shown.

7.3.2 Macroscale Press-Fit Tibial Component Implantation Results

Distributions of equivalent plastic strain, von Mises equivalent stress and pressure stress are shown in Figures 7-5, 7-6 and 7-7 for the three section views illustrated in Figure 7-3. Simulations are performed using a VM plasticity formulation and a CFI plasticity formulation for the trabecular material with a friction coefficient of 0.2 at the bone-implant interface (Figures 7-5, 7-6 and 7-7). As previously stated, the proximal tibial stem is press-fit into the trabecular bone with an interference of 1 mm (Figure 7-1). As shown in Figure 7-5(A), at 50% implantation, higher localisations of equivalent plastic strain are evident at the bone-implant interface for the CFI plasticity formulation than for the VM plasticity formulation. It should also be noted that the plastic zone extends further into the peri-prosthetic trabecular bone for the VM plasticity formulation than for the CFI plasticity formulation (Figure 7-5(A)). Similar plastic strain results are also evident at full implantation for both plasticity formulations, as shown in Figure 7-5(B).

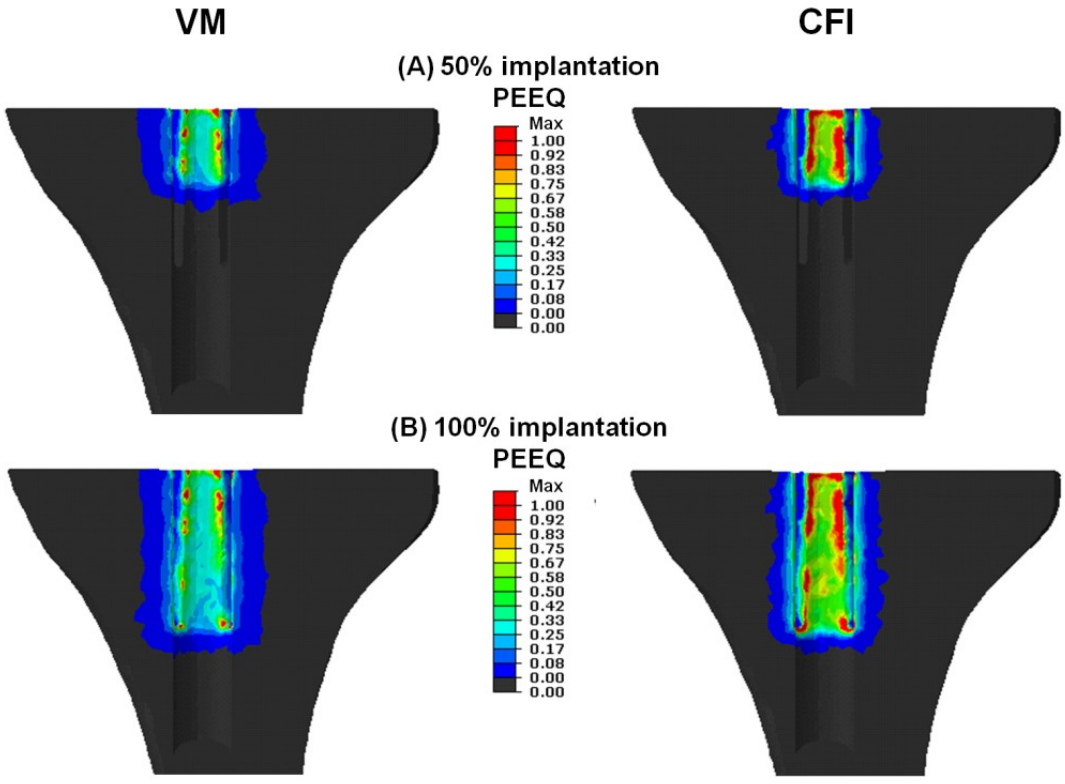

Figure 7-5 Coronal section views of equivalent plastic strain computational results of the press-fit implantation of a tibial component using a von Mises (VM) plasticity formulation (left) and a crushable foam with isotropic hardening (CFI) plasticity formulation (right) for the synthetic trabecular bone (μ = 0.2) at (A) 50% implantation and (B) 100% implantation. For clarity the implant and cortical bone are not shown.

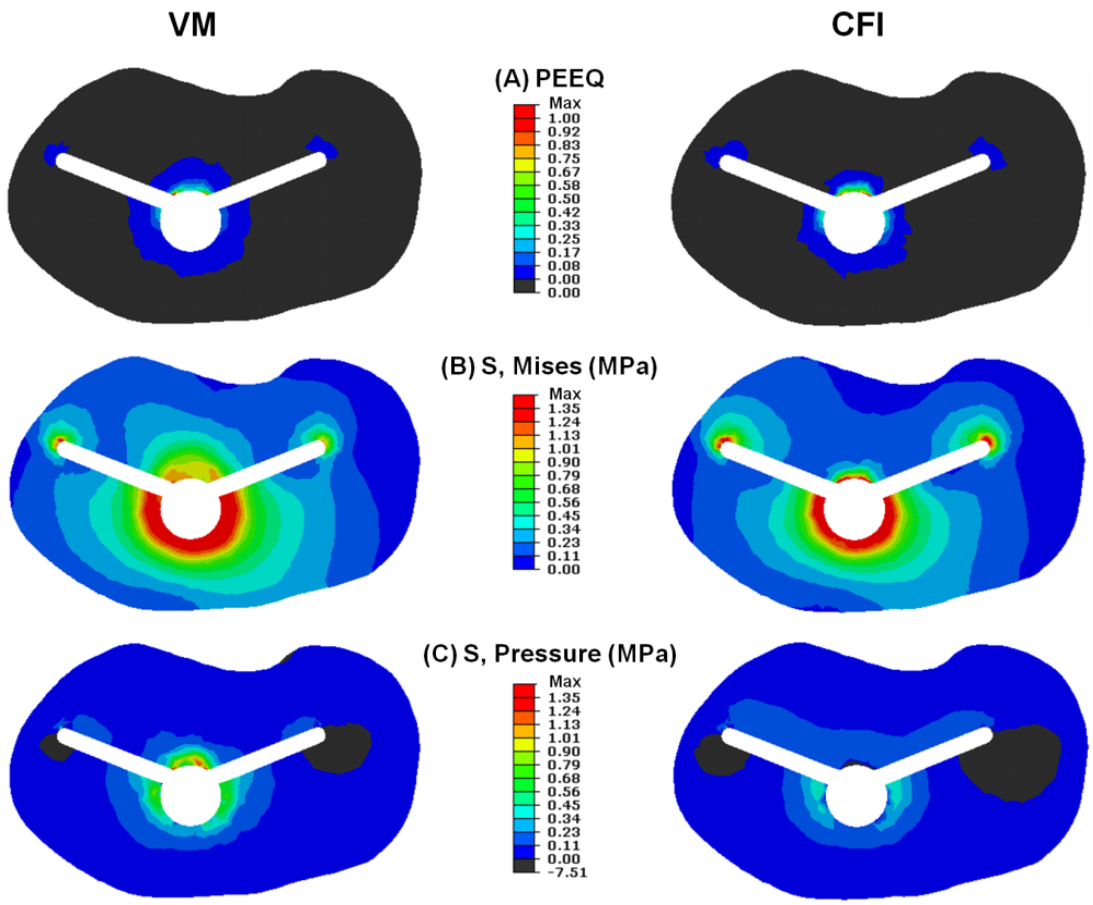

Figure 7-6 Transverse section views taken at 5 mm from the tibial cut surface of the press-fit implantation of the tibial component following full implantation. Results are presented for a von Mises (VM) plasticity formulation (left) and a crushable foam with isotropic hardening (CFI) plasticity formulation (right) for the synthetic trabecular bone (μ = 0.2). Contour plots are presented for the computed distribution of: (A) Equivalent plastic strain; (B) Von Mises equivalent stress; (C) Pressure stress. For clarity the implant and cortical bone are not shown.

Computational results are shown for a transverse section taken at 5 mm from the tibial cut surface in Figure 7-6 for both plasticity formulations. Again, as shown in Figure 7-6(A), a larger zone of plastic strain is evident for the VM plasticity formulation (extending ~4.1 mm from the bone-implant interface) than for the CFI plasticity formulation (extending ~5.7 mm from the bone-implant interface). The distribution of high von Mises equivalent stress is more localised at the bone-implant interface for the CFI plasticity formulation in comparison to the VM plasticity formulation, where regions of high stresses extend further into the peri-prosthetic bone (Figure 7-6(B)). In Figure 7-6(C), higher pressures are computed in the peri-prosthetic bone for the VM plasticity formulation than the CFI plasticity

formulation, due to pressure dependent yielding in the latter case. As expected, very similar trends of stress and plastic strain are also evident for a transverse section at 15 mm from the tibial cut surface (Figure 7-7). Overall, the predicted stress states are quite different at the implant-bone interface between the two plasticity formulations.

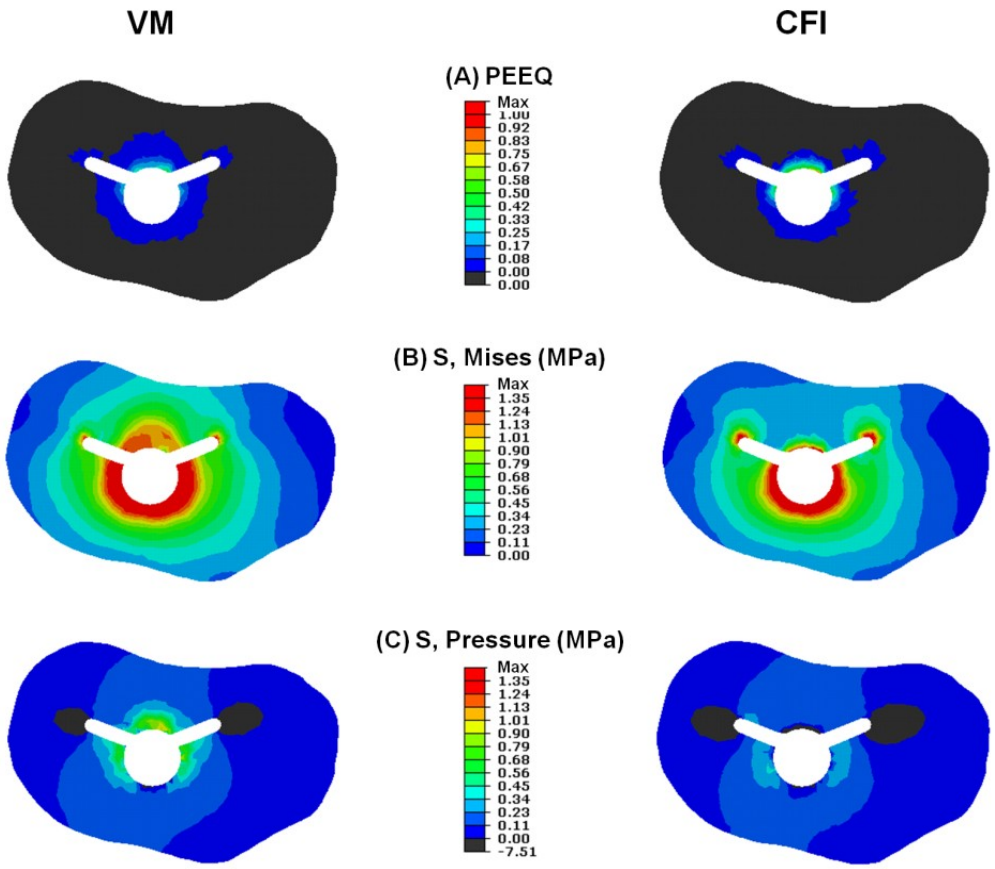

Figure 7-7 Transverse section views taken at 15 mm from the tibial cut surface of the press-fit implantation of the tibial component following full implantation. Results are presented for a von Mises (VM) plasticity formulation (left) and a crushable foam with isotropic hardening (CFI) plasticity formulation (right) for the synthetic trabecular bone (μ = 0.2). Contour plots are presented for the computed distribution of: (A) Equivalent plastic strain; (B) Von Mises equivalent stress; (C) Pressure stress. For clarity the implant and cortical bone are not shown.

The predicted force-displacement results for the macroscale press-fit implantation of the tibial component for the VM and CFI plasticity formulations are shown in Figure 7-8, again with a friction coefficient of 0.2 at the bone-implant interface. Experimentally measured force-displacement insertion results are also shown in Figure 7-8. As expected given the differences in the predicted stress states, significant differences in insertion force are predicted for both plasticity

formulations. For the CFI plasticity formulation, a friction coefficient of 0.2 provides a good match to the experimental results. However, when a VM plasticity formulation with a friction coefficient of 0.2 is used to model the synthetic trabecular material the computed results generally over predict the experimental implantation results.

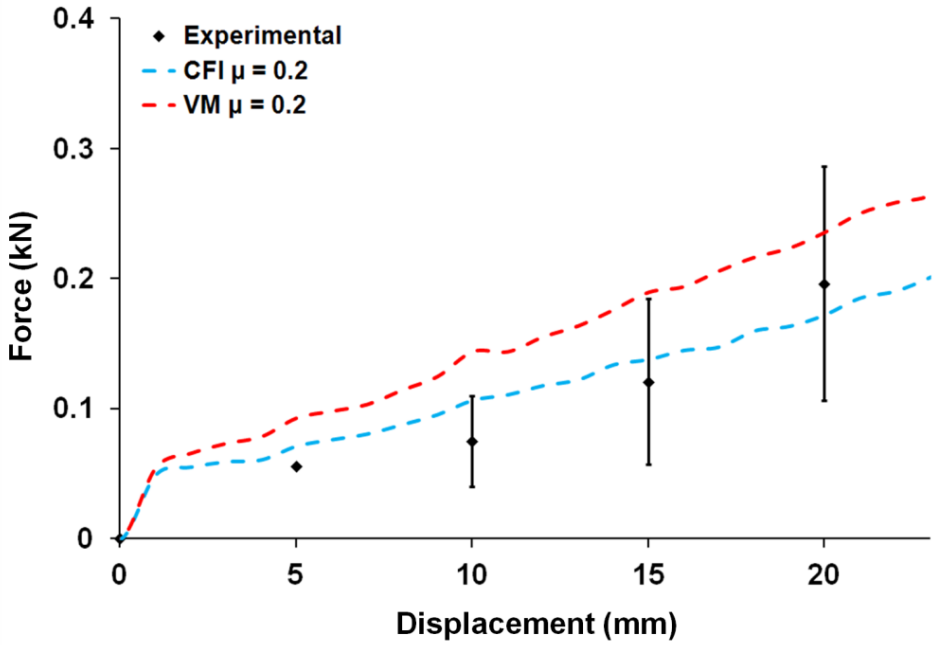

Figure 7-8 Experimentally measured implantation force during displacement of the press-fit tibial component into a synthetic tibia. Predicted results are also presented for a von Mises (VM) plasticity formulation and a crushable foam with isotropic hardening (CFI) plasticity formulation with a friction coefficient (μ) of 0.2 at the implant and bone.

A parametric investigation of the effect of friction coefficient on the predicted results for the macroscale tibial component implantation is shown in Figure 7-9. For higher friction coefficients, bigger differences are noted between the two plasticity formulations, with the VM plasticity formulation becoming more inaccurate. For example, for a friction coefficient of 0.3 at 20 mm insertion, the predicted force is ~31% higher for the VM plasticity formulation than for the CFI plasticity formulation. The present study demonstrates that in addition to using the correct plasticity formulation for trabecular bone, friction plays an important role during insertion at the bone-implant interface. To further emphasise this, a simulation with frictionless contact ($\mu = 0$) at the bone-implant interface is also shown in Figure 7-9, providing highly inaccurate results for both the VM and CFI plasticity formulations.

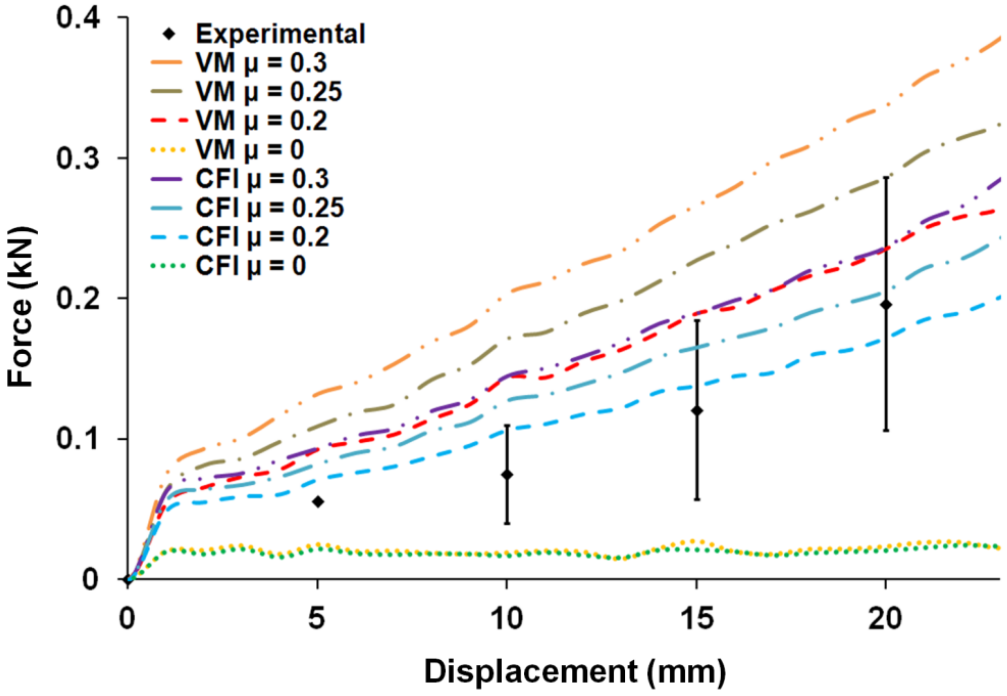

Figure 7-9 Predicted results of the tibial component implantation into a synthetic tibia for a von Mises (VM) plasticity formulation and a crushable foam with isotropic hardening (CFI) plasticity formulation with friction coefficients (μ) of between 0 and 0.3 at the implant and bone. The experimental force-displacement results are also shown for comparison.

7.4 Discussion

The present study examines plasticity in the peri-prosthetic trabecular bone during press-fit tibial component implantation in TKA. It is revealed that the computed stress distribution, implantation force and plastic deformation in the trabecular bone is highly dependent on the plasticity formulation implemented. By incorporating pressure dependent yielding using a CFI plasticity formulation to simulate the trabecular bone during implantation, highly localised stress concentrations and plastic deformation are computed at the bone-implant interface. If the pressure dependent yield is neglected using a traditional VM plasticity formulation, a significantly different peri-prosthetic stress distribution and implantation force is computed in the trabecular bone. The results demonstrate the importance of modelling the implantation of press-fit stem prostheses due to the high levels of stress and deformation computed in the peri-prosthetic trabecular bone during this process. Moreover, the study demonstrates the significance of choosing the correct plasticity formulation to model the inelastic deformation of the trabecular bone during implantation. The importance of incorporating friction at the bone-implant interface during simulation of the stem insertion process is also emphasised.

The significance of implementing the correct plasticity formulation when simulating the inelastic deformation of trabecular bone during the implantation process of press-fit stems in total arthroplasty prostheses is demonstrated in the present study. Overall, the predicted stress states in the trabecular material are quite different at the implant-bone interface for both the VM plasticity formulation and the CFI plasticity formulation. Unlike the VM plasticity formulation, the multiaxial stress state developed in the trabecular material during press-fit stem implantation leads to pressure dependent yielding for the CFI plasticity formulation. Highly localised pressures are computed near the bone-implant interface for the CFI plasticity formulation which leads to high levels of localised plastic yielding directly at the interface; hence, lower stresses and pressures are computed further into the trabecular material. Although the present study focuses on PU, a synthetic trabecular analogue material, the ability of a CFI plasticity formulation to capture the multiaxial pressure dependent plasticity of natural trabecular bone has previously been observed (Chapter 5 and Chapter 6). Highly localised peri-prosthetic plasticity has also been observed experimentally during vertebral fusion device subsidence

(Chapter 6). Correct prediction of this stress distribution at the bone implant-interface will have implications for device design and in particular for peri-prosthetic bone remodelling and initial implant stability of the tibial component, which have been investigated in previous biomechanical studies (Efe et al. 2011; Luring et al. 2006; Peters et al. 2003; Seki et al. 1997; Skwara et al. 2009). To our knowledge, the current study is the first to implement the CFI plasticity formulation for the trabecular material in the investigation of press-fit stem implantation in total arthroplasty.

In the present study, for a friction coefficient of 0.2 at the bone-implant interface during implantation, the CFI plasticity formulation provides a reasonable match to the experimental data, whereas, the VM plasticity formulation over predicts the experimental results. An increase in friction results in an increase in the difference in force predicted for both plasticity formulations. For a frictionless implantation, highly inaccurate insertion forces are computed for both plasticity formulations, indicating the importance of the role of friction at the interface during press-fit implantation. A study by Grant et al. (2007) measured friction coefficients of 0.22-0.71 for dry sawbone PU on grit-blasted or porous-beaded titanium. However, it should be noted that the applied contact pressures (≤1 MPa) of Grant et al. (2007) are not sufficiently high to result in plastic deformation of the PU. In comparison to an elastic case, localised plasticity at the implant-bone interface may lead to significant changes in the PU surface roughness and hence to the friction coefficient. Indeed, it could be suggested that the experimental-computational approach used in the present study, using an accurate pressure dependent plasticity formulation for the PU, provides a method of calibrating the appropriate friction coefficient during press-fit stem insertion where localised plasticity occurs at the contact surface. In the present study, a friction coefficient of ~0.2 is found to give the closest correlation to the experimental implantation data when a CFI plasticity formulation is used. Experimental errors may have occurred due to malalignment or slippage of the tibial stem during implantation, although due care was taken during bone preparation and implantation to account for the 3° posterior slope of the Genesis II tibial component. An increase in experimental standard deviation is evident in the insertion results which may be a result of debris generated due to the large deformation of the PU, a feature that is not incorporated into the computational models. The present study

firmly establishes that it is extremely important to consider friction at the bone-implant interface (in addition to using an appropriate plasticity formulation) when modelling press-fit stem implantation. A previous study of Monea et al. (2012) included friction (μ = 0-0.2) at the interface for the insertion of a femoral hip arthroplasty stem with press-fit rings. Earlier studies investigating press-fit stem implantation using interface elements at the bone-implant interface (Helgason et al. 2008; Ramamurti et al. 1997; Taylor et al. 1995), without directly simulating the insertion process, fail to capture the significant effect of friction at the interface.

The importance of implementing a pressure dependent plasticity formulation, such as the CFI plasticity formulation, in the simulation of the press-fit stem implantation process is evident in the present work. Implantation stresses computed in the present study are significant to cause yielding of the trabecular material and are comparable or higher to trabecular stresses that occur during normal physiological loading (Monea et al. 2012; Taylor et al. 1995). Despite this, numerous previous arthroplasty studies that aim to accurately predict stresses in the cortical and trabecular bone, neglect to consider these significant stresses generated during implantation and solely investigated the posted-implanted case (Au et al. 2007; Au et al. 2005; Completo et al. 2007; Completo et al. 2006; Feerick et al. 2012; Kluess et al. 2009). Apart from the study of Monea et al. (2012) that employed a linear elastic model during stem insertion modelling, other studies neglected to simulate the actual press-fit stem insertion process and employed interface elements to simulate the post-implantation press-fit conditions, assuming linear elasticity (Ramamurti et al. 1997) or a VM plasticity formulation (Helgason et al. 2008; Taylor et al. 1995) for the trabecular material.

Linear elasticity has also been employed for the investigation of press-fit acetabular cups in hip arthroplasty, either by simulating the insertion process (Clarke et al. 2012; Spears et al. 1999) or by neglecting the insertion process and using a volume increase via thermal expansion of the elements (Bellini et al. 2007; Dalstra and Huiskes 1994) to generate prestresses due to implantation in the trabecular material. A recent study by Souffrant et al. (2012) investigated pressure dependent yielding by implementing a crushable foam with volumetric hardening (CFV) plasticity formulation for the synthetic trabecular material when investigating the stability of press-fit acetabular cups in hip arthroplasty. The implantation of a press-fit

acetabular cup is, however, quite different to a press-fit stem implantation as it involves very little sliding during insertion. Chapter 6 investigated the subsidence of a vertebral interbody fusion device into ovine vertebrae and a good correlation to the experimental results was achieved when a CFI and a CFV plasticity formulation were used to represent the trabecular bone.

Trabecular bone in the proximal tibia is natural confined by a stiff cortical shell and undergoes multiaxial compressive loading during normal physiological loading in addition to during the press-fit implantation of a TKA tibial component. Therefore, the material parameters used for the plasticity formulations in macroscale testing should be validated against multiaxial loading conditions such as confined compression testing as demonstrated in the present study. Under confined compression a CFI plasticity formulation captures the inelastic pressure dependent behaviour of the 10 pcf cellular rigid PU, with the predicted results being qualitatively similar to the experimental stress-strain curves. The results of the present study are in agreement with the confined compression results of Chapter 5 that demonstrate the ability of a CFI plasticity formulation to predict the inelastic behaviour of bovine tibial trabecular bone and an alternate grade of cellular rigid PU (20 pcf, ρ = 0.32 g/cm^3). For a VM plasticity formulation the PU stresses are largely over predicted PU under confined compression due to the absence of pressure dependent yielding. It should also be noted that for an alternative grade and type of PU, solid rigid PU (50 pcf), Chapter 5 demonstrated that no pressure dependent yielding is observed under confined compression. Unlike the cellular PU used in the present study, the 50 pcf near poreless solid rigid PU obeys a VM plasticity formulation, hence it is not representative of natural porous trabecular bone under multiaxial loading, due to the fact that it lacks a cellular structure (Chapter 5). Therefore, when choosing a synthetic substitute for trabecular bone for experimentation that involves inelastic multiaxial deformation, it is important to select a type and grade of PU that also undergoes similar pressure dependent yielding to trabecular bone.

A limitation of the current work is the use of PU as a substitute for natural trabecular bone. Synthetic bones were used due to their reproducibility in terms of material properties, consistent specimen size, consistent porosity and availability. The measured values of Young's modulus (39.13±5.90 MPa) and yield stress

(1.35±0.16 MPa) for the PU under uniaxial compression are in the lower range of reported values for human proximal tibial trabecular bone (Goldstein et al. 1983; Morgan and Keaveny 2001; Røhl et al. 1991) and may be representative of osteoporotic trabecular bone. However, as previously stated, under confined compression similar pressure dependent yield behaviour is observed for the PU to that observed for trabecular bone (Chapter 5). The friction coefficient between the implant and PU was not directly measured in the present study. However as mentioned previously, the localised crushing and yielding of the PU that occurs during the implantation process, makes standard friction measuring difficult. A relationship between contact stress, pressure dependent plasticity and friction coefficient is beyond the scope of the present study but warrants future investigation. It may be considered a limitation that a single implant geometry was considered in the present work. However, it is likely that similar differences in predicted results for the VM and CFI plasticity formulations would also occur for other implant geometries and press-fit stems in other arthroplasty locations. It is a common assumption in computational studies that trabecular bone is homogenous and isotropic, although, it is widely accepted that trabecular bone is both anisotropic and heterogeneous. In addition to incorporating a pressure dependent plasticity of the trabecular bone, incorporation of anisotropic and heterogeneous trabecular properties in the computational models may yield improved results.

7.5 Conclusions

The present study demonstrates the importance of implementing the correct plasticity formulation for trabecular bone when simulating the inelastic trabecular deformation during the implantation of a press-fit tibial component in TKA. The computed stress distribution, implantation force and plastic deformation in the trabecular bone is highly dependent on the plasticity formulation used. These differences in stress distributions can be explained by the fact that the multiaxial stress state developed in the trabecular material during press-fit stem implantation leads to pressure dependent yielding for the CFI plasticity formulation; hence, reducing the stresses in the peri-prosthetic bone. For a VM plasticity formulation, the pressure dependent yielding is neglected and a very different stress state, implantation force and plastic deformation are predicted. In order to accurately capture the inelastic deformation of trabecular bone during press-fit stem implantation in total arthroplasty, the results of the present study highlight the importance of: (i) simulating the insertion process of press-fit stem implantation; (ii) implementing a pressure dependent plasticity formulation, such as the CFI plasticity formulation, for the trabecular material; (iii) incorporating friction at the implant-bone interface during stem insertion. The implications of simulating the implantation process and correctly modelling the trabecular bone plasticity should be considered in the design and assessment of press-fit total arthroplasty prostheses.

7.6 References

AOA (2011) Australian orthopaedic association national joint replacement registry. Demographics of knee arthroplasty, supplementary report.

Au, A. G., James Raso, V., Liggins, A. B., Amirfazli, A. (2007) Contribution of loading conditions and material properties to stress shielding near the tibial component of total knee replacements. J Biomech 40 (6):1410-1416.

Au, A. G., Liggins, A. B., Raso, V. J., Amirfazli, A. (2005) A parametric analysis of fixation post shape in tibial knee prostheses. Med Eng Phys 27 (2):123-134.

Bellini, C. M., Galbusera, F., Ceroni, R. G., Raimondi, M. T. (2007) Loss in mechanical contact of cementless acetabular prostheses due to post-operative weight bearing: A biomechanical model. Med Eng Phys 29 (2):175-181.

Bozic, K. J., Kurtz, S. M., Lau, E., Ong, K., Chiu, V., Vail, T. P., Rubash, H. E., Berry, D. J. (2010) The epidemiology of revision total knee arthroplasty in the united states. Clinical Orthop 468 (1):45-51.

CJRR (2008-2009) Hip and knee replacements in canada. Canadian joint replacement registry.

Clarke, S. G., Phillips, A. T. M., Bull, A. M. J., Cobb, J. P. (2012) A hierarchy of computationally derived surgical and patient influences on metal on metal press-fit acetabular cup failure. J Biomech 45 (9):1698-1704.

Completo, A., Fonseca, F., Simoes, J. A. (2007) Finite element and experimental cortex strains of the intact and implanted tibia. J Biomech Eng 129 (5):791-797.

Completo, A., Simöes, J. A., Fonseca, F. (2006) A finite element analysis of long stemmed distal tip fixation conditions in tibial knee replacement. J Biomech 39 (Supplement 1):S517-S518.

Dalstra, M., Huiskes, R. (1994) Prestresses around the acetabulum generated by screwed cups. Clin Mater 16 (3):145-154.

Efe, T., Figiel, J., Danek, S., Tibesku, C. O., Paletta, J. R. J., Skwara, A. (2011) Initial stability of tibial components in primary knee arthroplasty. A cadaver study comparing cemented and cementless fixation techniques. Acta Orthop Belg 29 (15):50.

Feerick, E. M., Kennedy, J., Mullett, H., FitzPatrick, D., McGarry, J. P. (2012) Investigation of metallic and carbon fibre peek fracture fixation devices for three-part proximal humeral fractures. Med Eng Phys In Press.

Goldstein, S. A., Wilson, D. L., Sonstegard, D. A., Matthews, L. S. (1983) The mechanical properties of human tibial trabecular bone as a function of metaphyseal location. J Biomech 16 (12):965-969.

Grant, J. A., Bishop, N. E., Götzen, N., Sprecher, C., Honl, M., Morlock, M. M. (2007) Artificial composite bone as a model of human trabecular bone: The implant-bone interface. 40 (5):1158-1164.

Helgason, B., Viceconti, M., Rúnarsson, T. P., Brynjólfsson, S. (2008) On the mechanical stability of porous coated press fit titanium implants: A finite element study of a pushout test. J Biomech 41 (8):1675-1681.

Kluess, D., Souffrant, R., Mittelmeier, W., Wree, A., Schmitz, K.-P., Bader, R. (2009) A convenient approach for finite-element-analyses of orthopaedic implants in bone contact: Modeling and experimental validation. Comput Method Biomec 95 (1):23-30.

Luring, C., Perlick, L., Trepte, C., Linhardt, O., Perlick, C., Plitz, W., Grifka, J. (2006) Micromotion in cemented rotating platform total knee arthroplasty: Cemented tibial stem versus hybrid fixation. Arch Orthop Trauma Surg 126 (1):45-48.

Monea, A. G., Pastrav, L. C., Mulier, M., Van der Perre, G., Jaecques, S. V. (2012) Numerical simulation of the insertion process of an uncemented hip prosthesis in order to evaluate the influence of residual stress and contact distribution on the stem initial stability. Comput Method Biomec:1-14.

Morgan, E. F., Keaveny, T. M. (2001) Dependence of yield strain of human trabecular bone on anatomic site. J Biomech 34 (5):569-577.

Peters, C. L., Craig, M. A., Mohr, R. A., Bachus, K. N. (2003) Tibial component fixation with cement: Full-versus surface-cementation techniques. Clin Orthop 409:158.

Ramamurti, B. S., Orr, T. E., Bragdon, C. R., Lowenstein, J. D., Jasty, M., Harris, W. H. (1997) Factors influencing stability at the interface between a porous surface and cancellous bone: A finite element analysis of a canine in vivo micromotion experiment. J Biomed Mater Res 36 (2):274-280.

Røhl, L., Larsen, E., Linde, F., Odgaard, A., Jørgensen, J. (1991) Tensile and compressive properties of cancellous bone. J Biomech 24 (12):1143-1149.

Sawbones Europe, A. B. (2012) Product catalogue.

Seki, T., Bourgeault, C., Chareancholvanich, A. K., Lew, W., Bechtold, J. E., Gustilo, R. B. (1997) Does a central stem affect bone strain and the stability of a cemented tibial tray in primary and revision tka. Trans Orthop Res Soc 22:635.

Sharkey, P. F., Hozack, W. J., Rothman, R. H., Shastri, S., Jacoby, S. M. (2002) Why are total knee arthroplasties failing today? Clinical Orthop 404:7-13.

Skwara, A., Figiel, J., Knott, T., Paletta, J. R. J., Fuchs-Winkelmann, S., Tibesku, C. O. (2009) Primary stability of tibial components in tka: In vitro comparison of two cementing techniques. Arthroscopy 17 (10):1199-1205.

Souffrant, R., Zietz, C., Fritsche, A., Kluess, D., Mittelmeier, W., Bader, R. (2012) Advanced material modelling in numerical simulation of primary acetabular press-fit cup stability. Comput Method Biomec 15 (8):787-793.

Spears, I. R., Morlock, M. M., Pfleiderer, M., Schneider, E., Hille, E. (1999) The influence of friction and interference on the seating of a hemispherical press-fit cup: A finite element investigation. J Biomech 32 (11):1183-1189.

Taylor, M., Tanner, K. E., Freeman, M. A. R., Yettram, A. L. (1995) Cancellous bone stresses surrounding the femoral component of a hip prosthesis: An elastic-plastic finite element analysis. Med Eng Phys 17 (7):544-550.

Chapter 8

Concluding Remarks

The overall aim of this thesis is to provide a better understanding of the post yield behaviour of trabecular bone using experimental and computational analyses and to investigate the importance of multiaxial trabecular bone plasticity in the implantation and failure of orthopaedic devices. Experimental confined compression testing of trabecular bone samples reveal a distinctive yield point in the stress-strain curve followed by a stress plateau. It is demonstrated that crushable foam plasticity formulations based on a pressure dependent yield criterion provide an accurate representation of the response of trabecular bone to confined compression tests. Similar pressure dependent yield behaviour is also observed for synthetic trabecular bone under confined compression. Two macroscale orthopaedic applications are investigated, the surgical implantation of press-fit stemmed tibial components in total knee arthroplasty and the subsidence of vertebral interbody fusion devices into trabecular bone. Both macroscale applications demonstrate the importance of implementing continuum based plasticity formulation with an elliptical yield surface in the von Mises equivalent stress-pressure plane in predicting experimentally observed behaviour. In the technical studies of Chapters 4, 5, 6 and 7, detailed and focused discussions of the specific findings of each chapter have been presented. Therefore, the purpose of the current chapter is to briefly summarise the key findings of the thesis and to outline the significance of these findings for the analysis, design and development of orthopaedic devices. Some indications for possible future experimental and computational studies are also suggested.

In Chapter 4, the effect of full cementation and surface cementation of the tibial component in total knee arthroplasty on the stress/strain state in the underlying bone is investigated. Experimental measurement and computational prediction of surface cortical bone strains demonstrate differences in the full and surface cementation techniques. Computational investigation of the trabecular bone stress/strain state provides further insight into the differences between the two cementation techniques,

with predicted differences in trabecular bone strain being far more pronounced than for the cortical strain. This suggests that for the assessment of device design, an exclusive reliance on cortical strain measurements offers limited insight, particularly for press-fit implants where the peri-prosthetic trabecular bone stress/strain state is critical. The computational models predict that both cementation techniques result in lower trabecular bone stresses beneath the baseplate in comparison to the intact case, with a greater reduction computed for full cementation. Additionally, bone remodelling simulations predict greater proximal bone resorption for full cementation. Predicted negative bone remodelling around the proximal stem for full cementation may increase the rate of aseptic loosening. Therefore, it is advocated that the surface cementation technique should be performed if the patient has sufficient bone stock to achieve good primary fixation. The findings of Chapter 4 are aligned with the bone remodelling predictions in a recent computational study of Chong et al. (2011) and with the clinical bone mineral density results of Lonner et al. (2001). In addition to the bone remodelling predictions, Chapter 4 also provides a detailed analysis of the peri-prosthetic trabecular bone stress state, revealing that von Mises equivalent stresses are close to the reported yield stress, and that high pressures are computed near the implant-bone interface. For adequate press-fit cementless stem fixation, it is paramount that the peri-prosthetic stress state is accurately characterised. In the overall perspective of this thesis, the prediction of high trabecular von Mises equivalent stress and pressures is particularly significant and provides a strong motivation for investigation of the multiaxial inelastic deformation of trabecular bone.

In Chapter 5, the pressure dependent inelastic behaviour of natural and synthetic trabecular bone is investigated. The multiaxial stress state of trabecular bone is evident in the initial elastic simulations presented in Chapter 4.Trabecular bone is naturally confined by a stiff cortical shell and physiological loading results in a multiaxial stress state, particularly in the peri-prosthetic bone surrounding an implant. Studies to date have primarily relied on uniaxial compression testing to characterise trabecular bone (Goldstein 1987; Goldstein et al. 1983; Harrison et al. 2008; Keaveny et al. 1993; Keaveny et al. 1997; Keaveny et al. 1994; Keyak et al. 1996; Kopperdahl and Keaveny 1998; Linde and Hvid 1989; Morgan and Keaveny

2001; Mosekilde and Danielsen 1987; Røhl et al. 1991). Linde and Hvid et al. (1989) performed confined compression testing only in the elastic regime. Only the study of Charlebois et al. (2010) has considered the post yield behaviour of trabecular bone under confined compression. The confined compression experiments in the present work display a distinctive yield point followed by a near constant stress plateau. The results of Chapter 5 demonstrate that the Drucker-Prager and Mohr-Coulomb plasticity formulations are not suitable for modelling the inelastic behaviour of trabecular bone under a triaxial stress state. For these plasticity formulations the von Mises equivalent yield stress increases with increasing pressure, therefore the distinctive and plateau behaviour is not computed for confined compression as increased pressure due to the triaxial stress state does not result in plastic behaviour. Additionally, the pressure independent von Mises plasticity formulation also fails to accurately predict the response of trabecular bone to confined compression. In contrast, crushable foam plasticity formulations provide an accurate prediction of the inelastic behaviour of trabecular bone under confined compression loading, capturing the distinctive yield point and post yield stress plateau observed experimentally. This is due to the fact that the crushable foam plasticity formulations define an elliptical yield surface in the von Mises equivalent stress-pressure plane whereby an increase in pressure results in a decrease in von Mises equivalent yield stress. Without considering multiaxial yield behaviour, previous studies have implemented the von Mises, Mohr-Coulomb and Drucker-Prager plasticity formulations for trabecular bone (Bessho et al. 2007; Derikx et al. 2011; Keyak 2001; Keyak and Rossi 2000; Wang et al. 2008).

In addition to the characterisation of trabecular bone, Chapter 5 also presents an analysis of the multiaxial pressure dependent yield behaviour of sawbone polyurethane foams. Sawbone foams have been extensively used as a trabecular bone analogue material in the assessment of device performance (Agneskirchner et al. 2006; Completo et al. 2007a; Completo et al. 2007b; Poukalova et al. 2010; Vanlommel et al. 2011). Similar to trabecular bone, characterisation of polyurethane foam is primarily limited to uniaxial testing with a focus on the elastic regime. The results of this thesis show that the multiaxial post yield behaviour of synthetic bone is very similar to natural trabecular bone when a sufficient porosity is used.

However, confined compression testing of a more solid synthetic foam that does not contain a cellular structure (99.9% closed cell) reveals a stress-strain curve that is dissimilar to natural trabecular bone; such solid foams are better described by a pressure independent von Mises plasticity formulation. Hence, in the design of synthetic foams as trabecular bone analogues, decreasing the porosity in order to increase the Young's modulus will significantly affect the multiaxial post yield behaviour. Hence, for applications in which inelastic behaviour of peri-prosthetic foam may occur, the post yield behaviour of the foam, in addition to its elastic behaviour should be carefully considered. The practical importance of pressure dependent yielding of trabecular bone is further explored in subsequent chapters, in which multiaxial plasticity during vertebral device subsidence (Chapter 6 part B) and during press-fit implantation of a tibial component in total knee arthroplasty (Chapter 7) is investigated. Firstly, however, the role of the trabecular bone microstructure in the apparent level multiaxial yield behaviour is investigated in part A of Chapter 6.

The investigations of Chapter 6 are subdivided into two distinct parts. In part A, multiaxial compression loading of microstructural based trabecular bone models provide insight into the role of the trabecular microarchitecture in the apparent level yield behaviour of trabecular bone. The simulations uncover that, even under hydrostatic compression loading, localised stress concentrations and material yielding of individual trabeculae occur at a microscale level, resulting in a distinctive yield point in the apparent stress-strain curve. It is demonstrated that such localisations in the trabecular microarchitecture effect pressure dependent plasticity at the apparent level and are broadly independent of the plasticity formulation implemented at a microstructural level. Previous microstructural based models have primarily relied on uniaxial compression testing to investigate the role of the microstructural architecture in the yielding of trabecular bone at the apparent level (Bayraktar and Keaveny 2004; Guillén et al. 2011; Harrison et al. 2012; Niebur et al. 2000; Verhulp et al. 2008), apart from the studies of Niebur et al. (2002) and Bayraktar et al. (2004) in which biaxial strain and axial-shear testing was simulated using a principal strain based modulus reduction approach. In this chapter, continuum based crushable foam plasticity formulations are shown to replicate the

apparent level multiaxial stress-strain behaviour of the microstructural models, not just for confined compression, but also for hydrostatic compression. These analyses demonstrate the potential of microstructural based models of trabecular bone under multiaxial loading to inform the selection/development of continuum based models.

In part B of Chapter 6, a joint experimental-computational macroscale investigation of the subsidence of a vertebral interbody fusion device into trabecular bone is performed. Experimental imaging of the vertebral trabecular bone during the subsidence testing provides novel measurements of trabecular whitening regions, which signify localised plastic deformation, crushing and microdamage of trabeculae (Jungmann et al. 2011; Thurner et al. 2007; Thurner et al. 2006). Previous experimental investigations of fusion device subsidence have primarily relied on measuring the maximum failure load to evaluate subsidence resistance (Closkey et al. 1993; Hollowell et al. 1996; Lim et al. 2001; Lowe et al. 2004; Oxland et al. 2003; Steffen et al. 1998; Steffen et al. 2000). The experimentally measured whitening regions correlate well with regions of plastic deformation predicted during device subsidence using a crushable foam plasticity formulation. In addition to predicting the plastic zone, the crushable foam plasticity formulation also accurately predicts the subsidence forces. The von Mises, Hill and Drucker-Prager plasticity formulations fail to capture both the subsidence forces and plastic zones. The chapter further highlights the need for incorporating a pressure dependent plasticity formulation, such as the crushable foam plasticity formulations, for continuum based trabecular bone models that involve multiaxial plasticity. The experimental and computational techniques presented in part B of Chapter 6 have the potential to improve the design of interbody fusion devices: the experimental visualisation technique should be used to monitor the onset of yielding and to identify the resultant plastic zone; pressure dependent plasticity should be used for the accurate prediction of device subsidence.

In Chapter 7, simulation of the press-fit implantation of a tibial component stem into synthetic tibiae reveals that the computed stress distribution, implantation force and plastic deformation in the trabecular bone are highly dependent on the plasticity

formulation implemented. In comparison to a von Mises plasticity formulation, the incorporation of a crushable foam plasticity formulation for the trabecular bone results in more localised stress concentrations and plasticity at the bone-implant interface. The results of this chapter emphasise the significance of implementing a pressure dependent crushable foam plasticity formulation for the trabecular bone, despite many previous studies assuming linear elasticity (Monea et al. 2012; Ramamurti et al. 1997) or a von Mises plasticity formulation (Helgason et al. 2008; Taylor et al. 1995) for the investigation of the press-fit arthroplasty stems. Additionally, the present chapter highlights the significance of simulating the actual press-fit stem insertion process and also firmly establishes the importance of considering the role of friction at the implant-bone interface during implantation. Many previous studies have neglected to simulate the actual press-fit stem insertion process and alternatively employed interference elements to simulate the post-implantation press-fit conditions (Helgason et al. 2008; Ramamurti et al. 1997; Taylor et al. 1995). An in-depth understanding of the multiaxial post yield behaviour of trabecular bone is essential in order to enhance the analysis, design and development of devices that achieve primary fixation through press-fit anchorage. In order to facilitate future computational investigations of the press-fit stem implantation, further friction testing is required that precisely measures the friction coefficient between the implant and trabecular bone, including friction tests in which the applied normal load is sufficiently high to cause localised yielding. Future studies are also necessary to establish the optimum press-fit (amount of interference) for specific device designs in order to achieve good initial device fixation and to encourage positive bone remodelling and ingrowth. The findings of Chapter 7 may aid in the future computational simulation of press-fit device implantation.

The findings of this thesis are applicable to many other orthopaedic applications. The crushable foam plasticity formulations could be applied to various surgical procedures where large inelastic deformation of trabecular bone occurs including: orthopaedic screw insertion for locking plate fixation or intramedullary rod fixation; acetabular cup and femoral stem implantation in total hip arthroplasty; and stem implantation in total shoulder arthroplasty. Failure or subsidence of the aforementioned devices could also be investigated. Chapter 7 demonstrates the

importance of modelling the press-fit implantation process. Future studies should be conducted to further extend the implantation simulations presented in this thesis to include the fixation, post-implantation physiological loading and bone remodelling.

The focus of the present thesis is on the multiaxial pressure dependent yielding of trabecular bone. Uniaxial and confined compression simulations are used to calibrate the plasticity formulations. More extensive experimental loading is required to further develop constitutive formulations for the multiaxial plasticity of trabecular bone. Constitutive formulations should incorporate asymmetric yielding of trabecular bone in tension and compression, which has been reported experimentally (Keaveny et al. 1994; Kopperdahl and Keaveny 1998; Morgan and Keaveny 2001). A relationship between the apparent density and the von Mises equivalent stress to pressure yield ratio should also be explored. Various plasticity formulations have been proposed to describe a multiaxial yield surface of trabecular bone including the fabric-based models (Charlebois et al. 2010; Rincon-Kohli and Zysset 2009) the Tsai-Wu plasticity formulation (Fenech and Keaveny 1999; Keaveny et al. 1999), a cellular solid criterion (Fenech and Keaveny 1999) and the modified super-ellipsoid yield criterion (Bayraktar et al. 2004). Although many plasticity formulations have been proposed for trabecular bone, few have been applied to macroscale applications of multiaxial trabecular bone plasticity, such as those performed in the present study for vertebral subsidence and press-fit stem implantation. It would be interesting to examine the ability of these plasticity formulations to capture the subsidence forces and plastic zones in Chapter 6. Damage formulations have also been proposed for trabecular bone based on reducing the post yield modulus (Harrison et al. 2012; Niebur et al. 2002; Niebur et al. 2000; Verhulp et al. 2008). The experimental testing in the present study indicates that the inelastic deformation of trabecular bone is not recoverable and therefore a plasticity formulation must be used. However, cyclic testing should be implemented to investigate if a damage formulation is required, in tandem with a pressure dependent plasticity formulation for an enhanced continuum representation of trabecular bone.

In summary, the work presented in this thesis provides insight into the multiaxial post yield behaviour of trabecular bone. The initial simulations presented in Chapter 4 demonstrate a multiaxial stress state in the trabecular bone for both full and surface cementation techniques of the tibial component. High von Mises equivalent stress and pressure are predicted in the peri-prosthetic trabecular bone for both cementation techniques, demonstrating the importance of multiaxial loading and the potential for inelastic behaviour. In Chapter 5, the multiaxial yield behaviour of natural and synthetic trabecular bone is investigated under confined compression loading conditions. It is demonstrated that the pressure dependent crushable foam plasticity formulations accurately capture the post yield behaviour of trabecular bone. In part A of Chapter 6, using μCT based models of trabecular bone, it is shown that localised yielding of trabeculae affect the apparent level multiaxial plasticity of trabecular bone. In part B of Chapter 6 and in Chapter 7, two macroscale orthopaedic device applications that involve multiaxial trabecular bone plasticity are investigated: the subsidence of a vertebral interbody fusion device; and the press-fit stem implantation of a tibial component. During subsidence testing, the plastic zone and subsidence force are characterised experimentally. Both applications demonstrate that it is critical to incorporate pressure dependent yield behaviour in macroscale applications in order to accurately predict the multiaxial stress state in the peri-prosthetic trabecular bone. Continuum based pressure dependent crushable foam plasticity formulations accurately predict the multiaxial pressure dependent inelastic deformation of trabecular bone during device subsidence and during press-fit stem implantation. The implementation of continuum based crushable foam plasticity formulations for the simulation of the inelastic behaviour of trabecular bone may aid in the future analysis, design and development of orthopaedic devices.

References

Agneskirchner, J., Freiling, D., Hurschler, C., Lobenhoffer, P. (2006) Primary stability of four different implants for opening wedge high tibial osteotomy. Knee Surg Sports Traumatol Arthrosc 14 (3):291-300.

Bayraktar, H. H., Gupta, A., Kwon, R. Y., Papadopoulos, P., Keaveny, T. M. (2004) The modified super-ellipsoid yield criterion for human trabecular bone. J Biomech Eng 126 (6):677-684.

Bayraktar, H. H., Keaveny, T. M. (2004) Mechanisms of uniformity of yield strains for trabecular bone. J Biomech 37 (11):1671-1678.

Bessho, M., Ohnishi, I., Matsuyama, J., Matsumoto, T., Imai, K., Nakamura, K. (2007) Prediction of strength and strain of the proximal femur by a ct-based finite element method. J Biomech 40 (8):1745-1753.

Charlebois, M., Pretterklieber, M., Zysset, P. K. (2010) The role of fabric in the large strain compressive behavior of human trabecular bone. J Biomech Eng 132:1-10.

Chong, D. Y. R., Hansen, U. N., van der Venne, R., Verdonschot, N., Amis, A. A. (2011) The influence of tibial component fixation techniques on resorption of supporting bone stock after total knee replacement. J Biomech 44 (5):948-954.

Closkey, R. F., Parsons, J. R., Lee, C. K., Blacksin, M. F., Zimmerman, M. C. (1993) Mechanics of interbody spinal fusion. Analysis of critical bone graft area. Spine 18 (8):1011.

Completo, A., Fonseca, F., Simoes, J. A. (2007a) Finite element and experimental cortex strains of the intact and implanted tibia. J Biomech Eng 129 (5):791-797.

Completo, A., Fonseca, F., Simões, J. A. (2007b) Experimental validation of intact and implanted distal femur finite element models. J Biomech 40 (11):2467-2476.

Derikx, L. C., Vis, R., Meinders, T., Verdonschot, N., Tanck, E. (2011) Implementation of asymmetric yielding in case-specific finite element models improves the prediction of femoral fractures. Comput Method Biomech 14 (02):183-193.

Fenech, C. M., Keaveny, T. M. (1999) A cellular solid criterion for predicting the axial-shear failure properties of bovine trabecular bone. J Biomech Eng 121 (4):414-422.

Goldstein, S. A. (1987) The mechanical properties of trabecular bone: Dependence on anatomic location and function. J Biomech 20 (11-12):1055-1061.

Goldstein, S. A., Wilson, D. L., Sonstegard, D. A., Matthews, L. S. (1983) The mechanical properties of human tibial trabecular bone as a function of metaphyseal location. J Biomech 16 (12):965-969.

Guillén, T., Zhang, Q. H., Tozzi, G., Ohrndorf, A., Christ, H. J., Tong, J. (2011) Compressive behaviour of bovine cancellous bone and bone analogous materials, microct characterisation and fe analysis. J Mech Behav Biomed Mater 4 (7):1452-1461.

Harrison, N. M., McDonnell, P., Mullins, L., Wilson, N., O'Mahoney, D., McHugh, P. E. (2012) Failure modelling of trabecular bone using a non-linear combined damage and fracture voxel finite element approach. Biomech Model Mechanobiol:1-17.

Harrison, N. M., McDonnell, P. F., O'Mahoney, D. C., Kennedy, O. D., O'Brien, F. J., McHugh, P. E. (2008) Heterogeneous linear elastic trabecular bone modelling using micro-ct attenuation data and experimentally measured heterogeneous tissue properties. J Biomech 41 (11):2589-2596.

Helgason, B., Viceconti, M., Rúnarsson, T. P., Brynjólfsson, S. (2008) On the mechanical stability of porous coated press fit titanium implants: A finite element study of a pushout test. J Biomech 41 (8):1675-1681.

Hollowell, J. P., Vollmer, D. G., Wilson, C. R., Pintar, F. A., Yoganandan, N. (1996) Biomechanical analysis of thoracolumbar interbody constructs: How important is the endplate? Spine 21 (9):1032-1036.

Jungmann, R., Szabo, M. E., Schitter, G., Yue-Sing Tang, R., Vashishth, D., Hansma, P. K., Thurner, P. J. (2011) Local strain and damage mapping in single trabeculae during three-point bending tests. J Mech Behav Biomed Mater 4 (4):523-534.

Keaveny, T. M., Borchers, R. E., Gibson, L. J., Hayes, W. C. (1993) Trabecular bone modulus and strength can depend on specimen geometry. J Biomech 26 (8):991-1000.

Keaveny, T. M., Pinilla, T. P., Crawford, P. R., Kopperdahl, D. L., Lou, A. (1997) Systematic and random errors in compression testing of trabecular bone. J Orthop Res 15 (1):101-110.

Keaveny, T. M., Wachtel, E. F., Ford, C. M., Hayes, W. C. (1994) Differences between the tensile and compressive strengths of bovine tibial trabecular bone depend on modulus. J Biomech 27 (9):1137-1146.

Keaveny, T. M., Wachtel, E. F., Zadesky, S. P., Arramon, Y. P. (1999) Application of the tsai-wu quadratic multiaxial failure criterion to bovine trabecular bone. J Biomech Eng 121:99.

Keyak, J. H. (2001) Improved prediction of proximal femoral fracture load using nonlinear finite element models. Med Eng Phys 23 (3):165-173.

Keyak, J. H., Lee, I. Y., Nath, D. S., Skinner, H. B. (1996) Postfailure compressive behavior of tibial trabecular bone in three anatomic directions. J Biomed Mater Res 31 (3):373-378.

Keyak, J. H., Rossi, S. A. (2000) Prediction of femoral fracture load using finite element models: An examination of stress- and strain-based failure theories. J Biomech 33 (2):209-214.

Kopperdahl, D. L., Keaveny, T. M. (1998) Yield strain behavior of trabecular bone. J Biomech 31 (7):601-608.

Lim, T. H., Kwon, H., Jeon, C. H., Kim, J. G., Sokolowski, M., Natarajan, R., An, H. S., Bj Andersson, G. (2001) Effect of endplate conditions and bone mineral density on the compressive strength of the graft-endplate interface in anterior cervical spine fusion. Spine 26 (8):951-956.

Linde, F., Hvid, I. (1989) The effect of constraint on the mechanical behaviour of trabecular bone specimens. J Biomech 22 (5):485-490.

Lonner, J. H., Klotz, M., Levitz, C., Lotke, P. A. (2001) Changes in bone density after cemented total knee arthroplasty: Influence of stem design. J Arthroplasty 16 (1):107-111.

Lowe, T. G., Hashim, S., Wilson, L. A., O'Brien, M. F., Smith, D. A. B., Diekmann, M. J., Trommeter, J. (2004) A biomechanical study of regional endplate strength and cage morphology as it relates to structural interbody support. Spine 29 (21):2389-2394.

Monea, A. G., Pastrav, L. C., Mulier, M., Van der Perre, G., Jaecques, S. V. (2012) Numerical simulation of the insertion process of an uncemented hip prosthesis in order to evaluate the influence of residual stress and contact distribution on the stem initial stability. Comput Method Biomec:1-14.

Morgan, E. F., Keaveny, T. M. (2001) Dependence of yield strain of human trabecular bone on anatomic site. J Biomech 34 (5):569-577.

Mosekilde, L., Danielsen, C. C. (1987) Biomechanical competence of vertebral trabecular bone in relation to ash density and age in normal individuals. Bone 8 (2):79-85.

Niebur, G. L., Feldstein, M. J., Keaveny, T. M. (2002) Biaxial failure behavior of bovine tibial trabecular bone. J Biomech Eng 124 (6):699-705.

Niebur, G. L., Feldstein, M. J., Yuen, J. C., Chen, T. J., Keaveny, T. M. (2000) High-resolution finite element models with tissue strength asymmetry accurately predict failure of trabecular bone. J Biomech 33 (12):1575-1583.

Oxland, T. R., Grant, J. P., Dvorak, M. F., Fisher, C. G. (2003) Effects of endplate removal on the structural properties of the lower lumbar vertebral bodies. Spine 28 (8):771-777.

Poukalova, M., Yakacki, C. M., Guldberg, R. E., Lin, A., Saing, M., Gillogly, S. D., Gall, K. (2010) Pullout strength of suture anchors: Effect of mechanical properties of trabecular bone. J Biomech 43 (6):1138-1145.

Ramamurti, B. S., Orr, T. E., Bragdon, C. R., Lowenstein, J. D., Jasty, M., Harris, W. H. (1997) Factors influencing stability at the interface between a porous surface and cancellous bone: A finite element analysis of a canine in vivo micromotion experiment. J Biomed Mater Res 36 (2):274-280.

Rincon-Kohli, L., Zysset, P. (2009) Multi-axial mechanical properties of human trabecular bone. Biomech Model Mechanobiol 8 (3):195-208.

Røhl, L., Larsen, E., Linde, F., Odgaard, A., Jørgensen, J. (1991) Tensile and compressive properties of cancellous bone. J Biomech 24 (12):1143-1149.

Steffen, T., Gagliardi, P., Hurrynag, P., Aebi, M. Optimal implant-endplate interface for interbody spinal fusion devices. In: European Spine Society, Innsbruck, Austria, 1998.

Steffen, T., Tsantrizos, A., Aebi, M. (2000) Effect of implant design and endplate preparation on the compressive strength of interbody fusion constructs. Spine 25 (9):1077-1084.

Taylor, M., Tanner, K. E., Freeman, M. A. R., Yettram, A. L. (1995) Cancellous bone stresses surrounding the femoral component of a hip prosthesis: An elastic-plastic finite element analysis. Med Eng Phys 17 (7):544-550.

Thurner, P. J., Erickson, B., Jungmann, R., Schriock, Z., Weaver, J. C., Fantner, G. E., Schitter, G., Morse, D. E., Hansma, P. K. (2007) High-speed photography of compressed human trabecular bone correlates whitening to microscopic damage. Eng Fract Mech 74 (12):1928-1941.

Thurner, P. J., Erickson, B., Schriock, Z., Langan, J., Scott, J., Zhao, M., Weaver, J. C., Fantner, G. E., Turner, P., Kindt, J. H. (2006) High-speed photography of the development of microdamage in trabecular bone during compression. J Mater Res 21 (5):1093-1100.

Vanlommel, J., Luyckx, J. P., Labey, L., Innocenti, B., De Corte, R., Bellemans, J. (2011) Cementing the tibial component in total knee arthroplasty: Which technique is the best? J Arthroplasty 26 (3):492-496.

Verhulp, E., Van Rietbergen, B., Müller, R., Huiskes, R. (2008) Micro-finite element simulation of trabecular-bone post-yield behaviour - effects of material model, element size and type. Comput Method Biomech 11 (4):389-395.

Wang, X., Allen, M. R., Burr, D. B., Lavernia, E. J., Jeremic, B., Fyhrie, D. P. (2008) Identification of material parameters based on mohr-coulomb failure criterion for bisphosphonate treated canine vertebral cancellous bone. Bone 43 (4):775-780.